APPROACHES FOR OSCILLATION MONITORING AND DAMPING OF WIND INTEGRATED POWER GRID

by

Niroj Gurung

A dissertation submitted to the faculty of
The University of North Carolina at Charlotte
in partial fulfillment of the requirements
for the degree of Doctor of Philosophy in
Electrical Engineering

Charlotte

2018

Approved by:

Dr. Sukumar Kamalasadan

Dr. Yogendra P. Kakad

Dr. Robert Cox

Dr. David Young

ABSTRACT

NIROJ GURUNG. Approaches for Oscillation Monitoring and Damping of Wind Integrated Power Grid. (Under the direction of DR. SUKUMAR KAMALASADAN)

Wind energy has emerged as one of the major choice of sustainable energy especially due to lower generation cost and push for alternative sources of clean energy. However, the technological difference in wind generation is certain to create changes in dynamics of the power system that is mostly dominated by synchronous generators. For example, the dynamic stability of the system can be affected by wind generators such as Doubly Fed Induction Generators (DFIG) due to reduced inertia, new transmission lines, lower number of Power System Stabilizers (PSS) and so on. It is, therefore, essential to carefully analyze the impact of growing wind penetration on the stability of power system. This dissertation will focus specifically on the impact of DFIG based wind generation on power system stability. The ability to rapidly control the active and reactive power makes DFIG a dynamic source that can support the grid during disturbances and thus, can be used to enhance the dynamic stability of the system. In this research, first, modal analysis of DFIG integrated power grid is investigated. Second, based on the modal analysis and signal selection, active and reactive power PSS is designed. Then a power system oscillation damping controller design for DFIG is investigated. Various approaches for power oscillation damping is evaluated using local signals or remote signals. Moreover, to address the uncertainty in power system model used in planning, a measurement based approach for estimating the proper power system model is designed. The modal analysis of the estimated model can be used as an analytical tool to predict the performance of the system in time-domain. Further, a control approach is designed and implemented using the proposed identification on a small-scale and large-scale power grid.

ACKNOWLEDGEMENTS

First and foremost, my sincere gratitude goes to my supervisor Dr. Sukumar Kamalasadan for all his time and effort to provide me with guidance and valuable insight throughout my doctoral research. I really appreciate his friendly, inspiring and encouraging attitude as mentor to my research.

I would like to thank the members of the committee Dr. Yogendra Kakad, Dr. Robert Cox and Dr. David Young for their valuable guidance and feedback in this work.

I wish to acknowledge University of North Carolina at Charlotte for providing financial support to my doctoral research in the form of Graduate Assistant Support Plan (GASP) award.

I am thankful to my colleagues in Power Energy and Intelligent Systems Lab for their comments in this work.

Finally, I would like to thank my wife, my parents and my brother for being my ultimate source of love, support and inspiration.

DEDICATION

This dissertation is dedicated to my wife Susma, my brother Dilip and my parents.

TABLE OF CONTENTS

LIST OF FIGURES

LIST OF TABLES

LIST OF ABBREVIATIONS

DFIG An acronym for Doubly Fed Induction Generator.

FACTS an acronym for Flexible Alternating Current Transmission System

GSC An acronym for Grid Side Converter

HVDC an acronym for High Voltage Direct Current

RSC An acronym for Rotor Side Converter

SVC an acronym for Static Var Compensator

TCSC an acronym for Thyristor Controlled Series Capacitors

CHAPTER 1: INTRODUCTION

Growing concern for climate change and falling cost of wind energy generation has intensified the growth of wind power generation in US and around the world in last decade [1, 5]. According to the annual report released by Global Wind Energy Council (GWEC), total cumulative wind capacity of the world stands at 539.58 GW in 2017, 52.5 GW added in year 2017 alone [5]. China tops the list of countries with largest amount of installed wind capacity with 188.2 GW and comes USA, Germany, India and Spain. The total installed capacity of wind power in US was 89.07 GW with addition of 7.0 GW by the end of year 2017 [2, 3, 5]. Total installed wind power capacity has actually overtaken the total installed capacity of hydroelectric power capacity which is consistent at around 79 GW in US. Figure 1.1 shows the cumulative capacity, total annual and/or quarterly installation of wind capacity in US from year 2001 to 2017 [2]. The US Department of Energy (DOE) released *Wind Vision: A New Era for Wind Power in the United States* which shows wind energy can supply the U.S. with 10 percent of the country's electricity by 2020, 20 percent by 2030 and 35 percent by 2050 [4]. States have set their target of providing certain percentage of total end-use electricity via renewable sources by setting *Renewable Power Standard (RPS).*

The wind turbine generators (WTGs) distributed across a large area forming a wind farm, but the total output of the farm normally connects to the bulk power system at a single substation, in a fashion similar to conventional central-station generation [6]. There are many different generator types for wind-power applications in use today. Variable speed wind turbines utilizing doubly fed induction generators (DFIGs) are the most popular generation technology in the power industry. The

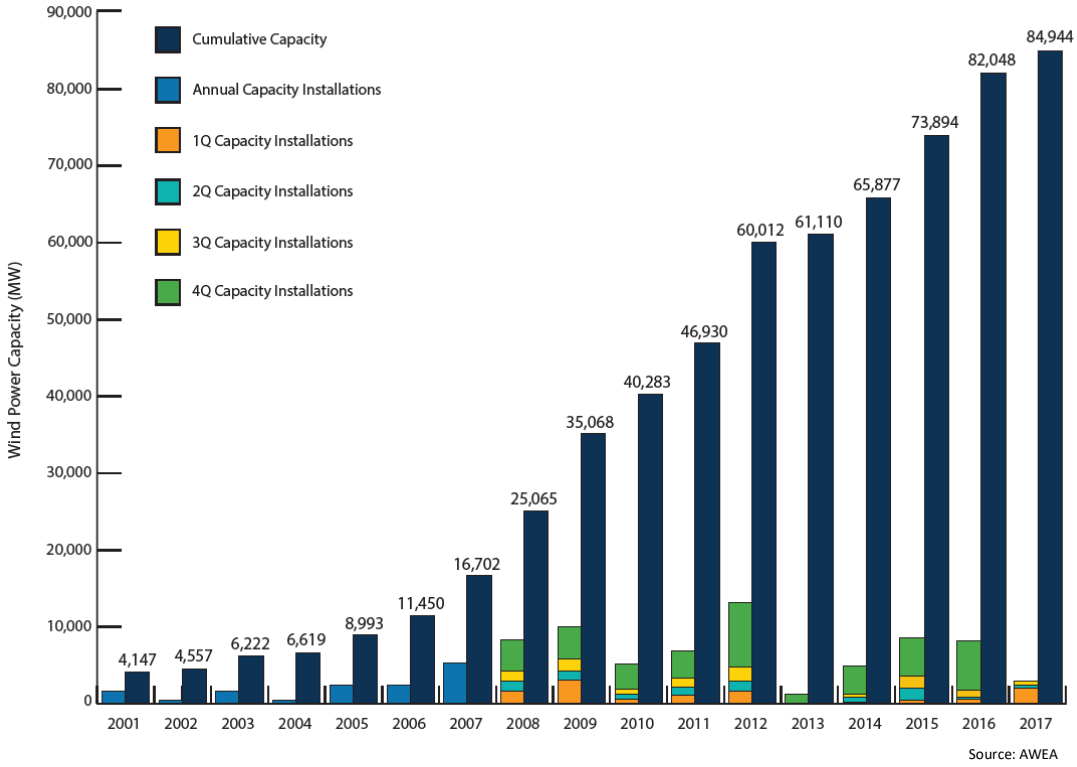

Figure 1.1: Installed Wind Power Capacity in US.

DFIG is capable of operating near its optimal turbine efficiency over a wider range of wind speeds through variable rotor speed operation(usually $\approx \pm 30\%$ slip). This is achieved through the application of a back-to-back converter that tightly controls the rotor current and allows for asynchronous operation. Consequently, the power system originally designed for conventional synchronous generation experiences change in dynamics and operating characteristics. This necessitates the assessment of power system stability under anticipated changes that the new generation topology will bring, and take appropriate action if required.

System stability and dynamics evaluation can be carried out by observing the behavior of the system when subjected to a disturbance. A stable power system is one in which the system dominant with synchronous machines when perturbed, will either return to their original state if there is no net change of power or will acquire a new state without losing synchronism [7]. The perturbations can be of

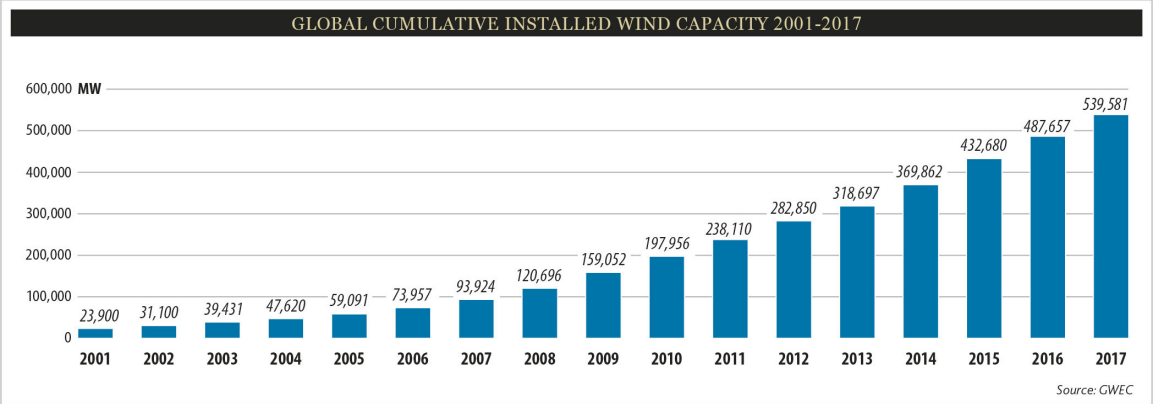

Figure 1.2: Installed Wind Power Capacity in the world.

several types and can lead to two major categories of rotor angle instabilities, namely, transient instability and small signal instability. Usually, the small perturbation causes a transient that is oscillatory in nature and if the system is stable, oscillations will be damped. Large perturbations such as three phase short circuit faults, on the other hand, may result in transients that instigate aperiodic angular separation of the generator rotors.

1.1 Power System Stability

Power System Stability is defined as the ability of an electric power system, for a given initial operating condition, to regain a state of operating equilibrium after being subjected to a physical disturbance, with most system variables bounded so that practically the entire system remains intact [28]. Power system is a highly nonlinear system whose operating point is constantly changing. If subjected to a disturbance, the stability of the system depends on the initial operating condition and the nature of the disturbance. Power systems are subjected to a wide range of disturbances, both small and large. Small disturbances in the form of load changes occur continually; the system must be able to adjust to the changing conditions and operate satisfactorily. It must also be able to survive numerous disturbances of a severe nature, such as a short circuit on a transmission line or loss of a large generator. A large disturbance may lead to structural changes due to the isolation of the faulted elements.

If following a disturbance the power system is stable, it will reach a new equilibrium state with the system integrity preserved. It means all generators and loads remain connected through a single contiguous transmission system. However, some generators and loads may be disconnected by the isolation of faulted elements or intentional tripping to preserve the continuity of operation of bulk of the system. Interconnected systems, for certain severe disturbances, may also be intentionally split into two or more "islands" to preserve as much of the generation and load as possible. The actions of automatic controls and possibly human operators will eventually restore the system to normal state. On the other hand, if the system is unstable, it will result in a run-away or run-down situation; for example, a progressive increase in angular separation of generator rotors, or a progressive decrease in bus voltages. An unstable system condition could lead to cascading outages and a shutdown of a major portion of the power system.

Power system stability is the property of a power system that ensures the stable operating equilibrium under normal conditions and restores an acceptable state of equilibrium when the system is subjected to a disturbance [27]. The ability of the network to cope with these disturbances and to restore the normal operating condition is addressed by stability studies. In order to obtain satisfactory system operation, synchronous machines that represents major portion of the electrical power generation should remain in synchronism. One of the major factors governing the stability is the dynamics of generator rotor angles and power-angle relationships [27].

In an interconnected system, the ability to restore equilibrium between electromagnetic torque and mechanical torque is determined by the rotor angle stability of each synchronous machine. With the increased number of wind farms in operation, which are asynchronous in nature, the system experiences change in dynamic characteristics. The characteristics associated with exploitation of wind energy and components used for power conversion does contribute to change in system dynamics.

Following a perturbation, the change in electromagnetic torque of the synchronous machine can be explained by two torque components, namely, the synchronizing torque component and the damping torque component. System stability depends on the existence of both components of torque for each of the synchronous machines [28]. Insufficient synchronizing torque results in non-oscillatory instability whereas insufficient damping torque results in oscillatory instability. In order to simplify the analysis of stability problems, the rotor angle stability is categorized into transient stability and small signal stability.

1.1.1 Transient Stability

Transient stability is the ability of a power system to maintain synchronism when subjected to a severe disturbance. Severe network disturbances include equipment outages, load changes or faults that result in large excursion of generator rotor angles. The resulting system response is influenced by the nonlinear power angle relationship. Transient stability depends on both the initial operating state of the system and the severity of the disturbance. Instability is usually caused due to insufficient synchronizing torque and results in aperiodic angular separation. The time frame of interest in transient stability studies is usually 3-5 seconds following the disturbance. The duration may extend up to 10-20 seconds for a very large system with dominant inter-area swings [27].

In a synchronous machine, if during a network disturbance the electrical torque falls below the mechanical torque, the rotor will accelerate causing the increase in rotor speed and angular position of the rotor flux vector. Since the increase in rotor angle results in an increase in the generator load torque, a mechanism exists to increase the electrical torque so as to match the mechanical torque. In case of DFIGs, generator load disturbances also give rise to variations in the speed and the position of the rotor. However, due to the asynchronous operation involved, the position of the rotor flux vector is not dependent on the physical position of the rotor and the synchronizing

torque angle characteristic does not exist [48]. The transient stability of a system with wind turbines also depends on factors such as fault conditions and network parameters. Wind speed, however, is assumed to be constant in transient stability simulations involving wind turbines. The mechanical power, on the other hand, is not constant as it depends on wind speed as well as the generator speed [56].

1.1.2 Small Signal Stability

In large power systems, the small-signal stability problem can be either local or global in nature. Power system oscillations are usually in the range between 0.1 and 2 Hz depending on the number of generators involved. Local oscillations lie in the upper part of the range and consist of the oscillation of a single generator or a group of generators against the rest of the system [27, 57]. Stability of these oscillations depends on the strength of the transmission system as seen by the power plant, generator excitation control systems and plant output. The accurate modeling of the exciter and other supplementary controls such as power system stabilizer (PSS) is essential for analyzing this type of problems.

In contrast inter area oscillations are in the lower part of the frequency range representing oscillations among the group of generators. Since an inter-area mode usually involves a large portion of an interconnected system, an elaborate representation of the full system is required to accurately study this phenomena. The most critical controls affecting inter-area-modes are the excitation control systems. In certain situations, speed governor characteristics may also have an impact. System operating conditions (load levels, major power transfers, etc) affect the characteristics of inter-area modes, particularly their mode shapes and damping. Other controls such as HVDC modulation and FACTS controllers could have a significant contribution to the damping of inter-area modes. As such, DFIG based wind turbines consisting of the power electronics converter imparts significant effect on the dynamic performance of the system. The time frame of interest in small signal stability studies is of the or-

der of 10-20 seconds following a disturbance [28]. The important point to note is that the DFIGs are asynchronous machines but the machines inject power into the system and as a result will affect the angular positions of all the other synchronous generators. In addition DFIGs do not contribute to the inertia of the system. Hence, the synchronizing capability of the synchronous generators in the system will be affected. This leads to a significant impact on the electromechanical modes of oscillation.

On the other hand, utilizing the fast active and reactive power control capabilities of these wind generators can be utilized to increase the damping of the poorly damped inter-area oscillatory modes. This requires proper design and tuning of supplementary damping controller for active and/or reactive power control of DFIG.

1.2 Research Motivation

There are 4 main types of wind turbines based on generation technology used [43]. Type 1 and Type 2 WTGs are induction generators directly coupled to the grid, and hence contribute in inertial response during grid disturbances. Type 3 and Type 4 WTGs are dominated by power converters which allow the operation of wind turbines over a wider range of speed and control active and reactive power independently. However, they do not provide any inertial response during grid disturbances due to the power electronic converter which effectively decouples the grid and the machine inertia.

Type 3 WTGs are doubly fed induction generators (DFIGs) with partially rated ($\approx$30%) power converter which provide controlled variable frequency voltage excitation to the rotor winding. Power electronic converter provides the flexibility to control active and reactive power independently while being partially rated. DFIG is the most widely used WTG topology in current market, and will likely continue to dominate the market in coming years. Meticulous analysis of grid dynamics under high wind generation scenario is necessary to understand the impact on the grid, and proper control methods should be developed to address any threat to the dynamic

stability of the system.

1.2.1 Problem Statement

DFIGs are based on generation technology that is different from the conventional synchronous generators. The grid dynamics is set to change as more and more wind generators come online. Synchronous generators are directly coupled with the grid and any change in grid is reflected in the dynamic performance of the synchronous generators. Synchronous generators usually have high inertia time constant but are lightly damped systems, and depends on the network to damp its rotor oscillation. Moreover, during the grid disturbance causing frequency deviation, the inertia of these generators respond automatically. Two types of torque are developed following any network disturbance, the first type is called synchronizing torque and is in phase with the rotor angle, and the second type is called damping torque which is in phase with the rotor speed deviation. Lack of synchronizing torque leads to aperiodic instability while lack of damping torque leads to oscillatory instability. The problem of low synchronizing torque is greatly solved by employing automatic voltage regulators. Lack of enough damping torque is the major issue related with power system rotor angle stability. DFIGs do not provide inertial response during grid disturbances. The turbine inertia is partially decoupled from the grid via power electronic converter. DFIGs reduce the net inertia of the system as the penetration level increases, and its impact on dynamic stability of the power system will likely become prominent. DFIGs affect the dynamic stability of power system in various ways such as replacing the synchronous generators, reducing the number of PSS, changing the power flow in critical tie-lines, by addition new lines to meet power transmission requirement and so on.

Grid code requirements have been implemented in various systems that require voltage and var control, active power control, frequency control, fault ride through capability, the capability of DFIG power management on damping power system os-

cillation is still not fully utilized [8]. As the wind power technology matures and penetration level increases, the system operator will require the wind turbine operators to provide dynamic support mechanism such as the inertial response and power oscillation damping support. First, it is essential to carefully study the impact of increasing amount of wind penetration on dynamic stability of the grid. According to [50], wind generators themselves do not induce new frequency oscillations because of the generation technology used in wind turbine. It has been suggested that DFIG can improve the damping of power system oscillation[10, 50]. According to ref. [15, 17], the DFIGs have good damping performance into a weak area of the grid. However, ref [51] showed that the DFIGs can have both beneficial and deteriorating impact on power system damping and sensitivity analysis of the modes with respect to inertia will provide rigid indicator of the DFIG impacts. It has been shown in [20] that the local and plant level control of wind farm influence damping. Ref. [18, 19, 20] put an argument that in general large scale wind integration has no noticeable effect on inter-area mode stability, however, the structural change that the wind generators bring might lead to poor damping.

The impact of DFIG is dependent on various factors such as location of the generation resources, local control topology, and grid characteristics. Irrespective of the negative or positive impacts of DFIGs, the need for wind generators to provide damping support to the low frequency electromechanical oscillations is imminent. This is because of the anticipated increment in the penetration level of wind power capacity as suggested by the current trend. It has been shown that the DFIG can improve the damping of the power grid as the penetration level increases, and also proposed a power system stabilizing control based on rotor flux magnitude and angle modulation [48, 49]. According to ref. [15], DFIGs provide good damping performance in a weak grid, compared to a conventional generator. A supplementary control strategy so that inertial response of DFIG can be used to provide the frequency and oscillation

damping support in [53]. The modes of response of the DFIG, as well as the stability of the reactive power control loop, were analyzed in [17, 21]. The idea of power oscillation damping support is essentially to use the advanced capability of DFIGs to change active and reactive power generation. By providing appropriate signals to DFIG controllers to modulate its active and reactive power, the improvement in power system oscillation damping can be achieved [21]. However, such control may result in deterioration of torsional and voltage dynamics of DFIG [21, 16].

1.2.2 Research Objectives

This research work has following objectives:

- To develop DFIG based wind turbine/generator models for small signal and large signal transient stability study.
- To design an optimal control of variable speed wind turbine/generator such as DFIG.
- To gain insight on small signal stability and transient stability of DFIG integrated power system under various scenarios such as replacing the existing synchronous generators by DFIG based wind generation through eigenvalue analysis and non-linear time domain simulation.
- To evaluate ability and efficacy of DFIG to damp grid oscillation via active and reactive power management.
- To design local Power System Stabilizer for DFIG.
- To design optimal Wide Area Control (WAC) methodologies to damp the electromechanical oscillation in wind integrated bulk power systems.

1.2.3 Proposed Approach

Eigenvalue analysis is a very powerful technique applied to linear time invariant (LTI) systems. It is a frequency domain analysis technique that provides an essential

information about time domain behavior of the system. Power system is a highly nonlinear system. However, for small signal perturbation, the properties of a power system about its operating point can be approximately described by a linearized model. Linearized model is a very useful to understand the power system dynamics in small signal stability terms. Eigenvalue analysis provides the information such as stability of the power system, the dynamic response to small perturbation dictated by damping ratio and frequency of dominant modes, participation analysis of various states/machines on power system modes of oscillation, controllability and observability analysis for suitable control design and so on.

The non-linear models based on differential and algebraic equations (DAEs) that describe the power system dynamics are required to test the controllers, and are developed using MATLAB-Simulink modeling environment. The model initialization is done based on power flow solution obtained by using available power flow solution techniques such Newton-Raphson method, Gauss-Seidel methods etc. The model initialized at a particular operating point is linearized using *linearize* function of Simulink Control Design Toolbox. Simulink Control Design uses a block-by-block approach to linearize models, instead of using full-model perturbation to obtain exact linearization. The MATLAB's linearization and eigenvalue analysis were validated against commercial software tools designed for small signal stability analysis of power system viz. *PSS/e, DSATools, PowerFactory.* The information obtained from the assessment of eigenvalues and eigenvectors such as critical modes can be verified in time-domain using non-linear simulation of models in MATLAB-Simulink. The controllers are designed using MATLAB inbuilt functions such as *lqi, lqg, kalman, place, n4sid* etc. The inbuilt functions of MATLAB optimization toolbox such as *fmincon* are used to solve the non-linear optimization problems such as pole placement control design using output feedback.

1.3 Research Contribution

The contribution of this work can be summarized as following:

- *Modal Analysis of DFIG*: Detailed model of DFIG was developed that include rotor and stator transients, and torsional dynamics of gearbox interfaced generator rotor and turbine, and control system. The detailed modal analysis provide the insight on inherent modes of the DFIG in open loop form and in closed loop form. This insight is useful for design of DFIG speed, voltage and current control.

- *Optimal Control Design for DFIG*: The PI control used in DFIG has its limitations during transients and parameter variation. A linear-quadratic-integral commonly known as *lqi* control is designed for DFIG speed control, and current control of RSC and GSC [37]. The controllers are based on state space models. The simulation results showed that the *lqi* controller performance is superior compared to PI controller.

- *Small signal stability analysis of DFIG integrated power system models*: The increasing level of DFIG into a grid was simulated to study its impact on small signal and transient stability of the grid. It was concluded that DFIG neither creates an oscillatory mode with the grid nor participates in existing system oscillatory modes. However, the system stability can be affected due to the structural changes in the system resulting from rising penetration of DFIG such as reduced system inertia, change in tie-line power flow and so on.

- *PSS Design for DFIG*: Thanks to the DFIG's capability to modulate its active and reactive power [39], DFIGs can be used to damp the power system oscillation using local signals such as bus frequency, angular deviation or power flow in neighboring transmission lines. The modal analysis and time domain

analysis showed that DFIGs can damp the oscillation quickly by producing active/reactive power in response to oscillation in feedback signals and also enhance the transient stability of the system.

- *Model based Wide Area Control of DFIG for Power System Oscillation Damping*: The limited visibility of inter-area modes in local signals reduce the potential of using DFIG control for power oscillation damping. The advance in phasor measurement technology has helped to realized wide area control of power systems that facilitate use of global/remote signals at the expense of added communication and data transfer cost. A linear-quadratic-gaussian (LQG) controller based on wide area measurement signals was designed [38]. The approach can be summarized as: a) linearization of power system mode, b) reduction of power system model, c) computation of state feedback gain matrix using *lqr*, d) Kalman filter/observer design using *kalman*. The simulation results showed that the controller effectively damped the inter-area modes of modified IEEE 68-bus, 16-machine system, which are otherwise poorly damped despite the presence of PSS in 12 out of 16 synchronous generators.

- *System Identification Based Wide Area Control of DFIG for Power System Oscillation Damping*: One of the challenges in power system planning is to obtain an accurate model to replicate the actual power system dynamics. System identification technique based on measurement of input and output can provide a reduced order model that carries information about actual system response in interested range of frequency. A canonical variate analysis (CVA) was used in this work to estimate subspace state space system model. The model is validated against actual system frequency response and validation time domain data-set. In next step, an optimal output feedback controller is obtained using non-linear optimization [41]. The objective Lyapunov function can include the

performance requirements such as damping of the critical inter-area modes in the identified model. The controller was tested with actual non-linear power system model and its efficacy and robustness against time-delay and operating point uncertainty has been investigated in small and large scale power system models.

1.4 Intellectual Merit and Broader Impact

The Intellectual Merit of the work is

1. This project provides a method to evaluate the impact of DFIG based WTG in power grid stability. The approach allows the power grid operator to evaluate the affect of variations in DFIG power with respect to location, size, and controllability.

2. This project provides a new method for controlling the DFIG that can stabilize the power grid based on wide area signals. The proposed method can factor in on the contributions of each wind generator based on DFIG size, controllability, and location. This ensures the optimal selection and utilization of the available resources for grid stability improvement.

3. The project also provides a new architecture that can identify the reduced order state-space model of the power grid based on input and output measurement. The main advantage of this approach is that signals for control can be selected while in operation based on online controllability and observability monitoring; it allows better for stabilization properties.

4. One of the drawbacks of the power system controller based on mathematical approximation of the model is its lack of ability to track the power system characteristics as the operation of the system changes. An online identification based stabilizer design can track the characteristics of power grid with operational changes, and tune the controller based on the identified model.

Broader Impact of the work is

1. The approach can be used to control other devices available for power system control and stabilization such as energy storage devices, other renewable generators and also FACTS devices. Proper coordination can achieve the optimal utilization of the available resources.

2. The system identification and control approach is generic, and can be used readily in other control areas.

3. The approach allows higher penetration of renewables on the power grid without compromising grid stability. This will eventually help us to reach the goal for reliable and sustainable energy solutions.

4. The approach can provide economical value and grid security as the capabilities of the existing devices are utilized in an optimal manner to ensure the reliable operation of the grid.

1.5 Thesis Organization

The remainder of this dissertation is organized as follows. In chapter 2, the dynamic model of synchronous generator and doubly-fed induction generator and their associated controls are presented. A new optimal control design for DFIG speed and converter control based on linear-quadratic-integral (LQI) approach is presented in chapter 2 as well. Modal analysis of DFIG and DFIG integrated power system is presented in chapter 3 to elaborate the modes of DFIG and the impact of DFIG penetration on electromechanical modes of the power system. Based on the conclusion of this chapter that the DFIG can sometimes adversely impact the power system oscillatory modes, design of power system stabilizer based on local signal selection is presented in chapter 4. The limited ability of the local PSS to damp the inter-area mode has been illustrated using IEEE 68-bus benchmark system. In chapter 5,

wide area measurement based linear-quadratic-gaussian (LQG) control is designed for DFIG that effectively damps the inter-area modes of oscillation. A new approach of optimal power oscillation damping control design based on identification of reduced order power system model is presented in chapter 6. Finally, the conclusions and the future works are presented in chapter 7.

CHAPTER 2: POWER SYSTEM MODELING

The modern power grid is composed of conventional synchronous generators and the controls associated with such generators such as excitation systems, PSS, FACTS devices such as TCSC, SVC, transmission network, loads etc. Recently, there is a surge of renewable power generators that are based on generation technology very different to that of conventional generators. Wind and solar are the two major sources that are rapidly growing into the modern power grid, and are certain to bring the changes in dynamic and steady state characteristics of the system. This thesis will focus on the impact of DFIG based wind generators on dynamic stability of the system.

DFIG is the most popular wind power generation topology in the current market, and will likely continue to dominate the new generation added in near future. DFIG is based on a wound rotor induction generator with controlled rotor excitation to provide independent control of active and reactive power. This results in decoupling the rotor and turbine inertia from the grid. Synchronous generators are directly coupled with the AC grid and hence, are the source of inertia to the grid in the sense that any disturbance in the grid can be observed in the rotor speed and angle of the synchronous generators. DFIGs remain indifferent to such scenarios unlike synchronous generators unless special control system is designed to make use of its inertial mass. A detailed model of DFIG is necessary to get the clearer picture of the impact of these newer generation topology on the existing grid, and also to understand the capability of the DFIGs to support the grid dynamics. The details on the dynamic models used to represent synchronous generators and their associated control and DFIG and their associated controls are discussed in the following sections.

2.1 Synchronous Generator

A round rotor synchronous generator can be represented in synchronous d-q reference frame rotating with rotor speed w_r with q-axis aligned along the rotor[27].

Stator voltage equations in p.u. can be written as:

$$v_q = -r_a i_q + \omega_r \psi_d + \frac{1}{\omega_B} p\psi_q \tag{2.1}$$

$$v_d = -r_a i_d - \omega_r \psi_q + \frac{1}{\omega_B} p\psi_d \tag{2.2}$$

$$v_0 = -r_a i_0 + \frac{1}{\omega_B} p\psi_0 \tag{2.3}$$

Where,

v_q, v_d and v_0 denote stator voltage in q, d and 0-axes respectively,

i_q, i_d and i_0 denote stator current in q, d and 0-axes respectively,

ψ_q, ψ_d and ψ_0 denote stator flux induced in q, d and 0-axes respectively,

r_a denotes armature resistance,

ω_r denotes rotor speed,

ω_B denotes base speed, and

p denotes differential operator i.e. d/dt.

Similarly, rotor voltage equations in p.u. can be written as:

$$v_{fd} = -r_{fd} i_{fd} + \frac{1}{\omega_B} p\psi_{fd} \tag{2.4}$$

$$0 = -r_{1d} i_{1d} + \frac{1}{\omega_B} p\psi_{1d} \tag{2.5}$$

$$0 = -r_{1q} i_{1q} + \frac{1}{\omega_B} p\psi_{1q} \tag{2.6}$$

$$0 = -r_{2q} i_{2q} + \frac{1}{\omega_B} p\psi_{2q} \tag{2.7}$$

where,

v_{fd} denotes rotor field voltage,

r_{fd}, r_{1d}, r_{1q} and r_{2q} denote field and amortisseur resistance,

i_{fd}, i_{1d}, i_{1q} and i_{2q} denote field and amortisseur circuit currents, and

ψ_{fd}, ψ_{1d}, ψ_{1q} and ψ_{2q} denote field and amortisseur flux linkages.

Stator flux linkage equations in p.u. can be written as:

$$\psi_d = -L_d i_d + L_{ad} i_{fd} + L_{ad} i_{1d} \tag{2.8}$$

$$\psi_q = -L_q i_q + L_{aq} i_{1q} + L_{aq} i_{2q} \tag{2.9}$$

$$\psi_0 = -L_0 i_0 \tag{2.10}$$

where,

L_{ad} and L_{aq} denote mutual inductance between stator and rotor windings,

L_l denotes leakage inductance,

$L_d = L_{ad} + L_l$, $L_q = L_{aq} + L_l$ and L_0 represent stator inductance.

Rotor flux equations in p.u. can be written as:

$$\psi_{fd} = -L_{ad} i_d + L_{ffd} i_{fd} + L_{f1d} i_{1d} \tag{2.11}$$

$$\psi_{1d} = -L_{ad} i_d + L_{f1d} i_{fd} + L_{11d} i_{1d} \tag{2.12}$$

$$\psi_{1q} = -L_{aq} i_q + L_{11q} i_{1q} + L_{aq} i_{2q} \tag{2.13}$$

$$\psi_{2q} = -L_{aq} i_q + L_{aq} i_{1q} + L_{22q} i_{2q} \tag{2.14}$$

where,

$L_{ffd} = L_{fd} + L_{f1d}$, $L_{11d} = L_{1d} + L_{f1d}$, $L_{11q} = L_{1q} + L_{aq}$, $L_{22q} = L_{2q} + L_{aq}$ denote inductance of rotor winding.

Electromagnetic torque (T_e) produced by the generator in p.u. is given by:

$$T_{eg} = \psi_d i_q - \psi_q i_d \tag{2.15}$$

A lumped-mass model of the turbine with inertia constnt 'H_g' is used and the

electomechanical dynamics of the turbine and generator can be expressed in p.u. as:

$$\frac{d\delta}{dt} = \omega_B(\omega_g - \omega_s) = \omega_B \Delta\omega_g \tag{2.16}$$

$$2H_g \frac{d\Delta\omega_g}{dt} = T_m - T_{eg} - D_g \Delta\omega_g \tag{2.17}$$

Here, δ is the rotor angle in radians, T_m is the mechanical torque, D_g is the rotor damping coefficient, ω_g is the rotor angular velocity and ω_s is the synchronous angular velocity.

2.2 Exciter and Power System Stabilizer

The main function of the Automatic Voltage Regulator (AVR) is to regulate the generator terminal voltage at the required set-point. According to equation (2.2), (2.8), (2.11) and (2.11), the voltage v_d can be controlled by controlling the field current i_{fd}. Thus, AVR controls the field voltage (v_{fd}) to induce required i_{fd}. There are variety of AVR structure used in the large scale generators across North America and around the world. We will use two types of AVRs for the excitation of the generators. The first type is an IEEE standard DC exciter known as IEEE-DC4B. The second type is standard static excite also known as IEEE-ST1A. A simplified IEEE-ST1A structure with a voltage transducer modeled as a low pass filter with time constant 'T_r' and static gain 'K_A' is shown in Figure 2.1.

The differential equations governing the operations of IEEE-DC4B and IEEE-ST1A are given by equation (2.18) and (2.19) respectively: beginalign

$$\begin{aligned} E_{fd} &= K_A(V_{ref} + V_{pss} - V_r) \\ \text{where, } e_{fdmin} &\leq E_{fd} \leq e_{fdmax} \\ T_r \frac{dV_r}{dt} &= V_t - V_r \end{aligned} \tag{2.18}$$

$$
\begin{aligned}
T_{ex}\frac{dE_{fd}}{dt} &= V_a - (K_e E_{fd} + E_{fd} A_{ex} e^{B_{ex} E_{fd}}), \\
\text{where, } e_{fdmin} \leq V_a &\leq e_{fdmax} \\
T_r \frac{dV_r}{dt} &= V_t - V_r \\
T_f \frac{dV_f}{dt} &= E_{fd} - V_f \\
T_a \frac{dV_a}{dt} &= K_a V_{PID} - V_a \\
\text{where, } e_{fdmin}/K_a \leq V_{PID} &\leq e_{fdmax}/K_a \\
V_{PID} = (V_{ref} + V_{pss} - V_r - \frac{K_f}{T_f}[E_{fd} - V_f])[K_p + \frac{K_i}{s} + &\frac{sK_d}{sT_d + 1}]
\end{aligned}
\tag{2.19}
$$

Here, E_{fd} is the field excitation voltage, K_e is the exciter gain, $T_{ex}$the exciter time constant, T_r is the input filter time constant, V_r is the input filter emf, K_f is the stabilizer gain, T_f the stabilizer time constant, V_f the stabilizer emf, A_{ex} and B_{ex} are the saturation constants, K_a the dc regulator gain, T_a is the regulator time constant, V_a is the regulator emf, K_p, K_i, K_d and T_d are the PID-controller parameters, K_A is the static regulator gain, V_{ref} is the reference voltage and V_{pss} is the output reference voltage from the power system stabilizer (PSS).

Excitation systems with high gain and fast response times greatly aid transient stability by increasing synchronizing torque, however, they can also deteriorate small signal stability by inducing negative damping torque. PSS control is a supplementary controller added on top of existing voltage regulator to provides a positive contribution by damping generator rotor angle swings which usually lie in frequency range of 0.1 to 5Hz. PSSs are usually designed to damp the local oscillation even though they are beneficial in aiding the damping of inter-area oscillation as well. Locally available signals such as rotor speed or slip, terminal voltage of the generator, real power or reactive power generated are used as feedback signals. The signals with high observability of local mode are selected. A PSS with slip speed (Δw_r) added as

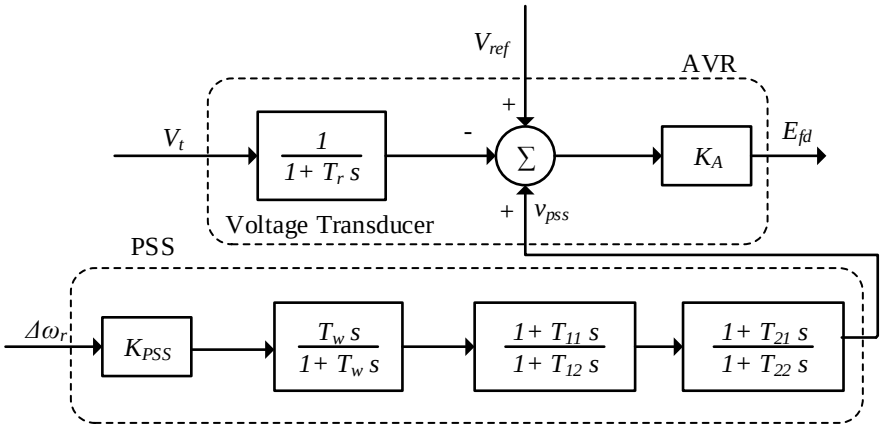

Figure 2.1: AVR (ST1A) with PSS loop(PSS1A).

supplementary loop in AVR 'ST1A' is shown in Figure 2.1. The dynamic equation of PSS can be written as:

$$V_{pss} = K_{PSS}\frac{sT_w}{1+sT_w}\frac{1+sT_{11}}{1+sT_{12}}\frac{1+sT_{21}}{1+sT_{22}}\Delta w_r \tag{2.20}$$

Here, K_{PSS} is the PSS gain, T_w is the washout time constant, T_{i1} and T_{i2} are the i^{th} stage lead and lag time constants, respectively[27].

2.3 Loads and Network Interface

The transient of the network is ignored. The algebraic network balance equations are expressed in common reference frame. So the generator currents and voltages are rotated by the phase angle δ as shown in following equation [65]:

$$I_{gi} = I_{Qi} + jI_{Di} = (I_{qi} + jI_{di})e^{j\delta_i} \tag{2.21}$$

$$V_{gi} = V_{Qi} + jV_{Di} = (V_{qi} + jV_{di})e^{j\delta_i} \tag{2.22}$$

where, I_{gi} and V_{gi} are the current and voltage of i^{th} generator. The generators are modeled as current injection source. Assuming that the current injection occurs at the generator buses only, the current injection column vector I is given as $I_j = I_{gi}$

if the j^{th} node is connected t the i^{th} generator, and $I_j = 0$ if otherwise. The load admittance matrix Y_L are taken as constant shunt impedances. The network shunt admittance matrix Y_N is formed using the line admittance, and the augmented with Y_L to give $Y_{Aug} = Y_N + Y_L$, and thus, the column vector of bus voltages V is given by:

$$V = (Y_{Aug})^{-1} I \tag{2.23}$$

2.4 Doubly Fed Induction Generator (DFIG)

A doubly fed induction generator consists of a wind turbine, an induction generator and a back-to-back converter. Wind turbine converts the kinetic energy of wind to

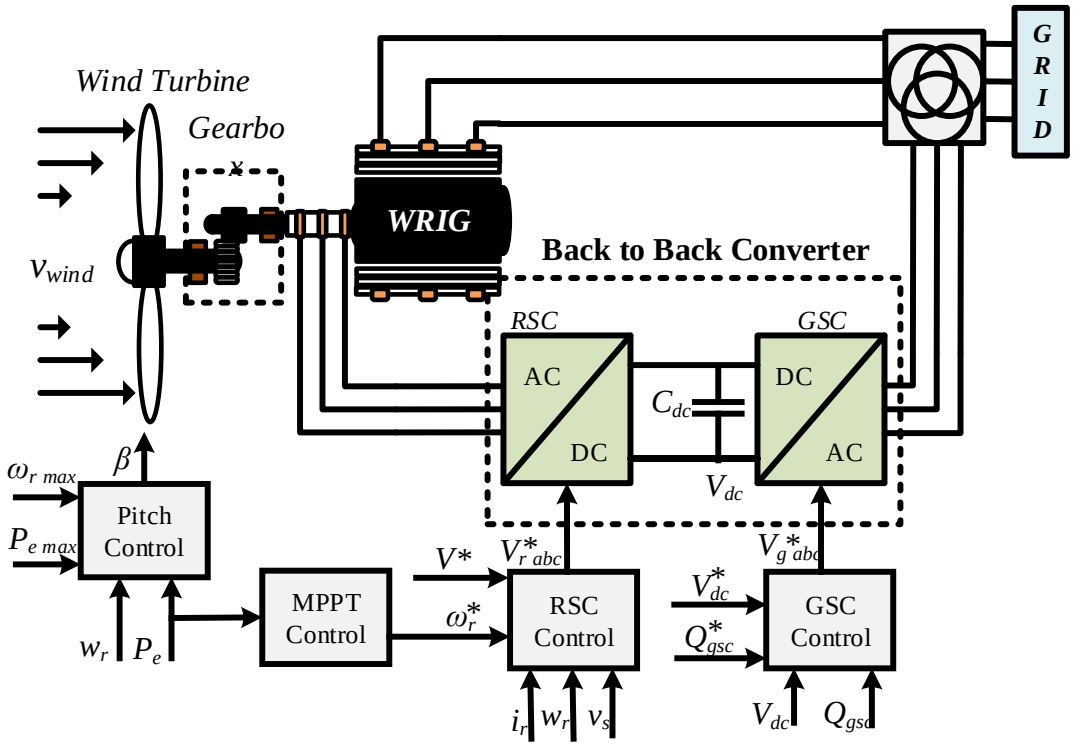

Figure 2.2: Schematic of Doubly Fed Induction Generator.

mechanical energy and the generator converts this mechanical energy into electrical energy. The shaft of the turbine is connected to a wound rotor induction generator

via gearbox setup. The induction generator has a rotor excitation via AC/DC/AC voltage source converter that is connected between three phase rotor winding and the grid.The stator windings are connected directly to the grid. The schematic of grid connected DFIG is shown in 2.2.

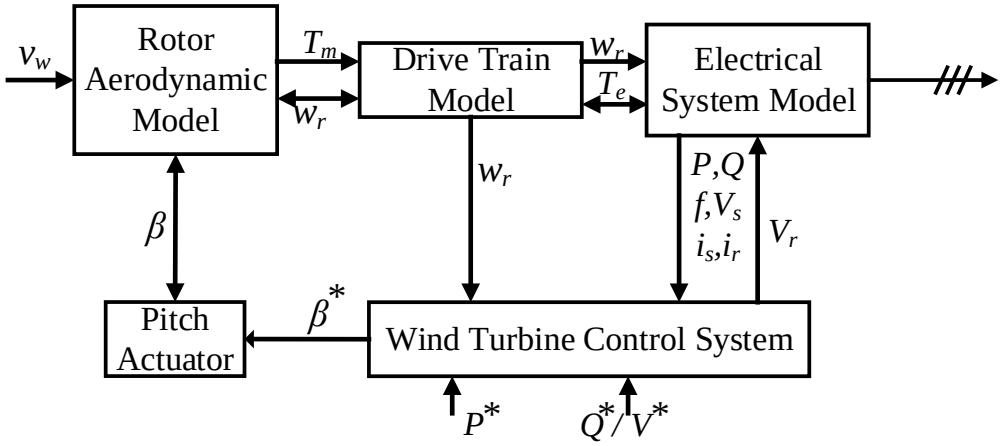

Figure 2.3: Block diagram representation of Wind Turbine Generator and Control.

A dynamic representation of a wind turbine and generator control is shown in figure 2.3. It is composed of:

- Rotor aerodynamic system: This system represents the turbine aerodynamics and computes the mechanical torque or power extracted from the wind, depending on the incoming wind speed, turbine rotor speed and blade pitch angle.

- Drive train system: It represents the mechanical system of the wind turbine, composed of turbine rotor, shafts, gearbox and generator. The drive train model computes the turbine and generator speeds by using the mechanical torque extracted from the wind and the generator torque as input variables.

- Blade pitch angle control system: This system is responsible of controlling the movement of the blade pitch angle.

- Electrical system: In the electrical system, the mechanical power is converted

in electrical power and delivered to grid. It consists of the electrical generator and power converters, if any, depending on the wind turbine concept.

- Wind turbine control system: This system models the wind turbine control in order to achieve the operation desired (active power reference, reactive power reference or terminal voltage reference).

2.4.1 Aerodynamic Model of Wind Turbine

The rotor aerodynamic model expresses the mechanical torque or power extracted from the wind. It can be derived from the blade element momentum (BEM)method [9]. This method is based on a separation of the blades into a number of sections along the length of each blade. Each blade section is characterized by the blade geometry, and the aerodynamic properties are given for each section from the hub to the blade tip as functions of the local radius. The static forces on the blade element, and consequently the corresponding shaft torque are calculated in this method for a given wind speed, a given rotor speed and a given blade pitch angle. However, modeling the rotor using BEM method has a number of drawbacks [10]:

- Instead of only one wind speed signal, an array of wind speed signals has to be applied.
- Detailed information about the rotor geometry should be available.
- Computations become complicated and lengthy.

To solve these problems, a simplified model of the wind turbine rotor derived from the disk actuator theory is normally used when the electrical behavior of the system is the main point of interest. In the disk actuator theory, the mechanical power extracted from the wind is calculated from an algebraic equation:

$$P_m = \frac{\rho}{2} A_r v_w^3 \eta C_p(\lambda, \beta) \tag{2.24}$$

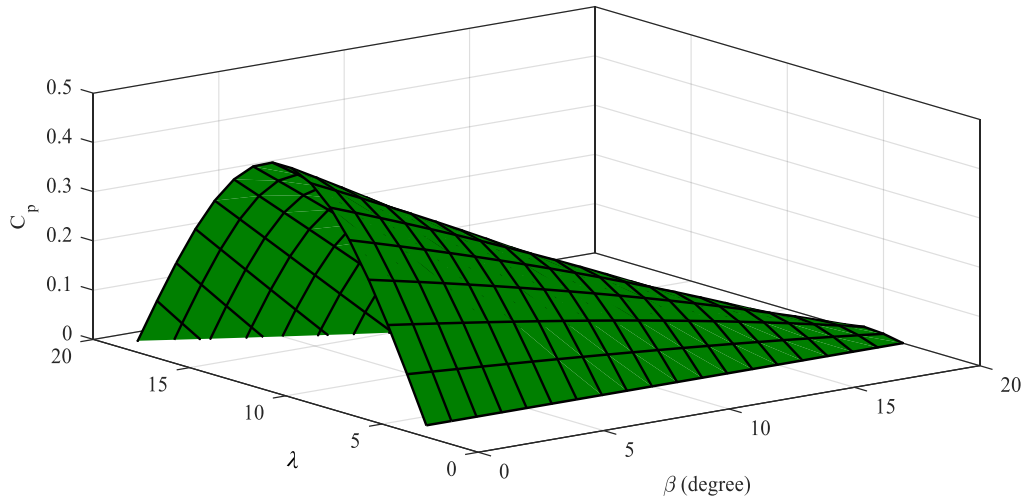

Figure 2.4: Variation of C_p with variation of λ and β.

where, P_m is the mechanical power extracted from the wind, ρ is the air density, A_r is the area swept by the rotor blades, v_w is the wind speed, η is the turbine efficiency C_p is the power coefficient, λ is the tip speed ratio β is the blade pitch angle. The tip speed ratio is calculated as:

$$\lambda = K_b \frac{w_r}{V_w} \tag{2.25}$$

where, K_b is equivalent wind turbine radius coefficient w_r is the rotational speed of the turbine Power coefficient C_p is computed as:

$$C_p = (\frac{4}{9} - \frac{\beta}{60}) sin(\frac{\pi}{2} 20 \frac{\lambda - 3}{150 - 3\beta}) - 2\frac{\beta}{1087}(\lambda - 3) \tag{2.26}$$

Figure 2.4 shows the variation of C_p as a function of λ and β. The coefficient of power decreases with increasing the pitch angle of the rotor blades and exhibits maximum value for a specific value of tip speed ratio which is also called optimal tip speed ratio λ_{opt}. This information is used in designing a pitch controller which controls the pitch angle β to prevent the over-speeding of the turbine when the wind velocity exceeds the rated speed or during grid disturbance where the generator cannot send the power to the grid.

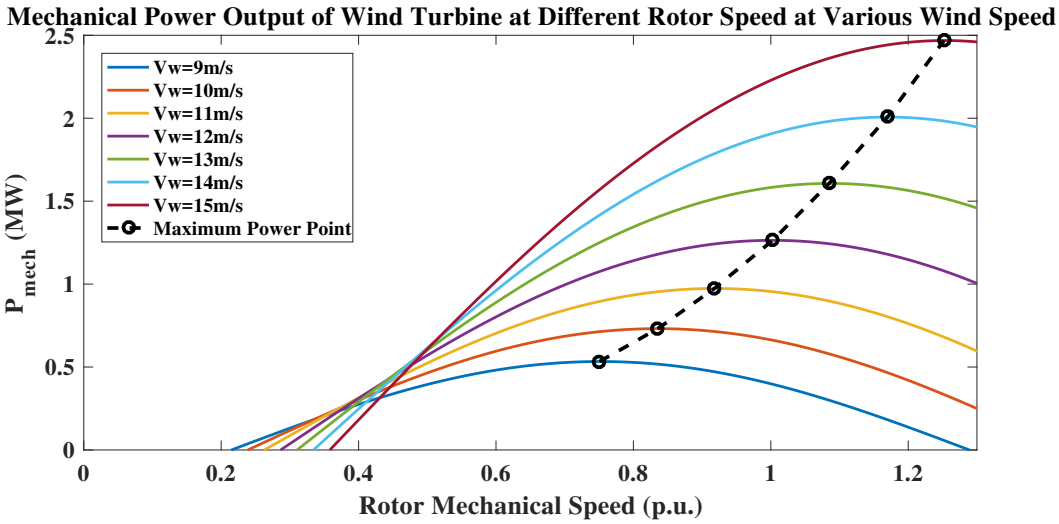

Figure 2.5: Mechanical power vs rotor speed at different wind velocity.

Figure 2.5 shows a typical variation of mechanical power of wind turbine at different turbine speed, and wind speed. The figure illustrates that the ability of a wind turbine to operate in variable rotor speed (as a function of wind velocity) would enable maximum aerodynamic efficiency of the turbine. Generally, a look-up table based on turbine testing is provided such that reference turbine speed can be generated as a function of wind velocity to ensure the turbine operates in maximum power point within a certain permissible range of wind velocity.

2.4.1.1 Pitch Angle Control

The mechanical power output of the wind turbine can be changed by changing the blade pitch angle because it directly varies the power coefficient of the wind turbine. A reduction in the mechanical power of the rotor can be achieved by minimizing the angle of attack above its critical value. Pitch angle control serves following purposes:

1. Optimizing the power output of the wind turbine, by maximizing the mechanical power output for a given wind speed, this is generally applied for low and moderate wind speeds below rated wind speed.

2. Preventing excess mechanical power output in strong winds above rated wind

speeds. This keeps a check on the mechanical power and keeps it below the rated value in strong winds.

3. To prevent disconnected wind turbines from turning

An standard pitch controller is shown in Figure 2.6.

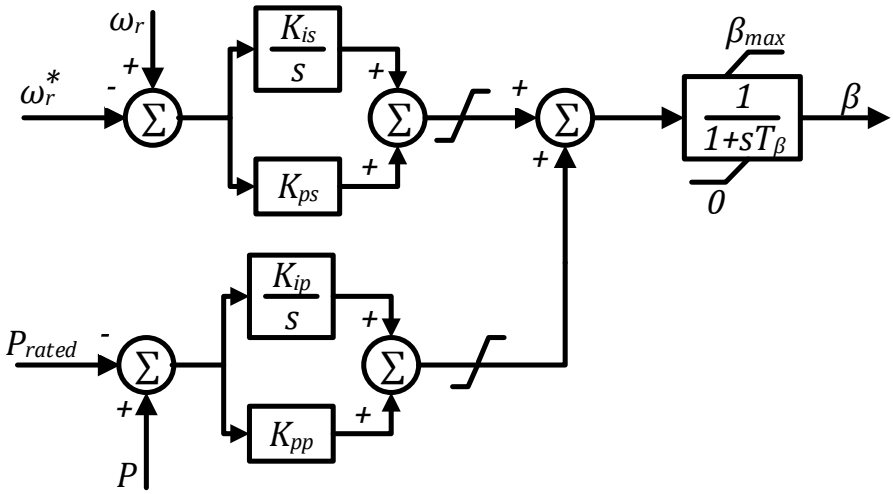

Figure 2.6: Blade Pitch Angle Controller.

2.4.1.2 Maximum Power Point Control

It is desirable to derive maximum power possible from the wind turbine if the wind speed is within its rated wind speed limit and keeping the power derived constant at rated maximum power when the wind speed exceeds the rated speed. The pitch angle controller maintains the optimum blade pitch angle to maximize the power coefficient of the turbine for wind speed below rated wind speed. From figure 2, it is evident that the maximum power extraction is possible if optimal tip speed ratio is maintained, and the power would be a cubic function of wind speed. MPPT control of wind turbine is based on look-up table which is usually provided by the wind turbine developer. MPPT either provides power reference as a function of measured rotor speed or vice-versa.

2.4.2 Drive Train Model

The drive train of a wind turbine is composed of the rotating masses and the connecting shafts, including a possible gearbox. To represent the dynamic of the wind turbine in power system transient analysis, several models of the drive train are reported in literature.

Six rotating masses (three blades, hub, gearbox and generator) are considered in the six-mass drive train model [12, 13]. Each rotor blade is modeled by a separate inertia, elastically connected to the hub. In addition, hub, gearbox and generator are represented by its inertia, which are considered to be elastically connected via springs.

In the three-mass drive train model [12, 13], the three rotating masses are turbine, gearbox and generator, elastically coupled each other. In this case, the turbine inertia is calculated from the combined weight of three blades and hub, and the mutual-damping between hub and blades is ignored.

However, these models are not commonly used for large power system simulation studies because the model order is high. The models mostly used are the two-mass model and the one-mass or lumped-mass model.

2.4.2.1 Lumped One Mass Model

If shafts are assumed to be very rigid and we are not interested in studying impact on the grid than the wind turbine dynamics, the lumped single mass model of drive train with inertia time constant H_{tot} is used. In case of DFIG wind turbine, one mass model can be acceptable as the turbine and grid dynamics are effectively decoupled via power electronics converter. It can be written as:

$$2H_{tot}\frac{dw_m}{dt} = T_m - T_e \tag{2.27}$$

where, T_m is the mechanical torque, T_e is the electromagnetic torque produced by the generator, w_m is the mechanical rotor speed.

2.4.2.2 Two Mass Model

In the two-mass model, the inertia of the gearbox is neglected and only the transformation ratio of the gearbox is included in the model when the wind turbine has gearbox. Thus, the model is composed of two masses, turbine (three blades and hub) represented by inertia constant H_t and generator represented by inertia constant H_g, elastically connected via springs. The equations are:

$$2H_t \frac{dw_t}{dt} = T_m - T_{sh} \tag{2.28}$$

$$2H_g \frac{dw_r}{dt} = T_{sh} - T_e \tag{2.29}$$

$$\frac{d\theta_{tw}}{dt} = (w_t - w_r)w_B \tag{2.30}$$

where w_t and w_r $[p.u.]$ are the turbine and rotor speed and T_{sh} is the shaft torque given by:

$$T_{sh} = K_d \theta_{tw} + D_d \frac{d\theta_{tw}}{dt} \tag{2.31}$$

where Θ_{tw} [rad] is the shaft twist angle, K_d the shaft stiffness and D_d the damping coefficient. After substitution of T_{sh} in and putting $s = w_s - w_r$, we get the drive-train 2 mass model as:

$$2H_t \frac{dw_t}{dt} = T_m - (K\theta_{tw} + D(w_t - (1-s))w_B) \tag{2.32}$$

$$-2H_g \frac{ds}{dt} = (K_d\theta_{tw} + D_d(w_t - (1-s)w_s)w_B) - T_e \tag{2.33}$$

$$\frac{d\theta_{tw}}{dt} = (w_t - (1-s)w_s)w_B \tag{2.34}$$

The two-mass model is usually preferred, because it represents more accurately the dynamic of the wind turbine when the power converter is blocked during grid

faults. Figure 2.7 compares the dynamic transients captured with single mass model and two-mass model. The two-mass model accounts for the fact that turbine and

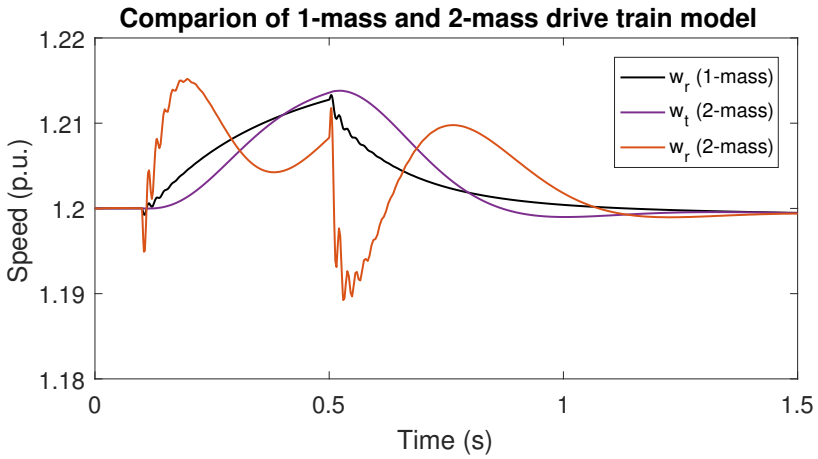

Figure 2.7: Comparison of Lumped Single Mass and Two Mass Model.

generator may oscillate with respect to each other, and hence, is better representation of wind turbine drive train model considering the weaker connection between rotor and turbine shaft via gearbox. This can be seen in Figure 2.7 as rotor is oscillating against the turbine during grid voltage sag from 0.1 to 0.5 sec.

2.4.3 Induction Generator Model

The voltage and flux linkage equation in per unit representing DFIG in d-$q$reference frame rotating at synchronous speed $w_e[p.u.]$ can be written as:

$$v_{qs} = -r_s i_{qs} + w\psi_{ds} + \frac{1}{w_B}\frac{d\psi_{qs}}{dt} \tag{2.35}$$

$$v_{ds} = -r_s i_{ds} - w_e\psi_{qs} + \frac{1}{w_B}\frac{d\psi_{ds}}{dt} \tag{2.36}$$

$$v_{qr} = r_r i_{qr} + (w_e - w_r)\psi_{dr} + \frac{1}{w_B}\frac{d\psi_{qr}}{dt} \tag{2.37}$$

$$v_{dr} = r_r i_{dr} - (w_e - w_r)\psi_{qr} + \frac{1}{w_B}\frac{d\psi_{dr}}{dt} \tag{2.38}$$

$$\psi_{qs} = -L_{ss} i_{qs} + L_m i_{qr} \tag{2.39}$$

$$\psi_{ds} = -L_{ss} i_{ds} + L_m i_{dr} \tag{2.40}$$

$$\psi_{qr} = -L_m i_{qs} + L_{rr} i_{qr} \tag{2.41}$$

$$\psi_{dr} = -L_m i_{ds} + L_{rr} i_{dr} \tag{2.42}$$

The above equations are based on our assumption of current coming out of the stator and current flowing into the rotor taken as positive. The electric torque generated can be estimated by:

$$T_e = L_m(i_{qs} i_{dr} - i_{ds} i_{qr}) \tag{2.43}$$

$$T_e = (\psi_{qs} i_{ds} - \psi_{ds} i_{qs}) \tag{2.44}$$

$$T_e = (\psi_{qr} i_{dr} - \psi_{dr} i_{qr}) \tag{2.45}$$

$$T_e = (L_m/L_{ss})(\psi_{qs} i_{dr} - \psi_{ds} i_{qr}) \tag{2.46}$$

$$T_e = (L_m/L_{rr})(\psi_{qr} i_{ds} - \psi_{dr} i_{qs}) \tag{2.47}$$

2.4.3.1 Comparison of 2nd and 4th Order Induction Generator Transients

Figure 2.8 shows the difference while considering the stator dynamics vs ignoring the stator dynamics. The supplied voltage dipped from 0.1 sec to 0.3 sec, and the result shows that the 4th order model is able to represent the faster stator flux dynamics while 2nd order model ignores the sator flux dynamics.

2.4.4 Converter Model

The ac-dc-ac converter in the rotor circuit figure 2.2 is required to produce rotor voltage at slip frequency. Modern design use two pulse-width modulated (PWM) inverters connected back-to-back via a dc-link. This configuration allows bidirectional power flows in the rotor circuit and hence operation at both sub- and super-synchronous speed.

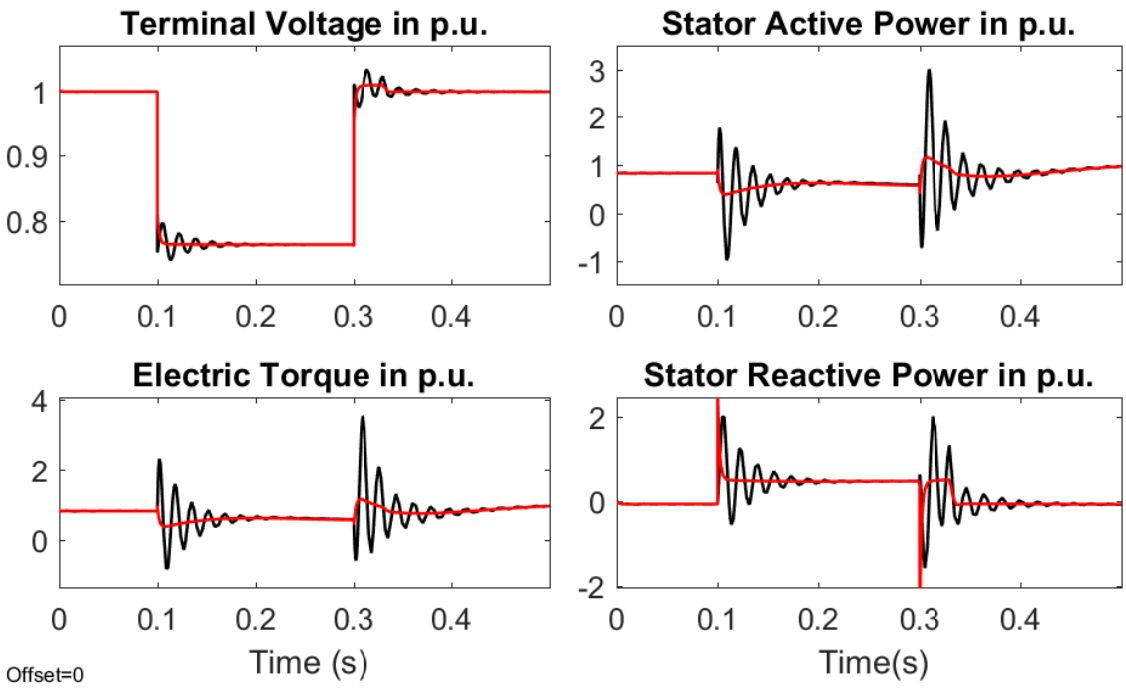

Figure 2.8: Comparison transient of 2^{nd} order (red) and 4^{th} order (black) induction generator model.

There are several ways to control the ac-dc-ac converter. Usually the control algorithm of the converters are formulated in a synchronously rotating two-axis frame so that decoupled control can be achieved for real and reactive power in each converter. The control objectives of the RSC and GSC have to be coordinated so that the system is stable. The RSC is controlled to extract the maximum wind power in subrated region and track constant torque in rated region (the mechanical torque and speed is controlled in this region by pitch angle control mechanism as explained earlier). The GSC maintains the constant dc-link capacitor voltage. The reactive power can be fed in or consumed by both RSC and GSC control. However, RSC control is preferred which essentially controls the rotor excitation to produce desired value of reactive power from the stator. The reactive power support via GSC requires the rating of converter near the DFIG rating, which undermines the DFIG advantage of being able to achieve active and reactive power control via partially rated converter. The converters can be modeled as a controlled voltage or current sources.

2.5 Conventional Vector Control of DFIG

Stator flux oriented vector control is implemented for rotor side converter control and grid voltage vector oriented vector control is implemented for grid side converter control.

2.5.1 Rotor Side Converter Control

The objective of rotor side converter (RSC) control is to make the active and reactive power track their reference by controlling rotor excitation voltage. If the arbitrary d-q reference frame is aligned and rotated synchronously along stator flux vector, then following equation can be formulated by neglecting the effect of stator resistance:

$$\psi_{ds} = \psi_s, \qquad \psi_{qs} = 0 \tag{2.48}$$

$$v_{qs} \approx v_s \qquad v_{ds} \approx 0 \tag{2.49}$$

The stator active and reactive power can be written as:

$$P_s = v_{qs} i_{qs}, \quad Q_s = v_{qs} i_{ds} \tag{2.50}$$

The stator current can be written in terms of rotor currents as:

$$i_{qs} = \frac{L_m}{L_{rr}} i_{qr} \tag{2.51}$$

$$i_{ds} = \frac{L_m}{L_{rr}} i_{qr} + \psi_{ds} \tag{2.52}$$

Thus, active and reactive power can be re-written as:

$$P_s = v_{qs} \frac{L_m}{L_{rr}} i_{qr} \tag{2.53}$$

$$Q_s = v_{qs} \frac{L_m}{L_{rr}} i_{qr} + v_{qs} \psi_{ds} \tag{2.54}$$

The stator voltage v_{qs} of grid connected DFIG can be assumed to be constant. Thus from equation 2.53 and 2.54, it can be realized that the control of active and reactive power can be achieved by controlling the rotor quadrature axis and direct axis current, respectively.

The rotor voltage equations can be written as

$$v_{qr} = r_r i_{qr} + \sigma L_{rr} \frac{d}{dt} i_{qr} + (w_e - w_r)(\sigma L_{rr} i_{dr} + \frac{L_m \psi_{ds}}{L_{ss}}) \tag{2.55}$$

$$v_{dr} = r_r i_{dr} + \sigma L_{rr} \frac{d}{dt} i_{dr} - (w_e - w_r)\sigma L_{rr} i_{qr} \tag{2.56}$$

$$v_{qr} = v'_{qr} + (w_e - w_r)(\sigma L_{rr} i_{dr} + \frac{L_m \psi_{ds}}{L_{ss}}) \tag{2.57}$$

$$v_{dr} = v'_{dr} - (w_e - w_r)\sigma L_{rr} i_{qr} \tag{2.58}$$

where, $v'_{qr} = r_r i_{qr} + \sigma L_{rr} \frac{d}{dt} i_{qr}$ and $v'_{dr} = r_r i_{dr} + \sigma L_{rr} \frac{d}{dt} i_{dr}$

Thus the reference v'_{qr} and v'_{dr} are obtained from quadrature and direct axis rotor current control loop and the decoupling term as shown in equation (52) are added to obtain the reference for v_{qr} and v_{dr} respectively. The control block diagrams are

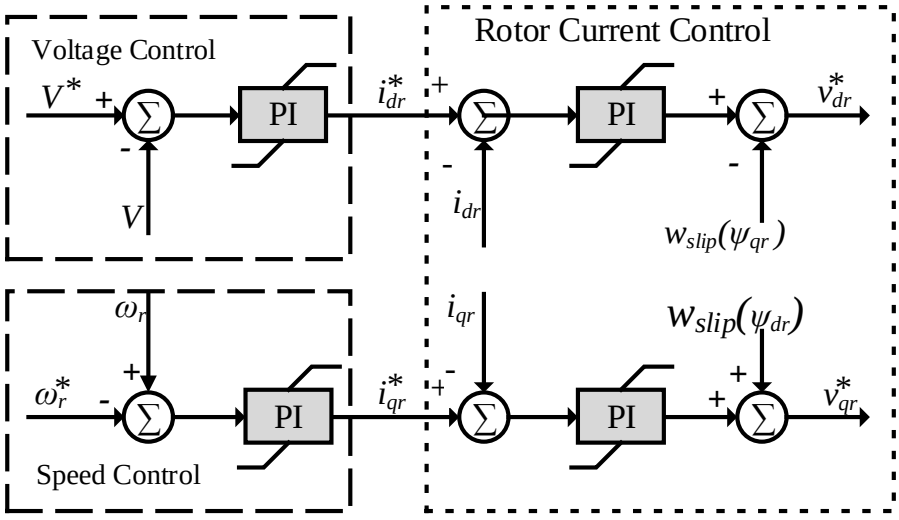

Figure 2.9: RSC control structure with outer loop for speed and voltage control, and inner loop for direct and quadrature axis rotor current control.

shown in the Figure 2.9:

The controller equations are given as:

$$\frac{dx_{ip}}{dt} = -w_{r\ ref} + w_r \tag{2.59}$$

$$\frac{dx_{iq}}{dt} = i_{qrref} - i_{qr} \tag{2.60}$$

$$\frac{dx_v}{dt} = v_{sref} - v_s \tag{2.61}$$

$$\frac{dx_{id}}{dt} = i_{drref} - i_{dr} i_{qrref} = K_{pw}(-w_{r\ ref} + w_r) + K_{iw} x_{iw} \tag{2.62}$$

$$i_{drref} = K_{pv}(v_{sref} - v_s) + K_{iv} x_{iv} \tag{2.63}$$

$$v_{qr} = K_{pq}(i_{qrref} - i_{qr}) + K_{iq} x_{iq} + (w_{slip})\psi_{dr} \tag{2.64}$$

$$v_{dr} = K_{pd}(i_{drref} - i_{dr}) + K_{id} x_{id} - w_{slip}\psi_{qr} \tag{2.65}$$

x_{iv}, x_{iw}, x_{iq} and x_{id} are the state variables associated with integral control gains K_{iv}, K_{iw}, K_{iq} and K_{id} respectively. K_{pv}, K_{pw}, K_{pq} and K_{pd} are the proportional control gains.

2.5.2 Grid Side Converter Control

Grid side converter (GSC) is a three-phase AC to DC converter connecting the dc-link capacitor to the three phase ac grid. The main purpose of GSC is to maintain the constant dc-link voltage irrespective of the power flowing rotor to the grid or vice-versa. The dc-link voltage is thus controlled by controlling the active power flowing from the grid to the rotor side converter or vice-versa. The GSC can also be used to support the reactive power requirement of the grid, however, this would require the higher rating of the power converter. The most widely used technique of GSC control is to align the direct axis of two-axis d-q reference frame along the grid voltage vector such that the active power and hence the dc-link voltage can be controlled by controlling the direct-axis component of the current while the reactive power can be controlled by controlling the quadrature-axis current. This is also called

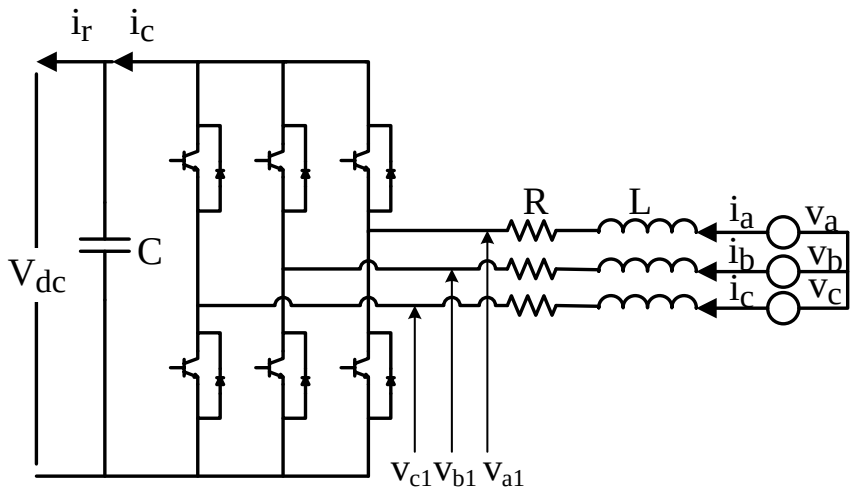

Figure 2.10: Grid side converter arrangement.

Voltage Oriented Vector Control. The schematic diagram of GSC is shown in Figure 2.10.

From Figure 2.10, the Kirchhoff's voltage law gives:

$$\begin{bmatrix} v_a \\ v_b \\ v_c \end{bmatrix} = R \begin{bmatrix} i_a \\ i_b \\ i_c \end{bmatrix} + L\frac{d}{dt} \begin{bmatrix} i_a \\ i_b \\ i_c \end{bmatrix} + \begin{bmatrix} v_{a1} \\ v_{b1} \\ v_{c1} \end{bmatrix} \tag{2.66}$$

where L and R are tje line inductance and resistance, respectively. Using Park's transformation to transform the abc form of 2.66 into the dq reference frame rotating at the grid frequency w_e, we get:

$$\begin{bmatrix} v_d \\ v_q \end{bmatrix} = R \begin{bmatrix} i_d \\ i_q \end{bmatrix} + L\frac{d}{dt} \begin{bmatrix} i_d \\ i_q \end{bmatrix} + Lw_e \begin{bmatrix} -i_q \\ i_d \end{bmatrix} + \begin{bmatrix} v_{d1} \\ v_{q1} \end{bmatrix} \tag{2.67}$$

If q-axis is aligned along the voltage vector, $v_d = 0$, so the (2.67) can be written as:

$$\begin{bmatrix} v_{d1} \\ v_{q1} \end{bmatrix} = -R \begin{bmatrix} i_d \\ i_q \end{bmatrix} - L\frac{d}{dt} \begin{bmatrix} i_d \\ i_q \end{bmatrix} - Lw_e \begin{bmatrix} -i_q \\ i_d \end{bmatrix} + \begin{bmatrix} 0 \\ v_q \end{bmatrix} \tag{2.68}$$

Also, we can write

$$\begin{bmatrix} v_{d1} \\ v_{q1} \end{bmatrix} = -R \begin{bmatrix} i_d \\ i_q \end{bmatrix} - L\frac{d}{dt} \begin{bmatrix} i_d \\ i_q \end{bmatrix} - Lw_e \begin{bmatrix} -i_q \\ i_d \end{bmatrix} + \begin{bmatrix} 0 \\ v_q \end{bmatrix} \tag{2.69}$$

$$\begin{bmatrix} v_{d1} \\ v_{q1} \end{bmatrix} = \begin{bmatrix} v'_d \\ v'_q \end{bmatrix} + \begin{bmatrix} Lw_e i_q \\ -Lw_e i_d + v_q \end{bmatrix} \tag{2.70}$$

where,

$$\begin{bmatrix} v'_d \\ v'_q \end{bmatrix} = -R \begin{bmatrix} i_d \\ i_q \end{bmatrix} - L\frac{d}{dt} \begin{bmatrix} i_d \\ i_q \end{bmatrix} \tag{2.71}$$

The active and reactive power flowing from GSC is

$$\begin{bmatrix} P \\ Q \end{bmatrix} = \begin{bmatrix} v_q i_q \\ v_q i_d \end{bmatrix} \tag{2.72}$$

The DC-link voltage can be maintained constant by balancing the active power flow between the grid and the rotor side converter. A PI controller driven by error in DC-link voltage tracking, thus provides the set-point for q-axis current i_{qg}. The error of q-axis current tracking is provides the reference voltage set-point v'_q. The error in tracking reactive power (usually set at 0) is provides reference set-point for d-axis current i_{dg}, and the error is d-axis current tracking is used to drive the set-point v'_d. The resulting control architecture for GSC is illustrated in Figure 2.11.

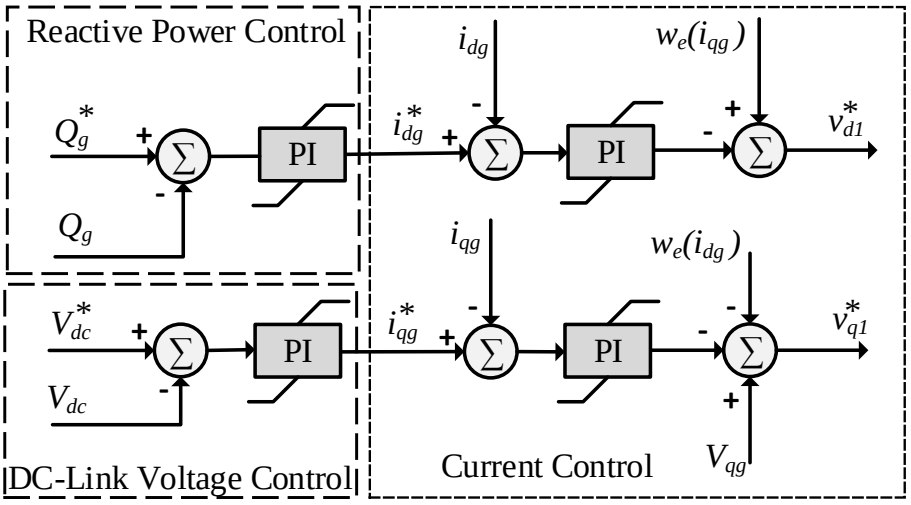

Figure 2.11: PI based Vector Control of GSC.

2.6 Rotor Flux Magnitude and Angle Control

Rotor Flux Magnitude and Angle control (FMAC) was proposed by Anaya et al. This technique is very similar to the traditional voltage excitation and power angle control employed in synchronous generators. The decoupled control of reactive and active power is achieved by controlling the magnitude and angle of rotor flux. The stator dynamics are neglected and hence reduced order model of DFIG is obtained.

$$v_{qs} = -r_s i_{qs} + w_e \psi_{ds} \tag{2.73}$$

$$v_{ds} = -r_s i_{ds} - w_e \psi_{qs} \tag{2.74}$$

$$v_{qr} = r_r i_{qr} + w_{slip} \psi_{dr} + \frac{d}{dt}\psi_{qr} \tag{2.75}$$

$$v_{dr} = r_r i_{dr} - w_{slip} \psi_{qr} + \frac{d}{dt}\psi_{dr} \tag{2.76}$$

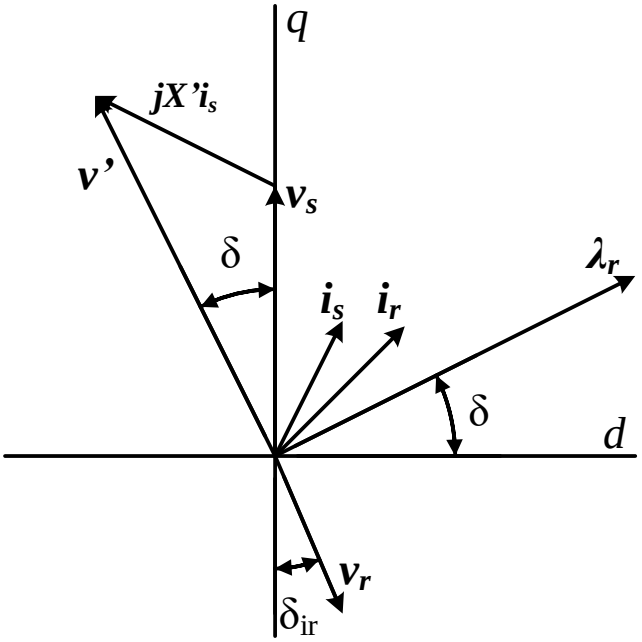

Figure 2.12: Vector Diagram representation of DFIG.

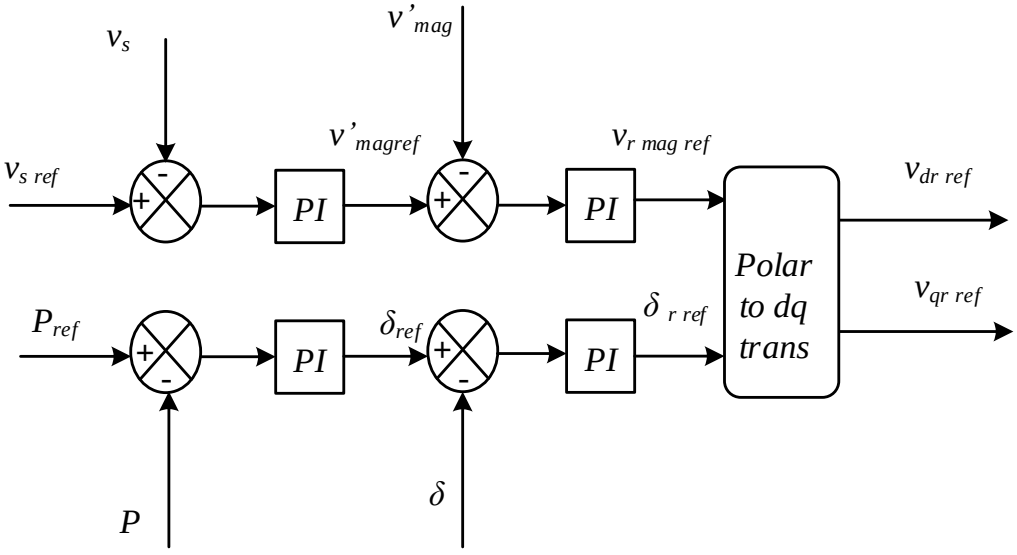

Figure 2.13: Rotor Flux Magnitude and Angle Control of DFIG.

The equations can be modeled with voltage behind transient reactance as:

$$\frac{dv'_q}{dt} = -\frac{1}{T'_0}[v'_q - (X_s - X'_s)i_{ds}] - w_{slip}v'_d + \frac{L_m}{L_{rr}}v_{dr} \tag{2.77}$$

$$\frac{dv'_d}{dt} = -\frac{1}{T'_0}[v'_d - (X_s - X'_s)i_{qs}] + w_{slip}v'_q - \frac{L_m}{L_{rr}}v_{qr} \tag{2.78}$$

$$v_{ds} = -r_s i_{ds} - X'_s i_{qs} + v'_d \tag{2.79}$$

$$v_{qs} = -r_s i_{qs} + X'_s i_{ds} + v'_q \tag{2.80}$$

In vector form:

$$\frac{d\vec{v'}}{dt} = -\frac{1}{T'_0}[\vec{v'} - j(X_s - X'_s)\vec{i_s}] - jw_{slip}\vec{v'} - j\frac{L_m}{L_{rr}}\vec{v_r} \tag{2.81}$$

where $\vec{v'} = v'_d + jv'_q$, $\vec{v_r} = v_{dr} + jv_{qr}$, and $\vec{i_s} = i_{ds} + ji_{qs}$ In steady state, $\frac{d\vec{v'}}{dt} = 0$, so that

$$0 = -\frac{1}{T'_0}[\vec{v'} - j(X_s - X'_s)\vec{i_s}] - jw_{slip}\vec{v'} - j\frac{L_m}{L_{rr}}\vec{v_r} \tag{2.82}$$

Anaya et al then proposes that for normal operating values of w_{slip} *(when the DFIG rotor speed is distinct from synchronous speed)*, the term having divider T'_0 is very small compared with the final two terms , so that

$$w_{slip}\vec{\mathbf{v'}} = \frac{L_m}{L_{rr}}\vec{v_r} \tag{2.83}$$

and

$$\frac{L_m}{L_{rr}} \simeq 1 \; i.e. \; \vec{v_r} \approx s\vec{\mathbf{v'}} \tag{2.84}$$

Since the magnitude of the internal voltage varies only slightly, the magnitude of the rotor voltage is proportional to the slip magnitude. Further, for subsynchronous operation where slip w_{slip} is positive, v_r is approximately in phase with the internal voltage vector v', and for supersynchronous operation where w_{slip} is negative, the two

voltage vectors are approximately in anti-phase.

The angle δ in Figure 2.12 which defines the angle between the internal voltage vector v' and stator terminal voltage v_s and also the angle between the rotor flux ψ_r and stator flux ψ_s is determined by the power output of the generator. Thus, controlling the position of the rotor flux with respect to stator flux enables the control of the generator power output. This equivalent to controlling the position of internal voltage v' with respect to stator terminal voltage v_s. The reference for rotor voltage $|v_r|$and angle δ_{ir} obtained from rotor flux magnitude and angle control loop respectively. The control strategy is illustrated in the schematic shown in Figure 2.13.

The control topology for rotor side converter control has been elaborately explained in [23]. Aligning the direction of the q-axis of the synchronously rotating d-q reference frame with the stator voltage, v_{ds} becomes zero and v_{qs} is equal to the terminal voltage value. The rotor-side converter controller aims to control the DFIG output active power and reactive power for tracking the different input of the WT torque and maintaining accurate relations between the terminal voltage and control setting, and then, the active power and reactive power can be controlled independently by v_{qr} and v_{dr}, respectively.

2.7 Optimal State Feedback Control of DFIG

Though PI based vector control is the most widely used DFIG control topology, it often performs poorly in transient disturbance scenarios, is affected by parameter variation and the tuning of individual control gains is a cumbersome task. Therefore, a linear-quadratic-integral (LQI) optimal state feedback controller has been proposed. It is a linear-quadratic-regulator (LQR) with state augmentation using integral action to ensure the desired reference tracking while providing the optimal feedback gain parameters to minimize the quadratic cost function of control input and state variables. LQI control is a more systematic method of designing control law for the optimal performance of linear multi-variable system such as DFIG. First, state space model

for current control of RSC and GSC are developed. State space model is developed for rotor speed control. The control design procedure is described briefly.

2.7.1 State Space Model of RSC

In a stator flux oriented d-q reference frame, the quadrature axis rotor currents i_{qr} and direct axis rotor current i_{dr} are controlled by controlling the rotor voltages v_{qr} and v_{dr} respectively. If the stator dynamics are neglected, i.e. $\frac{d}{dt}\psi_s = 0$, the state space model of RSC can be written as:

$$\frac{d}{dt}\begin{bmatrix} i_{qr} \\ i_{dr} \end{bmatrix} = \begin{bmatrix} -\frac{r_r}{\sigma L_{rr}} & -w_{slip} \\ w_{slip} & -\frac{r_r}{\sigma L_{rr}} \end{bmatrix} \begin{bmatrix} i_{qr} \\ i_{dr} \end{bmatrix} + \frac{1}{\sigma L_{rr}} \begin{bmatrix} v_{qr} \\ v_{dr} \end{bmatrix} + w_{slip}\frac{L_m}{\sigma L_{ss} L_{rr}}\psi_{ds} \tag{2.85}$$

where, $\sigma = \frac{L_{ss}L_{rr} - L_m^2}{L_{ss}L_{rr}}$. If $w_{slip}\frac{L_m}{\sigma L_{ss}L_{rr}}\psi_{ds}$.

2.7.2 State Space Model of GSC

The mathematical state space model of GSC in a voltage oriented d-q reference frame can be written as:

$$\frac{d}{dt}\begin{bmatrix} i_d \\ i_q \end{bmatrix} = \begin{bmatrix} -\frac{R}{L} & w_e \\ -w_e & -\frac{R}{L} \end{bmatrix} \begin{bmatrix} i_d \\ i_q \end{bmatrix} + \frac{1}{L}\begin{bmatrix} v_{d1} \\ v_{q1} \end{bmatrix} + \frac{1}{L}v_d \tag{2.86}$$

where, R and L are the resistance and reactance of filter in p.u. The reference signal $i_{d\ ref}$ is derived from dc-link voltage controller which is PI controller in this case. However, state feedback control can be designed for de-link control as well. $i_{q\ ref}$ is assumed to be zero as the GSC does not support any reactive power for voltage control.

2.7.3 State Space Model of Mechanical Speed Control

The main purpose of DFIG speed control is to derive set-point for DFIG electric torque/power/i_{qr}. A lumped single mass model has been assumed and the controller

has been tested in a two mass model system. In stator flux oriented d-q frame, the electrical torque generated by the generator can be written as:

$$T_e = \frac{L_m}{L_{ss}} \psi_{ds} i_{qr} \tag{2.87}$$

Then, rotor-turbine mechanical dynamics can be represented by:

$$\frac{dw_r}{dt} = \frac{T_m}{2H} - \frac{1}{2H} \frac{L_m}{L_{ss}} \psi_{ds} i_{qr} \tag{2.88}$$

2.7.4 Linear Quadratic Integral (LQI) control

The novel state space model are type-0 servo system which do not involve integrator in the dynamics of currents and speed. However, the integral action needs to be incorporated in the system to ensure a zero steady-state error. This is achieved by state augmentation by having the integrator in the feed forward path between the error comparator and the plant. This will include additional states to the system. The mathematical formulation of LQR based state feedback control with integral action is detailed here.

2.7.4.1 Mathematical Formulation of Error Dynamics

The state space model of a general type-0 MIMO servo system utilizing integral action, using state augmentation can be expressed mathematically as:

$$\dot{x}(t) = Ax(t) + Bu(t) \tag{2.89}$$

$$y(t) = Cx(t) \tag{2.90}$$

$$\zeta(t) = r(t) - y(t) = r(t) - Cx(t) \tag{2.91}$$

where,

$x = (x_1\ x_2 ...\ x_n)^T$ is the $(n \times 1)$ state vector

$y = (y_1\ y_2 ...\ y_p)^T$ is the $(p \times 1)$ output vector

$u = (u_1\ u_2 ...\ u_m)$ is the $(m \times 1)$ input vector

$r = (r_1\ r_2 ...\ r_p)$ is the $(p \times 1)$ reference-input vector

$\zeta = (\zeta_1\ \zeta_2 ...\ \zeta_p)$ is the $(p \times 1)$ vector representing the integral of the tracking errors (augmented states)

C is the output matrix

A linear state feedback and added states can be given as:

$$u(t) = -Kx(t) + K_I\zeta(t) \tag{2.92}$$

where, K is a $(m \times n)$ state feedback gain matrix and K_I is a $(m \times p)$ integral gain matrix. The state space dynamic model for the system obtained after the state augmentation can be written in matrix form by combining 2.89 and 2.90 as:

$$\begin{bmatrix} \dot{x}(t) \\ \dot{\zeta(t)} \end{bmatrix} = \begin{bmatrix} A & 0 \\ -C & 0 \end{bmatrix} \begin{bmatrix} x(t) \\ \zeta(t) \end{bmatrix} + \begin{bmatrix} B \\ 0 \end{bmatrix} u(t) + \begin{bmatrix} 0 \\ I \end{bmatrix} r(t) \tag{2.93}$$

where, I is a $(p \times p)$ identity matrix. In steady state, 2.93 can be written as:

$$\begin{bmatrix} \dot{x}(\infty) \\ \dot{\zeta(\infty)} \end{bmatrix} = \begin{bmatrix} A & 0 \\ -C & 0 \end{bmatrix} \begin{bmatrix} x(\infty) \\ \zeta(\infty) \end{bmatrix} + \begin{bmatrix} B \\ 0 \end{bmatrix} u(\infty) + \begin{bmatrix} 0 \\ I \end{bmatrix} r(\infty) \tag{2.94}$$

Considering $r(t)$ as a vector of step inputs, we have $r(\infty) = r(t) = r(constant)$ for $t > 0$. Subtracting 2.94 from 2.93, the error dynamics can be obtained as:

$$\begin{bmatrix} \dot{x}(t) - \dot{x}(\infty) \\ \dot{(\zeta)}(t) - \dot{\zeta(\infty)} \end{bmatrix} = \begin{bmatrix} A & 0 \\ -C & 0 \end{bmatrix} \begin{bmatrix} x(t) - x(\infty) \\ \zeta(t) - \zeta(\infty) \end{bmatrix} + \begin{bmatrix} B \\ 0 \end{bmatrix} \begin{bmatrix} u(t) - u(\infty) \end{bmatrix} \tag{2.95}$$

Now, we define:

$$x(t) - x(\infty) = x_e(t) \tag{2.96}$$

$$\zeta(t) - \zeta(\infty) = \zeta_e(t) \tag{2.97}$$

$$u(t) - u(\infty) = u_e(t) \tag{2.98}$$

Replacing these values in 2.95, following expression can be written:

$$\begin{bmatrix} \dot{x_e}(t) \\ \dot{\zeta_e}(t) \end{bmatrix} = \begin{bmatrix} A & 0 \\ -C & 0 \end{bmatrix} \begin{bmatrix} x_e(t) \\ \zeta_e(t) \end{bmatrix} + \begin{bmatrix} B \\ 0 \end{bmatrix} u_e(t) \tag{2.99}$$

If we define a $((n+m) \times 1)$ order error vector as:
$e(t) = \begin{bmatrix} x_e(t) \\ \zeta_e(t) \end{bmatrix}$
then, equation 2.99 can be written as:

$$\dot{e}(t) = \bar{A}e(t) + \bar{B}u_e(t) \tag{2.100}$$

where, $\bar{A} = \begin{bmatrix} A & 0 \\ -C & 0 \end{bmatrix}$ and $\bar{B} = \begin{bmatrix} B \\ 0 \end{bmatrix}$. From equation 2.92 and 2.100,

$$u_e(t) = -Kx_e(t) + K_I\zeta_e(t) = -\bar{K}e(t) \tag{2.101}$$

where, $\bar{K} = \begin{bmatrix} K & -K_I \end{bmatrix}$ Thus, the closed loop error dynamics can be written as:

$$\dot{e}(t) = (\bar{A} - \bar{B}\bar{K})e(t) \tag{2.102}$$

Thus, it becomes evident that the problem of designing a state feedback law to track the reference values is transformed to a regulator design problem. The gain matrix $\bar{K}$ is to be designed such that error vector $e(t)$ converges to zero at steady state.

2.7.4.2 Linear Quadratic Regulator (LQR) design

The LQR approach provides a systematic way of computing the feedback gain-matrix K for making MIMO error dynamics of (2.100) asymptotically stable. The gain matrix K is computed by minimizing a quadratic performance index given [55] as:

$$J = \int_{t=0}^{t=\infty} (x_e^T(t)Qx_e(t) + U_e^T(t)Ru_e(t))dt \tag{2.103}$$

where, Q and R are both positive-definite matrices. In (2.103), the second term in right-hand side is accountable for the expenditure of energy of the control signals and the first term is accountable for the energy of the plant states. The feedback law is thus an optimal compromise between the control effort and the response speed, and at the same time ensures the stable operation of the system.

The optimal gain matrix is obtained that minimizes the performance index (2.103) is given as:

$$\bar{K} = \begin{bmatrix} K & -K_I \end{bmatrix} = R^{-1}\bar{B}P \tag{2.104}$$

where, P is a positive-definite matrix and is the solution of the following reduced-matrix Ricatti equation:

$$\bar{A}P + P\bar{A} - P\bar{B}R^{-1}\bar{B}P + Q = 0 \tag{2.105}$$

From (2.101) and (2.104), the feedback control law for error dynamics of (2.100) can be written as:

$$u_e(t) = -R^{-1}\bar{B}Pe(t) = -R^{-1}\bar{B}P \begin{bmatrix} x_e(t) \\ \zeta_e(t) \end{bmatrix} \tag{2.106}$$

This means, the optimal state feedback control law for the given system in (2.93) can

be formulated as:

$$u(t) = -R^{-1}\bar{B}P \begin{bmatrix} x(t) \\ \zeta(t) \end{bmatrix} \tag{2.107}$$

Equation (2.107) gives the state feedback control law with the optimal gain matrix and hence, drive the error matrix $e(t)$ to zero and the system states track their reference value in steady state.

2.7.5 LQI Control for RSC

Based on the state space model obtained for speed control of DFIG, optimal state feedback gain is proposed with the optimal feedback gain matrix derived using equation (2.104) and the proposed control schematic is shown in Figure 2.14. The integral gain K_{isp} ensure DFIG rotor speed w_r tracks reference w_r^*. The output of the controller is i_{qr}^* which is assumed to be equal to i_{qr} which in turn controls the electric torque T_e or generated power P. Proposed optimal LQI control for RSC current control is shown in Figure 2.14. The objective of the controller is that rotor currents i_{qr} and i_{dr} track the respective reference signals i_{qr}^* and i_{dr}^*. i_{qr}^* is derived from speed controller. i_{dr}^* is derived either from voltage controller or reactive power controller and is derived from a PI controller in this case.

2.7.6 LQI Control for GSC

The GSC controller maintains constant dc-link voltage irrespective of the power flowing to or from the rotor via rotor side converter. The error in DC-link voltage tracking drives the PI controller to derive the reference for the d-axis current in grid voltage vector oriented d-q plane as shown in Figure 2.15. Similarly, the error in reactive power set-point tracking drives a PI controller to derive the reference set-point for q-axis current. The proposed LQI control for current control of GSC is shown in Figure 2.15.

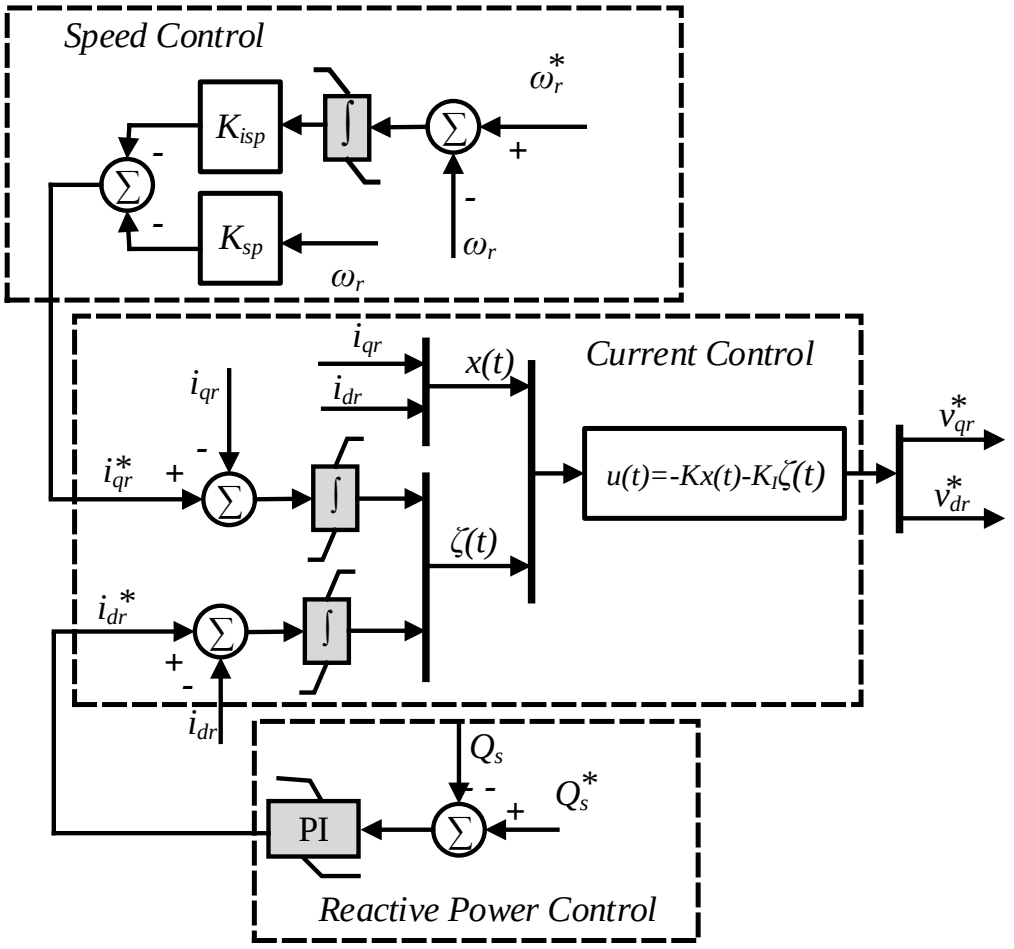

Figure 2.14: State Feedback Control of RSC.

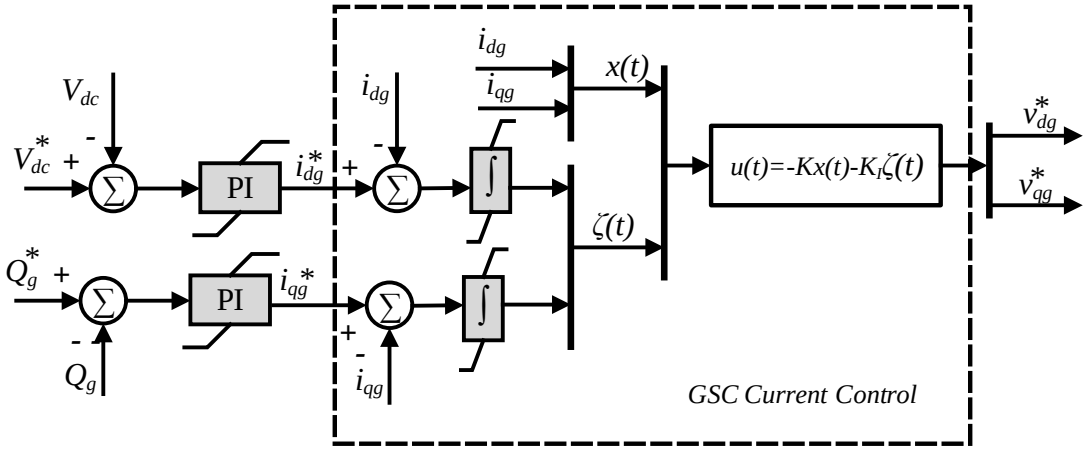

Figure 2.15: State Feedback Control of GSC.

2.8 Time Domain Simulation of LQI control vs PI Control

In order to test the performance of the proposed LQI controller, time domain simulation results are presented. Step response of the proposed control architecture for RSC, GSC and speed are observed first. Further, the performance of the proposed architecture in the real-wind scenario is evaluated.

The reference signal i_{qr}^{*} is changed in steps such that $i_{qr}^{*} = [0, 0.2, 0.3, 0.15]$ at $t = [0, 1, 2, 3.5](sec)$ .The reference i_{dr}^{*} is also changed in steps such that $i_{qr}^{*} = [0, -0.2, -0.3, -0.15]$ at $t = [0, 1.5, 2.5, 4](sec)$. The result is shown in Figure 2.16 which also shows the results with a standard PI-based vector control for comparison purpose. Better decoupled control (0.01 p.u change) and smaller ripple in rotor current is evident from the result.

2.8.1 RSC Current Control Step Response

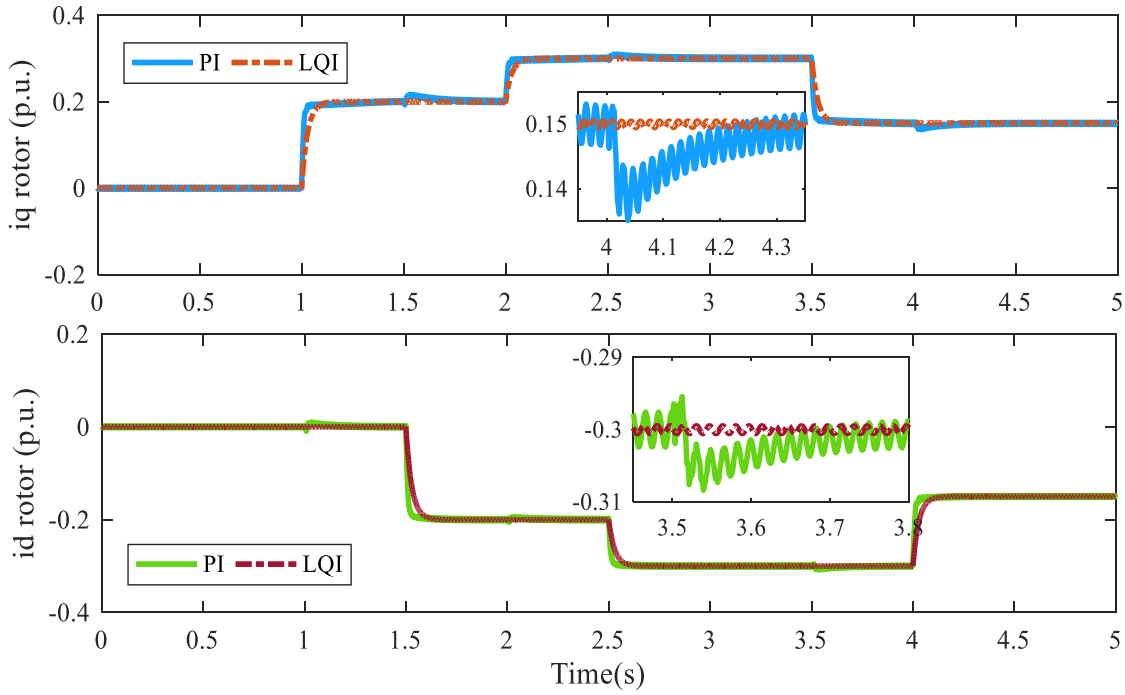

Figure 2.16: Comparison of LQI control vs PI Control for RSC current control.

2.8.2 GSC Current Control Step Response

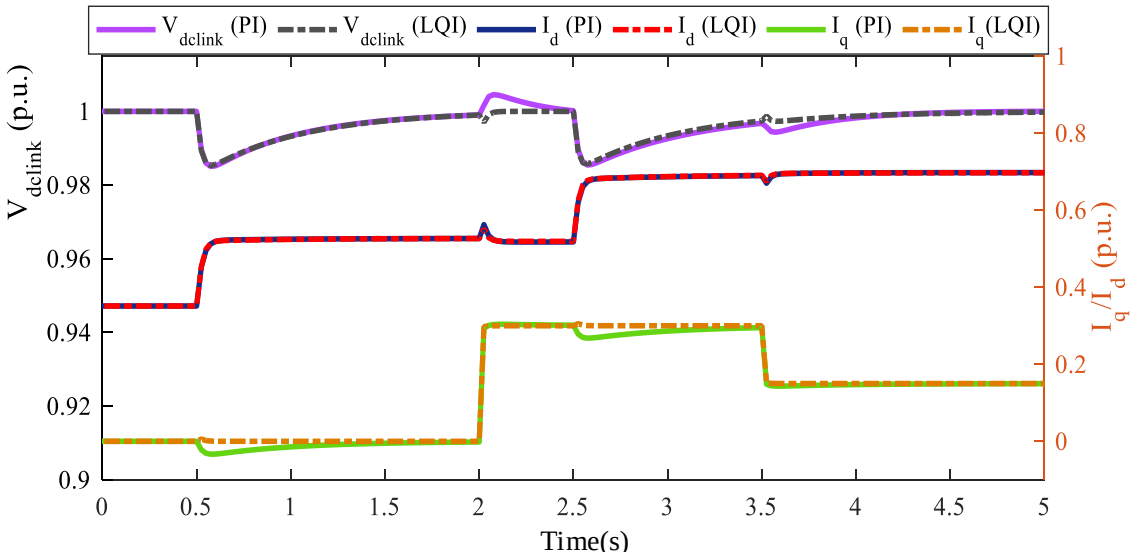

Figure 2.17: Comparison of LQI control vs PI Control for GSC current control.

Step change in d-axis current reference such that $i^*_{dg} = [0.5, 0.7]p.u.$ at time $t = [0.5, 2.5]$ sec. Step change in q-axis current reference such that $i^*_{qg} = [0.3, 0.15]p.u.$ at time $t = [2, 3.5]$ sec. The time domain simulation result with PI controller and LQI controller are shown in figure 2.17. DC link voltage (at the top) shows better response with the proposed lqi controller. It responds to change in d-axis current only with the proposed lqi controller while it was disturbed by changing q-axis current as well with PI controller. Better decoupling of q-axis and d-axis current present the superiority of proposed controller in comparison to the commonly used PI based vector control technique.

2.8.3 DFIG Speed Control Step Response

The proposed LQI speed controller was tested with step changes in wind speed that resulted in step change of rotor speed reference $w_{r\ ref}$. Figure 2.18 shows the rotor speed with the LQI controller compared to variously tuned PI controllers. The change in i^*_{qr} and equivalently stator power P_s is also shown in Figure 2.18. LQI is able to track the reference speed with zero overshoot and shorter settling time (≈4.07

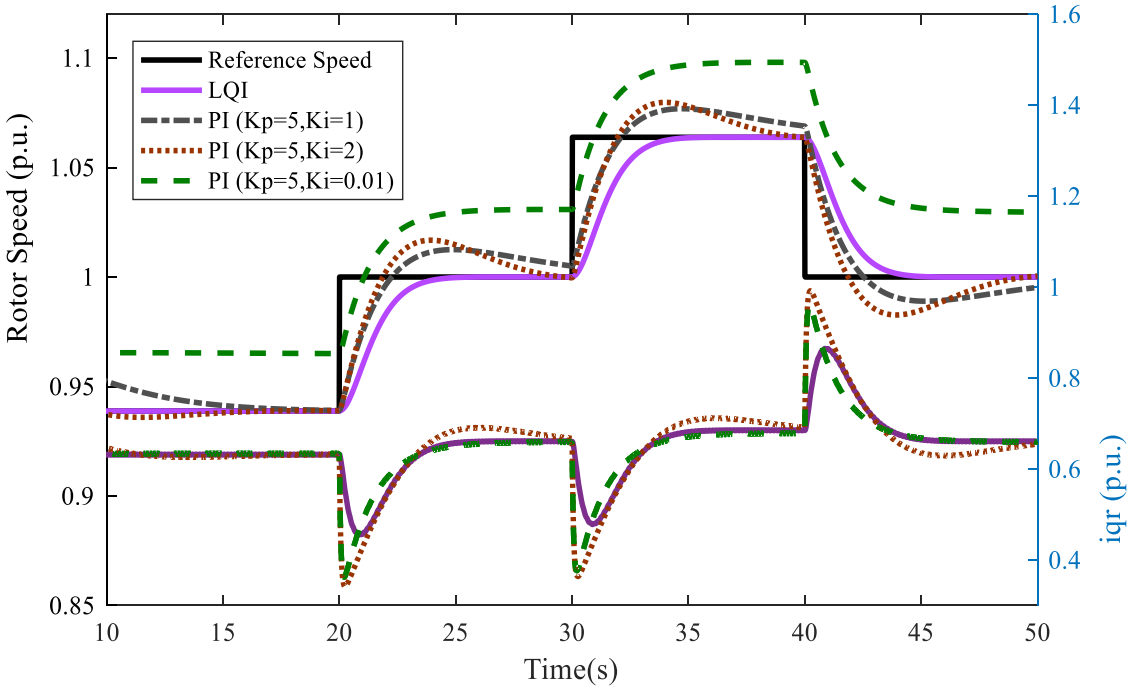

Figure 2.18: Comparison of LQI control vs PI Control for DFIG speed control.

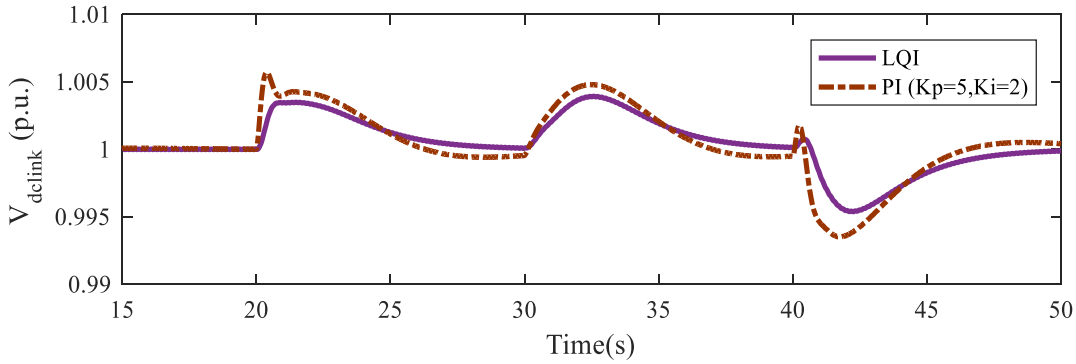

Figure 2.19: DC link voltage with LQI control vs PI Control for DFIG speed control.

seconds) while PI struggled because of higher overshoot (22.20% for K_p=5, K_i=2) and longer settling time (≈9.12 seconds). LQI controller provides much smoother transition in DFIG power in speed step changes, which is also reflected in dc-link voltage. DC-link voltage when LQI based speed control is used is compared to that of PI based speed control in Figure 2.19.

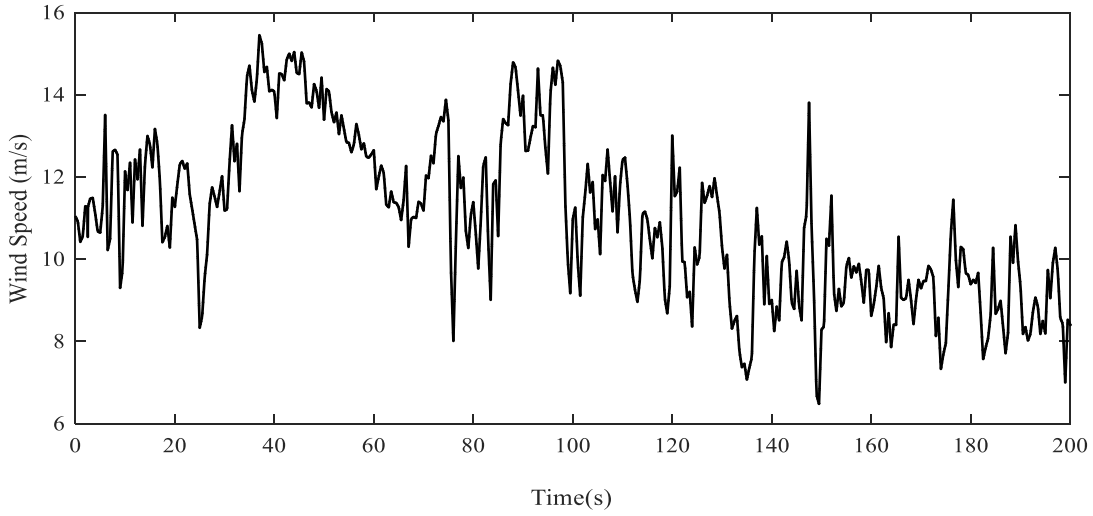

Figure 2.20: Wind profile used in the test study.

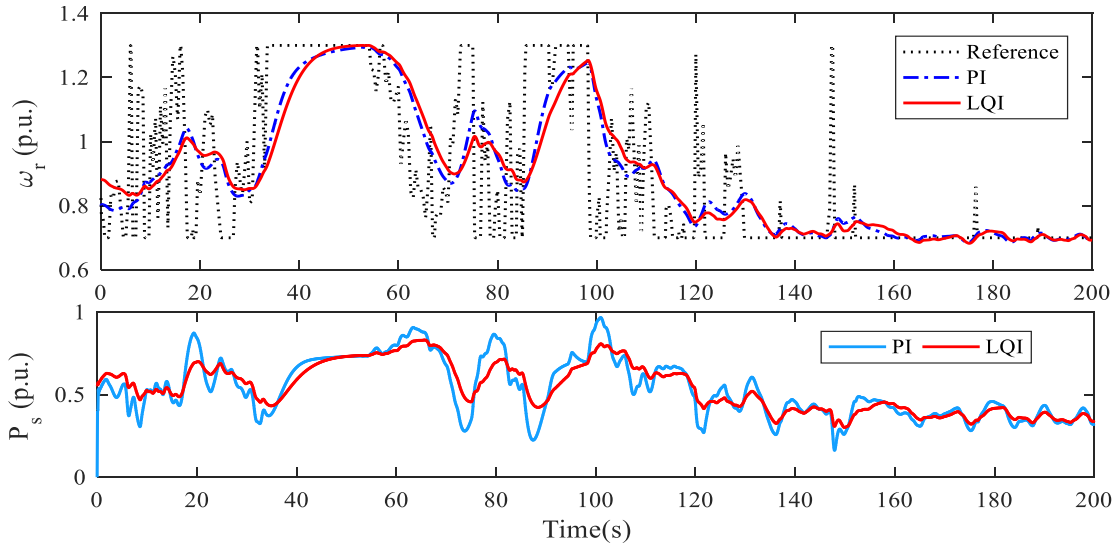

Figure 2.21: DFIG rotor speed w_r and Stator Active Power P_s.

2.8.4 Real Wind Test

The proposed control architecture is tested in real wind pattern as shown in Figure 2.20. The rotor speed $w_{r\ ref}$ and stator power P_s" are shown in Figure 2.21. The results show that the LQI controller can track the speed reference while maintaining much smoother power profile (up to 0.3 p.u). The lower ramp-rate of the power delivered from wind turbine to the grid means reduced impact on voltage and frequency,

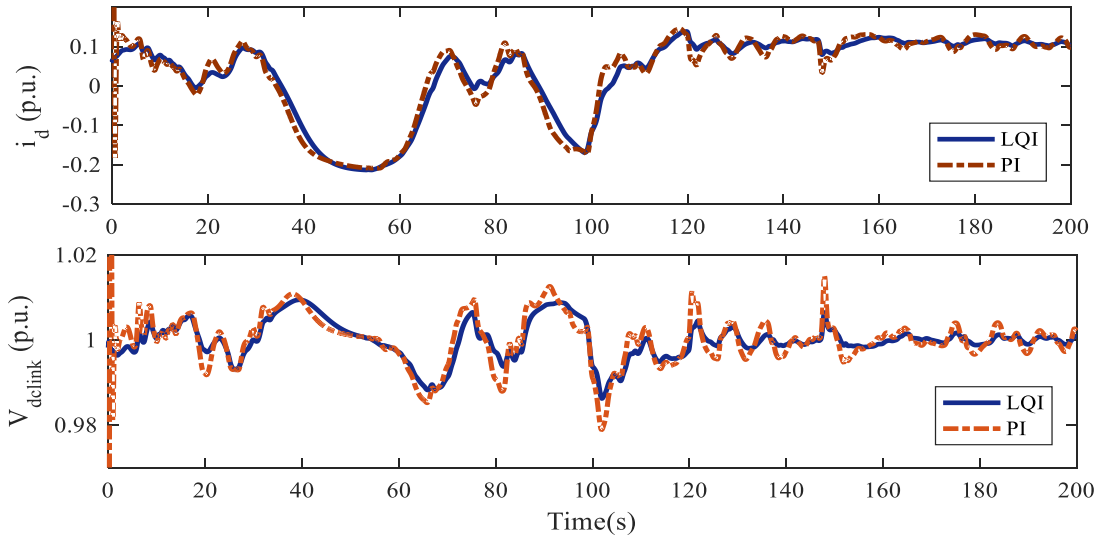

Figure 2.22: GSC d-axis curretn i_d and DC link capacitor voltage.

and reduced regulation requirement for the grid operator, especially with increasing penetration of wind power in the grid. The proposed control technique also maintains the dc-link voltage closer to reference set-point as shown in Figure 2.22.

2.9 Summary

In this chapter, mathematical differential and algebraic equations representing a round rotor synchronous generator was discussed. An standard static excited based on thyristor and a power system stabilizer used to provide damping torque is presented which will be used in our further test and study.

In this chapter, mathematical modeling of doubly fed induction generator and its control has been discussed. An aerodynamic model which results in conversion of kinetic energy of wind as a virtue of its velocity into mechanical torque than rotates the turbine. The turbine mechanical torque is a function of wind speed, rotor speed, and pitch angle. Though multi-mass model are usually required to study the actual dynamics of a wind turbine, the model has been greatly simplified by using lumped single mass model of drive train. Two mass model of drive train has been presented which is used in most of the works of this dissertation. Two mass model treats

mechanical drive train as two separate masses representing turbine and generator separately, and hence, we can observe and study the torsional dynamics of generator and turbine shaft. The induction generator can be represented by a set of voltage and flux equations in d-q reference frame. Second order or fourth order can be used to represent the induction generator depending upon whether stator dynamics need to be studied in the model or not.

Back-to-back converter that provides variable frequency excitation to the rotor winding forms the heart of the DFIG as it facilitates the independent control of active and reactive power. It is composed of two voltage source converters, viz rotor side converter and grid side converter. Rotor side converter allows the control of active and reactive power by controlling the rotor voltage in stator flux oriented d-q reference frame. Grid side converter allows the flow of power from rotor to grid or grid to rotor by maintaining the constant dc-link voltage. Vector control is the widely discussed control topology. An optimal linear quadratic integral controller for dfig controller has been proposed and the results are presented, which show considerable improvements over conventional vector control technique.

CHAPTER 3: MODAL ANALYSIS OF DFIG INTEGRATED POWER SYSTEM

This chapter presents the modal analysis of a grid connected DFIG in both open loop mode and closed loop mode. Open loop mode refers to a DFIG that operates without controlled rotor voltage i.e. the rotor voltage is set constant. Closed loop mode refers to a DFIG with all the controllers taken into consideration, specifically the controlled rotor excitation voltage to achieve active and reactive power control. The DFIGs are integrated to the power grid models interfaced appropriately, and the impact on the grid is assessed. Impact of DFIG on grid is focused on identifying the positive or negative impacts that DFIG can have on slow electromechanical modes of the power system.

3.1 Modal Analysis of DFIG connected to an Infinite Bus

Modal analysis of a DFIG connected to an infinite bus is discussed in this section. By considering an infinite bus, we can assume the voltage and angle of infinite grid to be constant irrespective of the active and reactive power flow from the DFIG. DFIG drive train includes a turbine connected to the generator rotor via gearbox mechanism, three-phase stator windings directly connected to the grid, and rotor windings energized with controlled voltage through back-to-back converter. In power system stability study, the high frequency switching dynamics of the converter are ignored [34], and the converter is represented by an active power balance between RSC and GSC. Depending on whether we consider stator dynamics or not and whether one mass-lumped model or two-mass model is used to represent the drive train model, different models can be defined. For a more detailed study of drive train oscillation that usually exists in a DFIG due to the presence of gear-box interface between the

turbine and the generator shaft, two mass representation of drive-train is preferred. If we include the decoupled active and reactive power control of DFIG, the dynamics of the system changes significantly which will be shown in following subsections.

3.1.1 Open Loop DFIG

In the absence converter control, DFIG acts like a squirrel cage induction generator (SCIG). Two different models are considered as:

- **Model A** considers rotor and stator dynamics represented by equation (2.35)-(2.38) and single mass lumped model of Drive train given by equation 2.27. It is a 5^{th} order model.

- **Model B** considers rotor and stator dynamics represented by equation (2.35)-(2.38) and two mass model of Drive train given by equation (2.32)-(2.34). It is an 8^{th} order model.

Model A exhibits two oscillatory modes as seen from Table 3.1. First one is **stator mode** because it has high participation of stator flux. It has oscillation frequency $\approx$ 60 Hz, and damping ratio $\approx$ 0.09. The second mode is slower **electro-mechanical mode** with oscillation frequency $\approx$ 4 Hz and damping ratio 0.59. Rotor flux ψ_{qr} and mechanical speed w_r show higher participation in this mode.

Table 3.1: Eigenvalues of Model A

Mode	σ	Freq. [Hz]	Damping (ζ)	Participating States	Remark
$\lambda_{1,2}$	-33.8	59.48	0.09	$\psi_{ds,qs}$	Stator Mode
$\lambda_{3,4}$	-18.3	3.94	0.59	ψ_{qr}, w_r	Electromechanical Mode
λ_5	-37.1	0	1	ψ_{dr}	

Model B exhibits three oscillatory mode as seen in Table 3.2. **Stator mode** similar to Model A. **Electromechanical mode** of Model B has higher oscillatory frequency $\approx$ 16 Hz because of the comparatively smaller generator inertia $H_g = 0.5$

sec. This mode has damping ratio of 0.12. Another **mechanical/torsional mode** appears due to gearbox interfaced generator shaft and turbine, which are represented by two mass model. This mode has damping ratio of 0.37.

Table 3.2: Eigenvalues of Model B

Mode	σ	Freq. [Hz]	Damping (ζ)	Participating States	Remark
$\lambda_{1,2}$	-33.8	59.48	0.09	$\psi_{ds,qs}$	Stator Mode
$\lambda_{3,4}$	-12.3	16.1	0.12	w_r, ψ_{qr}, θ_{tw}	Electromechanical Mode
$\lambda_{5,6}$	-7.45	2.95	0.37	w_t,θ_{tw}, ψ_{qr}	Torsional/Mechanical Mode
λ_7	-37.1	0	1	ψ_{dr}	

In order to understand the sensitivity of the DFIG modes with respect to its various parameters, the locus of these modes are plotted on changing the mechanical parameters of the turbine and generator viz. shaft stiffness K_d, damping coefficient D_d, generator inertia H_g and turbine inertia H_t. Figure 3.1 shows the locus of DFIG when K_d increases from 1 to 30 (p.u./rad). As the stiffness of the shaft increases, the participation of turbine inertia in the electromechanical mode increases, and frequency of oscillation decreases from $\approx$ 140 (rad/s) to $\approx$ 80 (rad/s), and the mode is better damped. The frequency of mechanical torsional mode increases from 7.57 to 22.4 (rad/sec), and this mode is better damped, meaning the two masses are tightly attached to each other.

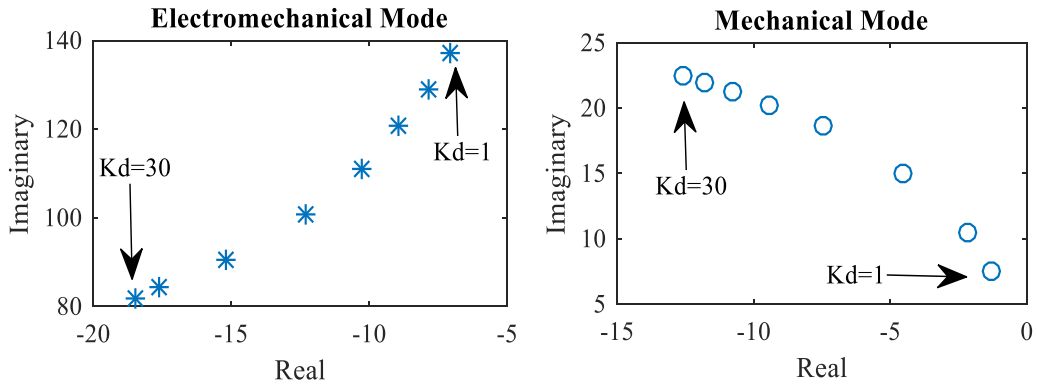

Figure 3.1: DFIG Open Loop Modes w.r.t. K_d [1-30 (p.u./rad)].

Figure 3.2 shows the locus of electromechanical and mechanical mode as damping coefficient D_d increases from 0.001 to 0.1 (p.u. sec/rad). Higher damping coefficient ensures better damping of torsional/mechanical mode, as well as electromechanical mode.

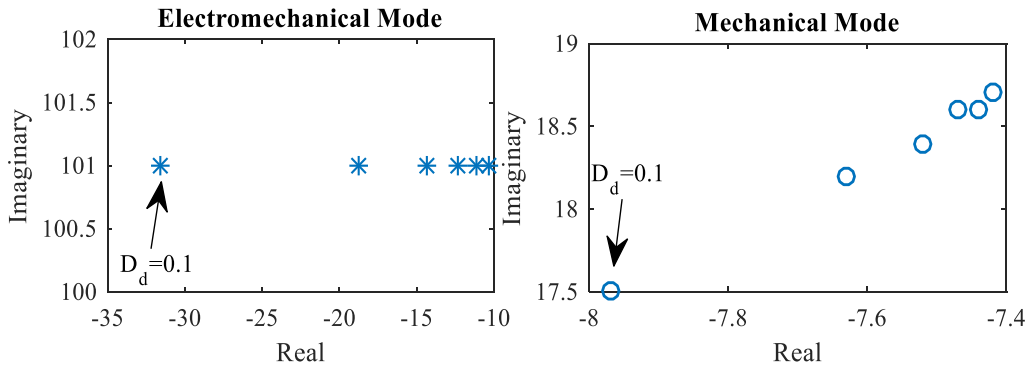

Figure 3.2: DFIG Open Loop Modes w.r.t. D_d [0.001-0.1(p.u. sec/rad)].

Figure 3.3 shows the locus of DFIG modes as generator rotor inertia H_g increases from 0.1 to 0.6 sec. The increasing mass of generator means decreasing frequency of electromechanical mode. There is slight increase in frequency of mechanical and slight drop in damping ratio as well.

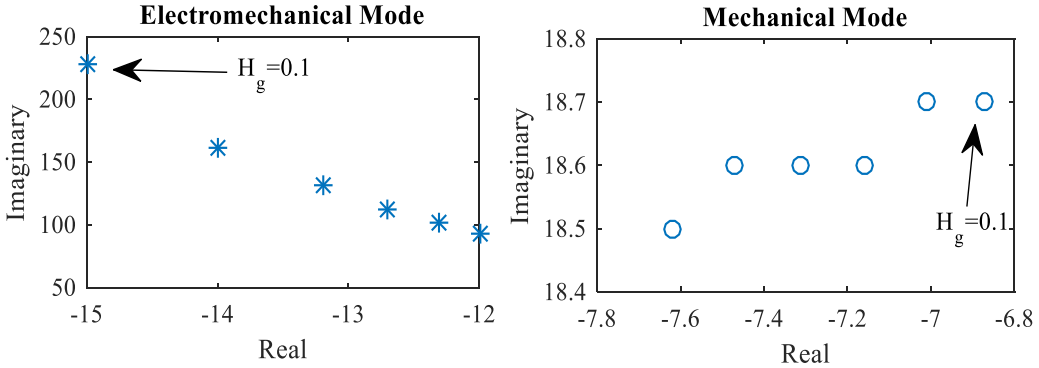

Figure 3.3: DFIG Open Loop Modes w.r.t. H_g [0.1-0.6 (sec)].

Figure 3.4 shows the DFIG modes when turbine inertia is increased from 1 to 6 sec. Increasing the turbine inertia decreases the frequency of mechanical mode from

32 (rad/s) to 12 (rad/s). The oscillation frequency of electromechanical mode drops from 104 (rad/s) to 100 (rad/s).

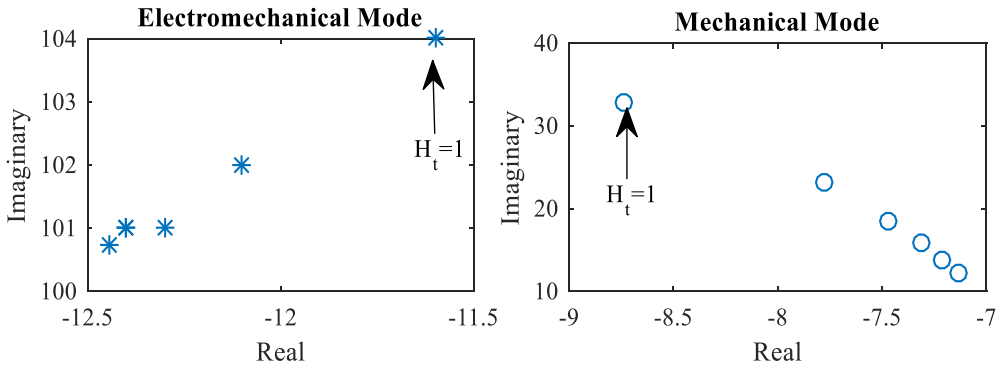

Figure 3.4: DFIG Open Loop Modes w.r.t. H_t [1-6 (sec)].

Figure 3.5 shows the locus of DFIG modes when generator speed w_r increases from 0.7 to 1.2 [p.u.]. The electromechanical mode oscillates with smaller frequency near synchronous speed. The damping is relatively better in super-synchronous region. The mechanical mode exhibits the oscillation frequency proportional to the magnitude of slip. Max frequency is 49 (rad/sec) at w_r=0.7 [p.u.]. The damping is highest at slip $\approx \pm$ 0.1.

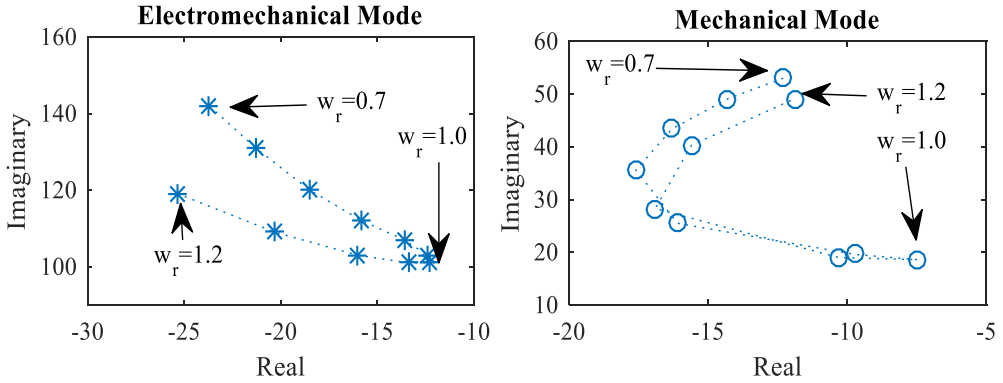

Figure 3.5: DFIG Open Loop Modes w.r.t. w_r [0.7-1.2 (p.u.)].

3.1.2 Closed Loop DFIG with Vector Control

In order to understand the dynamics of an actual DFIG, it is necessary to include the speed/ active power and voltage/reactive power controller. In this section, modal

analysis of closed loop DFIG considering the speed and voltage controller as shown in Figure 2.9 is presented. 7^{th} order open loop DFIG system with the speed and voltage control makes an 11^{th} order model of DFIG. We assess the eigenvalues of this system in three distinctive operating regions of operation distinguished by the rotor speed.

- **Subsynchronous** mode: The rotor speed is below synchronous speed. Let w_r=0.7 p.u. and the mechanical torque T_m=0.5 p.u.
- **Synchronous** mode: The rotor speed is at synchrnous speed i.e. w_r=1.0 p.u. and the mechanical torque T_m=0.75 p.u.
- **Supersynchronous** mode: The rotor speed is at synchrnous speed i.e. w_r=1.2 p.u. and the mechanical torque T_m=1.0 p.u.

The proportional and integral gains used in the base case are given in Table 3.3.

Table 3.3: PI controller gains

	Proportional	Integral
Speed Control	10	2
Voltage Control	5	10
i_{qr} Control	0.01	4.0
i_{dr} Control	0.01	0.01

Eigenvalues and the states with higher participation are shown in Table 3.4-3.6. In each modes of operation, a mode with frequency $\approx$ 59 Hz is present with high participation of stator flux $\psi_{ds,qs}$, and hence termed as stator mode. Another mode with frequency $\approx$ 10 Hz and high participation of shaft twist angle θ_{tw}, generator speed w_r and turbine speed w_t is called torsional mode. It is well damped, and it depends on shaft stiffness K_d and damping coefficient D_d. A highly mode with frequency $\approx$ 30 Hz with high participation of rotor flux and speed controller is observed, and is well damped under all operating conditions.

The sensitivity of the DFIG modes to different parameters like controller gains, grid strength and operating speed should be addressed to understand DFIG dynamics

Table 3.4: Eigenvalues of DFIG during at sub-synchronous mode

Eigenvalue	σ	Frequency [Hz]	Damping ratio (ζ)	Participating States
$\lambda_{1,2}$	-49	61.2	0.13	ψ_{ds},ψ_{qs}
$\lambda_{3,4}$	-47.0	37.26	0.20	$\psi_{qr}, x_{iq}, \psi_{dr}, w_r$
$\lambda_{5,6}$	-6.92	9.85	0.11	θ_{tw},w_r,w_t
λ_7	-75.0	0	1	ψ_{dr},x_{iq},
λ_8	-1.3	0	1	w_t
λ_9	-0.57	0	1	x_{id}
λ_{10}	-0.11	0	1	x_{iw}
λ_{11}	-0.069	0	1	x_{iv}

Table 3.5: Eigenvalues of DFIG during at synchronous mode

Eigenvalue	σ	Frequency [Hz]	Damping ratio (ζ)	Participating States
$\lambda_{1,2}$	-45	63.39	0.11	ψ_{ds},ψ_{qs}
$\lambda_{3,4}$	-43.0	28.9	0.20	$\psi_{qr}, x_{iq}, \psi_{dr}, w_r$
$\lambda_{5,6}$	-6.7	9.44	0.11	θ_{tw},w_r,w_t
λ_7	-93.0	0	1	ψ_{dr},x_{iq},
λ_8	-1.3	0	1	w_t
λ_9	-0.63	0	1	x_{id}
λ_{10}	-0.11	0	1	x_{iw}
λ_{11}	-0.1	0	1	x_{iv}

Table 3.6: Eigenvalues of DFIG during at super-synchronous mode

Eigenvalue	σ	Frequency [Hz]	Damping ratio (ζ)	Participating States
$\lambda_{1,2}$	-43	64.4	0.11	ψ_{ds},ψ_{qs}
$\lambda_{3,4}$	-56.0	30.87	0.28	$\psi_{qr}, x_{iq}, w_r, \psi_{dr}$
$\lambda_{5,6}$	-6.9	9.596	0.11	θ_{tw},w_r,w_t
λ_7	-70.0	0	1	ψ_{dr},x_{iq},
λ_8	-1.3	0	1	w_t
λ_9	-0.57	0	1	x_{id}
λ_{10}	-0.11	0	1	x_{iw}
λ_{11}	-0.069	0	1	x_{iv}

under varying operating scenarios. We will look only at the oscillatory modes if present and variation in its frequency and damping ratio by changing one parameter at a time while keeping other parameters consistent with the base case. Here base case

is defined by control gains given in Table 3.3, transmission line reactance x_e=0.01 p.u., rotor speed w_r=1.0 p.u. Frequency and damping ratio of stator mode and torsional mode with respect to q-axis rotor current control proportional gain K_{pq} and integral gain K_{iq} is shown in Figure 3.6. The damping of stator mode decreased when K_{pq} is increased, though the effect gets saturated at K_{pq} ≈1. Increasing the value of K_{pq} also reduced the damping ratio of torsional mode. The damping of both stator and torsional mode decreased with increasing value of K_{iq}.

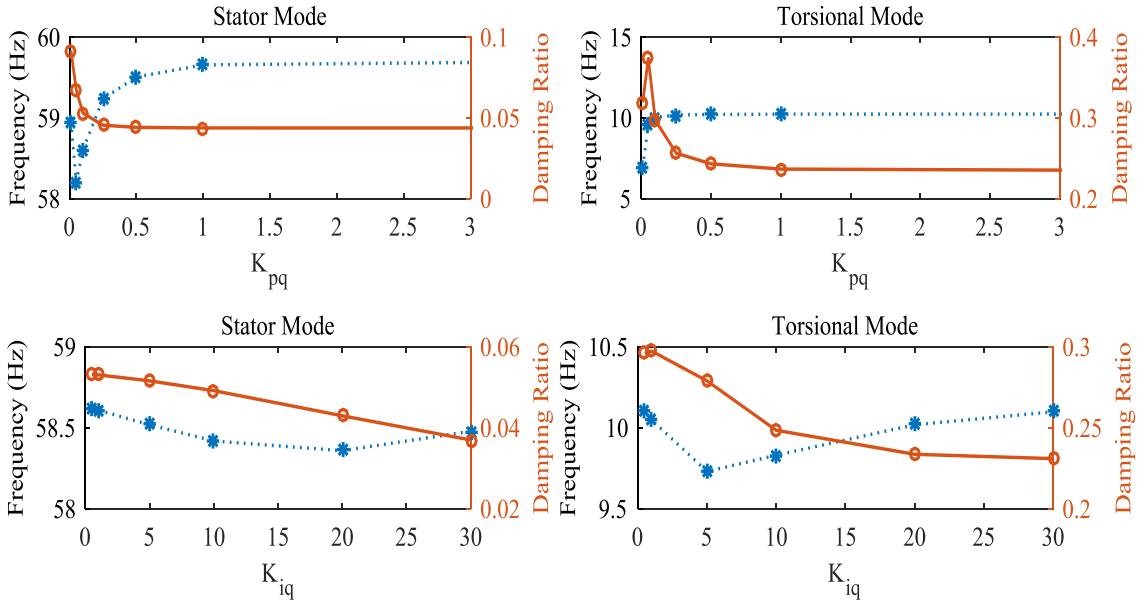

Figure 3.6: DFIG Modes w.r.t. i_{qr} controller gains K_{pq} and K_{iq}.

Frequency and damping ratio of stator mode and torsional mode with respect to d-axis rotor current control proportional gain K_{pd} and integral gain K_{id} is shown in Figure 3.7. The damping of stator flux mode decreased when K_{pd} increased. Stator flux has maximum damping at K_{id} ≈10, and tends to be lesser damped as K_{id} keeps increasing. There is very insignificant effect on torsional mode.

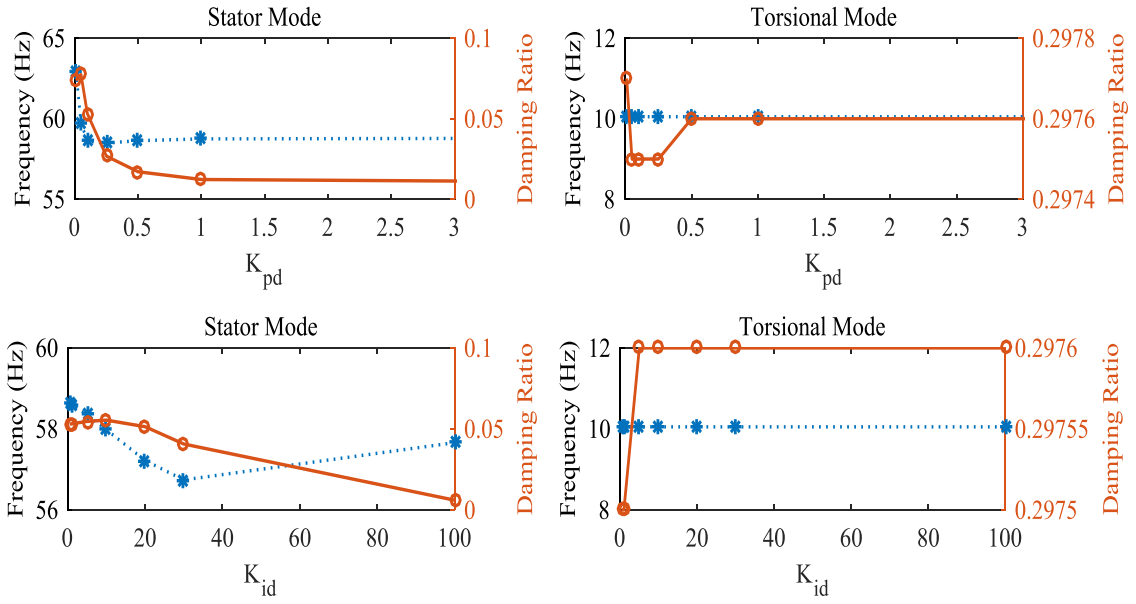

Figure 3.7: DFIG Modes w.r.t. i_{dr} controller gains K_{pd} and K_{id}.

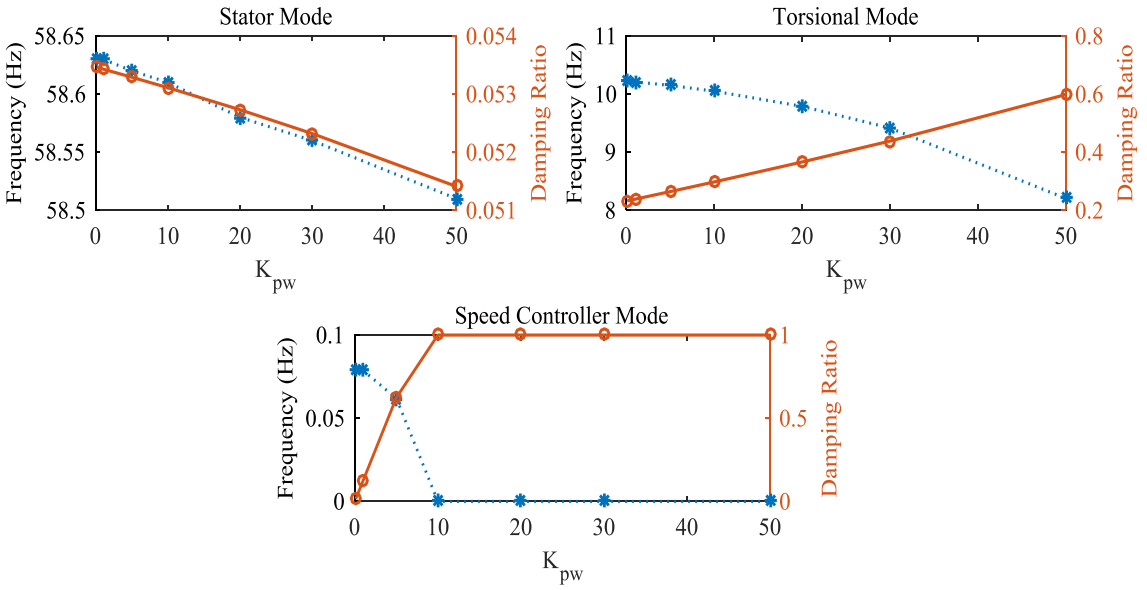

Figure 3.8: DFIG Modes w.r.t. speed controller gain K_{pw}.

The impact of changing speed controller proportional gain K_{pw} is shown in Figure 3.8. Increasing K_{pw} provides improved damping of torsional oscillation and reduces the frequency of oscillation; the stator flux mode experiences slight decrease in both frequency and damping. At lower value of K_{pw}, an oscillatory speed controller mode is

seen but disappears at values above 10. The integral gain of speed controller K_{iw} had no effect on stator dynamics, and its impact on speed controller mode and torsional mode is shown in Figure 3.9. Speed controller oscillatory mode appears when K_{iw} is greater than 2, the damping reduces and frequency increases as K_{iw} is further increased. Though the damping of torsional mode is seen to increase, the effect is minimal.

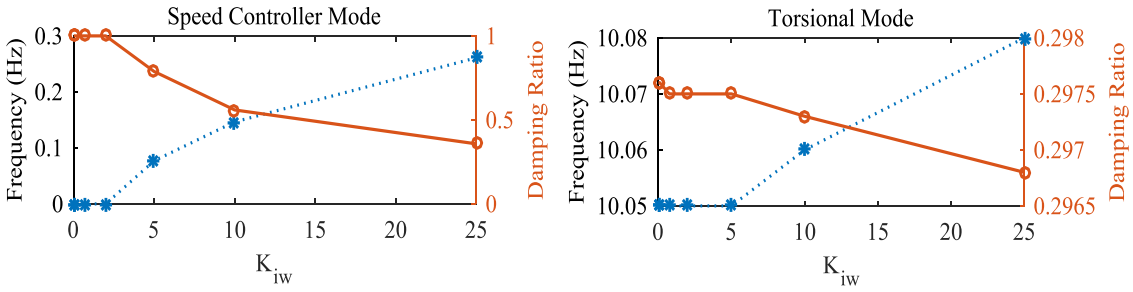

Figure 3.9: DFIG Modes w.r.t. speed controller gain K_{iw}.

The stator flux oscillation seems to be damped better as the strength of the tie-line decreases i.e. when value of line reactance x_e increases. This is very distinct when compared to an induction generator whose stator flux oscillation damping decreases. This is shown in Figure 3.10. Rotor flux mode damping ratio is seen to reduce slightly.

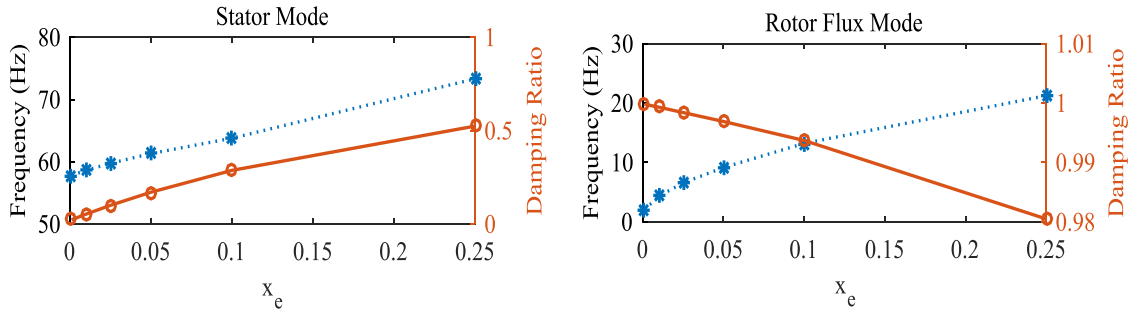

Figure 3.10: DFIG Modes w.r.t. tie-line reactance x_e between the infinite bus and DFIG bus.

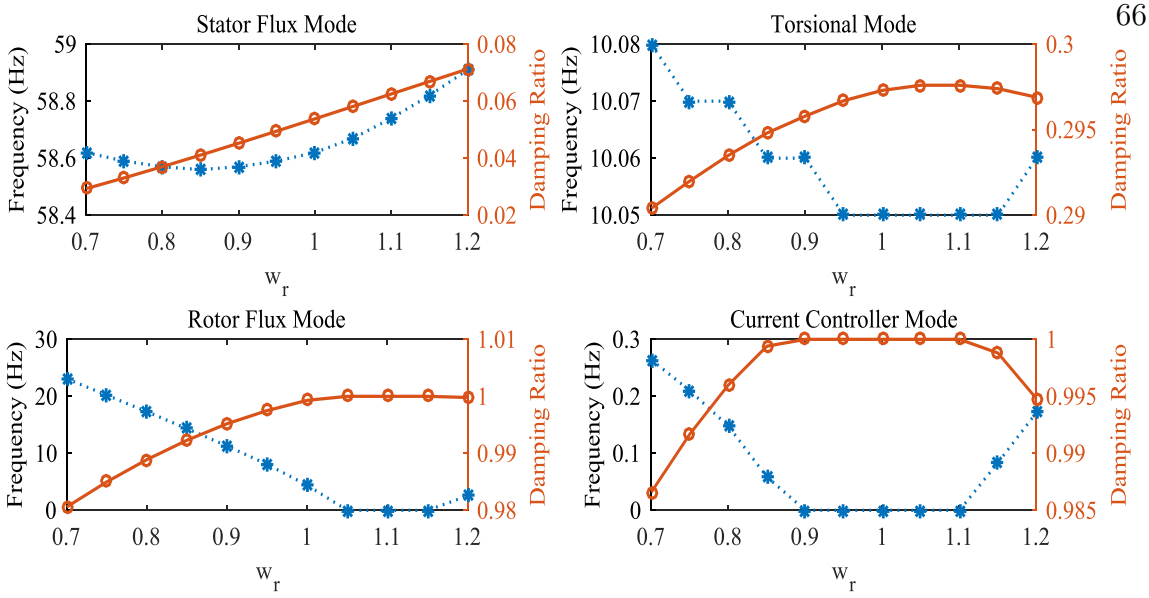

Figure 3.11: DFIG Modes w.r.t. generator speed w_r.

The sensitivity of DFIG modes with respect to the operating points is shown in Figure 3.11. The stator flux oscillation is damped better at higher rotor speeds. The torsional mode is damped best at synchronous speed with slight decrease in damping as rotor speed deviates from synchronous speed. Rotor flux oscillatory mode is also found at speeds other than the synchronous speed. Similarly, current controller modes appear in speeds other than the synchronous speed.

3.2 Modal Analysis of DFIG Integrated Power System

In order to study the impact of increasing DFIG penetration on power system small signal stability, a test system was selected as a representative power system model. DFIGs do not participate in an electromechanical oscillation neither they create any oscillatory modes of such kind. However, increasing penetration level of DFIGs can affect the grid oscillation dynamics in various ways. In general, the structural change in the power system that is caused by the DFIG affect the power system dynamics. For example, DFIGs can replace the existing synchronous generators leading to reduced system inertia, and DFIGs can affect the generators committed at a particular instant which might lead to high power flow in critical tie-lines.

3.2.1 Test System Used For the Study

11-bus, 4-machine test system [27] as shown in Figure 3.12 is used in this study. It consists of two areas A_1 and A_2 and each area has a pair of equivalent synchronous generators. The generators in bus 1,2,3 and 4 represented by SG_1, SG_2, SG_3 and SG_4 are equipped with 'IEEE ST1A' exciter. Only SG_1 and SG_3 are equipped with rotor slip feedback based PSS. The slow dynamics of the governors are ignored, and the mechanical torques to the generators are taken as constant inputs.

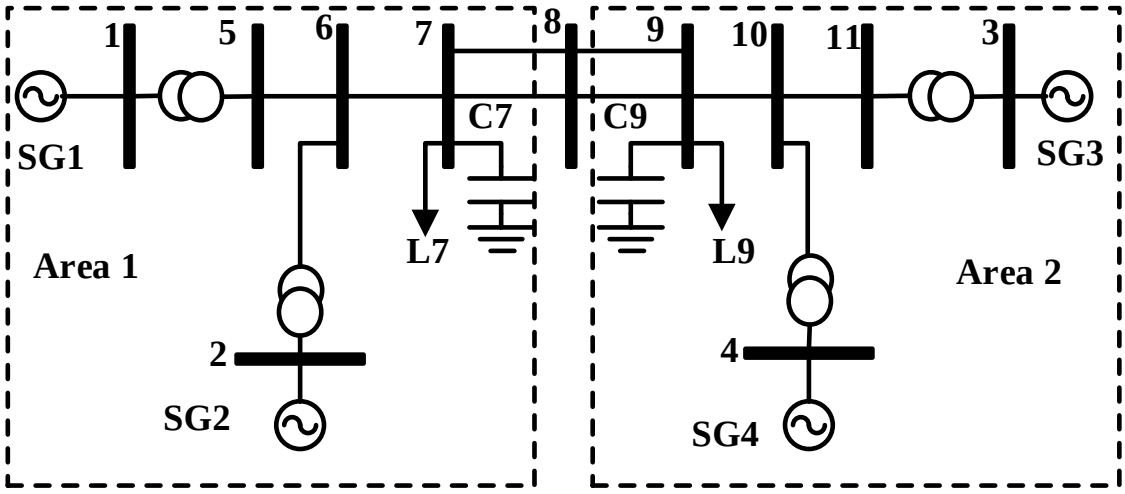

Figure 3.12: 11-bus, 4-machine Test System.

3.2.2 Supplementary Control of DFIG

A supplementary control loop based on the feedback from the point of common coupling (PCC) frequency deviation is shown in Figure 3.13 which active power set-point modulation signal to RSC controller. The objective of this control is to supply electric torque to damp the oscillation observed in the power system frequency caused by disturbance in the grid. The electrical behavior of the generator and converter is that of a current regulated voltage source converter. The conventional aspects of generator performance related to internal angle, excitation voltage and synchronism are largely irrelevant [52]. Consequently, there is no considerable lag in the signal

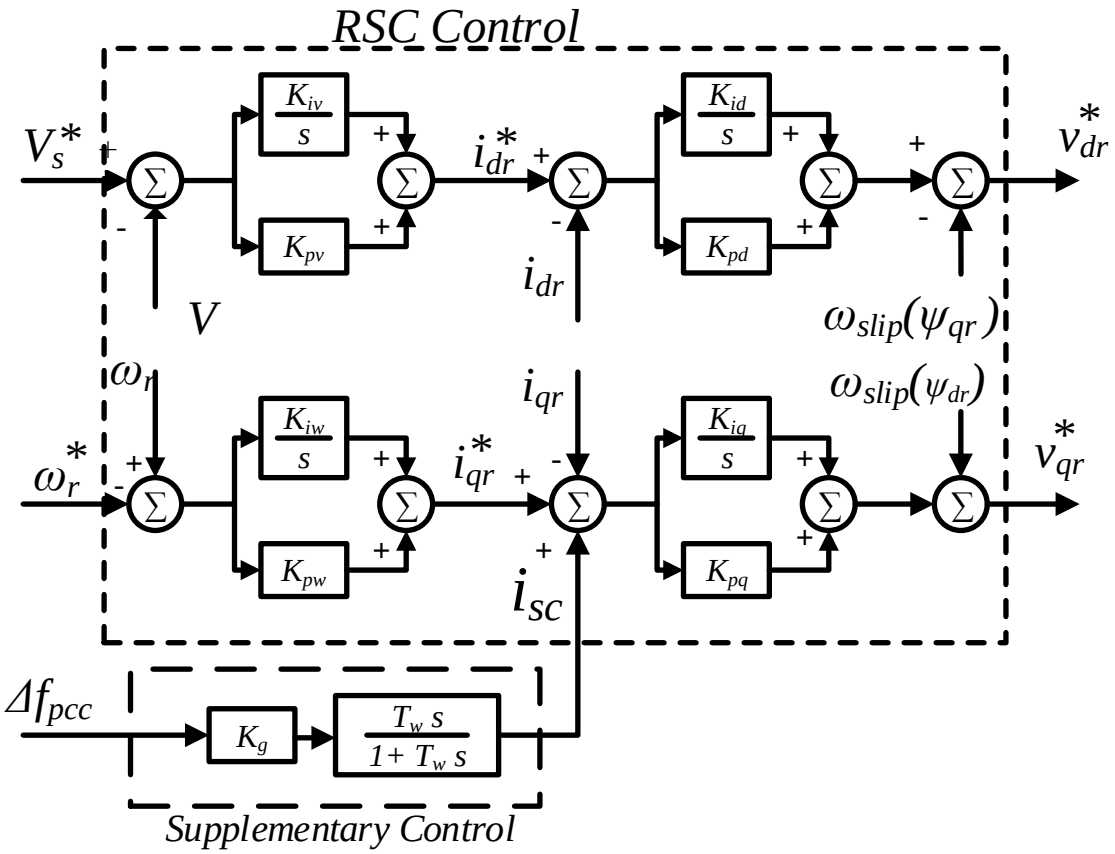

Figure 3.13: DFIG Control Augmented with Supplementary Control Loop.

through the converter. This rules out the need for the phase compensation block while adjusting the DFIG excitation to improve the damping. The controller consists of a proportional gain K_g and a washout filter with time constant T_w and produces a supplementary q-axis rotor current signal i_{sc} which is added to q-axis rotor current control loop. The gain is tuned to provide the maximum damping using root-locus based method.

3.2.3 Test Cases

It has been found that the generation loading and the tie-line power flow are two of the most dominant factors in power system stability. Two cases are developed for analyzing the performance of DFIG integrated grid, and effectiveness of supplementary control architecture discussed in section 3.2.2.

3.2.3.1 Case 1

In case 1, the power flow from A_1 to A_2 is changed in step of 50MW from 400MW to -400MW by adjusting the load L_7 and L_9 in two areas keeping the generation constant as illustrated in Figure 3.14.. Negative power flow means that the direction of power flow is reversed.

Following four sub-cases of case 1 are formulated to simulate the DFIG replacing a synchronous generator:

1.1 Base Case: All four generators have automatic voltage regulator and only SG_1 and SG_3 are equipped with PSS.

1.2 A DFIG replaces SG_4.

1.3 A DFIG replaces SG_3.

1.4 A DFIG replaces SG_3. Supplementary control loop is added to DFIG.

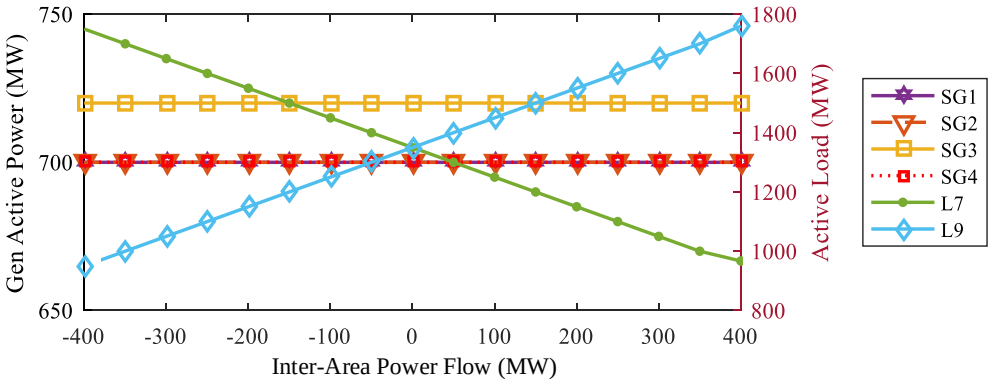

Figure 3.14: Case 1: Changing active load and constant generation.

3.2.3.2 Case 2

In case 2, power flow from A_1 to A_2 is changed in steps of 50 MW from 400MW to -100MW by increasing the generation of SG_3 and equally decreasing the generation of SG_1 and SG_2 while keeping the loads unchanged. This is illustrated in Figure 3.15.

Following three sub-cases of case 2 are considered for analysis::

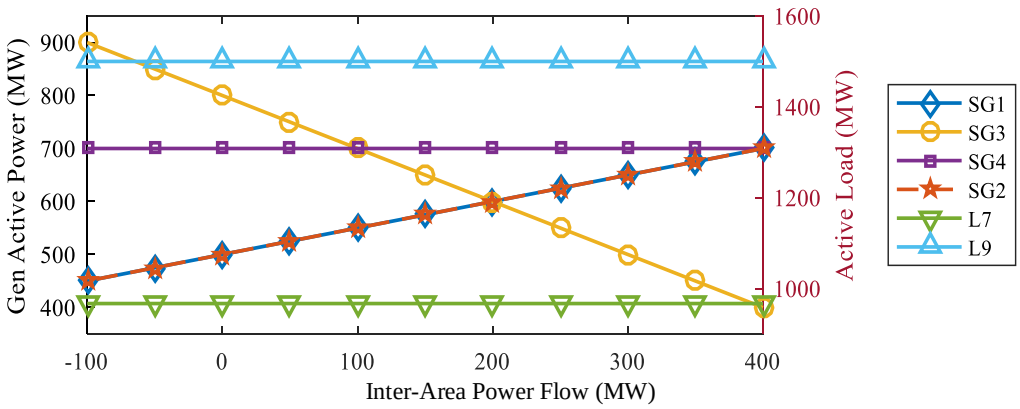

Figure 3.15: Case 2: Constant active load and changing generation.

2.1 Base Case: All four generators have automatic voltage regulator and only SG_1 and SG_3 are equipped with PSS.

2.2 A DFIG replaces SG_3.

2.3 A DFIG replaces SG_3. Supplementary control loop is added to DFIG.

3.2.4 Modal Analysis

The DAEs (differential and algebraic equations) representing the power system is linearized, thereby providing the state space matrices and eigenvalues for the linearized system. Looking at the frequency, damping ratio and high participating states, the electro-mechanical modes of the system can be distinguished. Generally, local modes have frequency ranging from 1 Hz to few Hz, while inter-area modes (IAM) are relatively slower with frequency ranging from 0.1 Hz to 0.7 Hz.

The test system chosen exhibits three distinct electromechanical modes characteristic of modern bulk power systems. The modes of the system in case 1.1 are shown in Table 3.7 and the mode shapes are shown in Figure 3.16.

Table 3.7: Electromechanical Modes of 11-bus, 4-machine System

Mode	freq. (Hz)	Damping (%)	States	Remark
-0.22 ± 3.90	0.62	5.77	$\omega_3, \omega_4, \omega_1, \omega_2$	Inter-Area Mode
-1.10 ± 7.83	1.24	13.92	ω_3, ω_4	Area 2 Mode
-1.10 ± 7.58	1.21	14.37	ω_1, ω_2	Area 1 Mode

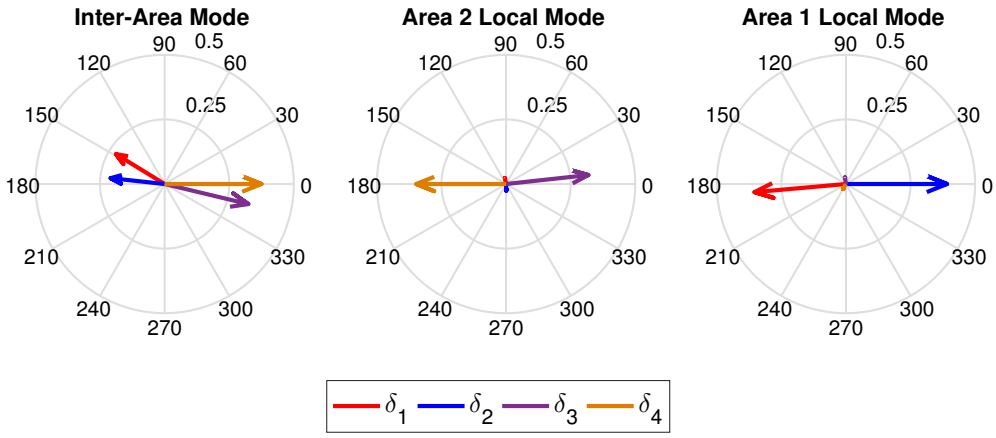

Figure 3.16: Mode shape of of generator rotor angles for case 1.1.

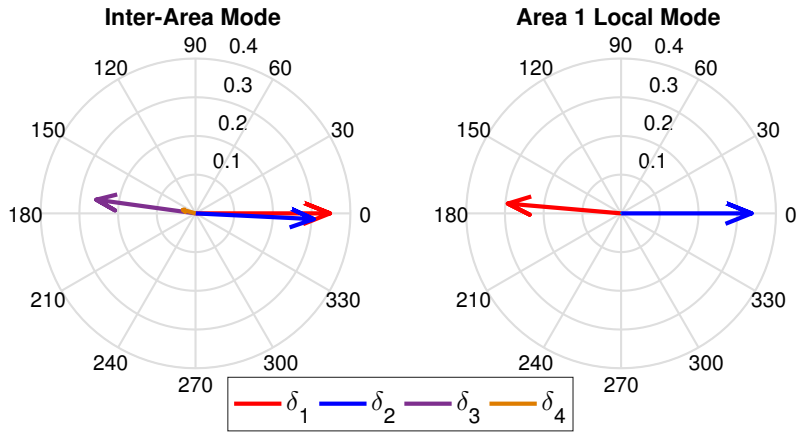

Figure 3.17: Mode shape of of generator angles for case 1.2. The area 2 local mode vanishes because DFIG does not oscillate against SG_4.

The local modes are relatively well-damped while IAM is poorly damped due to weak tie-line that connects the two areas. This section mainly focuses on IAM. The frequency and damping are affected by the loading of the tie-line. The mode shape in case 1.2 and 1.3 as shown in Figure 3.17 and 3.18 shows that the local mode of area 2 vanishes meaning the DFIG do not oscillate with SG_4. The inter-area mode exists in which SG_4 oscillate against the generators in area 1. The local mode in area 1 remains unchanged.

The locus of IAM for case 1.1, 1.2 and 1.3 are presented in Figure 3.19, 3.20 and

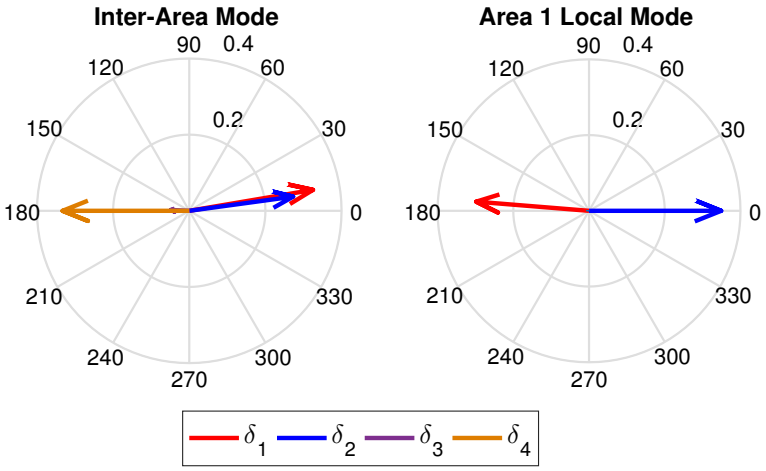

Figure 3.18: Mode shape of of bus angles for case 1.3. The area 2 local mode vanishes because DFIG does not oscillate against SG_4.

3.21 respectively. In all cases, the damping and frequency show variation with varying tie-line flow, with least damping when tie-line flow is 400MW from area A_2 to area A_1 and maximum frequency at around 0MW power flow. The damping ratio improved in case 1.2 compared to case 1.1 i.e. substituting SG_4 by DFIG improves IAM damping. However, the damping of IAM is very poor in case 1.3 and becomes unstable as the power flow from A_2 to A_1 approaches 400 MW as shown by the IAM moving from left-half plane to the right-half plane.

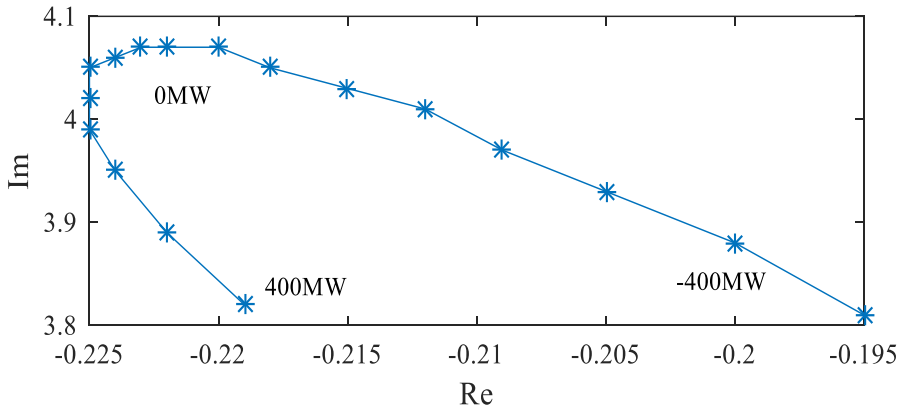

Figure 3.19: Locus of IAM in Case 1.1.

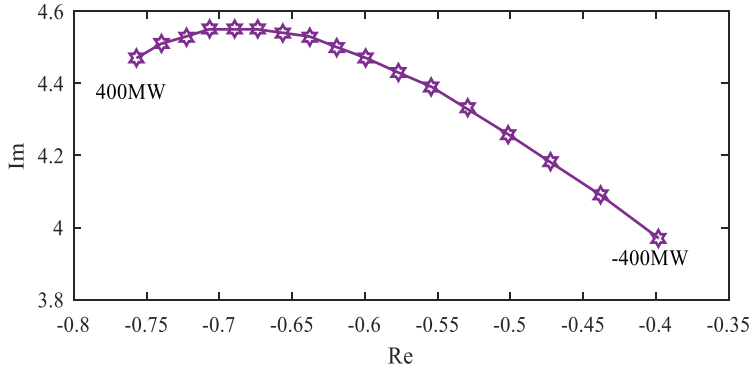

Figure 3.20: Locus of IAM in Case 1.2.

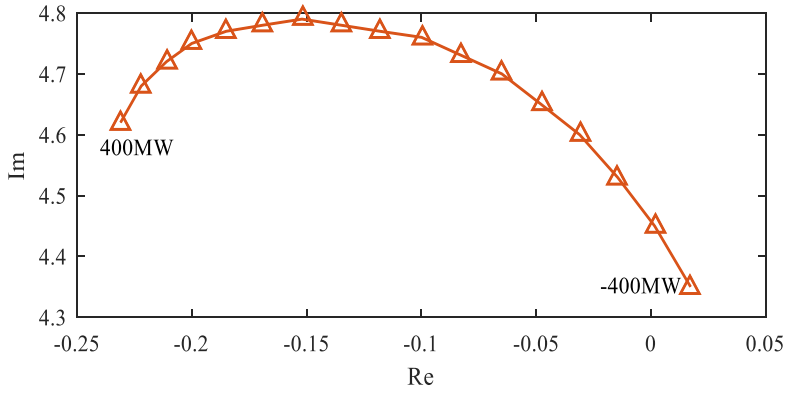

Figure 3.21: Locus of IAM in Case 1.3.

3.2.5 Tuning gain of DFIG Supplementary Control

As the damping of IAM with DFIG replacing SG_3 was worsened significantly, a supplementary controller as discussed in section II is implemented in case 1.4. The damping provided by this controller can be analyzed via modal analysis. The damping of IAM depends on the operating condition of the system and the proportional gain K_g. The washout filter time constant 'T_w' was kept constant at 10 sec. A procedure to tune the gain K_g based on root-locus method is used. The gain was tuned for initial operating point where 400MW power is flowing from A_1 to A_2. The locus of IAM as K_g is increased from 0 to 500 is shown in Figure 3.22 and IAM frequency and damping are shown in Figure 3.23. K_g=100 was chosen as it provided the maximum damping to the IAM. The locus of IAM as inter area power flow changed from 400MW

to -400MW is shown in Figure 3.24. The addition of supplementary control was able to improve the IAM damping much better than PSS equipped SG_3. The damping of IAM for case 1.1 to 1.4 can be summarized as shown in Figure 3.25.

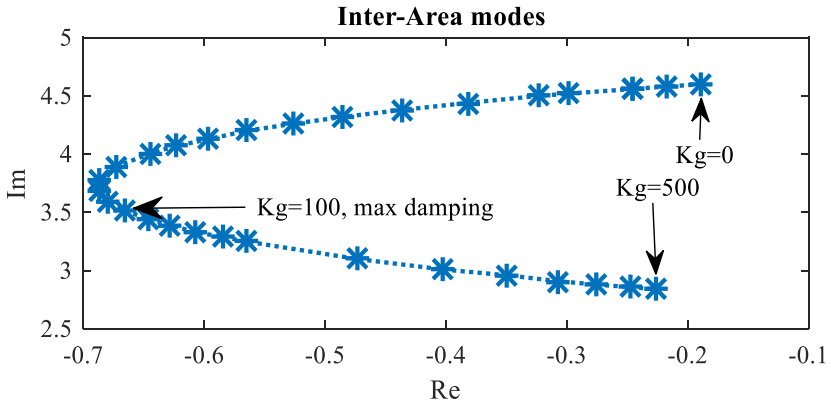

Figure 3.22: Locus of IAM as K_g increases from 0 to 500.

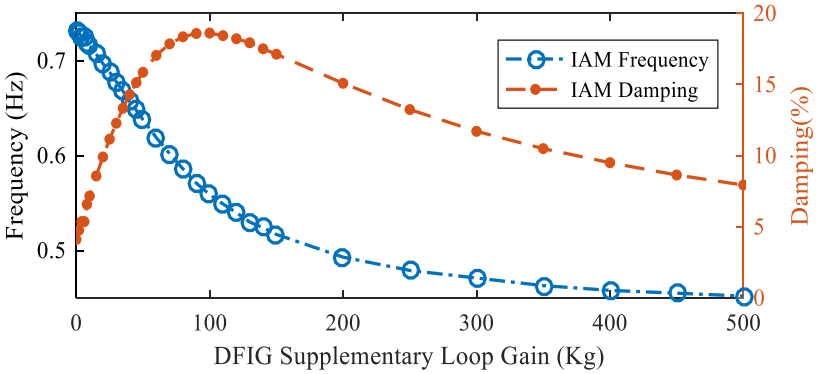

Figure 3.23: Frequency and damping of IAM as K_g increases from 0 to 500.

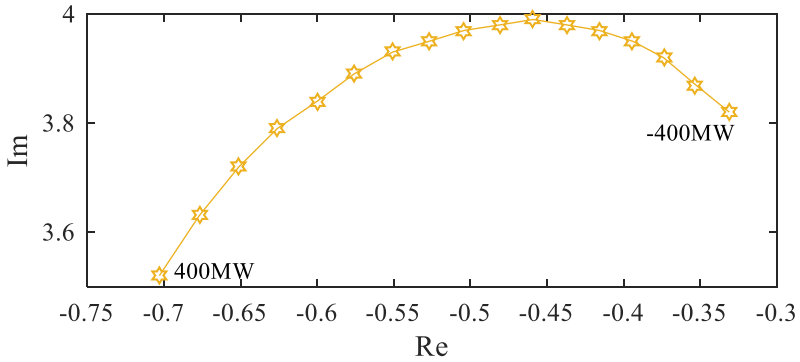

Figure 3.24: Locus of IAM in Case 1.4.

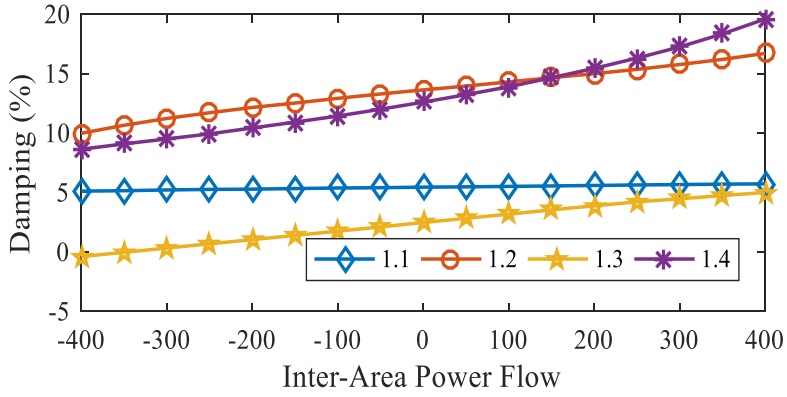

Figure 3.25: Damping of IAM as inter-area power flow changes in Case 1.

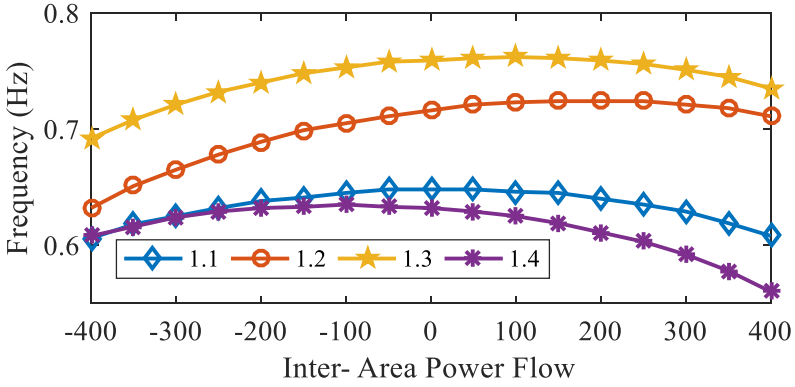

Figure 3.26: Frequency of IAM as inter-area power flow changes in Case 1.

The locus of IAM for case 2.1 2.2 and 2.3 are shown in Figure 3.27, 3.28 and 3.29 respectively. In case 2.2, when SG_3 is replaced by DFIG, the damping ratio is significantly reduced and moves towards instability region as the generation of DFIG is increased from 400MW to its nominal value of 900MW while inter-area flow is changed from 400MW to -100MW. Addition of supplementary loop to the DFIG power control was able to improve the damping of IAM much better than synchronous generator even though it is more sensitive to the tie-line flow. The damping tends to decrease as the generation from DFIG increases as it can be seen from Figure 3.30.

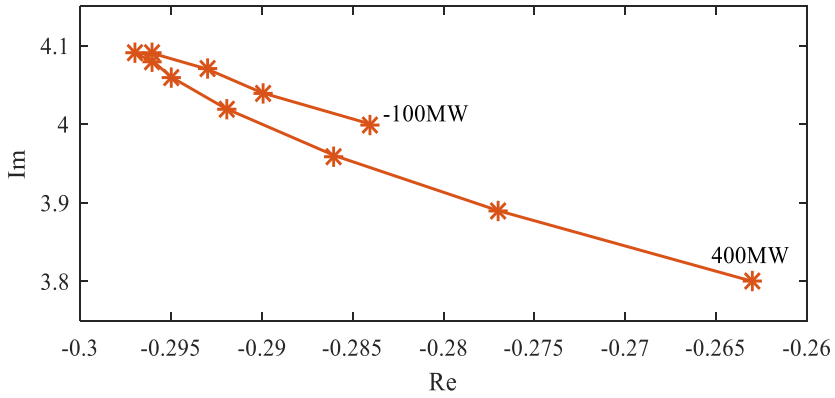

Figure 3.27: Locus of IAM in Case 2.1.

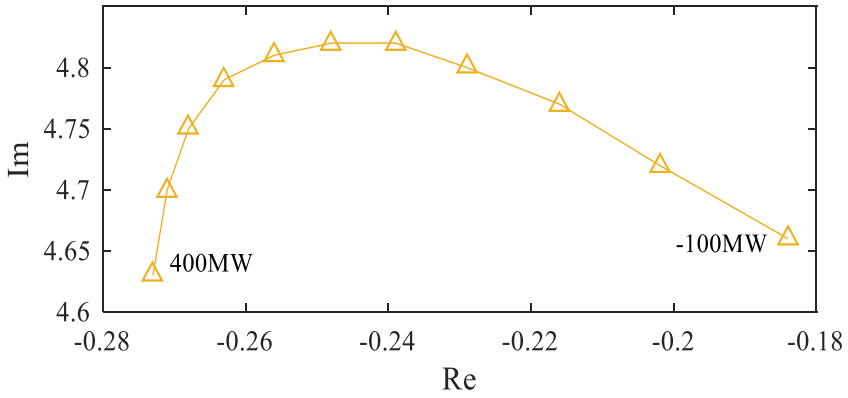

Figure 3.28: Locus of IAM in Case 2.2.

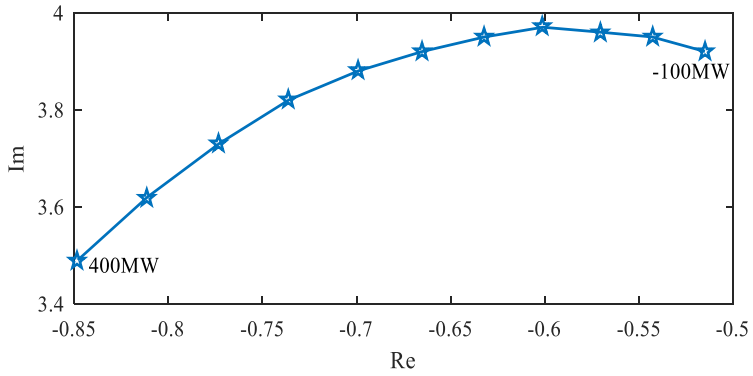

Figure 3.29: Locus of IAM in Case 2.3.

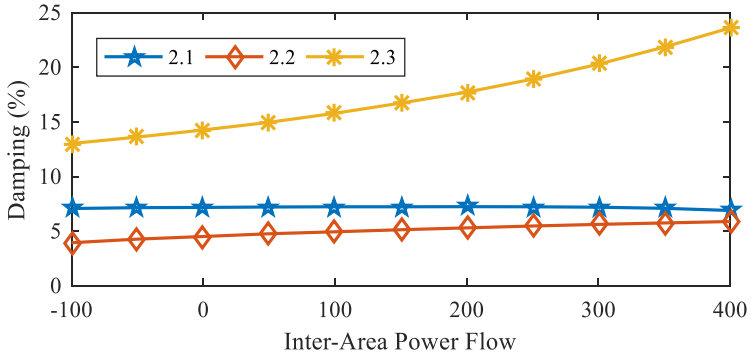

Figure 3.30: Damping of IAM as inter-area power flow changes in Case 2.

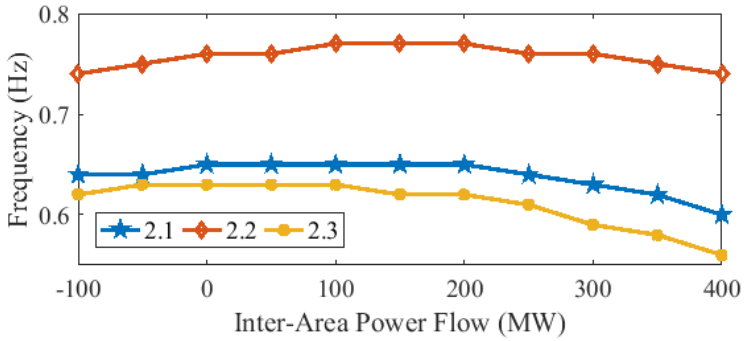

Figure 3.31: Frequency of IAM as inter-area power flow changes in Case 2.

3.2.6 Time-Domain Analysis

Time domain transient simulation is performed with non-linear model developed using MATLAB/Simulink. The response of the test system for selected operating point will be tested for four different sub-cases as discussed earlier. Small signal perturbation is provided by giving short pulse change in reference voltage of the synchronous generators. Large disturbance is created by three-phase fault in bus 8 for 0.2 second and eventually removing the fault. The mechanical power input of synchronous generators as well as doubly fed induction generators have been assumed to remain constant.

3.2.6.1 Small Signal Stability Analysis

In the first test, reference voltage of generators SG_2 and SG_4 were increased by 0.1 p.u. from time t=0 sec to 0.1 sec and t=0.5 sec to 0.6 sec respectively. The operating point for case 1.1 to 1.4 are selected such that 400MW flows from A_1 to A_2, with generators SG_1 through SG_4 producing 700, 700, 720 and 700 MW respectively. Load at bus 7 and 9 are 967 MW and 1767 MW respectively. Damping ratio obtained from modal analysis is shown in Table 3.8.

Table 3.8: IAM Damping Factor

Case 1.1	Case 1.2	Case 1.3	Case 1.4
5.724	16.697	4.994	19.58

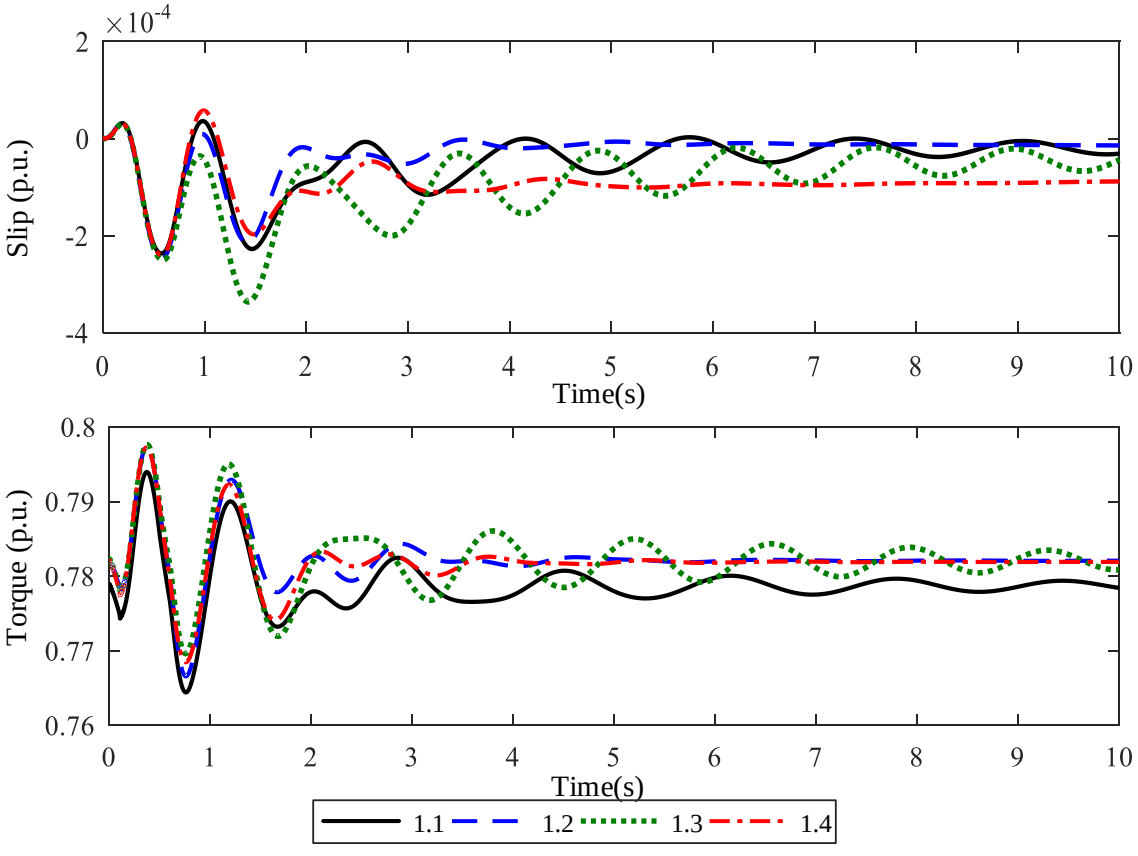

Figure 3.32: Slip and torque of SG_1 after perturbing V_{ref} of SG_2 and SG_4.

The eigenvalue analysis shows that replacing SG_4 with DFIG improves the damping

of the inter-area mode. On the other hand, replacing SG_3 deteriorates the inter-area mode damping. The addition of supplementary controller improves the damping of the inter-area mode. Rotor slip and electromagnetic torque of SG_1 in four cases 1.1 to 1.4 subjected to disturbance is shown in Figure 3.32. The inter-area mode is clearly visible and settles very slow in case 1.1, and is poorer in case 1.3. The oscillation damps faster in case 1.2 and faster in case 1.3. DFIG torque and speed is presented in Figure 3.33 which shows the participation of DFIG with supplementary control in oscillation damping by injecting damping torque proportional to the change in PCC frequency, which in turn affects the operating speed of the turbine. This indicates that the impact of DFIG is network dependent and should be assessed in case-by-case basis.

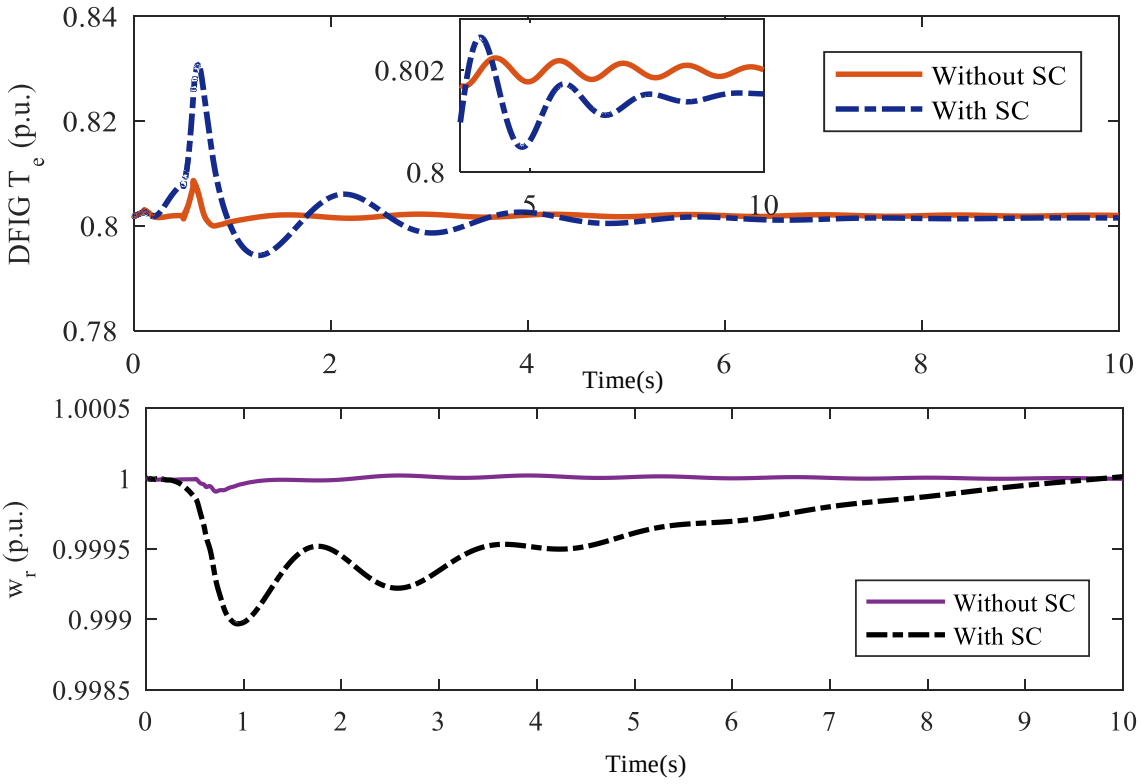

Figure 3.33: Torque and rotor speed of DFIG after perturbing V_{ref} of SG_2 and SG_4.

3.2.6.2 Transient Stability Analysis

In second test, three phase fault is applied at bus 8 for 0.2 sec and cleared naturally. Electromagnetic torque, slip and terminal voltage of generator at bus 2 are presented in Figure 3.34. The result is in agreement with the modal analysis result shown in Table 3.8. The post-fault oscillation damps out faster in case 1.2 compared to case

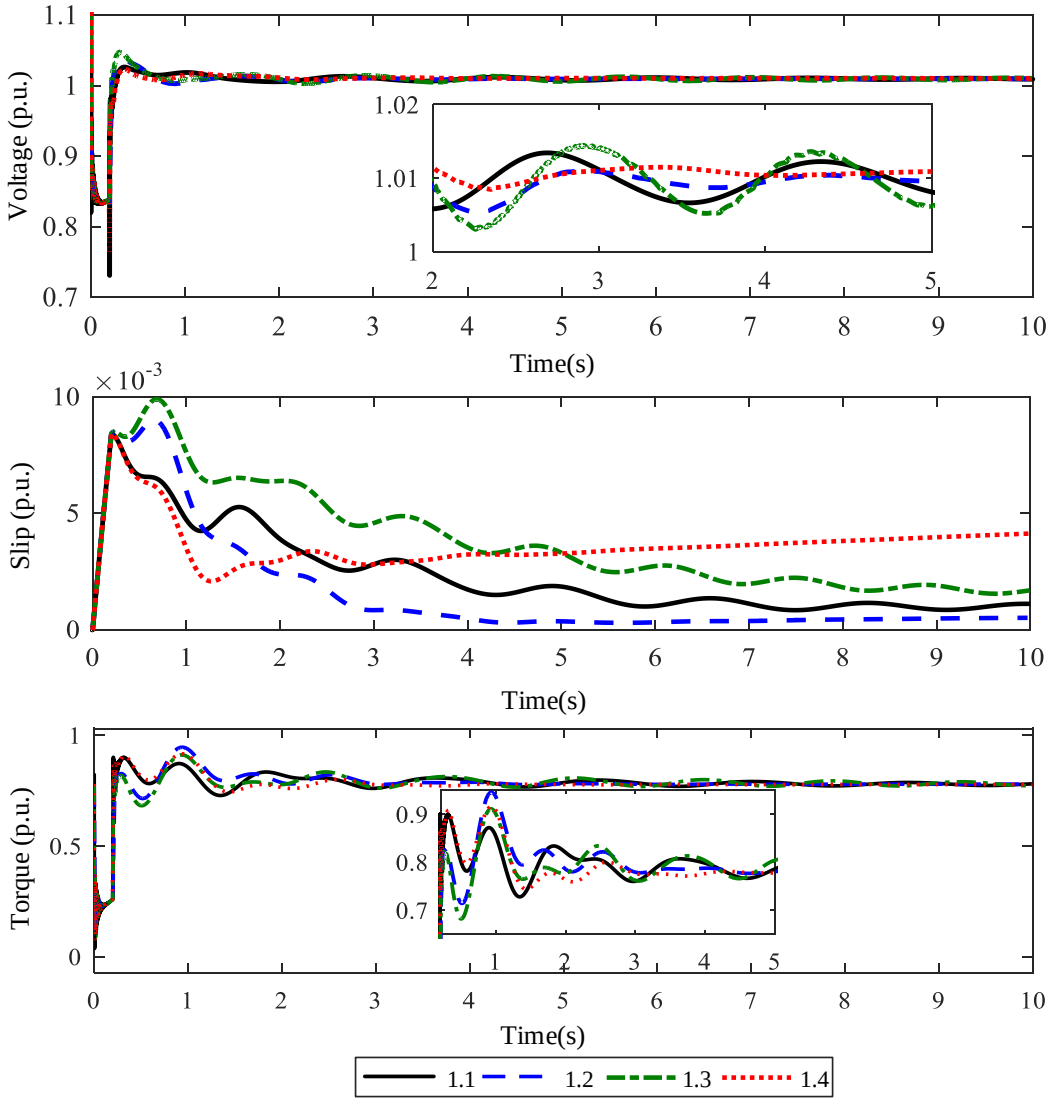

Figure 3.34: Voltage, slip and torque of SG_2 following three-phase fault.

1.1 and 1.3, but case 1.4 shows the best damping characteristics. The damping was poorest in case 1.3. It can be said that replacing SG_4 by DFIG improves the damping

even without any supplementary controller. Replacing SG_3 by DFIG deteriorates the damping and addition of supplementary damping controller achieves damping characteristics much batter than base case.

3.3 Summary

This chapter presented the modal analysis of open loop and closed loop model of DFIG, and sensitivity analysis of DFIG mode wrt to DFIG and controller parameters. In order to study the impact of DFIG penetration on small signal stability of power system, modal analysis of DFIG integrated power grid model in different scenarios was performed, and the results revealed that the penetration of DFIG can sometimes improve the damping of power system electromechanical modes and deteriorate the damping of those modes at other times. Replacing synchronous generator 4 of the test system revealed improved damping of the inter-area mode, but replacing the synchronous generator 3 deteriorated the inter-area mode damping. The IAM became unstable as the power flowing from area 2 to area 1 increased to around 350 MW. It can be concluded that though DFIG do not inherently participate in the electromechanical mode, it can affect the dynamics of the system due to the structural changes in the grid. The supplementary control of DFIG torque in response to the grid frequency oscillation improved the damping to the electromechanical oscillation. However, this comes at the cost of oscillation in the DFIG rotor which is proportional to the supplementary controller gain K_g during grid disturbance. Non-linear time domain simulation with small and large disturbance is presented to verify the results obtained via modal analysis.

CHAPTER 4: SIGNAL SELECTION BASED DESIGN OF POWER SYSTEM STABILIZER FOR DFIG

4.1 Introduction

Chapter 3 showed that DFIG can have positive and negative impact on dynamic stability of the grid and should be considered on cas by case basis. Location of DFIG is one of the important factors that influence the grid impact. But the location of the wind generators is driven by the availability of the resources and other socio-economic aspects. The rising level of DFIG penetration require oscillation damping capability of DFIG. A lot of work has been done in the past in the area of power oscillation damping control inclusive of FACTS devices and HVDC lines. Lately, the DFIGs are seen as being capable of supporting the power system in damping the oscillation. This chapter will explore the capability of DFIG to support power system oscillation damping and design a damping controller for DFIG based generation.

The increasing amount of wind power generation essentially replaces the conventional synchronous generators of the power system, thereby, reducing the total inertia of the system. Reduced inertia of the system is expected to hamper the system response during contingencies. It is clear that small signal as well as transient rotor angle stability is be affected by the changing dynamics of the power grid. This chapter focuses on the impact of increasing DFIG penetration and techniques to overcome the stability issues using DFIG control. The technique of using modified Rotor Side Converter (RSC) control and Grid Side Converter (GSC) control with a supplementary control loop and their capability to damp the power system oscillation have been investigated using modal analysis and non-linear time-domain analysis. The results are evaluated on Kundur two area four machine test system and IEEE 68-bus benchmark

system.

The main contribution of this chapter are listed below:

- The selection of input and output signals are performed based on controllability and observability analysis.
- The ability to incorporate RSC as well as GSC for oscillation damping are analyzed.
- The PSS design and its impact is studied on small as well as larger scale power system are analyzed.
- The limited observability of inter-area mode in local signal is shown to have limited impact on damping inter-area modes in a large scale multi-area power system with multiple inter-area modes.

4.2 DFIG Integrated Power Grid Model

A number of models can be found on the literature that represent power system dynamic behavior. Power system study requires the test and analysis of any new controller during small signal and large signal perturbation. The small signal perturbation maintains the approximate linearity of the system around an operating point, and are generally used to show the damping action of the controller when compared to the open loop case. Such test should avoid the saturation of the controller output and field voltage of the generators [29]. A power system model with following characteristics are suitable for small signal stability analysis of power system and to design damping controllers such as PSS in synchronous generators:

- A multi-machine system that displays local and inter-area modes. Intra-plant modes can be present for better representation of practical system conditions. At least one of the modes must be poorly damped in the absence of damping controls.

- A conventional method of damping control approach should be present in the system that can provide satisfactory damping performance.

In this works, two different models are selected for control design and performance assessment. A smaller scale power system model is used to validate the concept of damping control is design. Then the control is tested on second model which represents a larger scale power system model that requires coordination among multiple modes and multiple controllers.

4.2.1 Model 1

The first model is an 11-bus, 4-machine test system [27] modified as shown in Figure 4.1 to include DFIG based wind generator. It consists of two areas A_1 and

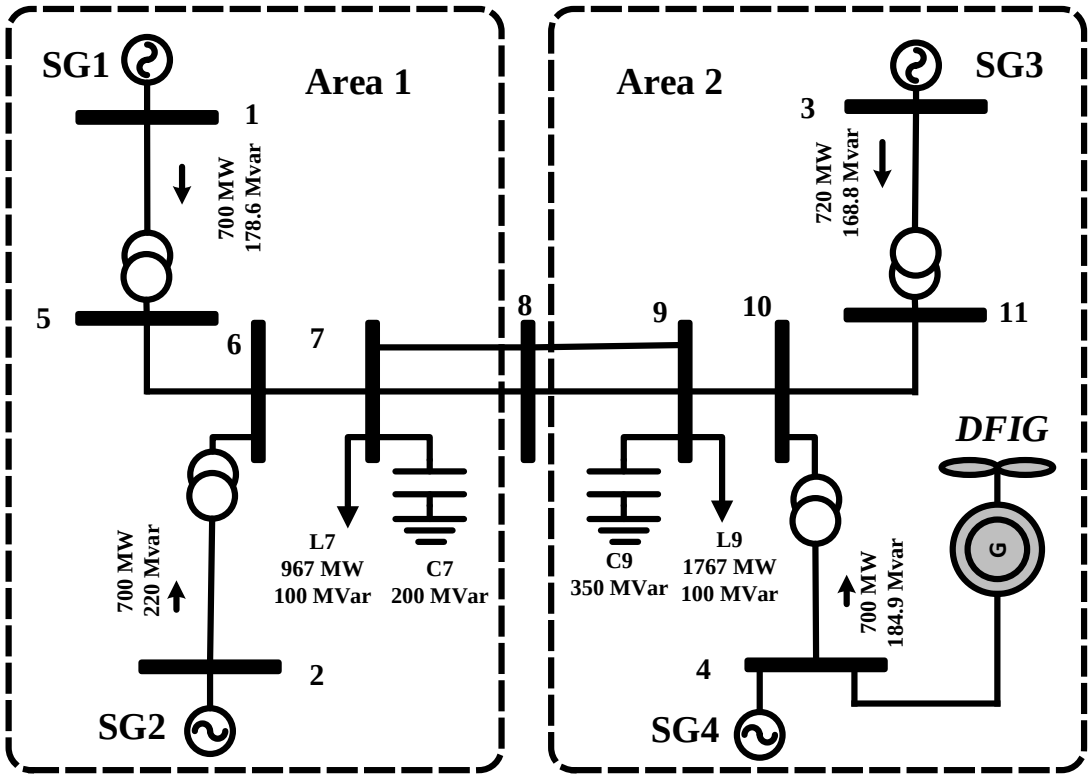

Figure 4.1: Two Area, 11 Bus System with DFIG connected alongside SG_4 at bus 4.

A_2 and each area has a pair of equivalent synchronous generators. There are four

synchronous generators in bus 1, 2, 3 and 4 represented by SG_1, SG_2, SG_3 and SG_4. The slow dynamics of the governors are ignored, and the mechanical torques to the generators are assumed constant which is reasonable as our simulation run is only for 10 seconds. All the synchronous generators are equipped with IEEE standard 'IEEE ST1A' exciter as shown in Figure 2.1. There are two local modes corresponding to two areas, and an inter-area mode. The local modes are damping is satisfactory, however, the inter-area mode damping is not satisfactory and can become stable when tie-lines are over-stressed. Appropriate design of PSS on all generators provide satisfactory damping of all the modes.

An aggregated model DFIG based Wind Farm is connected at bus 4. One of the premise of rising DFIG penetration is that the DFIGs can replace the synchronous generators where PSS is installed. The impact of DFIG increasing penetration on system stability on such system scenario has already been done in previous chapter. In this section, the focus is on controller design and implementation on DFIG to investigate the DFIG power oscillation damping capability, and identify the controller impact on the system as well as the DFIG itself.

4.2.2 Model 2

The second model is IEEE 68-bus, 16-machine and 5-area power system depicted in Figure 4.2. It is an approximate model of New England (NETS) and New York (NYPS) interconnected network. Detailed description of the system and its characteristics including machine, control and network parameters are available in [65]. The generators G1 to G8, and G10 to G12 have DC excitation systems (DC4B); G9 has fast static excitation (ST1A), while the generators G13 to G16 have manual excitation because they represent an area equivalents, and not the physical generators. This system has eigenvalues in the right half plane i.e. the system is unstable. The eigenvalues are shifted to left half plane when PSS is installed on Generators G1 through G12. However, there are three inter-area modes with high participation

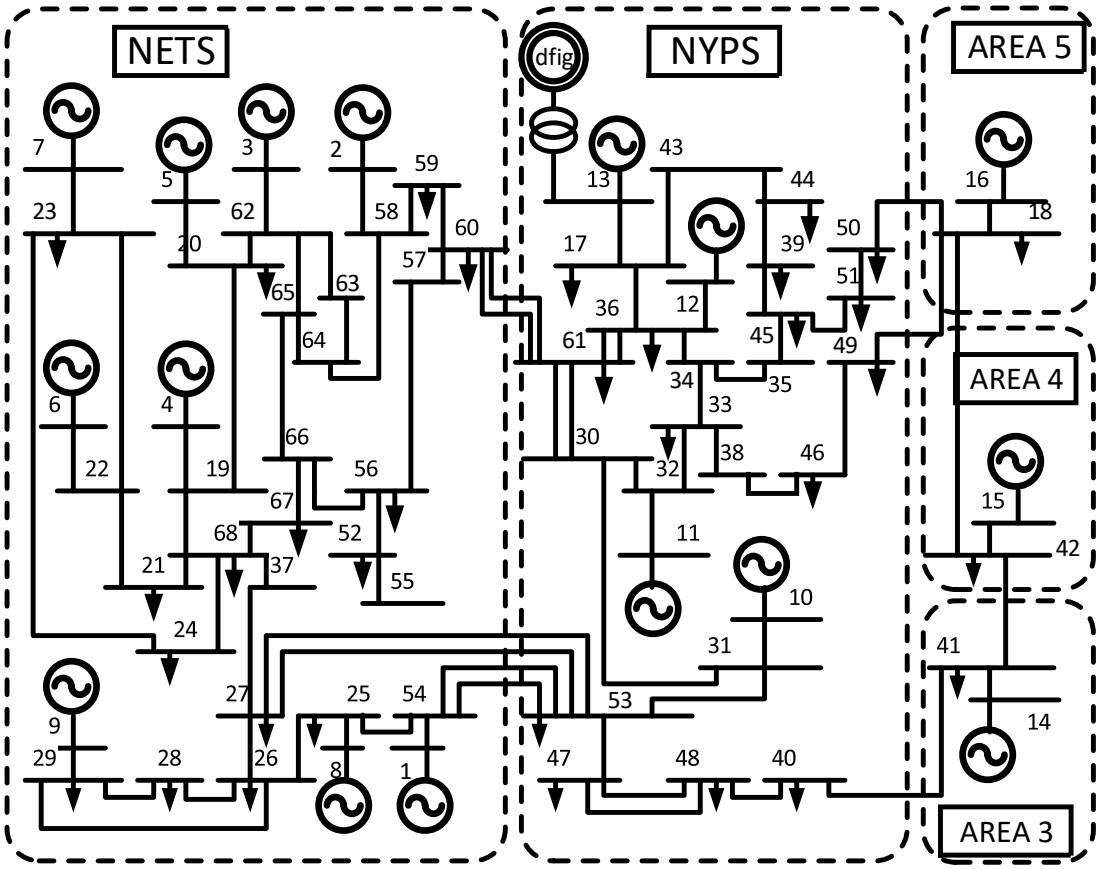

Figure 4.2: IEEE 68-bus, 5-area benchmark system.

which offer challenge of designing damping controller to damp the multiple inter-area modes simultaneously. To simulate the penetration of wind generation, we assume that DFIG based wind farm replaces 50% of the generation from G13. An aggregated model of DFIG is used to represent the equivalent wind farm model.

4.3 Eigenvalue Analysis of Model 1

The modal analysis of the test system revealed that the system exhibits three distinct modes of oscillation in the frequency range of 0.1 to 2.5Hz. Figure 4.3 shows the mode shape of 4 synchronous generators in those three modes. The inter-area mode, in which generators of area 1 oscillate against the generators of area 2, is the critical mode because its unstable ($\zeta = -1.67\%$) and slower (f=0.65 Hz). Any perturbation in the system would result in rising oscillation between two areas and

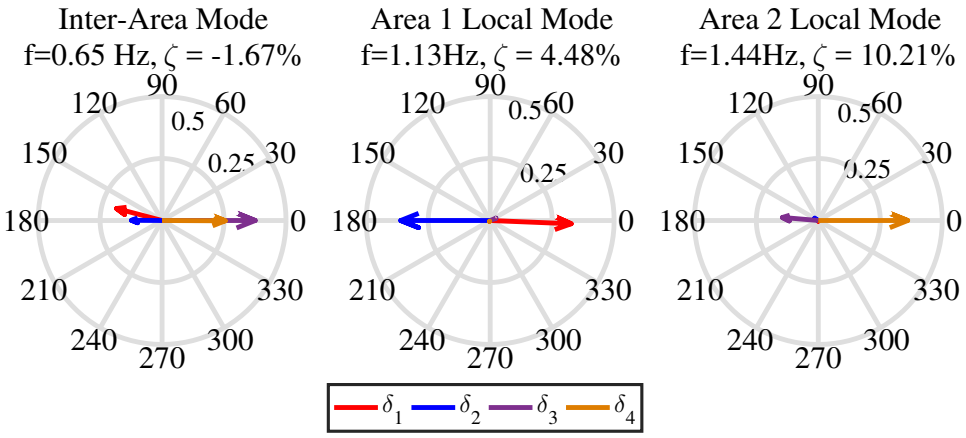

Figure 4.3: Mode shape of electromechanical modes with conventional PVdq Control in DFIG.

will ultimately result in separation of two areas due to relay operation. The damping of such mode should be as high as possible to minimize large power swing in the tie-line. Two intra-area/local modes are present in which the generators of a particular area oscillate against on another. These are relatively better damped, though area 1 local mode damping is below 5%.

4.4 Need for Power System Stabilizers in DFIG

The damping of electromechanical modes are dependent on the system operating condition such as generator loading, tie-line flow, exciter type etc. High gain static exciters such as the 'ST1A' greatly help in maintaining the transient stability or first-swing stability which is directly related with the synchronizing torque produced due to high speed operation of exciters. However, the damping torque is greatly reduced resulting in a poorly damped oscillatory modes. The inter-area mode is the most affected, and it becomes worst with increasing amount of power flow in the tie-line that loosely connects the two areas. The inter-area mode becomes unstable after the threshold limit of the tie-line flow is crossed. In other words, the small signal stability is limiting the power transfer capability from the tie-line. In order to

maintain the robustness and reliability of the system, the system operators such as Transmission System Operators (TSOs) and Independent System Operators (ISOs) determine the minimum amount of the damping that the system must have especially for low frequency modes such as inter-area modes even during contingencies where a critical element such as a transmission line or generators might be taken offline. Thus, the capability of DFIG to damp the inter-area mode of oscillation will be vital to maintain the critical damping limit of the system, and ensure the robust and reliable performance of the system. The control techniques discussed in previous section will be studied and their efficacy will be quantified in this section. For the testing the control performance, an operating point in which DFIG penetration level at bus 4 is 50% has been chosen. Such a scenario is reasonable and already a reality in countries relying heavily on renewable generation. The DFIGs will be required to provide power system stabilizing functionality in the future at such a high penetration level.

4.5 PSS for DFIG

The PSS for DFIG can be incorporated using RSC control as well as GSC control and are called RSCMod and GSCMod respectively. The capability of RSCMod and GSCMod to damp inter-area and local area modes will be evaluated for three cases:

1. **PVdq**: Conventional Vector Control without supplementary control loop.
2. **RSCMod**: RSC controller modified by adding the supplementary control loop.
3. **GSCMod**: GSC controller modified by adding the supplementary control loop.

The following section discusses the modification of RSC control and GSC control enhance power system oscillatory stability.

4.5.1 Modified Rotor Side Converter Control

RSC controller is designed for provide active and reactive power independently. In a stator flux-oriented d-q reference frame rotating at synchrnous speed, this is achieved by control of q-axis rotor voltage (v_{qr}) and d-axis rotor voltage (v_{dr}). This control topology is popularly termed as vector control. In order to provide power oscillation damping support, a reference signal is generated to be added as supplementary control loop on top of existing vector control of RSC. The references signal generated is based on local or global measurement depending upong the damping enhancement requirement. Local signals are usually sufficient for providing damping support provided that the oscillation are observable in the local signals. This would omit the requirement of communication infrastructure that is necessary for global measurement based control popularly termed as wide area control (WAC). A

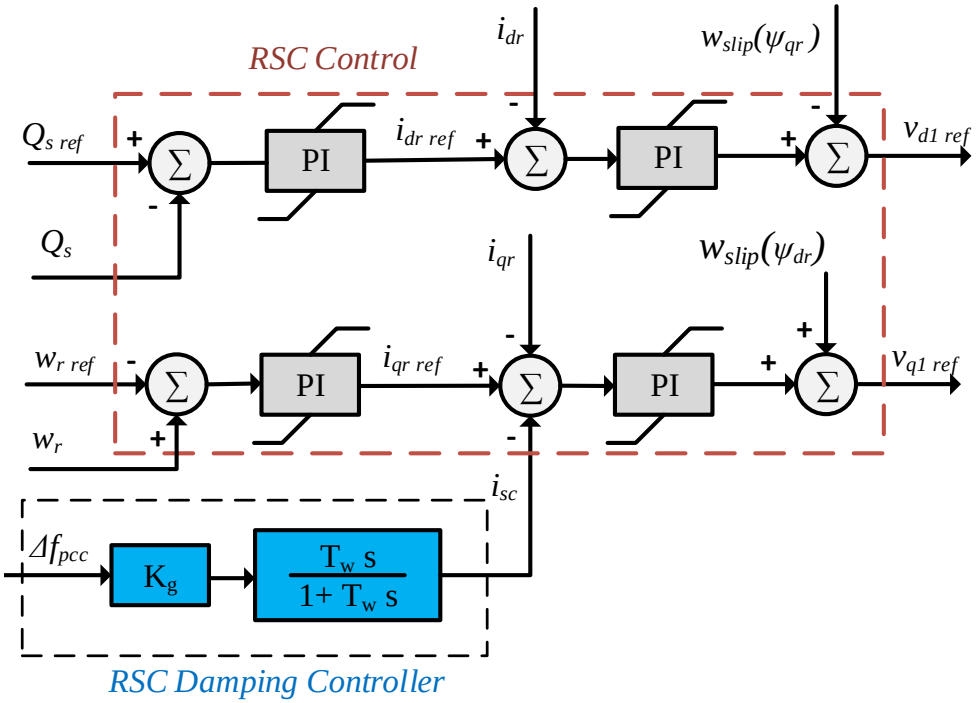

Figure 4.4: RSCMod: Modified RSC Vector Control Architecture.

frequency deviation feedback is has been used to design a supplementary damping controller as shown in Figure 4.4. Other signals such as active power generation,

reactive power generation, voltage, power flow in tie-line can be used and the signal selection should be based on observability and controllability analysis of the particular mode/modes of interest. The feedback loop consists of a gain 'K_g' and a washout filter with time constant 'T_w' and produces a supplementary current reference for RSC current controller during grid oscillation. The washout filter ensures that the supplementary controller does not produce any control set-point during steady state opeartion. The lead-lag compensator design has been neglected. It is a reasonable assumption because of the fast bandwidth of RSC current controller and thus any lag introduced by the controller at frequencies of grid oscillation is negligible. This is true for local measurement only where the communication delay is also negligible. This is not true for remote signals based control where control and communication time delay is considerably higher, and proper tuning of lead-lag compensator might be necessary. The supplementary controller produces the supplementary q-axis rotor current (i_{sc}) i.e. by modulating q-axis rotor current (i_{qr}), DFIG torque (T_{dfig}) is produced to damp the targeted oscillatory mode/s.

K_g is tuned to provide the maximum damping to the dominant inter-area mode using root-locus based method. The low frequency oscillation with the least damping ratio is usually the most dominant mode in a system. The modified RSC controller will be referred as RSCMod.

4.5.2 Modified Grid Side Converter Control

Voltage vector oriented control technique is employed to control GSC. It utilizes quadrature axis current (i_{qg}) to control the active power of GSC and hence, the DC-Link Capacitor voltage. Similarly, direct axis current (i_{dg}) to control the reactive power of GSC. A supplementary control loop based on frequency deviation feedback, similar to modified RSC control, is designed and fed to q-axis current control loop as shown in Figure 4.5. The supplementary control signal (i_{scg}) provides the capability to modulate the active power generated by GSC to damp the oscillation. This is

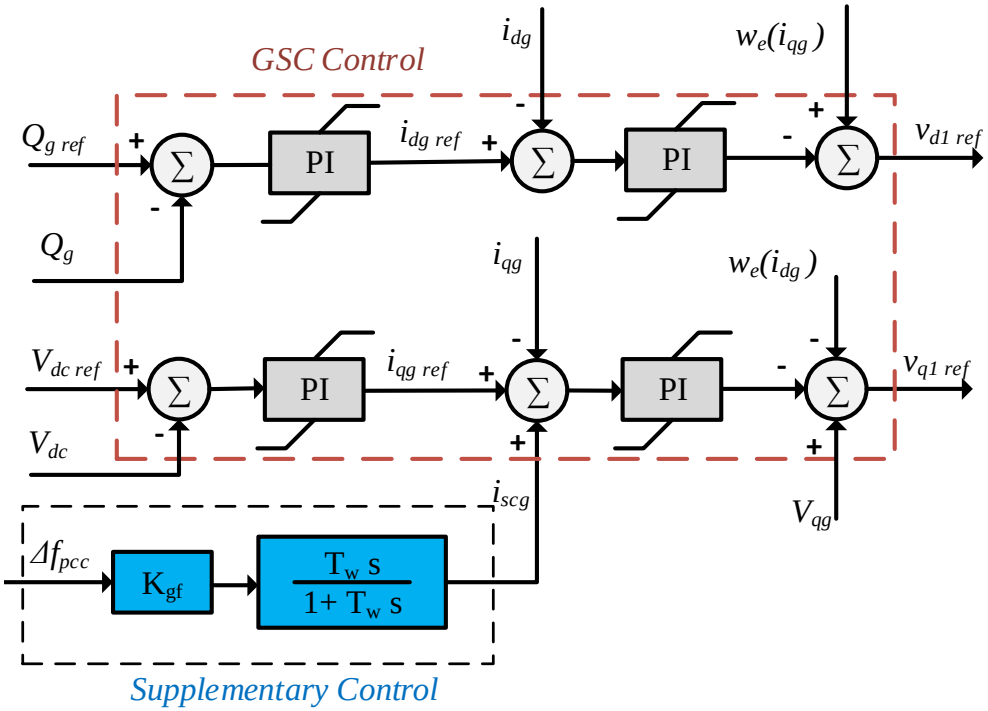

Figure 4.5: GSCMod: Modified GSC Vector Control Architecture.

actually utilizing the energy stored in DC-link capacitor. The modified GSC controller is referred as GSCMod.

4.6 Selection of Signals

As discussed earlier, the DFIG controllers are modified using feedback of locally available measurement signals. The available input signals are the supplementary signals for:

- $\mathbf{i_{qr}}$: By modulating q-axis rotor current, DFIG stator active power P_s is modulated.
- $\mathbf{i_{dr}}$: By modulating d-axis rotor current, DFIG stator reactive power Q_s is modulated.
- $\mathbf{i_{qg}}$: By modulating q-axis GSC current, GSC active power P_g is modulated, which affects DC-link capacitor voltage dynamics.
- $\mathbf{i_{dg}}$: By modulating d-axis GSC current, GSC reactive power Q_g is modulated.

Similarly, the available output signals that can be used for feedback are:

- Δf: Deviation in bus frequency.
- $\Delta\delta$: Deviation in bus phase angle.
- V_t: DFIG terminal voltage.
- P_{dfig}: DFIG active power injection.
- Q_{dfig}: DFIG reactive power injection.
- ω_r: DFIG rotor speed.

Controllability is a measure of the possibility of influencing the location of an oscillation mode by state feedback. Observability is a measure of the visibility of oscillation mode on a given output.The geometric measure of controllability $gm_{c,k}$ and observability $gm_{oj,k}$ associated with mode k are given by

$$gm_{c(i,k)} = \frac{|b_i^T \psi_k|}{||\psi_k||||b_i||} \tag{4.1}$$

$$gm_{o(j,k)} = \frac{|c_j \phi_k|}{||\phi_k||||c_j||} \tag{4.2}$$

where b_i is the i_{th} column of input matrix B and c_j is the j_{th} row of output matrix C, ψ_k and ϕ_k are the right and left eigenvector corresponding to mode k, $|x|$ and $||x||$ are the modulus and Euclidean norm of x respectively.

The geometric measure of controllability and observability for electromechanical modes of the Model 1 i.e. 4-machine, 11-bus system were computed and are shown in Figure 4.6 and Table 4.1 and 4.2 respectively. The combination of input signal with highest controllability and output signal with highest observability is chosen because this would result in the least amount of control effort to shift the electromechanical modes left, which results in faster damping of the modes in time domain. From controllability analysis, it is easy to see that the control of active power of DFIG

via i_{qr} modulation yields better results over control of reactive power of DFIG via i_{dr} modulation. Thus, a supplementary controller is added on top of i_{qr} controller. Similarly, supplementary control of GSC active power via i_{qg} modulation is selected. Both inter-area mode and area 2 local mode have highest observability in Δf, and is thus selected as input signal for PSS used in RSC and GSC. The area 1 local mode is not observable in any of the selected signals of DFIG since it is located in area 2.

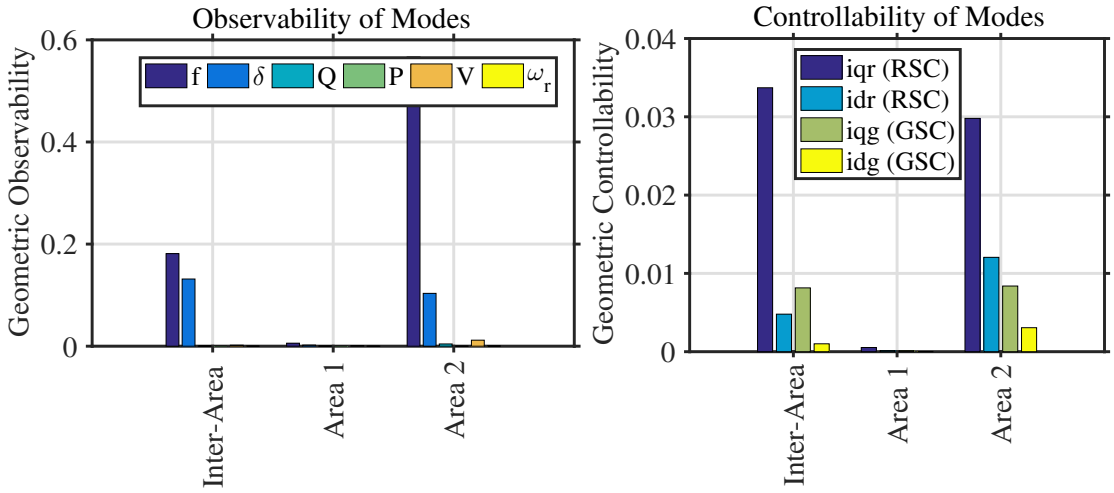

Figure 4.6: Geometric observability of electromechanical modes in available output signals and Controllability of electromechanical modes from available DFIG control inputs

Table 4.1: Controllability of Electromechanical Modes

Mode	$\mathbf{i_{qr}}$	$\mathbf{i_{dr}}$	$\mathbf{i_{qg}}$	$\mathbf{i_{dg}}$
Inter-Area Mode	0.0337	0.0048	0.0082	0.0010
Area 1 Local Mode	0.0005	0.0001	0.0001	0.0000
Area 2 Local Mode	0.0298	0.0121	0.0084	0.0030

Table 4.2: Observability of Electromechanical Modes

Mode	Δf	$\Delta\delta$	V_t	P_{dfig}	Q_{dfig}	ω_r
Inter-Area Mode	0.1812	0.1315	0.0020	0	0.0008	0.002
Area 1 Local Mode	0.0059	0.0022	0.0013	0	0.0005	0
Area 2 Local Mode	0.5666	0.1035	0.0118	0.0001	0.0044	0.0006

4.7 Simulation Results for Model 1

Results of eigenvalue analysis and time domain simulation of Model 1 are presented in this section to compare the system response in base case against proposed PSS incorporated in RSC Controller and GSC Controller.

4.7.1 Eigenvalue Analysis

The eigenvalues corresponding to inter-area and local oscillation modes of the system for PVdq, RSCMod and GSCMod are shown in Figure 4.7, and summarized in Table 4.3 and 4.4. RSCMod and GSCMod stabilized and increased the damping of the inter-area mode, which was unstable for PVdq control. IAM has negative damping of -1.67% when DFIG does not have any damping controller. Figure 4.8 shows the polar plot of right eigenvector of selected states for inter-area mode. The states that were selected are the speed of four synchronous generators, DFIG turbine speed and DC-link voltage. The polar plot of the right eigenvectors shows that the modes are not observable in the DFIG turbine speed and DC-link capacitor voltage for PVdq control. This also illustrates that the DFIGs do not participate in electromechanical oscillation with the grid.

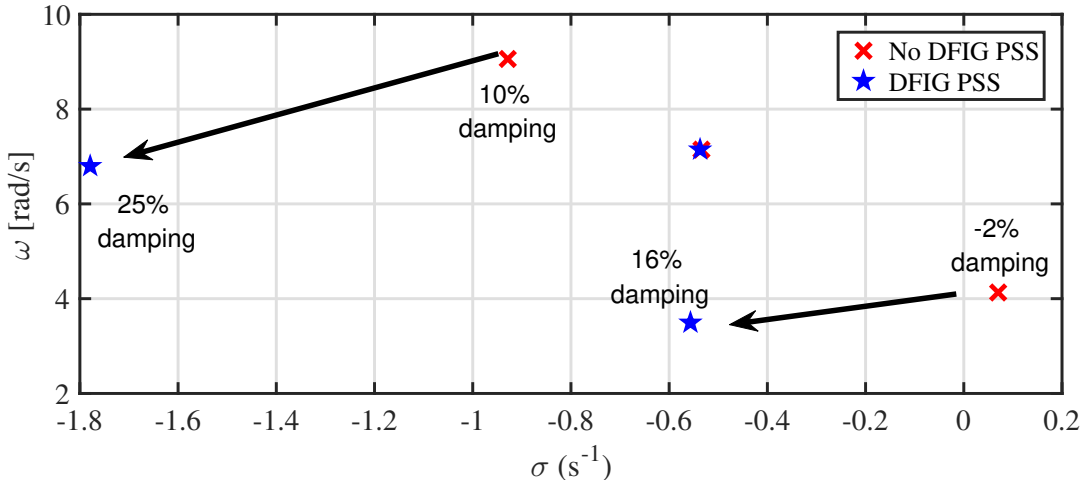

Figure 4.7: Plot showing local and inter-area modes of Two-Area System

Table 4.3: Impact of DFIG Control on Inter-Area Mode

	PVdq	**RSCMod**	**GSCMod**
Eigenvalue	0.069±4.1243i	-0.55599+3.4805i	-0.40619±3.8774i
Damping Factor (%)	-1.6728	15.7743	10.4188
Frequency (Hz)	0.65641	0.55394	0.61711
Dominant States	δ_3 , ω_3 , δ_1 , ω_1	δ_4 , δ_3 , ω_3 , δ_1 , ω_1 ,w_{td}	δ_3 , ω_3 , δ_4 ,δ_1 , ω_1 ,V_{dc}

Table 4.4: Impact of DFIG Control on Area 2 Local Mode

	PVdq	**RSCMod**	**GSCMod**
Eigenvalue	-0.93±9.0621i	-1.78±6.799i	-2.43±9.7903i
Damping Factor (%)	10.2087	25.3277	24.1006
Frequency (Hz)	1.4423	1.0821	1.5582
Dominant States	δ_3 , ω_3 , δ_4 , ω_4	δ_3 , ω_3 , δ_4 , ω_4 , w_{td}	δ_3 , ω_3 , δ_4 , ω_4 , V_{dc}

The modes become observable in DFIG turbine speed for RSCMod and in DC-link voltage for GSCMod as shown in Figure 4.8.

RSCMod controller with the frequency deviation feedback elevated the damping factor to 15.77%. The modulation of DFIG electromagnetic torque results in DFIG turbine oscillation with the frequency equal to frequency of the oscillator mode/s observable in the feedback signal. In this case, both area 2 local mode and inter-area mode are observable in the chosen feedback signal, and hence will be observable in the DFIG dynamics associated with electromechanical interaction between turbine and generator. The increased participation of DFIG in inter-area mode is illustrated by the observability of inter-area mode in wind turbine speed as shown in Figure 4.8. Similar conclusion holds true for area 2 local mode as well.

Similarly, GSCMod resulted in Inter-area mode damping factor of 10.42%. The participation of Dc-link capacitor can be verified by the observability of inter-area mode in DC-link voltage V_{dc} as shown in bottom plot of Figure 4.8. Moreover, the

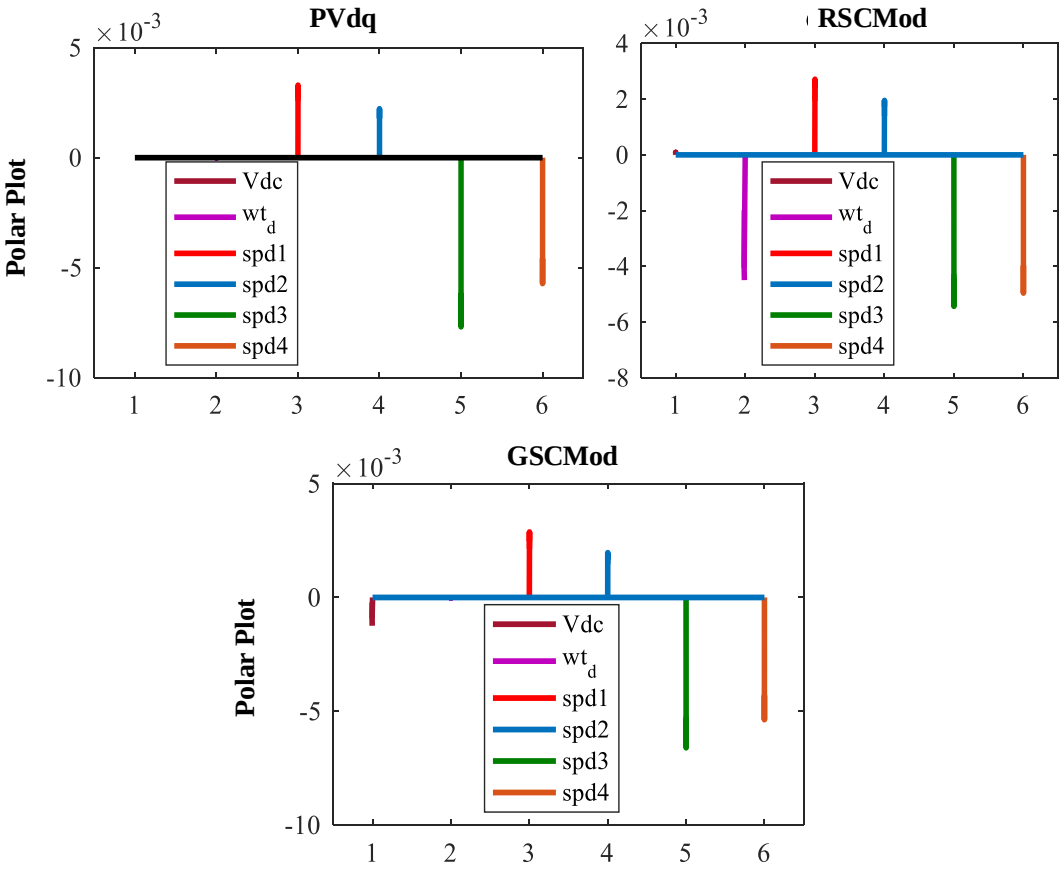

Figure 4.8: Inter-area mode shape with PVdq, RSCMod and GSCMod corresponding to Vdc, wt_d, and generator speeds (spd1, spd2, spd3 and spd4).

modification of RSC and GSC resulted in rise of local area 2 mode damping factor from 10.2% to 25.33% and 24.1% respectively.

4.7.2 Time Domain Analysis

The controllers are tested in Model 1 for two different types of perturbation:

Small Signal Perturbation: In order to simulate small signal perturbation of the system, reference voltage of generators SG_2 and SG_3 are increased by 0.1 p.u. for 0.5 sec at time t=0.5-1.0 sec. In order to observe the inter-area mode, the difference between rotor angle and speed of generators SG_4 and SG_1 were chosen. The simulation was run for 10 seconds and the results are shown in Figure 4.9 and 4.10. The result shows that the oscillation is damped faster with RSCMod or GSCMod in DFIG.

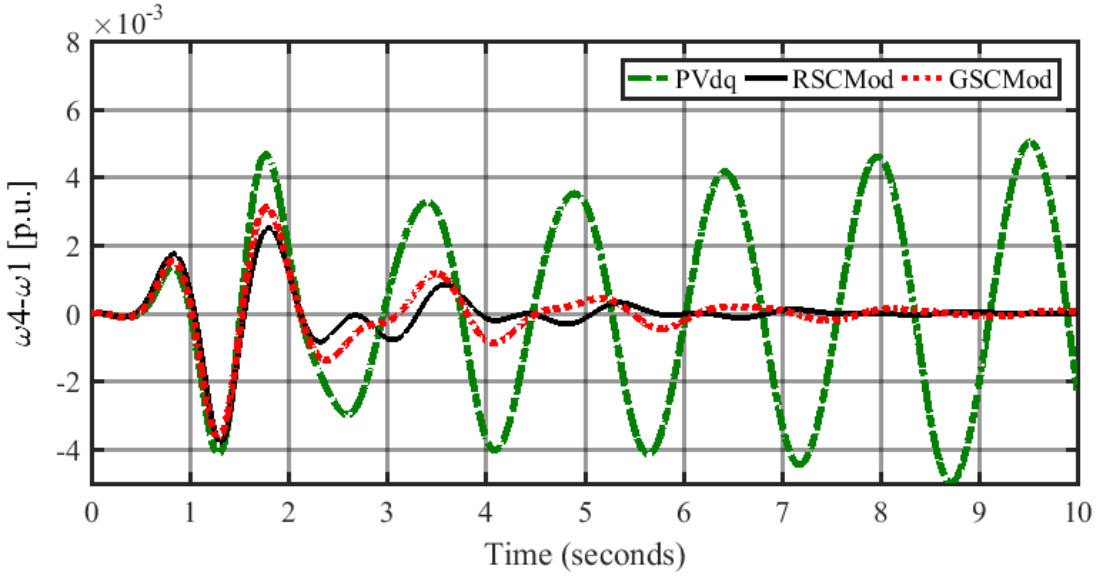

Figure 4.9: Difference between angular frequency of Generator SG_4 and SG_1

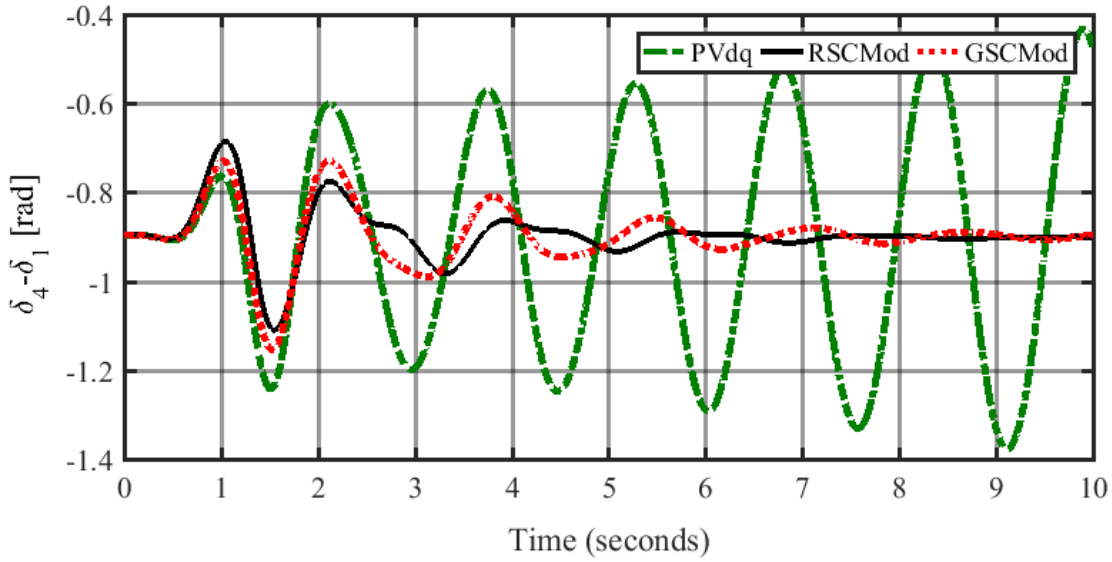

Figure 4.10: Angular separation of Generator SG_4 and SG_1

The system shows oscillatory instability in base case where DFIG is equipped with PVdq. The damping performance of RSCMod is better compared to GSCMod which affirms the results of eigenvalue analysis.

The inevitable drawback of the supplementary control loops added to RSC and GSC

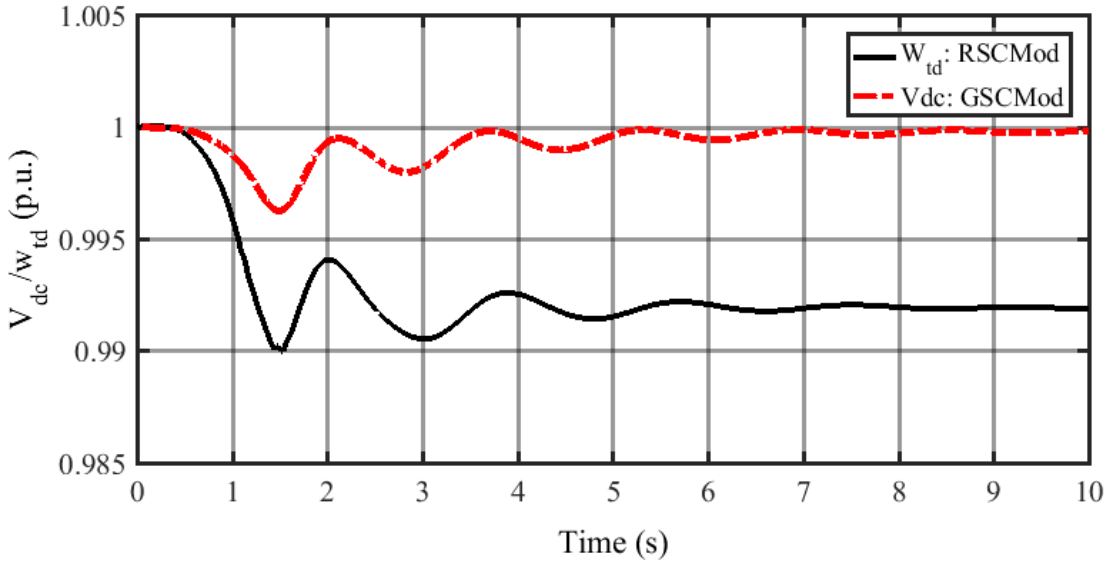

Figure 4.11: Impact on DFIG rotor speed with RSCMod and DC-link voltage due to GSCMod

controller is that such controller affects the dynamics of DFIG turbine speed (w_{td}) and DC-Link Voltage (V_{dc}) respectively. Figure 4.11 shows the resulting transient behavior of w_{td} and V_{dc} during the simulation of above described small signal stability test. This suggests that the compromise should be made between improvement of the system dynamic performance and DFIG dynamics.

Large Signal Perturbation: To simulate large signal perturbation, 3phase-ground fault was applied in Bus 9 and cleared naturally after 0.3 second. The terminal voltage of bus 4 and difference between rotor angle of generator SG_4 and SG_1 are shown in Figure 4.12. With PVdq control, the system becomes unstable in second swing as the angular separation between generator SG_4 and SG_1 keep rising. The two areas remain synchronized with RSCMod and GSCMod in DFIG. Eventually, the oscillation damps and returns to stable operating point. The oscillations are damped faster with RSCMod compared to GSCMod.

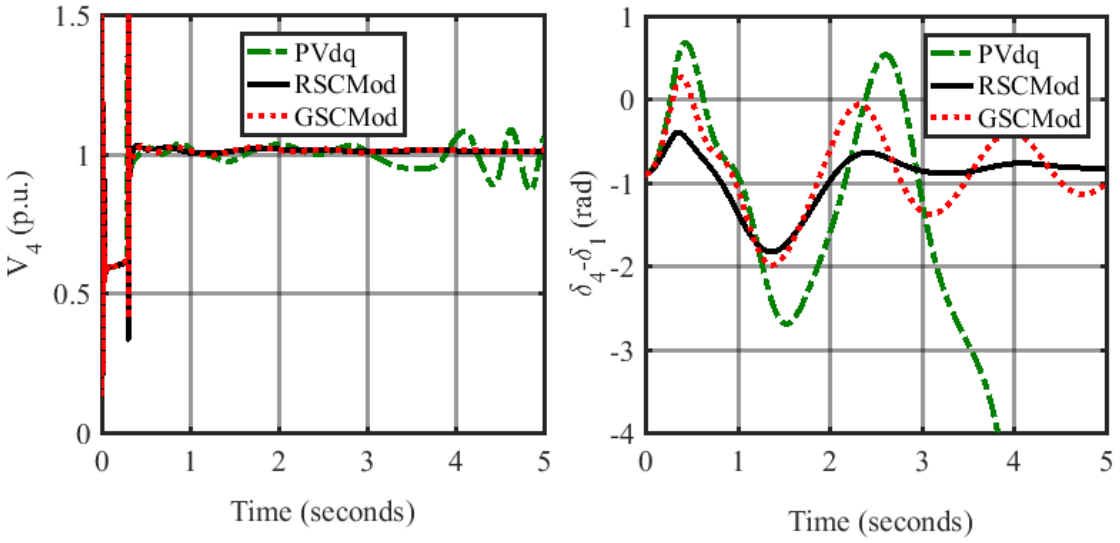

Figure 4.12: Terminal Voltage of Bus 4 and Angular separation between Generator SG_4 and SG_1 following 3 phase fault in bus 9.

4.8 Simulation Results for Model 2

In order to validate the scalability of the DFIG PSS, the simulation results of Model 2 are presented in this section.

4.8.1 Eigenvalue Analysis

There are four dominant inter-area modes as shown in Table 4.5. The DFIG connected at bus 13 has PVdq control. The table shows the mode frequency in Hz, damping in % and the participating generators with their mode shape. Mode shapes are the polar plots of the eigenvectors of a mode corresponding to the desired states. The mode shape can be used to determine the coherency of the generators in a particular mode. Matlab's *feather* function is used to plot the mode shape. Figure 4.13 shows the mode shapes the inter-area modes which shows the eigenvectors of the all the inter-area modes corresponding to slip of 16 synchronous generators.

There are 5 areas or groups of coherent generators and they are:

1. Area 1 which includes generators G1-G9,

2. Area 2 which includes generators G10-G13,

Table 4.5: Dominant Inter-Area Modes

Mode	Freq (Hz)	Damping (%)	Participating Generators
1	0.39	17.92	G1-G13 & G16 against G14-G15
2	0.52	2.37	G1-G9, G14-G15 against G10-G13 & G16
3	0.72	6.37	G1-G9, G15-G16 against G10-G14
4	0.78	3.49	G1-G9, G14 & G16 against G10-G13 & G15

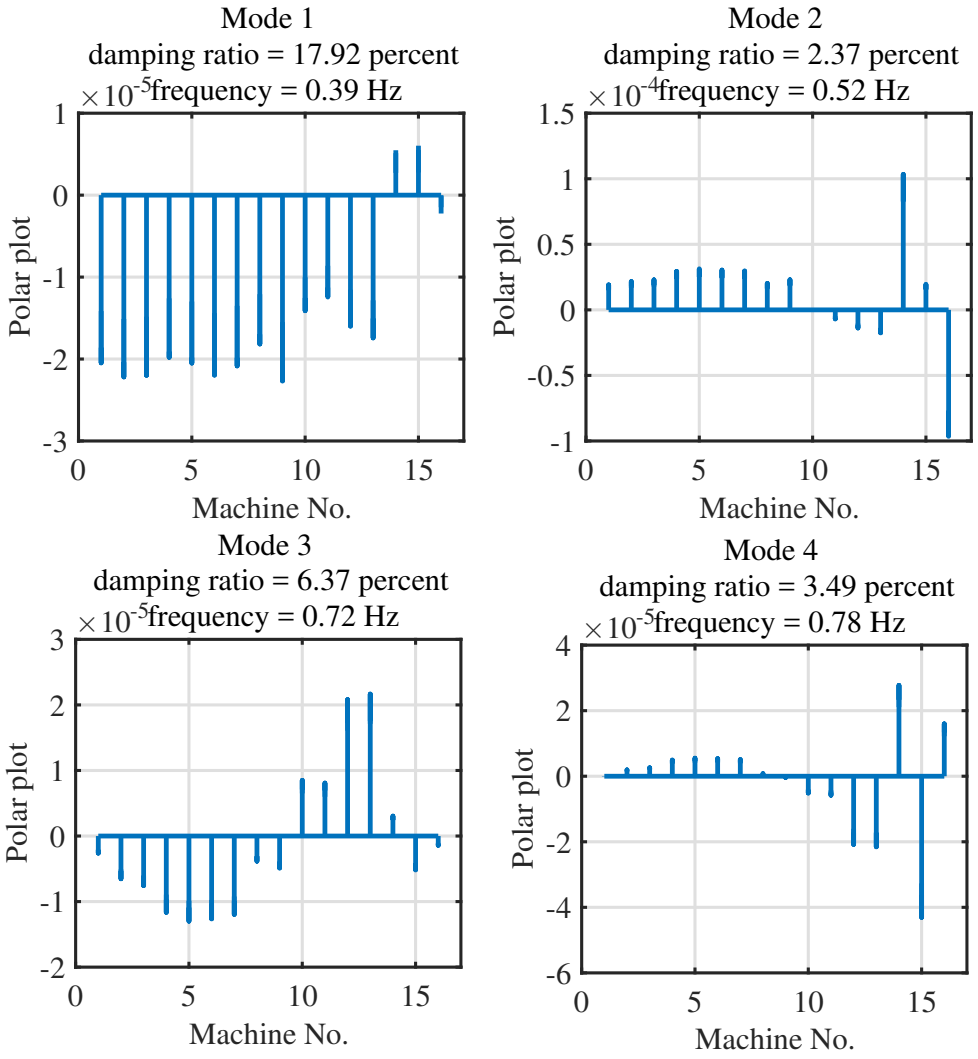

Figure 4.13: Mode shape of inter-area modes.

3. Area 3 which includes generator G14,

4. Area 4 which includes generator G15, and

5. Area 5 which includes generator G16.

Mode 1 is damped well after PSS is installed in generators G1-G12. Mode 2 involves oscillation of Area 1, 3 and 4 against Area 2 and 5. The damping ratio of this mode is 2.37% and is considered as a critical mode. Mode 3 represents oscillation of Area 1, 4 and 5 against Area 2 and 3. The damping ratio of this mode is 6.37% which is still below 10%. Mode 4 represents oscillation of Area 1 ,3 and 5 against Area 2 and 4. It has damping ratio of 3.49 %, thus, it is not well damped mode. In order to ensure oscillatory stability and reduce high magnitude power oscillation in tie-lines, these inter-area modes should be damped sufficiently.

Table 4.6: Impact of DFIG PSS

	PVdq		RSCMod		GSCMod	
Mode	f (Hz)	ζ (%)	f (Hz)	ζ (%)	f (Hz)	ζ (%)
1	0.39	17.92	0.39	18.09	0.39	18.00
2	0.52	2.37	0.52	2.38	0.52	2.37
3	0.72	6.37	0.72	7.05	0.72	6.71
4	0.78	3.49	0.78	3.53	0.78	3.51

RSCMod and GSCMod will be implemented on DFIG to influence positive damping on inter-area modes based on feedback of feedback of bus 13 slip frequency. The results are presented in Table 4.6. The result shows that the PSS implemented in DFIG in bus 13 via RSCMod and GSCMod have limited influence on inter-area modes of the system. Mode 3 damping saw a rise in its damping ratio from 6.37% in PVdq to 7.05% in RSCMod and 6.71% in GSCMod. This is the mode in which generator G13 has higher participation and is the most observable mode in frequency of bus 13. Figure 4.14 shows the eigenvalues of 68 bus system with PVdq, RSCMod and GSCMod respectively.

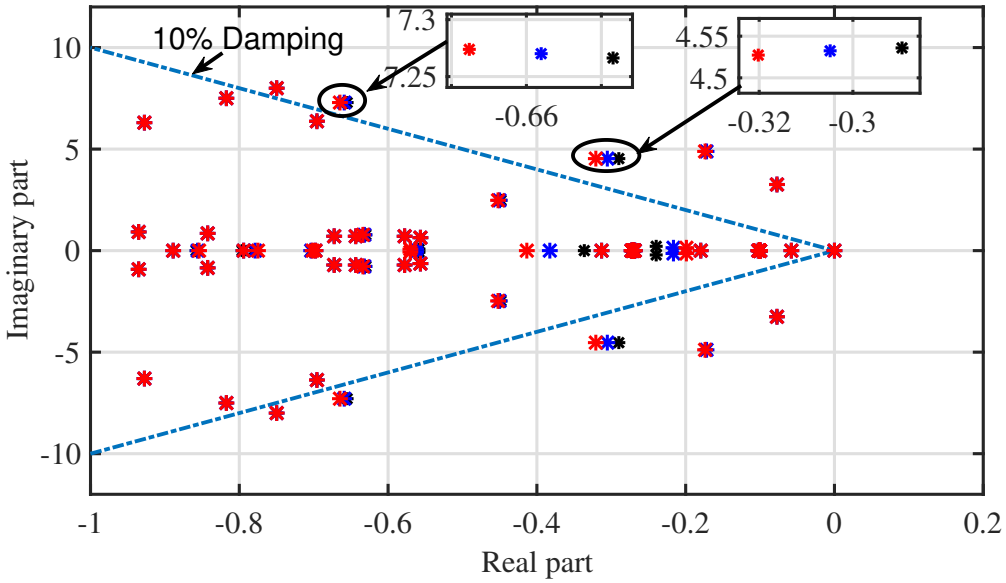

Figure 4.14: Eigenvalues of the system with PVdq (black), RSCMod (red) and GSC-Mod (blue).

4.8.2 Time Domain Analysis

The non-linear simulation of Model 2 with PVdq, RSCMod and GSCMod was performed to compare the dynamic response of the system in terms of small signal and transient stability. The eigenvalue analysis showed that the mode 2 damping improved, while other modes essentially remained unchanged with control of DFIG in bus 13. Time-domain simulation will make it easy to visualize this improvement if we can excite mode 2.

Based on the mode shape analysis, three plots are chosen to observe the three dominant inter-area modes i.e. mode 2-4. Mode 1 is well damped and will not be easy to distinguish in time domain. Three plots show:

1. **Plot 1** ($\omega_{14} - \omega_{16}$): This plot is selected to observe mode 2.

2. **Plot 2** ($\omega_{13} - \omega_{5}$): This plot is selected to observe mode 3.

3. **Plot 3** ($\omega_{14} - \omega_{15}$): This plot is selected to observe mode 4.

Here, ω_i represents the speed of i^{th} generator in per unit. It should, however, be noted that the signal will not show a single mode only, but a superposition of the modes, and mode 2 might become most dominant because of its dominance considering its lowest damping ratio and lowest frequency.

Similar to model 1, the system is subjected to two different categories of perturbations:

Small Signal Perturbation: In this test, the reference voltage of generators G7, G8, G10, G11 and 12 are increased by 0.1 p.u. from time t=0-5 seconds. The rotor slip speed of generators G13 and G15 with respect to generator G16 are shown in Figure 4.15. The mode 2 was successfully excited, and the result shows the improvement in

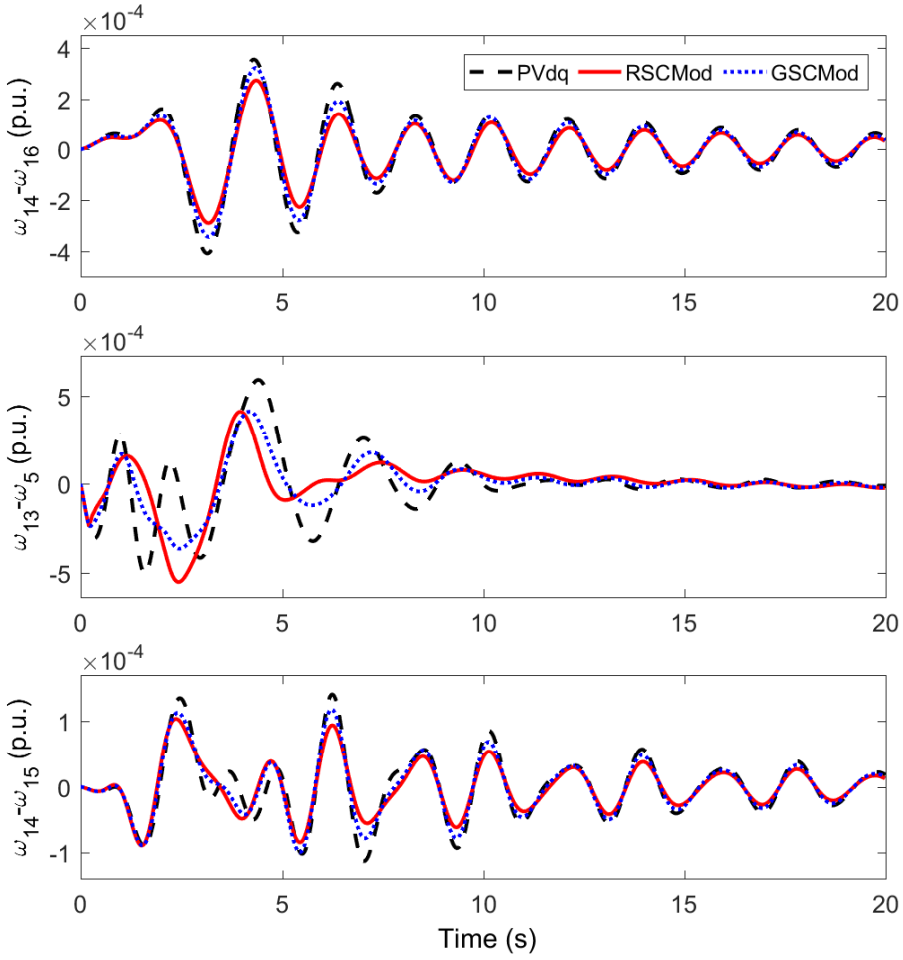

Figure 4.15: Comparison of PVdq, RSCMod and GSCMod for small signal perturbation of 68-bus system.

damping of mode 2 when RSCMod and GSCMod are implemented in DFIG, with RSCMod yielding slightly better performance than GSCMod.

Large Signal Perturbation: The controllers are tested by applying 3ph fault at different bus locations to excite the inter-area modes.

Case 1 - 3 phase-ground fault in bus 43 : In first test, 3phase to ground fault is applied at bus 43 and cleared after 10 cycles. This fault is nearest to generator G13. The plots as described earlier are shown in Figure 4.16. Plot 2 shows that the mode 3 was excited. Prony analysis was used to analyze the frequency components in the time-domain response. It can also be seen that the mode is damped faster with PSS in DFIG. RSCMod provides faster damping performance than GSCMod. Mode 2 is clearly observable in plot 3. The controller has very little impact on mode 2. It is hard to draw any conclusion regarding mode 4 from plot 1. However, transient

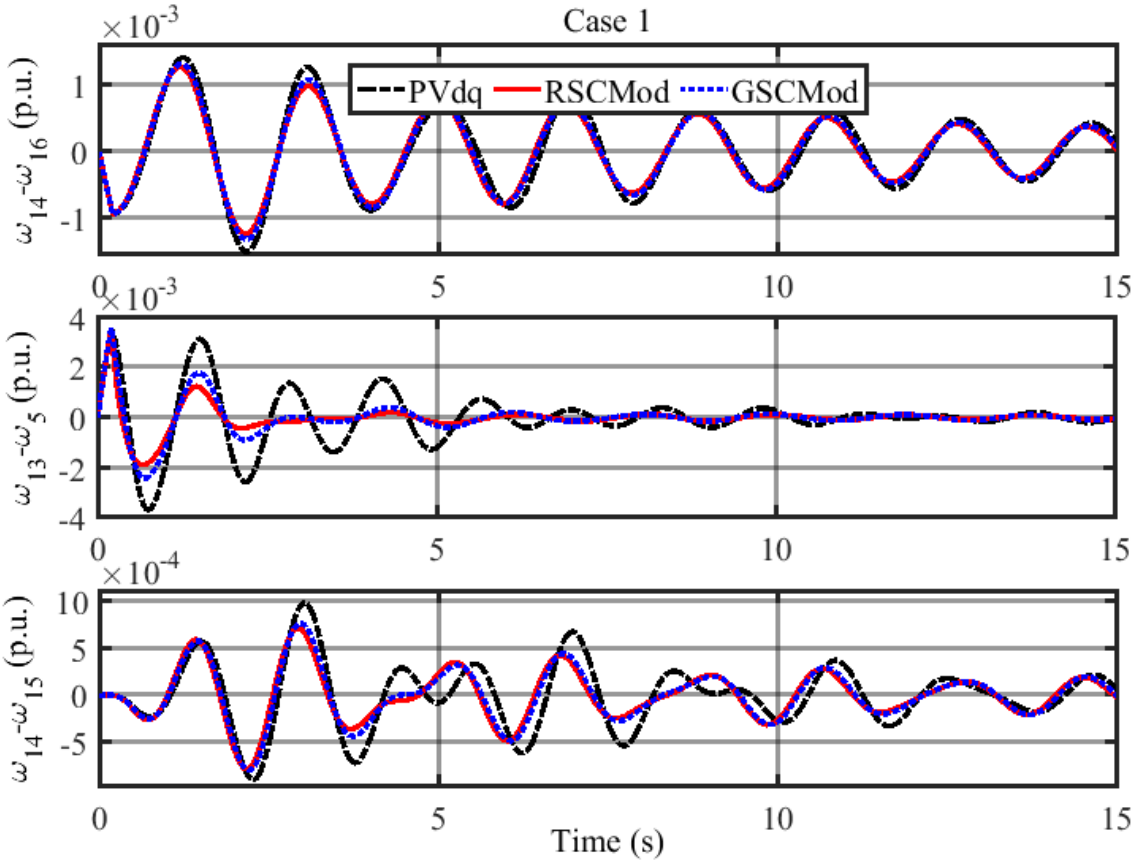

Figure 4.16: Comparison of PVdq, RSCMod and GSCMod for Case 1.

Case 2 - 3 phase-ground fault in bus 50: In second test, 3phase to ground fault is applied at bus 50 and cleared after 10 cycles. This fault is nearest to generator G11. Plot 1-3 in Figure 4.17 shows mode 3 is not excited with enough energy. Mode 2 is dominant in all plots.

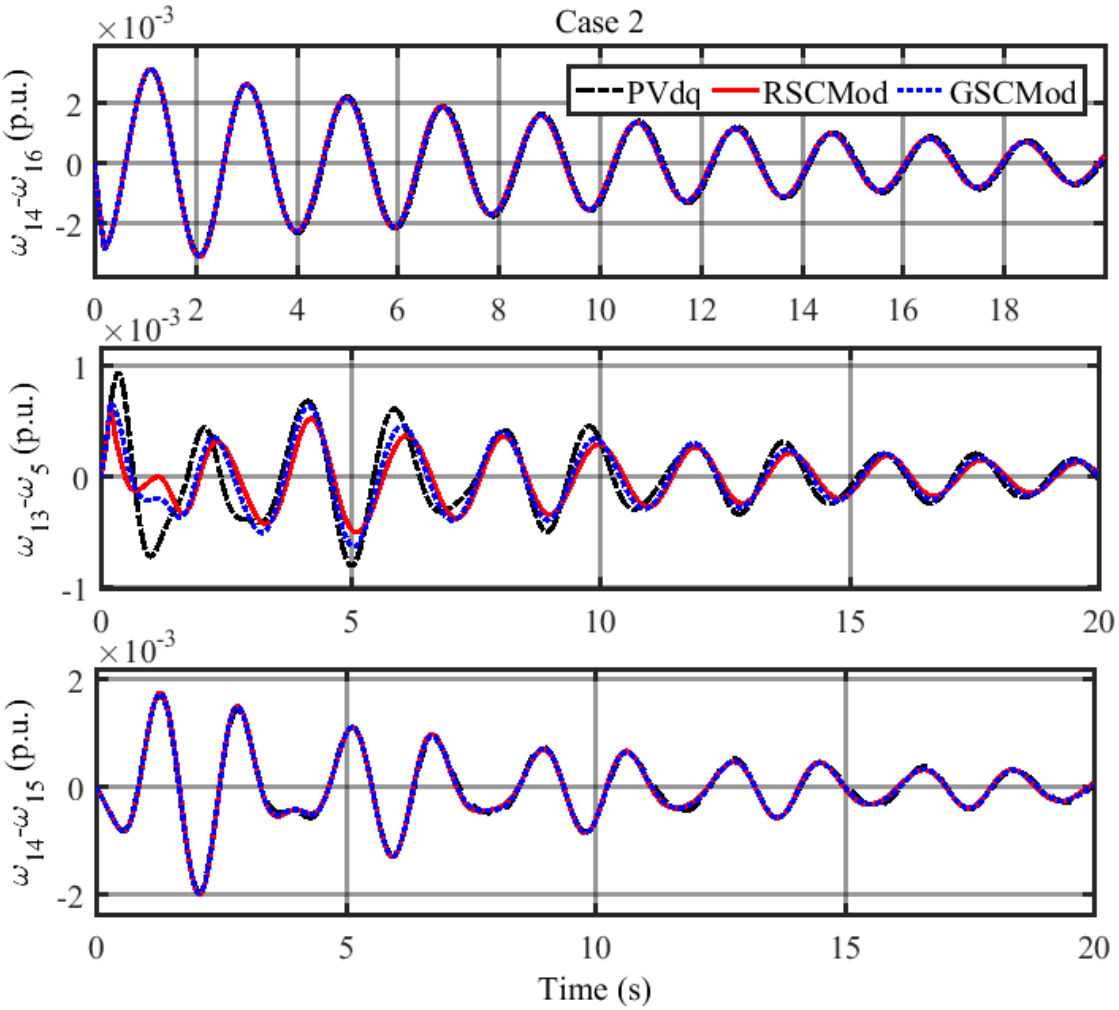

Figure 4.17: Comparison of PVdq, RSCMod and GSCMod for Case 2.

Case 3 - 3 phase-ground fault in bus 49: In third test, 3phase to ground fault is applied at bus 49 and cleared after 10 cycles. This fault is nearest to generator G10. Plot 1-3 in Figure 4.18 shows mode 3 is not excited, and mode 2 becomes dominant.

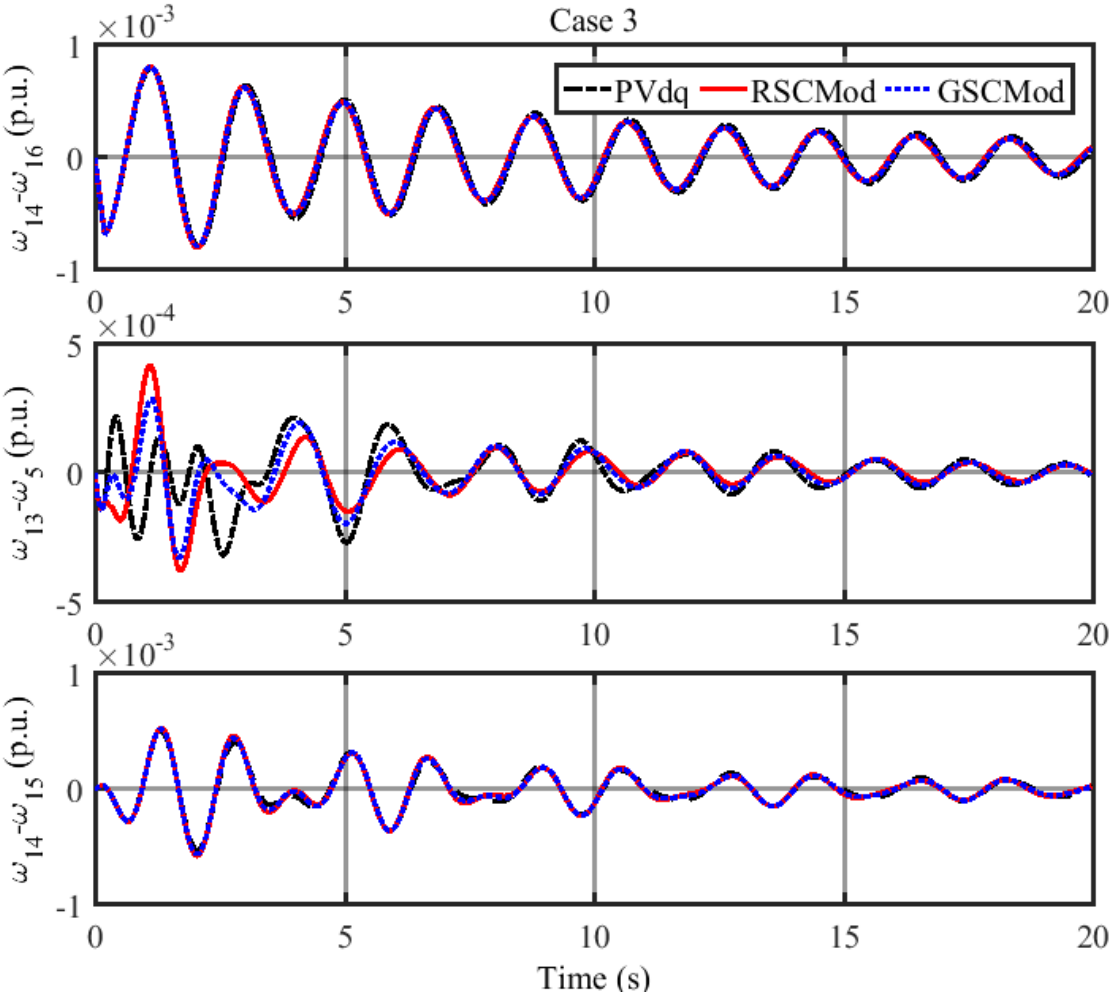

Figure 4.18: Comparison of PVdq, RSCMod and GSCMod for Case 3.

Case 4 - 3 phase-ground fault in bus 41: In fourth test, 3phase to ground fault is applied at bus 41 and cleared after 10 cycles. This fault is nearest to generator G10. Plot 1-3 are shown in Figure 4.19. Plot 1 shows dominant mode 2, and the response is very similar. Improvement in transient response is visible in plot 2 considering the oscillation magnitude till time t≈ 12 seconds. Afterwards, mode 2 becomes dominant. Plot 3 shows superimposed mode 2 and mode 4, and the response are very similar for three cases.

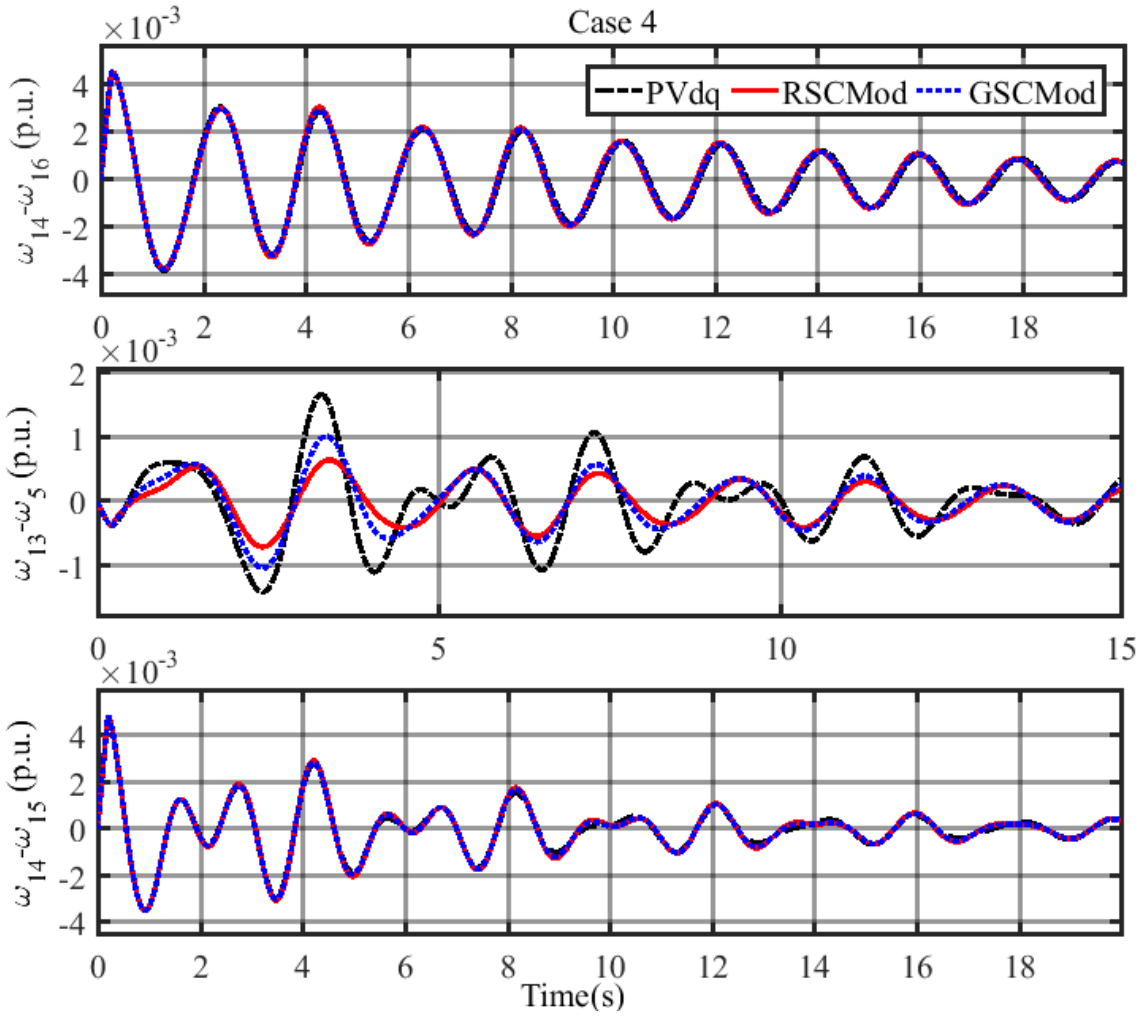

Figure 4.19: Comparison of PVdq, RSCMod and GSCMod for Case 4.

4.9 Summary

This chapter presented that the modification of existing DFIG control architecture can damp power system oscillation. PSS design methodology for DFIG based on RSC and GSC control are presented in this chapter. The local measurable signal signal for feedback is slected based on observability analysis of all the relevant measurement signals that are available locally, such as terminal voltage, frequency, active and reactive power injection from generator and so on. Both RSC and GSC has ability of modulating active or reactive power. The controllability analysis was used in this work to select the best input signal. Eventually, active power modulation based

RSCMod and GSCMod were formulated with slip frequency feedback. The controller was tested and verified in model 1: two area system and showed that this control technique enhanced the damping of inter-area as well as local mode. The similar control topology was tested on larger scale model 2: 68-bus system. The inherent issues of using local measurement feedback becomes evident due to lower observability of the modes in the selected signal worsened by limited controllability using available control inputs, suggesting requirement of wide area measurement based control to damp the oscillation.

CHAPTER 5: LINEAR-QUADRATIC GAUSSIAN BASED OPTIMAL POWER OSCILLATION DAMPING CONTROLLER DESIGN FOR DFIG

Chapter 4 demonstrated that DFIGs can damp the power system oscillation if proper feedback controller is designed to modulate its active power. Two different control methodologies were presented, the first method is to modulate DFIG torque via RSC control called RSCMod, and the second method is to modulate GSC active power via GSC control called GSCMod. The two controllers are only modulating the active power of the generator. This chapter will elaborate on that concept by developing an optimal control methodology for power system oscillation damping via DFIG active power control as well as reactive power control. Moreover, wide area signals are considered based on their higher observability of the modes.

The advance in technology means that it is now possible to design control based on remote signals from wide area measurement system (WAMS). The most popular industrial approach used in damping the power system oscillation has always been PSS used in synchronous generators. However, these controllers are limited in effectiveness mainly because of the following reasons [59, 60, 61, 71]:

- The PSS are designed based on linearized power system model around a nominal operating point. This restricts the validity of the controller to neighborhood of this point. But the power system is constantly changing due to load changes, transmission network changes, generation changes and so on. The addition of intermittent resources such as wind and solar adds to the volatility of the system operating condition. Inaccurate approximation of the power system parameters, and neglecting high frequency dynamics and other invalid assumptions only scrutinize the efficacy of the control.

- The local signals used in PSS do not guarantee the observability of the inter-area modes. Without observability of the modes, the controller cannot effectively provide any damping support, which might lead to system failure caused by insufficient damping.

The availability of phasor measurement units (PMUs) deployed in various locations provide the opportunity to utilize the remotely available signals with high observability of inter-area modes to design inter-area oscillation damping controller. In the past, the focus has been on designing wide area control for power system oscillation damping by addition of supplementary control signals from supervisory wide area controller to local controllers in synchronous generators to aid the damping of inter-area modes [59, 61, 62]. Recently, HVDCs and FACTS devices have been identified as effective devices in damping inter-area modes. Approaches based on either local or remote signals [63, 60, 66] are studied. Capability of using linear quadratic gaussian (LQG) to damp the power system oscillation using centralized thyristor controlled series capacitor (TCSC) has been discussed in [64]. LQG is a modern state-space technique for designing an optimal dynamic regulator by allowing a tradeoff between regulator performance and control effort. The literature are still lacking on design and implementation of optimal power oscillation damping control for DFIGs that are based on wide area measurement system. This chapter presents LQG based POD controller for DFIG that provides the supplementary reference signals for DFIG active and reactive power controller to enhance the damping of poorly damped inter-area modes. The control methodology is implemented on DFIG integrated two-area, 11-bus system and IEEE 68 bus benchmark system, and the performance is verified via modal analysis and non-linear time domain simulation.

5.1 DFIG Integrated Power Grid Model

The power system models used in this study are same as described in this section. The controller is first designed and tested on a smaller scale model and its scalability

is shown by testing similar control on larger scale system.

5.1.1 Model 1

Widely used 11-bus and 2-area system [27] has been modified with addition of 441MW wind farm represented by an aggregated DFIG model on bus 6 as shown in Figure 5.1. The load L9 and L7 are assumed to have increased to 2115MW and

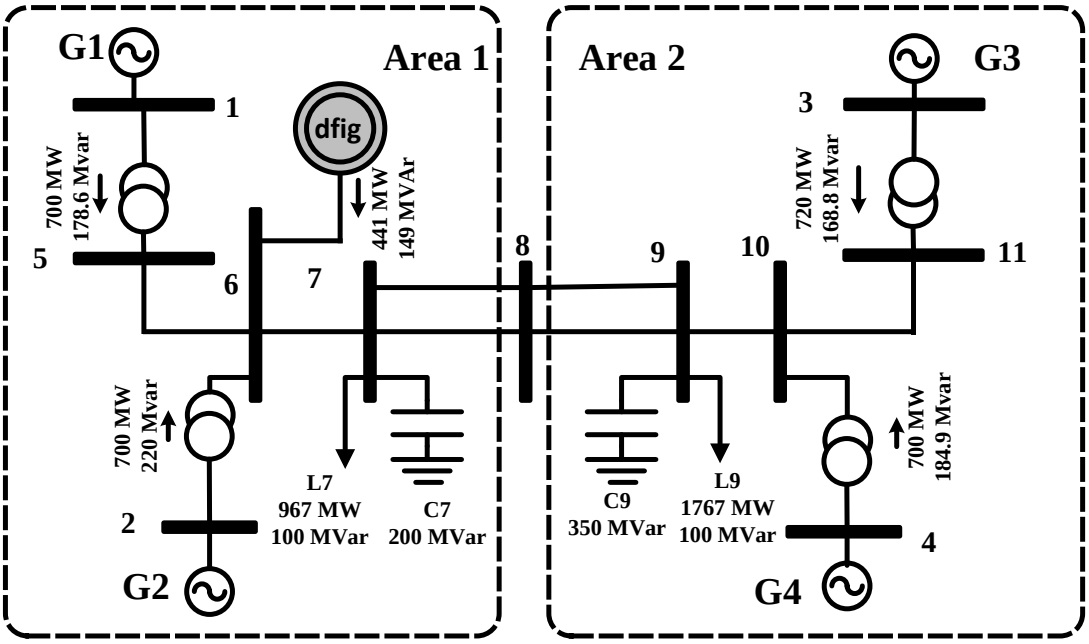

Figure 5.1: Two area system with one DFIG-based wind farm

1057MW respectively. All four synchronous generators G1-G4 are equipped with fast acting static exciters (ST1A). DFIG is operating in speed and voltage control mode. Suitable vector control topology are employed for rotor side converter and grid side converter control. This system exhibit two local area modes, and one inter-area mode. DFIG does not inherently participate in the electromechanical oscillation with the grid, however, the modes are affected by the rising level of power output from DFIG, and resulting network changes such as tie-line power flow changes.

5.1.2 Model 2

IEE 68-bus, 16-machine and 5-area power system depicted in Figure 5.2 is the larger scale model used in this study. It is an approximate model of New England (NETS) and New York (NYPS) interconnected network. Detailed description of the system and its characteristics including machine, control and network parameters are available in [65].

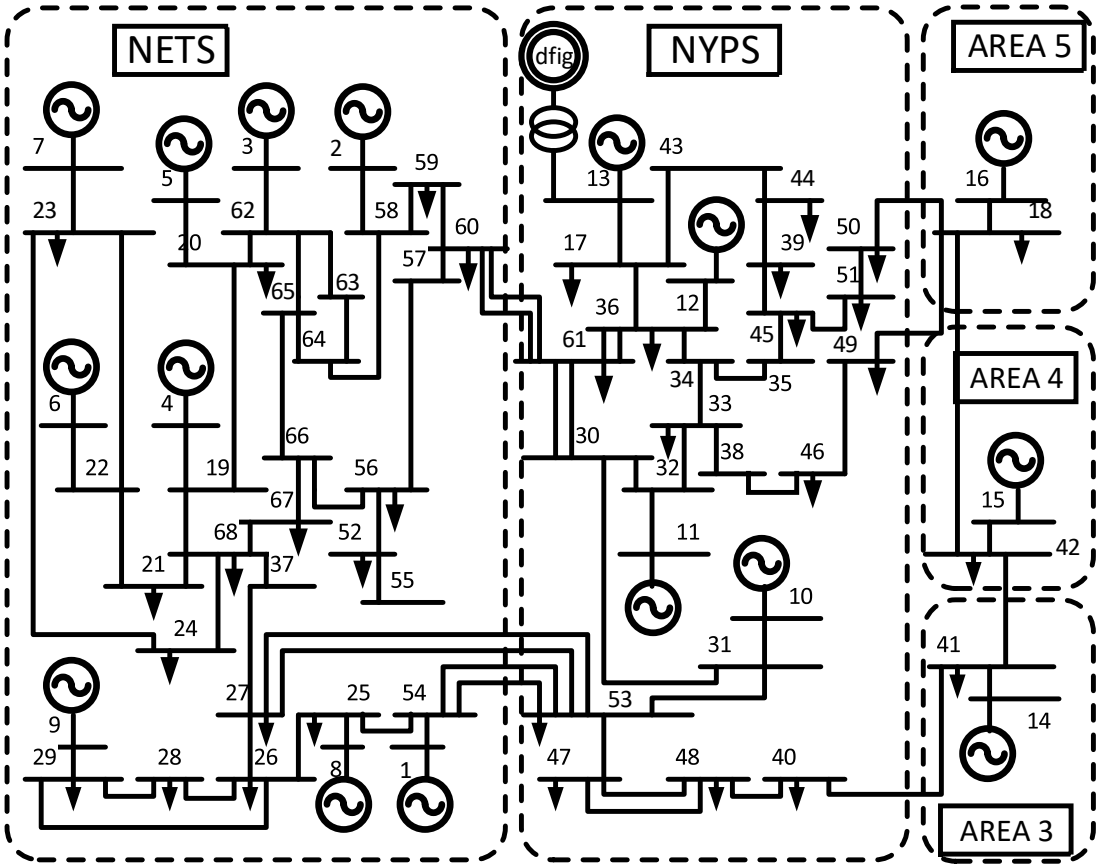

Figure 5.2: IEEE 68-bus 5-area benchmark system

The generators G1 to G8, and G10 to G12 have DC excitation systems (DC4B); G9 has fast static excitation (ST1A), while the generators G13 to G16 have manual excitation. Generators G1 through G12 are also equipped with a PSS that consists of three lead lag compensators and a washout block in series. The rest of the generators are assumed to have no PSS. Moreover, we assume that DFIG based wind

farm replaces 50% of the generation from G13 and is represented by an aggregated equivalent wind farm model. Following test cases are considered in this study:

Feedback Signal Selection

First, it is necessary to assess the modal controllability with reference signals that can modulate active and reactive power of DFIG, which are currently located in bus 13. The modes which are highly controllable from DFIG will be targeted. The feedback output signal selected should have high observability of the modes of interest. Assessment of modal observability in the available signals provides the basis for output feedback signal selection. The geometrical measure of controllability and observability is computed similar to section 4.6. For simplicity, only the generator speed deviations are considered as available signals for this study.

5.2 Power System Model Reduction

LQG control design produces a controller of order equal to that of the plant or even higher with the incorporation of the extra weights. As such the control design and implementation would be very complicated and time consuming. Model order reduction significantly reduces the complexity of the control design. The reduced model, however, should be a good approximate of the full order system, especially at the frequency range for which the controller is designed [68]. Balanced truncation method [69, 67] is used to compute a reduced-order approximation of the model by neglecting the states that have relatively low effect on the overall model response. State contributions are measured using Hankel singular values of $G(j\omega)$ given by square roots of the eigenvalues of product of their controllability grammian P and observability grammian Q respectively [64]:

$$\sigma_i = \sqrt{\lambda_i(PQ)} \tag{5.1}$$

where $\lambda_i(PQ)$ is the i^{th} largest eigenvalue of (PQ) and P, Q are the solutions of the following Lyapunov equalities:

$$PA^T + AP + BB^T = 0 \tag{5.2}$$

$$QA + A^TQ + C^TC = 0 \tag{5.3}$$

Here, A, B and C are state, input and output matrices.

5.3 LQG Based Control Design

The power system linearized model can be written in the following form:

$$\dot{x} = Ax + Bu + \Gamma w \tag{5.4}$$

$$y = Cx + v \tag{5.5}$$

where x is n-dimensional state vector, u is m-dimensional input vector and y is q-dimensional output vector. The plant is assumed to be strictly proper, linear, time-invariant, controllable, and observable. Moreover, w and v are the process and sensor noise inputs, respectively, assumed uncorrelated white Gaussian noise processes with known covariance matrices W and V, respectively [70]. Configuration of LQG control is shown in Figure 5.3.

The LQG control provides optimal control input u which minimizes the following quadratic cost function:

$$J = \lim_{T\to\infty} \frac{1}{T} E \int_0^T (z^TQz + u^TRu)d\tau \tag{5.6}$$

where z can represent either x or linear combination of the states. Matrices Q and R are appropriately chosen weighting parameters such that $Q^T = Q \geq 0$ and $R^T = R \geq 0$. Usually, both are diagonal matrices. The reduced order system is used to compute optimal state feedback control law given by:

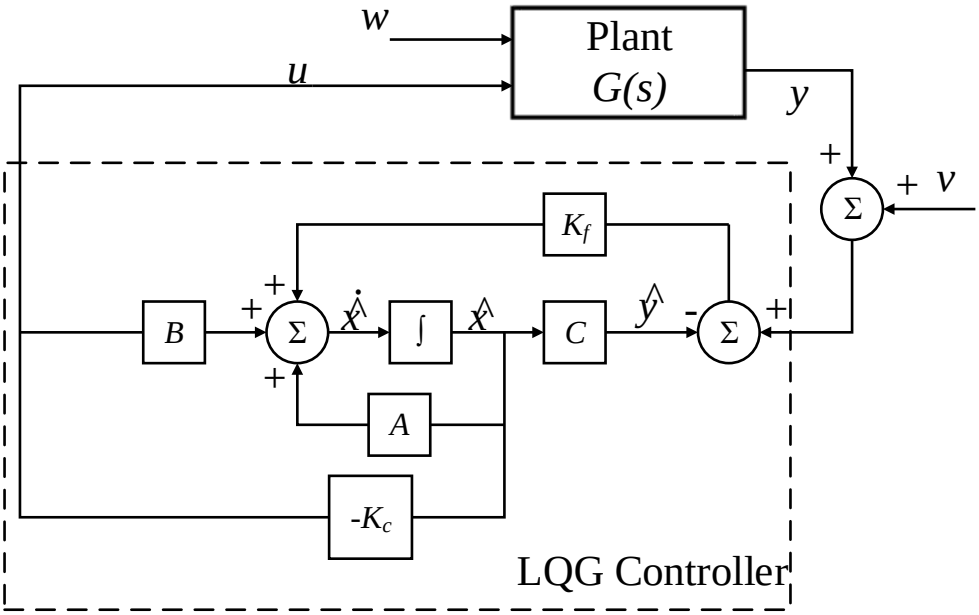

Figure 5.3: LQG Controller diagram

$$u = -K_c x \tag{5.7}$$

where $K_c = R^{-1}B^T P_c$ and P_c is the unique symmetric semidefinite solution of the algebraic Ricatti equation:

$$A^T P_c + P_c A + Q - P_c R^{-1} B^T P_c = 0 \tag{5.8}$$

subject to (A, B) being stabilizable, $R > 0$, $Q \geq 0$ and (Q, A) has no unobservable modes on the imaginary axis.

Measuring all the states of plants is infeasible, thus, an estimator (Kalman filter) is employed to provide the required estimates of the states from available/measured outputs. The structure of the Kalman filter is that of an ordinary state-estimator with:

$$\dot{\hat{x}} = A\hat{x} + Bu + K_f(y - C\hat{x}) \tag{5.9}$$

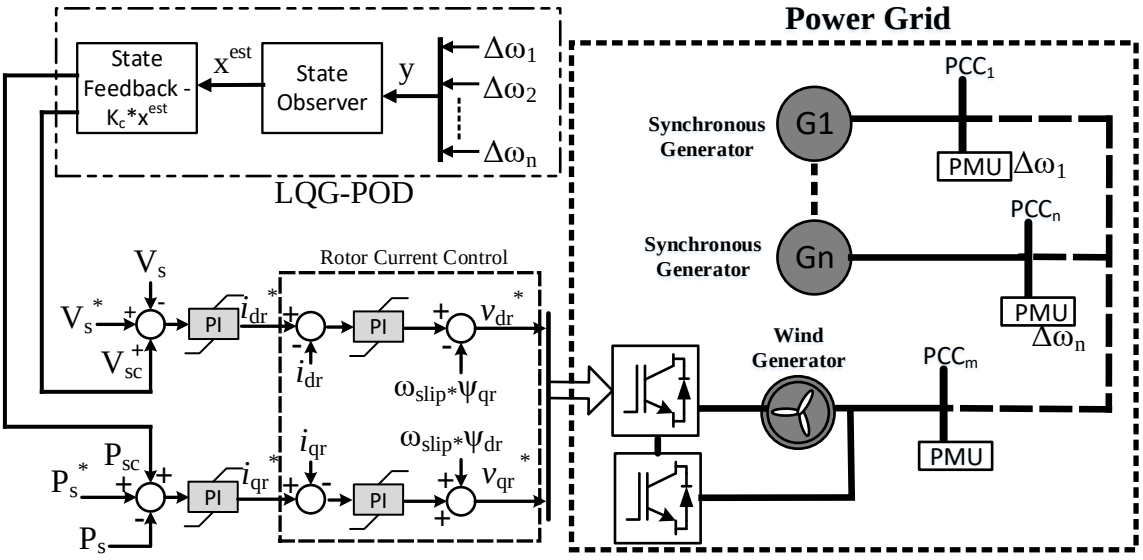

Figure 5.4: Proposed LQG-POD Controller for DFIG

where K_f is the Kalman filter gain that minimizes $J_f = E\{[x - \hat{x}]^T[x - \hat{x}]\}$, and is given by:

$$K_f = P_f C^T V^{-1} \tag{5.10}$$

and P_f is the unique symmetric positive semidefinite solution of the following algebraic Ricatti equation:

$$P_f A^T + A P_f - P_f C^T V^{-1} C P_f + \Gamma W \Gamma^T = 0 \tag{5.11}$$

subject to (C, A) being detectable, $V > 0$, $W \geq 0$ and $(A, \Gamma W \Gamma^T)$ has no uncontrollable modes on the imaginary axis. Finally, the optimal control law in the LQG formulation becomes:

$$u = -K_c \hat{x} \tag{5.12}$$

The proposed Linear-Quadratic-Gaussian based Power Oscillation Damping Controller (LQG-POD) is shown in Figure 5.4 which utilizes measured slip of pre-selected

generators.

5.4 Model Order Reduction and Control Design

As discussed in earlier section, the power system models are reduced to include only relevant dynamics under study. The reduced model is used to design a damping control that will be tested in full scale system.

5.4.1 Model 1

The two input signals that will be used to damp the oscillation are:

1. P_{sc}: Supplementary signal to DFIG active power controller

2. V_{sc}: Supplementary signal to DFIG voltage controller

The selected output signals are the slip speed of four synchronous generators i.e. $\Delta\omega_1$, $\Delta\omega_2$, $\Delta\omega_3$, and $\Delta\omega_4$.

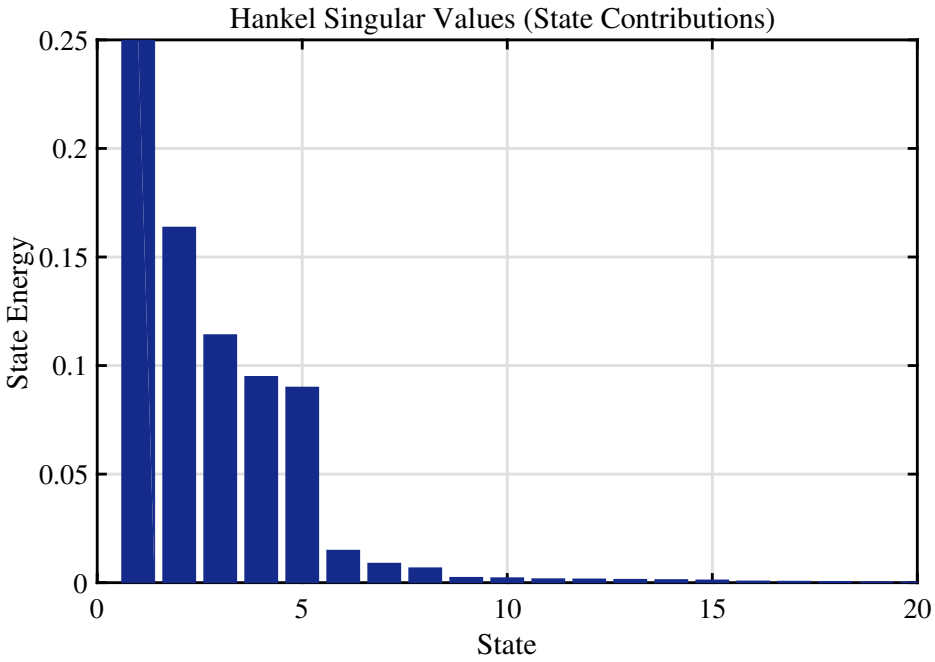

Figure 5.5: Hankel Singular Values corresponding to states of linearized model 1

The linearization of the model at the given operating point yields a linear model of the system. The linear model is 59^{th} order, with 2-inputs and 4-outputs. The Hankel

Singular value of the linearized model is shown in Figure 5.5. The figure shows that the contribution of 8 states are considerably higher and the state 9 on wards have very low contribution in the input/output behavior.

Balanced reduction of the model as explained in earlier section is implemented. The frequency response of full order (59) system is compared to reduced order system model of order 5, 6, 8, 10 and 12 using bode-magnitude plot as shown in Figure 5.6.

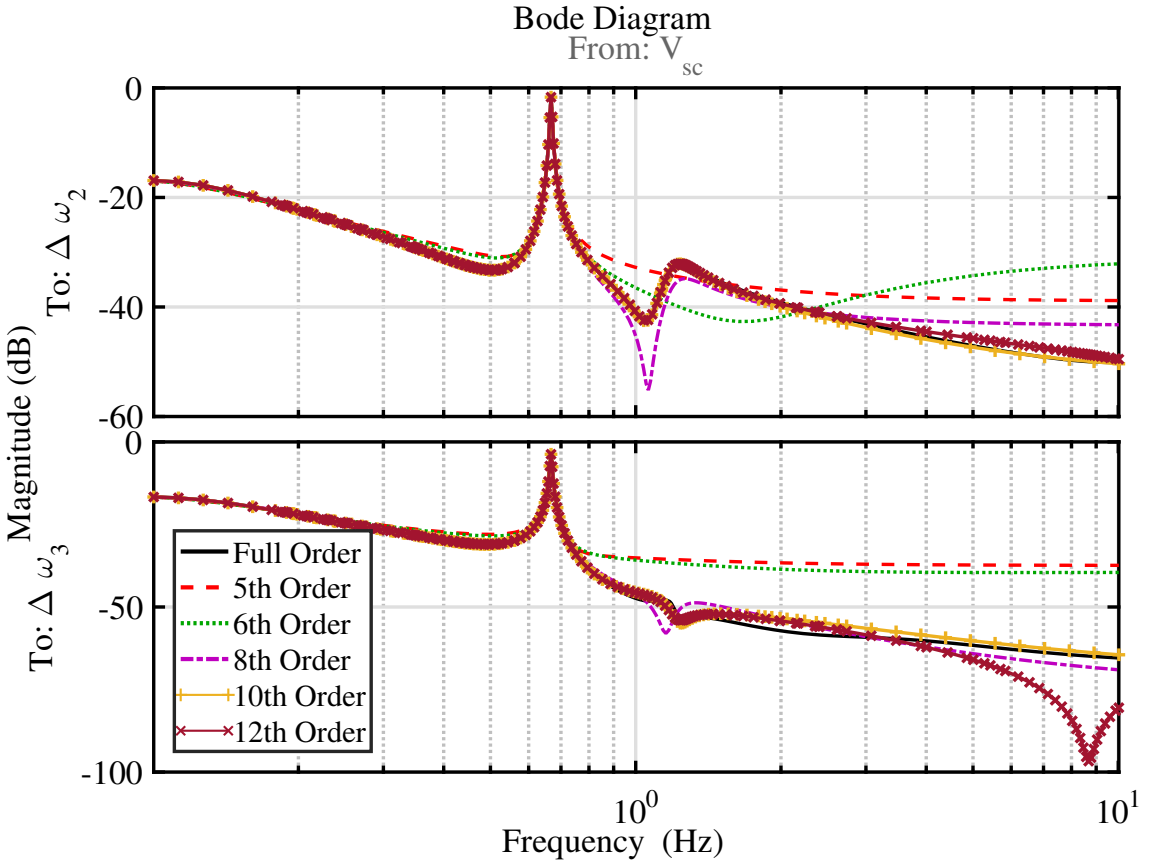

Figure 5.6: Model 1: Bode plot showing magnitude of slip of generator G_2 and G_3 from V_{sc}

It can be inferred from the figure that the reduced order model of order ≥ 8 produce very good match with the full order system response in our desired frequency range of 0.1-2 Hz. The accuracy of 10^{th} and 12^{th} order models are similar, and the accuracy did not increase for increasing model order above 12. This can be inferred from Hankel Singular Value plot as well. Therefore, 10^{th} order model was chosen for control design

purpose. Using 10^{th} order reduced model, a linear-quadratic regulator is designed. In this work, the value of weighing matrices were chosen as:

$$Q = C'_{red} \times C_{red}$$

$$R = 0.01 \times I_{m \times m}$$

where, C_{red} is the output matrix of reduced order model, and $I_{m \times m}$ is the identity matrix of order m, which is equal to the number of inputs. Kalman filter is designed using equation (5.10). The state matrices A_{red}, B_{red}, C_{red} and D_{red} of the reduced model is used to compute the Kalman gain. Thus, a Kalman filter is designed to estimate the states of the reduced order model. This marks the end of control design procedure.

5.4.2 Model 2

Model 2 has 181 states. It would be challenging to design a LQG controller with that many states. Moreover, the designed controller would also increase the order of the system with the controller itself is of order 181. Thus, balanced truncation method discussed is used to reduce the model. The plot of Hankel Singular values of the linearized model shown in Figure 5.7 shows that only 14 states have high contribution in input/output behavior of this model. Frequency response plot in Figure 5.8 shows compares the full-order model with reduced model or order 12, 16, 20, 25 and 30. The outputs shown in the figure are slip speed of generator G14 and G16. And the input is the supplementary signal to reactive power controller of DFIG.

12^{th} order model is not able to accurately replicate the frequency response of the full-order model. This can be because of neglecting the states with higher energy. The response of 16^{th} order model is very accurate in lower frequency but cannot capture the response well in frequency above 1Hz. The models of order 20, 25 and 30 are able to capture the frequency response of actual model with acceptable accuracy.

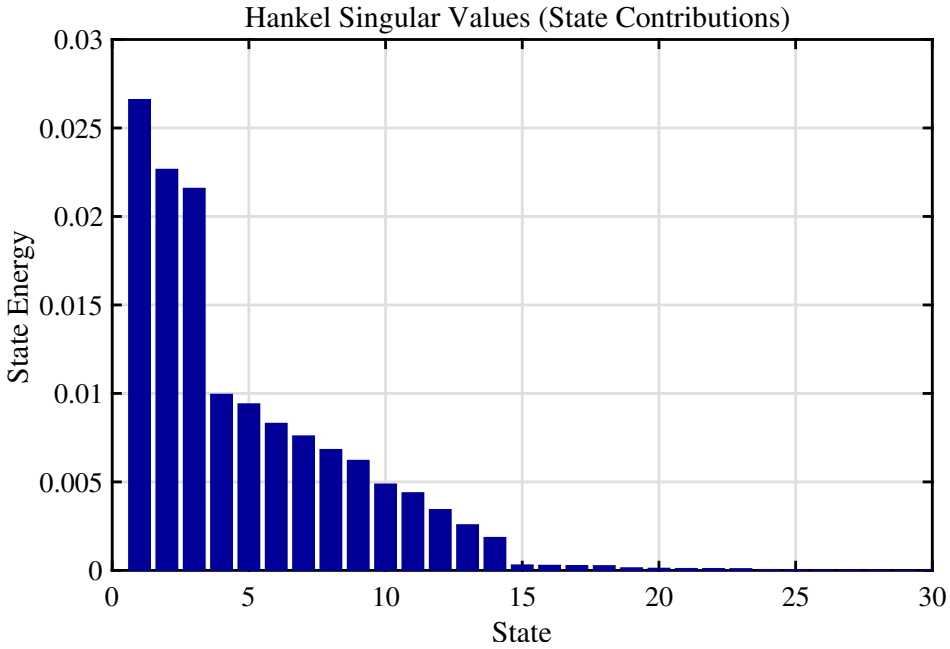

Figure 5.7: Hankel Singular Values corresponding to states of linearized model 2.

However, the gain in accuracy from order 20 to order 25 and order 30 is negligible. In order to design controller for damping inter-area modes, the frequency range of interest is usually 0.1 to 1 Hz. Thus, model order of 16 was found to be sufficient for control design purpose.

The supplementary reference signals in active power and reactive power controller of DFIG are the inputs i.e. two inputs. The slip speed of generators 5, 13, 14, 15 and 16 are considered as the available output signals i.e. 5 outputs. The selection of these generator speeds were made based on the observability analysis of four dominant inter-area modes. Those four modes are retained in the reduced order model as shown in Table 5.1. The states of the reduced system with highest participation are also shown. Mode 3 and mode 4 are well damped with damping greater than 10%. Mode 1 (0.52 Hz, 3%) and mode 2 (0.78 Hz, 4%) have damping below 5%. So in this control design, these two modes are targeted. The right eigenvector plotted for modes 1 and 2 are shown in Figure 5.9. The plot indicates higher observability of mode 1 and 2 in states $\mathbf{x_5}, \mathbf{x_2}, \mathbf{x_1}$ and higher observability of mode 2 in $\mathbf{x_4}, \mathbf{x_2}, \mathbf{x_1}$. This information will be useful in tuning the weights for LQG control design.

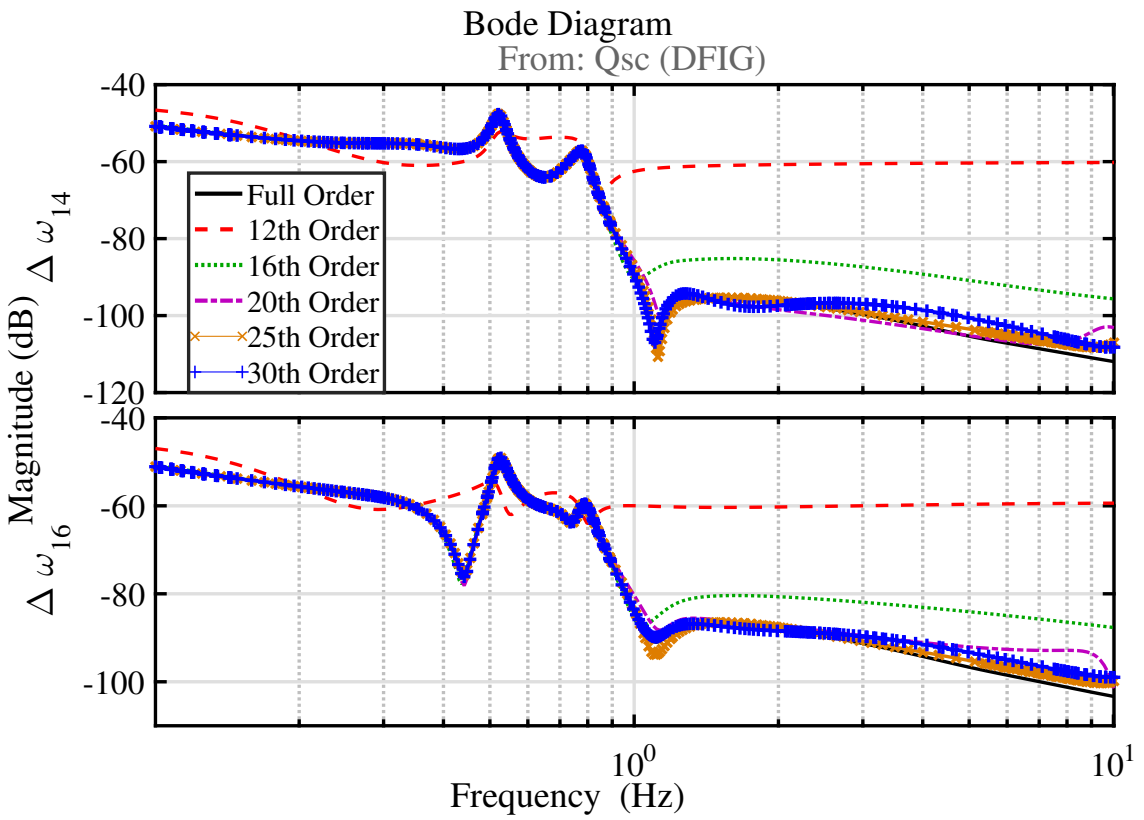

Figure 5.8: Model 2: Bode plot showing magnitude of slip of generator G14 and G16 from DFIG reactive power modulation

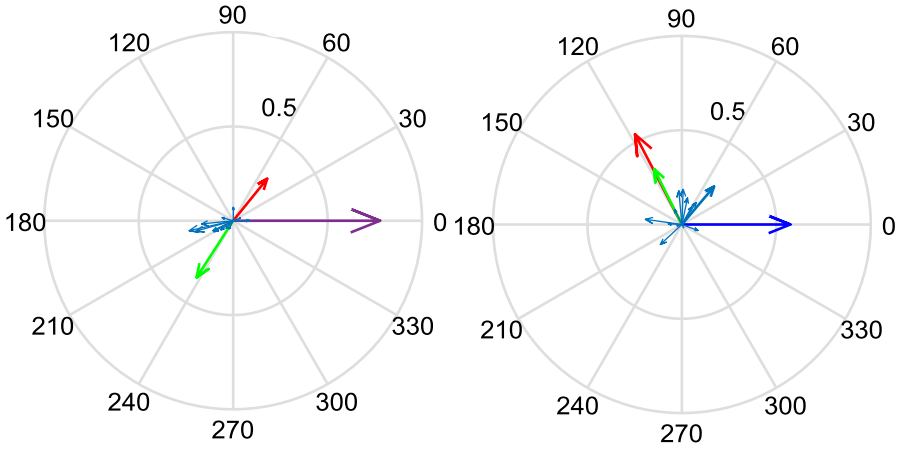

Figure 5.9: Polar plot of right eigenvector corresponding to mode 1 (left) and mode 2 (right) (red - x_1, green - x_2, dark blue - x_4, purple - x_5)

The reduced order model is used to design LQG controller. This means there is no direct systematic way for choosing the weighting matrices, thus, participation

Table 5.1: Dominant Inter-area Modes

Mode No.	Frequency (Hz)	Damping (%)	States with High Participation
1	**0.52**	**3**	$\mathbf{x_5}, \mathbf{x_2}, \mathbf{x_1}$
2	**0.78**	**4**	$\mathbf{x_4}, \mathbf{x_2}, \mathbf{x_1}$
3	0.74	11	x_9, x_6, x_{13}
4	1.17	15	x_9, x_{10}

factor analysis is used to achieve the design specifications. An initial guess for the state-weighting matrix was chosen via a participation factor analysis by setting higher weightage to the high participating states (as shown in Table 5.1). Based on participation and right eigenvector plot in Figure 5.9, higher weight was given to states $\mathbf{x_4}, \mathbf{x_5}, \mathbf{x_2}, \mathbf{x_1}$.

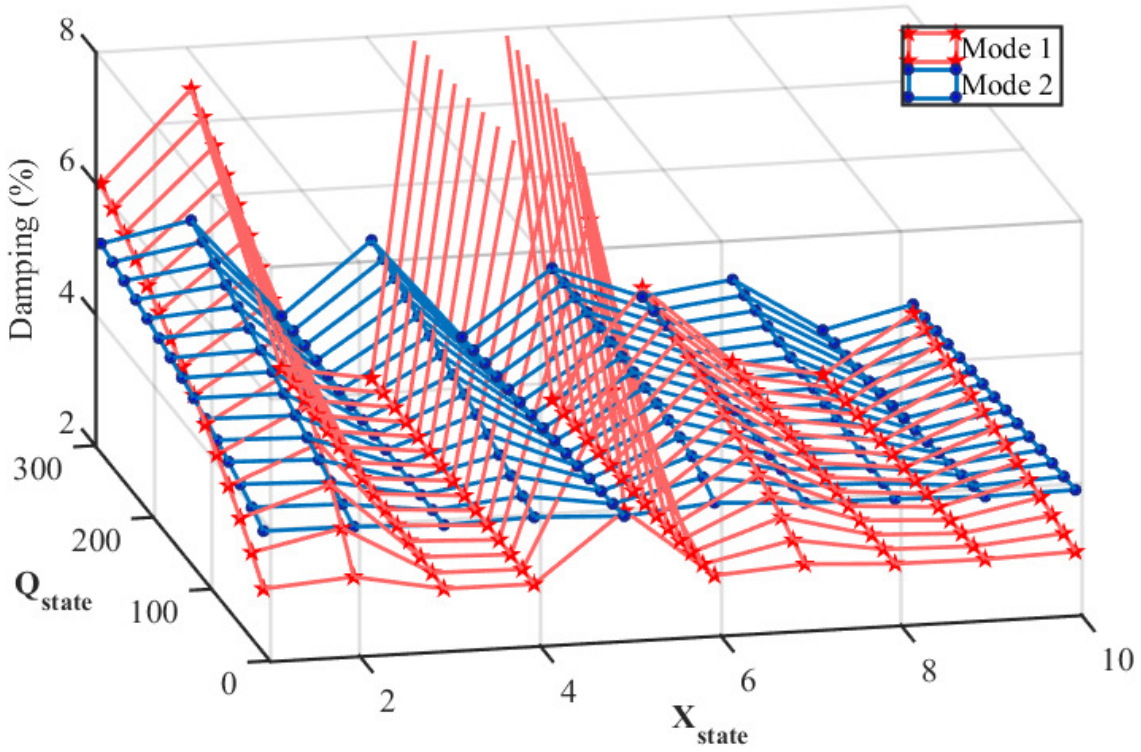

Figure 5.10: Damping of Mode 1 and 2 wrt weight of states x_1 to x_{10}

To tune the weights better, sensitivity of damping of the modes with respect to the weightage of each of these states and inputs was performed. The variation of

damping of modes 1 and 2 by changing the weightage of a state from 1-300 keeping other weights at unity, are shown in Figure 5.10. Increasing the weightage of states $\mathbf{x_1}$ and $\mathbf{x_2}$ improves the damping of both modes 1 and 2. Mode 1 damping improved for increasing weight of states $\mathbf{x_5}$, but this would decrease the damping of mode 2. Similarly, mode 2 damping improved for increasing weight of states $\mathbf{x_4}$, but this would decrease the damping of mode 1. These modes were found less sensitive to the weight of other states. For the given scenario, the damping of modes were more sensitive to the weight of input_1 i.e. P modulation. However, it is also important to consider that the gains computed should not have extreme values that would result in undesirable impact on DFIG and system during large transient events. Thus, maximum gain magnitude was set not to exceed 20. After several iterations, the following state and input weightage matrices were chosen to produce the optimal results. Final diagonal elements of the Q matrix are: (500 500 10 20 100 10 10 10 10 10 10 10 10 10 10 10)

The active power modulation had higher controllability than reactive power modulation. Thus, higher weightage was assigned to active power modulation to reduce excessive modulation of active power. The digonal elements of R matrix are: (0.5 0.2)

The resulting feedback gain matrix is:

K_c = [-19.9 15.6 3.9 -12.2 17.4 -7.2 -6.2 -0.4 17.0 -7.5 0.9 -1.3 -2.7 -1.0 -2.9 -1.1; 12.2 -11.6 0.6 9.0 -12.9 -0.3 8.0 7.2 -12.9 9.7 -6.6 1.9 0.4 0.2 0.1 0.9]

The modes of the system with and without the proposed LQG controller are shown in Figure 5.11 and Table 5.2. The damping of mode 1 increased to 12% and that of mode 2 increased to 7%. The greater improvement in damping of mode 1 can be justified via controllability analysis which reveal higher controllability of mode 1 with DFIG active and reactive power compared to mode 2. The damping of other modes were not hampered. In fact, the damping of mode 3 increased from 11% to 15%.

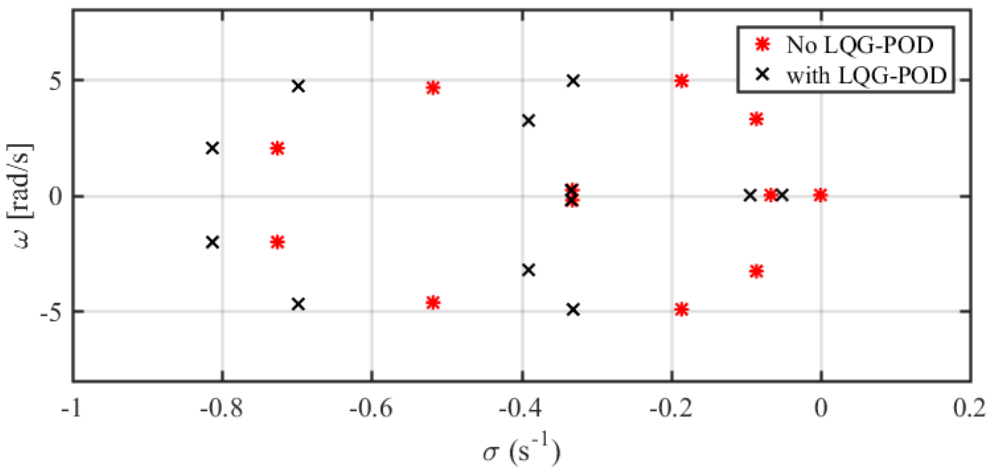

Figure 5.11: System Poles with and without LQG-POD

Table 5.2: system modes with and without the proposed controller

Mode No.	Frequency (Hz)	Damping (%) without control	Damping (%) with control
1	**0.52**	**3**	**12**
2	**0.78**	**4**	**7**
3	0.74	11	15
4	1.17	15	15

5.5 Time Domain Simulation

Time domain simulation is performed to confirm the results of small signal stability analysis. Both model 1 and 2 are subjected to disturbances that are commonly prevalent in power system to test the performance of the damping control.

5.5.1 Model 1

To analyze the effectiveness of the LQG based power oscillation damping controller for DFIG referred as 'LQG-POD', 4 different systems are formulated as listed below:

System A- No PSS + No LQG-POD: None of the generator PSS are online. DFIG is equipped with basic speed and voltage control.

System B- No PSS + LQG-POD: None of the generator PSS are online. DFIG is equipped with LQG-POD.

System C- PSS (G1) + No LQG-POD: PSS is installed in generator G1. DFIG does not have LQG-POD.

System D- PSS (G1) + LQG-POD: PSS is installed in generator G1. DFIG is equipped with LQG-POD.

Following test cases are considered to perturb the system and analyse the response of the system:

Case 1 - Small Signal Perturbation Test: The reference voltage of generators 2 is increased by 0.1 p.u. from time t=0-0.1 seconds. The reference voltage of generators 3 is increased by 0.1 p.u. from time t=0.5-0.55 seconds. This will excite inter-area mode as well as local area modes of both areas.

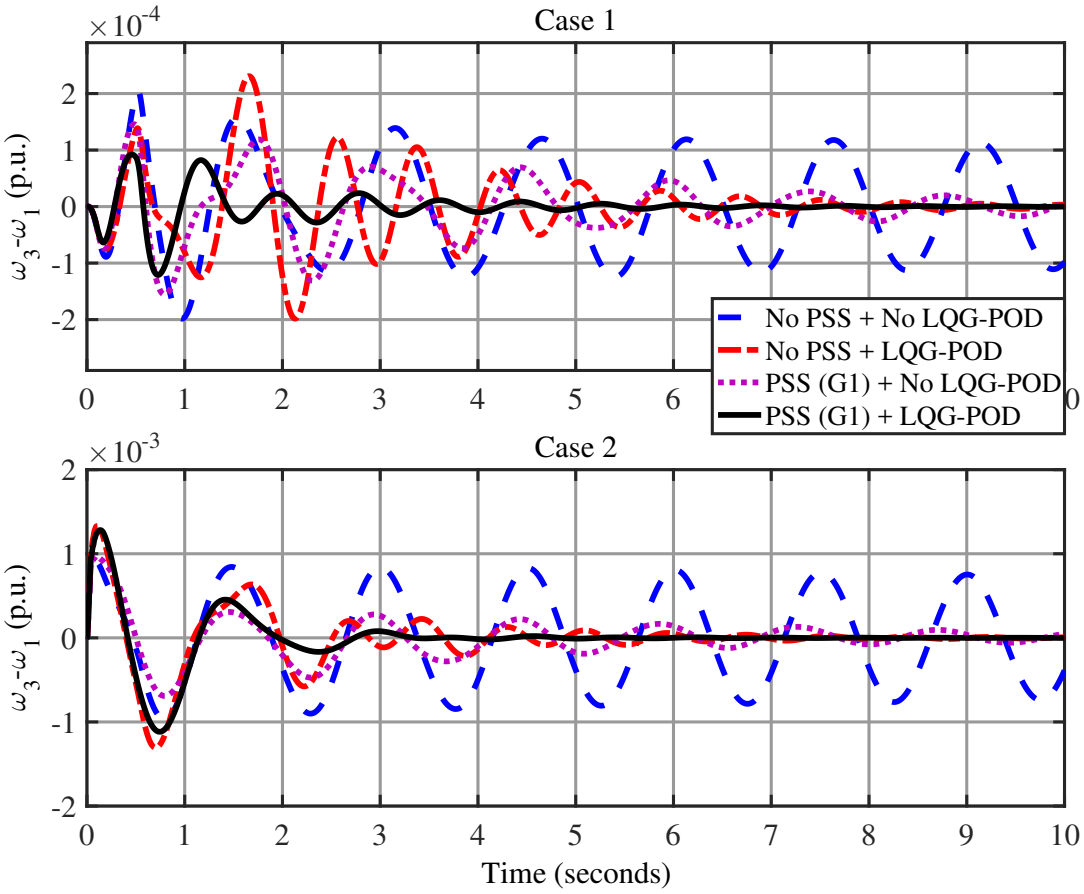

Figure 5.12: Non-linear time domain simulation of System A-B during test Case 1 (top) and Case 2 (bottom).

Case 2 - Large Signal Perturbation Test: 3-phase line to ground fault is applied on bus 8 for 3 cycles and cleared naturally. This will mostly excite inter-area mode.

The results of the simulation of the 4 systems are shown in Figure 5.12.

The difference in rotor speed/frequency of generator 3 and 1 was selected to observe the inter-area mode of the system based on their mode-shape analysis. From the comparison of system A and system B simulation under small and large signal perturbation, we can see the inter-area mode is damped much faster when LQG-POD is employed in DFIG. Similarly, comparison of system C and system D shows that the inter-area mode is damped much faster when LQG-POD is online. Also, it can be inferred that the LQG-POD coordinates well with existing generator PSS (in G1) to enhance the damping of the inter-area mode. The ability of the proposed LQG-POD is highly observable in case of large signal perturbation in which only inter-area mode is excited. In order to demonstrate the impact of LQG-POD on DFIG dynamics,

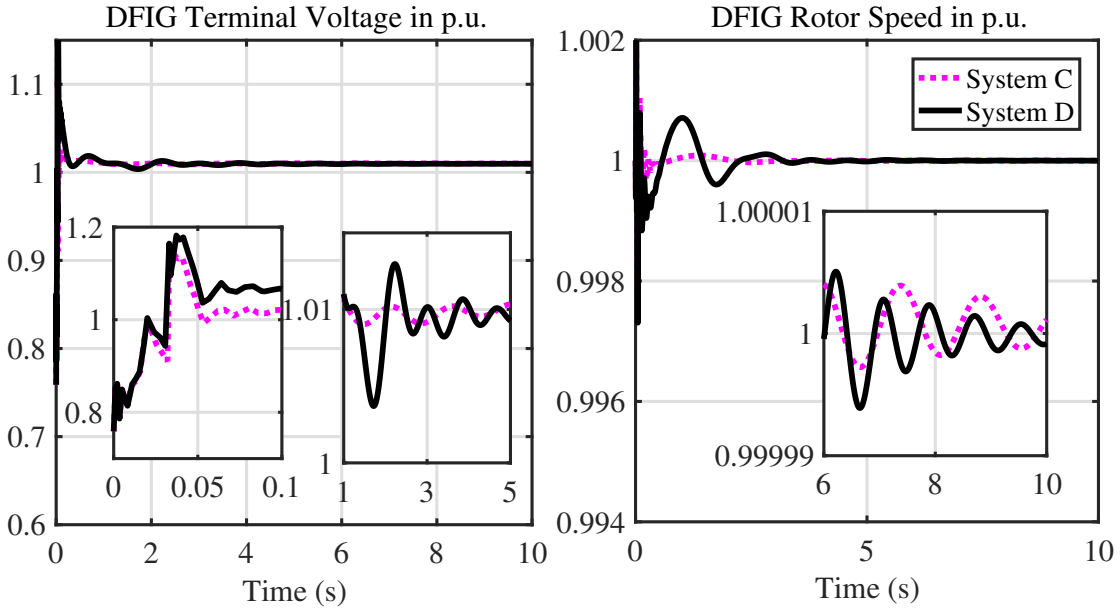

Figure 5.13: DFIG terminal voltage and rotor speed of Sysetm C (dotted purple) and System D (solid black) during test Case 2.

terminal voltage and rotor speed of DFIG of system C and system D during test case 2 are shown in Figure 5.13. The oscillation in the feedback signal is introduced in the voltage and speed of DFIG in system D. The oscillation of DFIG speed noticed in system C is due to the poorly damped inter-area oscillation.

5.5.2 Model 2

The performance of the proposed controller was tested with time domain simulation of nonlinear full order system subjected to small signal and large signal disturbance. Two systems are considered for simulation:

System 2A - No LQG-POD: The generators G1-G12 are equipped with PSS. But DFIG does not have the proposed LQG-POD.

System 2B - with LQG-POD: LQG-POD is employed in DFIG connected at bus 13. The generators are assumed to have their PSS online.

To show the benefit of the LQG-POD in DFIG to damp the inter-area modes, two test cases are formulated to represent two types of perturbations used to perturb the system.

Case 1 - Small Signal Perturbation: To simulate the system response to small signal perturbation, pulse signal of magnitude 0.1 p.u. and length of 0.25 seconds are applied at reference voltage of generator G9 at time t=0.5 seconds. The simulation results showing torque and slip of generator G15 with respect to generator G16 are shown in Figure 5.14. Significant improvement in system damping can be observed when the proposed controller is employed in modulating active and reactive power of DFIG. Poorly damped inter-area mode 2 with frequency $\approx$0.5 Hz is distinctly visible when the DFIG LQG-POD is not implemented. However, this mode damps much faster when LQG-POD is implemented.

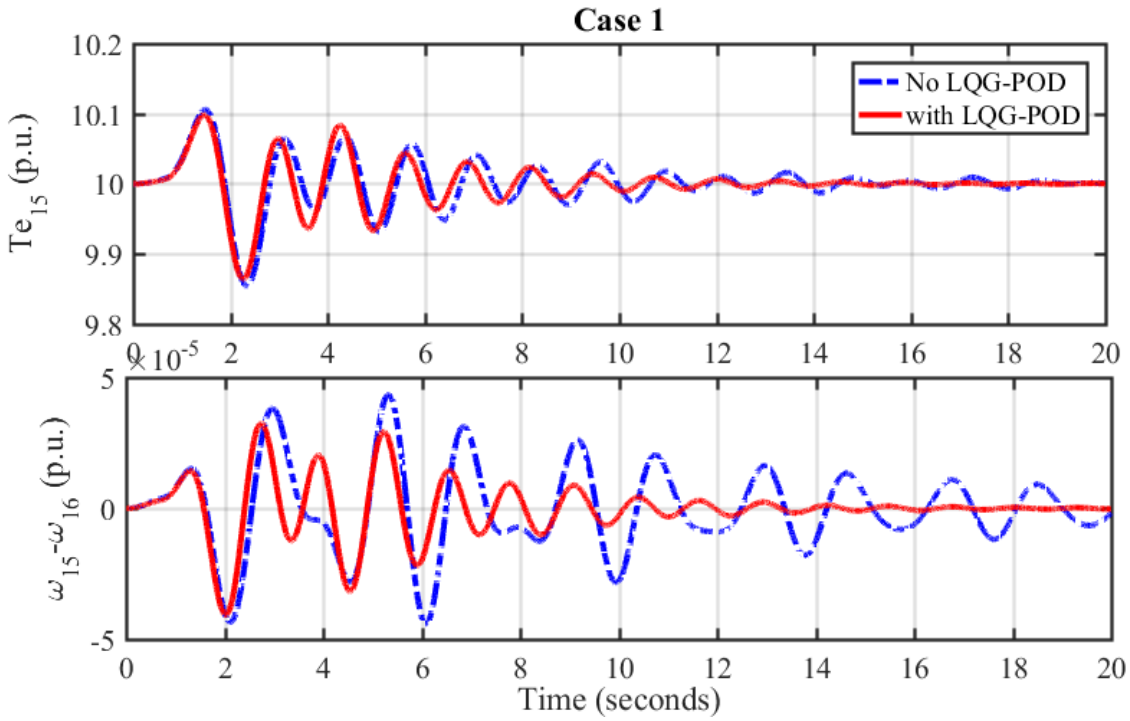

Figure 5.14: Generator G15 torque (top) and rotor slip w.r.t. swing generator G16 for small signal perturbation.

Case 2 - Large Signal Perturbation: Large disturbance is simulated by applying a three-phase bus fault at bus 9 at t=0.1 sec and naturally cleared after 0.1 second keeping the system topology intact. The results for two cases are shown in Figure 5.15. Poorly damped mode is visible in the system without controller and takes a long time to settle. The LQG-POD controller employed in DFIG was able to improve the damping of the mode as seen in Figure 5.15 and the settles a lot quicker. Thus, the DFIG POD controller was capable of supporting the damping of the inter-area modes which were poorly damped otherwise. This of course comes with the cost that active and reactive power of the DFIG are affected (Figure 5.16), especially during larger disturbance. The limiter can be employed to limit the impact on DFIG during large fault scenarios.

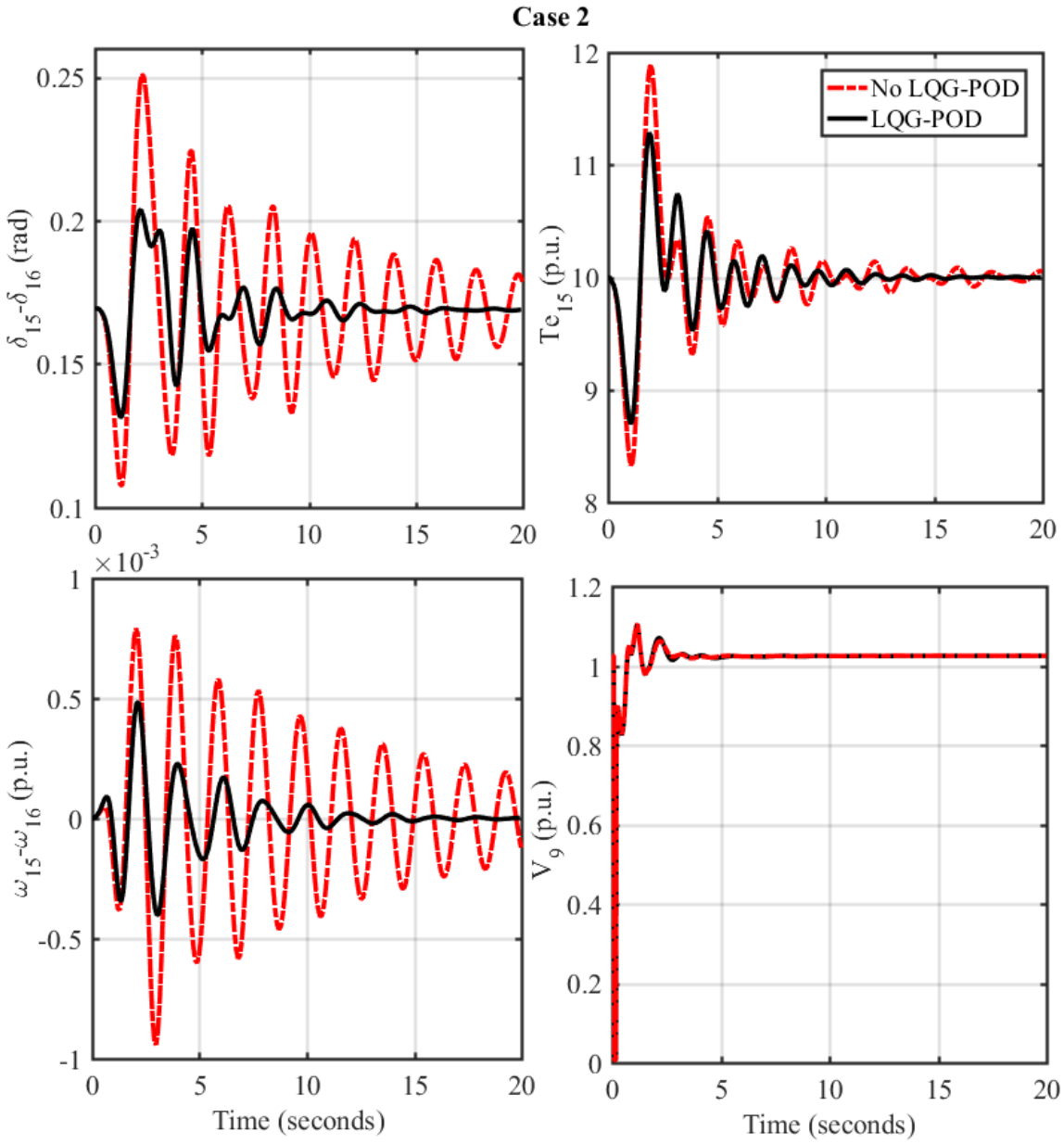

Figure 5.15: System response to bus 49 3phase-line-ground fault with and without LQG-POD.

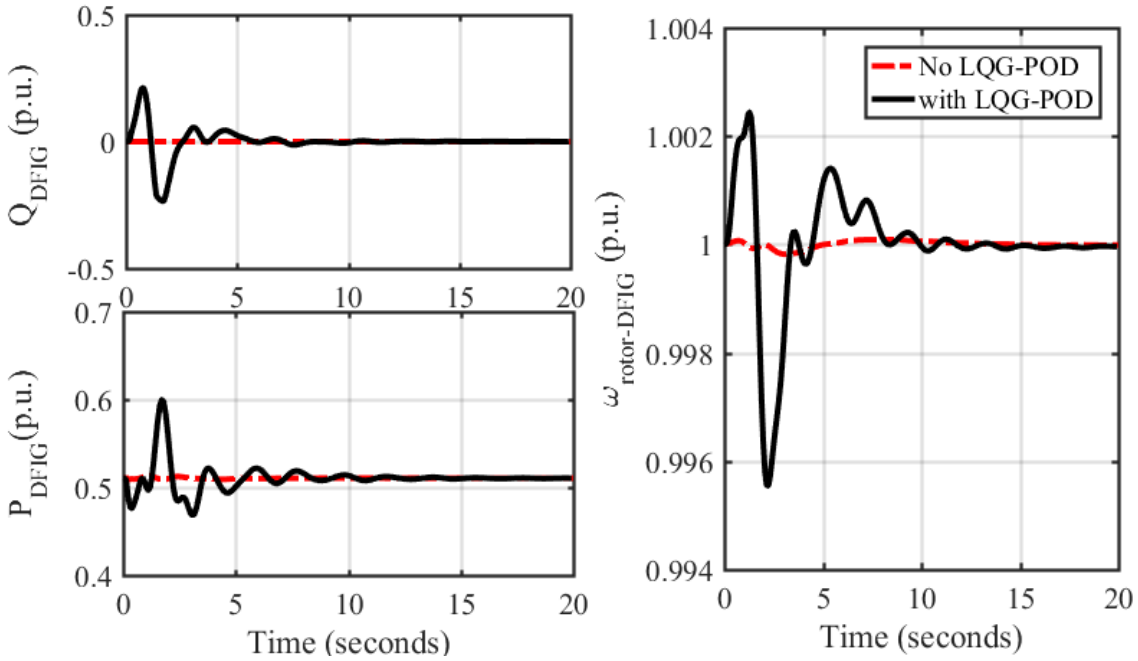

Figure 5.16: DFIG response to system oscillation during large disturbance

5.6 Summary

This chapter presented LQG based POD control technique for DFIG which improves the damping of low frequency power oscillation via modulation of active and reactive power. LQG technique is used to obtain the optimal state feedback that ensures stability and strikes a balance between input energy cost and controller performance. Balanced truncation is used to obtain the reduced order system. It simplifies the control design process. Kalman filter is used to estimate the states of the reduced system, and the estimated states are used for feedback. The performance of the proposed technique was verified via eigen analysis and non-linear time domain simulation. Simulation of the systems under both small signal and large signal perturbations showed effectiveness of the controller to damp the oscillation. The effectiveness of the control is higher when the inter-area modes with poor damping have higher controllability from DFIG active and reactive power modulation.

CHAPTER 6: SYSTEM IDENTIFICATION BASED OPTIMAL POWER OSCILLATION DAMPING CONTROL DESIGN FOR DFIG

Chapter 5 presented a LQG-POD for DFIG based on wide area measurement of power system. LQG is a standard state feedback control methodology for control of MIMO-systems with limited output measurement i.e. full states cannot be measured. This necessitates a state observer such as Kalman filter which estimate the states of the systems from available output signals provided that the control designer has a knowledge of state space model of the system and knowledge of input disturbance and output measurement noise. Moreover, this is a model based approach, meaning that the model is based on mathematical approximation of the power system model and the concern remains due to uncertainties caused by approximation and modeling error. It is not a trivial task to determine the uncertainty boundary of the system model. Therefore, measurement based approach are now being used to estimate the lower order model of the system. The efforts of building a measurement-based model are much less than those required for a model-based approach [74]. Various methods have been discussed in the literature to estimate the mode damping, frequency and mode-shape related to dominant inter-area modes of the system such as n4sid [72, 73], RLS [74, 75]. However, estimating the model and subsequent control design has not been addressed yet in the literature. Ref. [76] proposed an ARMAX model identification technique to identify the reduced order model and showed its applicability for control design, but does not show the validity of a control designed using such model.

In this chapter, a new method to damp the power system oscillation using measurement based identification of power system model has been proposed and evaluated. This method, a robust subspace identification algorithm evolved from Canonical vari-

ate analysis (CVA) [80], is used to identify the reduced order model of the large power system. This is a black-box modeling approach without having any priori knowledge of the system being estimated, except the system order. The system order is estimated using Akaike Information Criterion (AIC) [77]. The identified state space model is first validated, and used to design optimal output feedback controller for DFIG active and reactive power modulation to damp the power grid oscillation. The main advantage of this proposed technique is that the feedback controller can be optimized online whenever the new model estimate is available. The proposed method has been found to successfully damp the targeted modes of oscillation. This eliminates the poor performance of a controller designed based on particular operating point.

The major contributions of this work are:

- A novel wide-area controller that can dynamically control based on the changing operating points of the grid.
- A method that avoids detail modeling of the power grid for controller design purpose.
- The proposed method can be used to improve oscillatory stability as well as transient rotor angle stability of the power grid.
- The controller is robust against uncertainty such as time delay due to communication and control latency.

6.1 DFIG Integrated Power Grid Modeling

The proposed controller will be employed in DFIG integrated power system. Two different test systems are considered to test the efficacy of controller. First system is for the proof of concept verification and the second system is to show the scalability of the controller on a larger power grid model.

The two different benchmark systems are modified to include DFIGs. In the base case scenario, the DFIGs will be equipped with standard VC without any proposed

supplementary power oscillation damping control (POD). The performance improvement of the system with proposed POD in DFIGs will be compared with the base case. The two power grid models used are described briefly.

6.1.1 Model 1

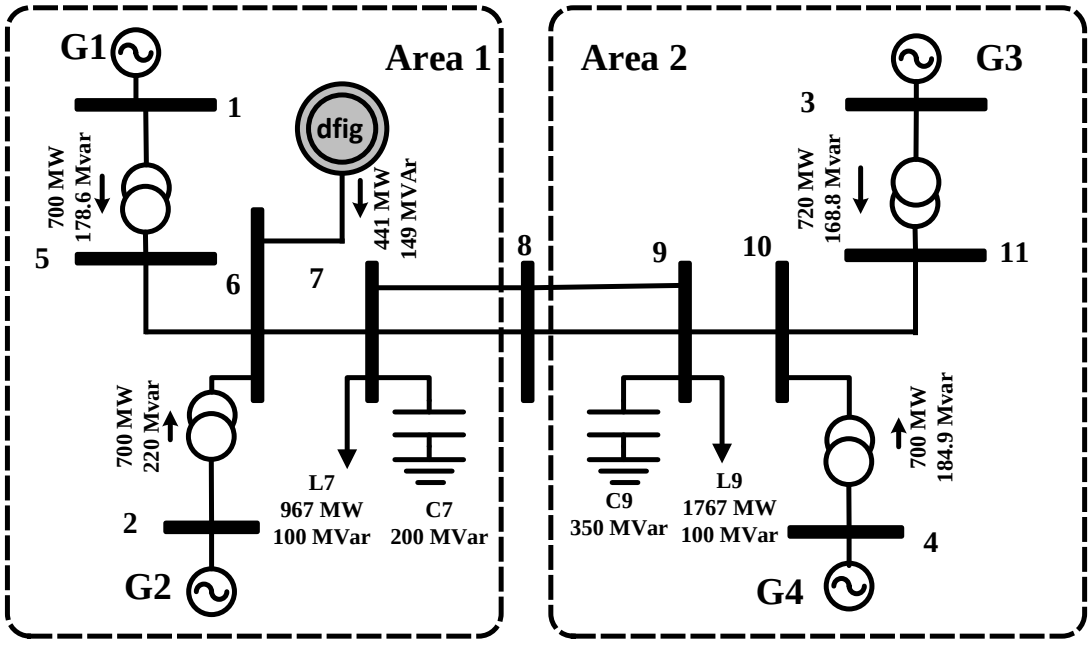

Figure 6.1: Two area system with one DFIG-based wind farm

Widely used 11-bus and 2-area system [27] has been modified with addition of 441MW wind farm represented by an aggregated DFIG model on bus 6 as shown in Figure 6.1. The load L9 and L7 are assumed to have increased to 2115MW and 1057MW respectively. All four synchronous generators G1-G4 are equipped with fast acting static exciters (ST1A). DFIG is operating in speed and voltage control mode. Suitable vector control topology are employed for rotor side converter and grid side converter control. This system exhibit two local area modes in which generators of each area oscillate against each other, and a low frequency inter-area mode in which generators of area 1 oscillate against the generators in area 2. DFIG does not inherently participate in the electromechanical oscillation with the grid, however, the

modes are affected by the rising level of power output from DFIG.

6.1.2 Model 2

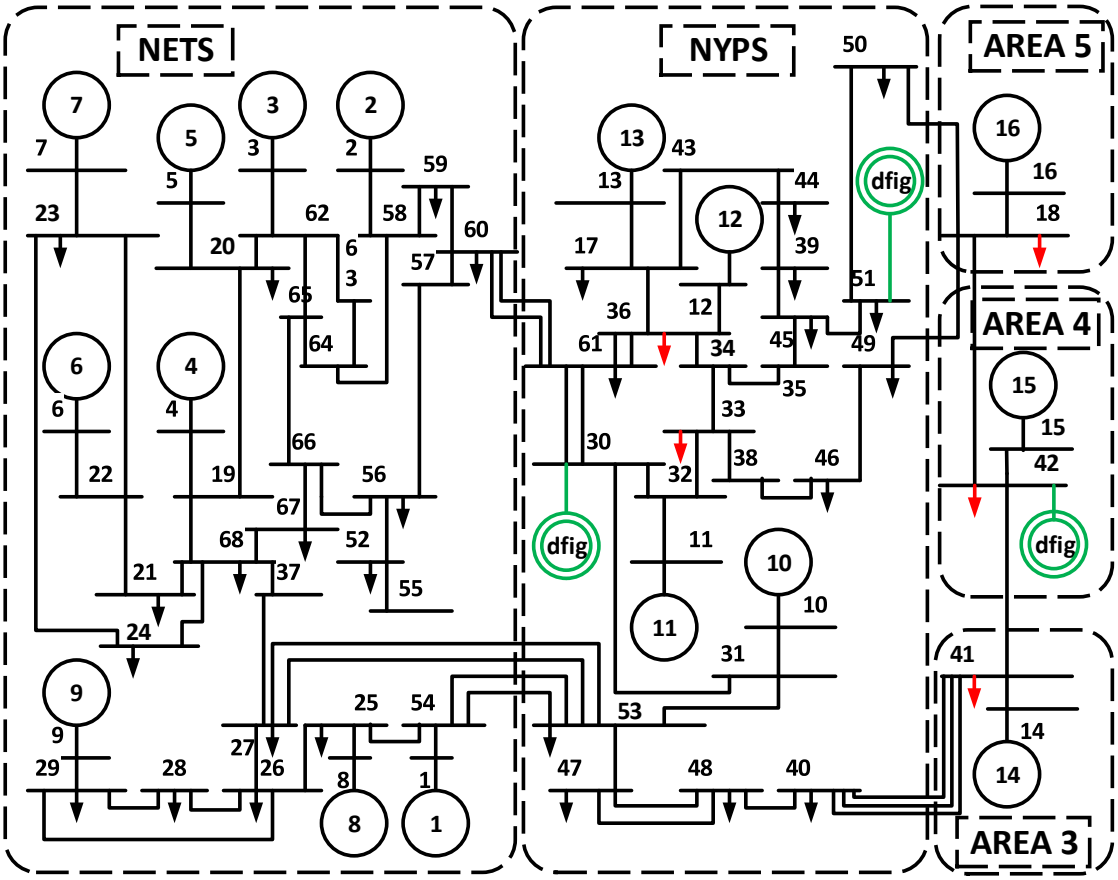

Figure 6.2: IEEE 68-bus and 5-area benchmark system including 3 DFIG-based wind farms

IEEE 68-bus and 5-area power system is modified to include 3 large wind farms as shown in Figure 6.2. It is an approximate model of New England (NETS) and New York (NYPS) interconnected network. Detailed description of the system and its characteristics including machine, control and network parameters are available in [54]. The generators G1 to G8, and G10 to G12 have DC excitation systems (DC4B); G9 has fast static excitation (ST1A), while the generators G13 to G16 have manual excitation. Generators G1 through G12 are also equipped with PSS (PSS1A). An aggregated model of DFIG-based wind farms are connected at bus 30 , 42 and

51 producing 500 MW, 1700 and 1000 MW respectively. The DFIGs are operating in speed and reactive power control mode. For this particular operating point, the generators are assumed to be operating at synchronous speed i.e. 1 p.u. To keep the generation from the existing synchronous generators at their respective values, the loads (marked red in Figure 6.2) are increased. The active power loads in bus 18, 33, 36, 41 and 42 were increased from their original value to 34.7 MW, 6.12 MW, 8.02 MW, 25 MW and 16.5 MW respectively. The reactive power references are generated from the load flow solution. The reactive power generated from the DFIGs at bus 30, 42 and 51 are -54 MVar, 230 MVar, and 270 MVar respectively.

6.2 Proposed Power Oscillation Damping Controller

The objective of designing a POD controller is to ensure that at least minimum level of damping is available during the steady-state condition after a major event such as fault or loss of critical line occur. This strategy ensures that a properly designed damping controller can enable increased power transfer limit of the critical lines in the system by enabling wider range of operation.

The architecture of the proposed POD controller for DFIG is shown in Figure 6.3. The controller is essentially an output feedback controller. The contribution of this research is in tuning the feedback gain matrix online/offline based on power system model identification. The proposed technique relies on two major blocks viz. system identification and optimization. The subspace state space system identification using modified canonical variate analysis (CVA) algorithm [80] is implemented to estimate a black box model of reduced order power system from a block of input and output measurement. The optimization block uses sequential quadratic programming (SQP) to tune the output feedback gain K_y so that the damping of the targeted inter-area modes of CVA estimated state space model is maximized. Then the optimized output feedback gain K_y is used in the actual system to damp the oscillation.

The supplementary reference set-point for active power (P_{sc}), and voltage (V_{sc}) or

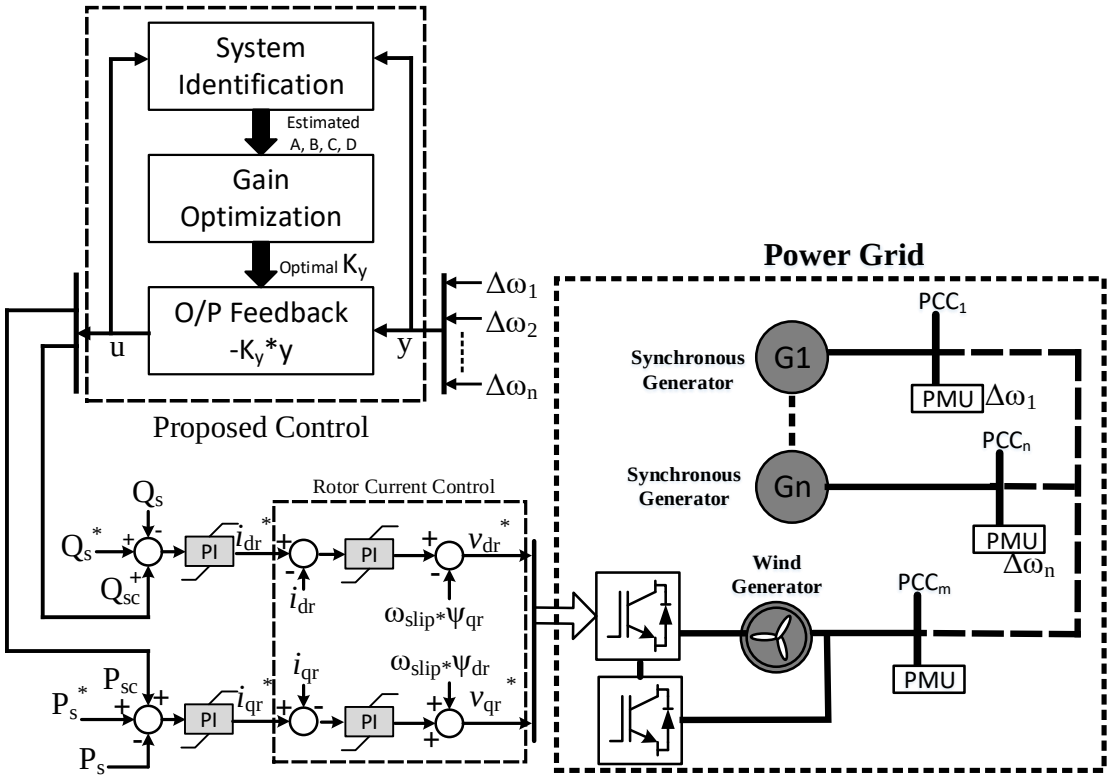

Figure 6.3: Online System Identification based Optimal Output Feedback Controller Architecture

reactive power (Q_{sc}) are the obvious choice for system inputs. First, it is necessary to assess the modal controllability with these inputs. The modes where DFIG shows higher controllability should be targeted. The feedback output signal selected should have high observability of the modes of interest. Thus, analysis of modal observability in the available signals is performed and the signals are prioritized accordingly. For convenience, only the generator speed deviations are considered as available signals for this study. Next subsections discuss each blocks in Figure 6.3. The selection of appropriate window size and model order will be discussed as well.

6.2.1 CVA State Space Identification

The subspace state space system identification based on Canonical Variate Analysis (CVA) was introduced in [80]. The computations involve a batch or time interval of

data for system identification. The batch nature of the algorithm has several major advantages over procedures that identify models using time recursive updating. In particular, there is no start up and the results are essentially exact in moderately small sample sizes. The Akaike information criterion (AIC) gives a precise determination of state order [77]. The AIC also permits precise comparison of models fitted using different time intervals to perform rigorous tests of hypotheses concerning the stationarity of the process, the optimal choice of data length for tracking time varying processes, and the presence of an abrupt change in the processes such as a system failure or state disturbance. The CVA method is fundamentally an approach to modeling, filtering, and control of a process by successive approximation of the memory or states of the process, i.e. by successively determining functions of the past that have the most information for prediction of the future. The CVA approach determines a general state space model such that the state corresponds to the Markov state of the process. The procedure involves:

- Determination of the canonical states of the process. The canonical sates are orthogonal and have property than an optimal state for a reduced order model of order r is obtained by selecting the first r canonical states.

- The state equations are computed by simple regression using the canonical states.

- The optimal state order can be determined by use of the Akaike information criterion (AIC).

The CVA method determines the canonical states first and the state space models are determined simply by regression. This is in contrast to other methods that determine a model of the system, and then obtain estimates of the states by deriving the corresponding Kalman filter. Most of the statistically efficient computational methods involve the use of an autoregressive moving average (ARMA) representation and

parameter optimization using an approximate maximum likelihood estimation (MLE) procedure. The MLE method involves an iterative search in the parameter space and has no 'a priori' bound on the required computation or convergence. In addition, the ARMA parameterization can be illconditioned particularly in the multivariable case. By contrast, the CVA computation involves primarily a singular value decomposition (SVD) which is one of the most numerically stable computational procedures available. The state space representation obtained is always well conditioned even for the multivariable case. As a result, the CVA method is ideally suited for automatic implementation of system identification on microprocessors including the automatic selection of the model state order.

The derivation is as follows. Consider a generic discrete state space model of a process as:

$$x(t+1) = Ax(t) + Bu(t) + Ke(t) \tag{6.1}$$

$$y(t) = Cx(t) + Du(t) + e(t) \tag{6.2}$$

where A, B, C, and D are state-space matrices. K is the disturbance matrix. $u(t)$ is the input, $y(t)$ is the output, $x(t)$ is the vector of nx states and $e(t)$ is the disturbance.

The measured input and output data are used to form past and future vectors which are subsequently used to compute sample covariance matrices. For any specified point, t, in this sequence, the past l-measurements of the output and input are assembled into a past vector, $p(t)$. Similarly, the measurements at the point t and a specified number of additional points are assembled into the future vector, $f(t)$, as shown in (6.3). The number of measurements used in the past and the future vectors can be different and can be selected automatically using Akaike Information Criteria (AIC).

$$p(t) = \begin{bmatrix} y(t-1) \\ y(t-2) \\ \vdots \\ y(t-l) \\ u(t-1) \\ u(t-2) \\ \vdots \\ u(t-l) \end{bmatrix}, \; f(t) = \begin{bmatrix} y(t+l-1) \\ y(t+l-2) \\ \vdots \\ y(t) \end{bmatrix} \tag{6.3}$$

Covariance matrices are computed as

$$\Sigma_{pf} = \frac{1}{N-2l-1} \sum_{t=l+1}^{N-L+1} p(t) f^T(t) \tag{6.4}$$

$$\Sigma_{pp} = \frac{1}{N-2l-1} \sum_{t=l+1}^{N-L+1} p(t) p^T(t) \tag{6.5}$$

$$\Sigma_{ff} = \frac{1}{N-2l-1} \sum_{t=l+1}^{N-L+1} f(t) f^T(t) \tag{6.6}$$

where

Σ_{pf} is the covariance matrix of the past and the future vector,

Σ_{pp} is the covariance matrix of the past vector with the past vector, and

Σ_{pf} is the covariance matrix of future vector with the future vector.

Matrix D is formed whose elements are the correlation coefficients between the elements of the past and future vectors as

$$D = \Sigma_{pp}^{-\frac{1}{2}} \Sigma_{pf} \theta^{-\frac{1}{2}} \tag{6.7}$$

where θ is an arbitrary weighting matrix. θ is chosen as Σ_{ff}. A singular value

decomposition of D matrix then yields

$$D = USV^T \tag{6.8}$$

such that

$$U^T U = V^T V = I \tag{6.9}$$

$$S = diag(s_1 \geq s_2 \geq, ..., s_n) \tag{6.10}$$

where U, and V are matrices of left and right singular vector, and S is a diagonal matrix of singular values.

The desired linear combination of the past and future vectors can be expressed as

$$c(t) = Jp(t) = U^T \Sigma_{pp}^{-1} p(t) \tag{6.11}$$

$$d(t) = Lf(t) = V^T \Sigma_{ff}^{-1/2} f(t) \tag{6.12}$$

and the covariance between the transformed past and future vectors is a diagonal matrix with the upper left element having the largest value and each succeeding element being equal to or less then the prior element.

$$\Sigma cd^T = \Sigma Jpf^T L^T = S \tag{6.13}$$

The order of the plant is determined by selecting the order, k, that minimizes the Akaike Information Criteria [77]. Subsequently, the first k rows of the J matrix are used to compute the state vector and the state space matrices. The AIC is expressed as twice the sum of the log likelihood function and the number of the free parameters.

$$AIC(k) = -2 \sum_{t=l+1}^{N-l+1} lnp(y_t | m_t, u_t, \theta_k) + 2p_k \tag{6.14}$$

The number of free parameters p_k is expressed as a function of the number of sensors, n, the number of controls, m, and the plant order, k.

$$p_k = 2kn + \frac{n(n+1)}{2} + km + nm \tag{6.15}$$

Equation (6.14) can be reduced to the following form

$$AIC(k) = (N - 2l + 1)[n(1 + ln2\pi) + ln[\Sigma_{\epsilon\epsilon}]] + 2p_k \tag{6.16}$$

where the error covariance matrix is given by

$$\Sigma_{\epsilon\epsilon} = \frac{1}{N - 2l + 1} \sum_{t=l+1}^{N-l+1} (y(t) - \hat{y}(t))(y(t) - \hat{y}(t))^T \tag{6.17}$$

The error is the difference between the measured sensor response vector $y(t)$ at time t, and the predicted sensor response vector $\hat{y}(t)$ using the measured data at time $t - 1$ and earlier. The predicted value of y is expressed as a function of the past vector. Since the past vector contains measured data at time $t - 1$ and earlier, the equation expresses the predicted value of y one step ahead of the measured data.

$$\hat{y}(t) = Hx()t = \Sigma_{yx}\Sigma_{xx}^{-1}x(t) = \Sigma_{yx}\Sigma_{xx}^{-1}J_k p(t) \tag{6.18}$$

Since the predicted sensor vector, $\hat{y}(t)$, is a function of the plant order, the error covariance matrix can be computed for all possible values of k and hence the AIC can be computed for all values of k. The values of k that minimizes the AIC is the selected order of the identified plant.

The state space matrices are computed from the measured covariance matrices as:

$$\begin{bmatrix} A & B \\ C & D \end{bmatrix} = \begin{bmatrix} J_k\Sigma_{p(t+1)p(t)}J_k^T & J_k\Sigma_{p(t+1)u(t)} \\ \Sigma_{y(t)p(t)}J_k^T & \Sigma_{y(t)u(t)} \end{bmatrix} \begin{bmatrix} J_k\Sigma_{p(t)p(t)}J_k^T & J_k\Sigma_{p(t)u(t)} \\ \Sigma_{u(t)p(t)}J_k^T & \Sigma_{u(t)u(t)} \end{bmatrix}^{-1} \tag{6.19}$$

6.2.2 Optimal Output Feedback Controller

The design of optimal output feedback controller is discussed in this section.

6.2.2.1 Output Feedback Controller

The linearized state space model of a power system can be written as:

$$\Delta\dot{x} = A\Delta x + B\Delta u \tag{6.20}$$

$$\Delta y = C\Delta x + D\Delta u \tag{6.21}$$

where, A, B, C and D are state space matrices, x, y and u are the state, output and input vector respectively.

The discrete model obtained by CVA in the form of equation (6.1) and (6.2) can be transformed to continuous form of equation (6.20) and (6.21). The modes of the system are given by the eigenvalues of state matrix A. To ensure reliable and robust operation of grid, all the modes should be located in the left half of plane and their damping ratio should be grater than a certain threshold as determined by the system operator. An output feedback controller can be designed to enhance the damping of the modes.

The output feedback can be expressed as:

$$u = -K_y\Delta y \tag{6.22}$$

where, K_y is output feedback gain matrix. Then, the equation (6.20) becomes:

$$\begin{aligned} \Delta\dot{x} &= [A - BK_yC]\Delta x \\ \Delta\dot{x} &= \tilde{A}\Delta x \end{aligned} \tag{6.23}$$

where, $\tilde{A}$ is the closed loop state matrix, and the eigenvalues of $\tilde{A}$ are the modes of the closed loop system.

Objective Cost Function: To increase the damping of least damped electromechanical modes, following objective function can be formulated as:

$$J_1 = \sum_{i=1}^{n_{cr}} Q(i)|\zeta_{th}(i) - \zeta(i)| \tag{6.24}$$

where n_{cr} is total number of critically damped inter-area modes, Q is the weightage vector such that $Q(i)$ correspond to penalize the i_{th} mode, ζ_{th} is the vector of threshold damping ratio determined by the power system operator and $\zeta(i)$ is the damping ratio of i_{th} critically damped mode. $|x|$ represent the absolute value of x. Absolute is necessary to ensure that damping criteria is satisfied and the generators are not excessively used.

If it is desired that the use of certain input say active power 'P_{sc}' be penalized more than the use of terminal voltage 'V_{sc}', the cost function can be modified as:

$$J_2 = \sum_{i=1}^{n_{cr}} Q(i)|\zeta_{th}(i) - \zeta(i)| + \sum_{j=1}^{n_u} R(j) \sum_{k=1}^{n_y} |K_y(j,k)| \tag{6.25}$$

where n_u and n_y are the number of inputs and outputs, $K_y(j,k)$ is the feedback gain from k^{th} output to the j^{th} input, R is the input weightage vector such that $R(j)$ penalizes the use of j_{th} input. This is also useful when there are more than one generators which can contribute in oscillation damping purpose. Vector R can be

manipulated to flexibly distribute the control effort among the available generators.

The controllability analysis can be helpful in determining the appropriate vector R. For example, from control point of view, it is desirable to utilize the generator which has the highest controllability of the modes of the system that requires damping improvement. So, setting very small value to the element of vector R corresponding to that particular generator provides higher utilization of that generator. Similarly, setting higher value to the generators with lower controllability will ensure lower utilization of those generator.

Again, if the oscillation in certain output needs to be penalized more than others, the cost function can be modified as:

$$J_3 = \sum_{i=1}^{n_{cr}} Q(i)|\zeta_{th}(i) - \zeta(i)| + \sum_{j=1}^{n_u}\sum_{k=1}^{n_y} R(j,k)|K_y(j,k)| \tag{6.26}$$

where $R(j,k)$ penalizes the gain between j_{th} input and k_{th} output.

By minimizing this cost function, the gain matrix K_y is computed that maximizes the damping of the least damped or critical modes under following constraints:

$$K_y^{min}(i,j) \leq K_y(i,j) \leq K_y^{max}(i,j) \tag{6.27}$$

where,

$K_y^{min}(i,j)$ is the minimum gain from j^{th} output to i^{th} input and

$K_y^{max}(i,j)$ is the maximum gain from j^{th} output to i^{th} input. Thus, the problem is a nonlinear constrained optimization and we will choose a reliable and matured method, sequential quadratic programming to solve this optimization problem.

6.2.2.2 Sequential Quadratic Programming (SQP)

SQP is one of the most successful methods for the numerical solution of constrained nonlinear optimization problems. It relies on a profound theoretical foundation and

provides powerful algorithmic tools for the solution of large-scale technologically relevant problems. The SQP methodology can be applied to nonlinear optimization problems (NLP) of the form [84]

$$\begin{aligned} &\text{Min } f(x) \\ &\text{subject to:} \\ &h(x) = 0, \text{ and } g(x) \leq 0 \end{aligned} \tag{6.28}$$

The Lagrangian of this problem can be written as,

$$L(x, \lambda, \mu) = f(x) + \lambda h(x) + \mu^T g(x) \tag{6.29}$$

where λ and μ are are vectors of multipliers. SQP is an iterative procedure which models the problem for a given iterate x^k by a quadratic programming sub-problem, solves that quadratic programming sub-problem, and then uses the solution to construct a new iterate x^{k+1}.

The sub-problem can be constructed by linearizing the constraints of around x^k, and it can be written as,

$$\begin{aligned} &\text{Min } \nabla f(x^k)(x - x^k) + \frac{1}{2}(x - x^k)^T H f(x^k)(x - x^k) \\ &\text{subject to} \\ &h(x^k) + \nabla h(x^k)(x - x^k) = 0 \\ &g(x^k) + \nabla g(x^k)(x - x^k) \leq 0 \end{aligned} \tag{6.30}$$

We need to update the estimates of the multipliers, and define the corresponding search directions, and then choose a step size and define the next iterate.

6.3 Model Identification and Validation

The CVA algorithm for subspace state space model identification was tested and validated in Model 1 and then in Model 2.

6.3.1 Model 1

The two inputs that can be used to perturb the system are dfig active power reference (P_{sc}), and dfig stator voltage reference (V_{sc}). Zero mean gaussian white noise of sampling frequency 10 Hz were used as input signal for perturbing P_{sc} and V_{sc}. The controllability of local and inter-area modes via DFIG power and voltage control is shown in Figure 6.4. The output signals are slip frequency ($\Delta\omega_r$) of generators G1

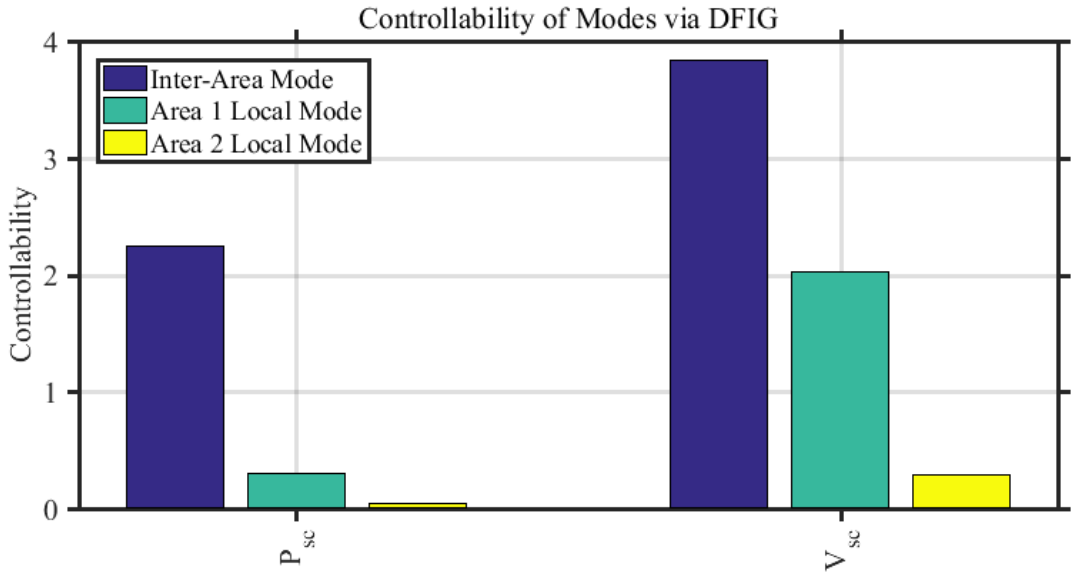

Figure 6.4: Controllability of modes via DFIG

through G4 which exhibit high observability of inter-area mode. The observability of the local and inter-area modes in frequency of 11 buses are shown in Figure 6.5. In this particular test, the simulation was run for 50 seconds. The data measurement sampling time was 0.1 seconds. This is equivalent to 10 Hz which is greater than the 5 times the local area mode frequency (1.12 Hz). Total of 500 data points are stored for each input and output.

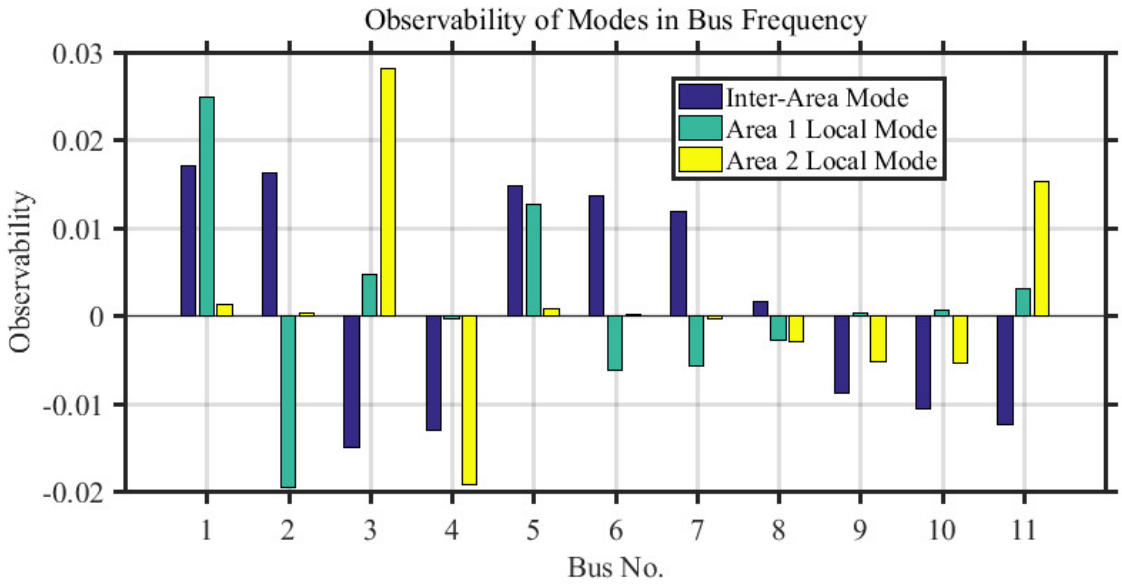

Figure 6.5: Observability of Modes in bus frequency

6.3.1.1 Analysis of Fitting Accuracy

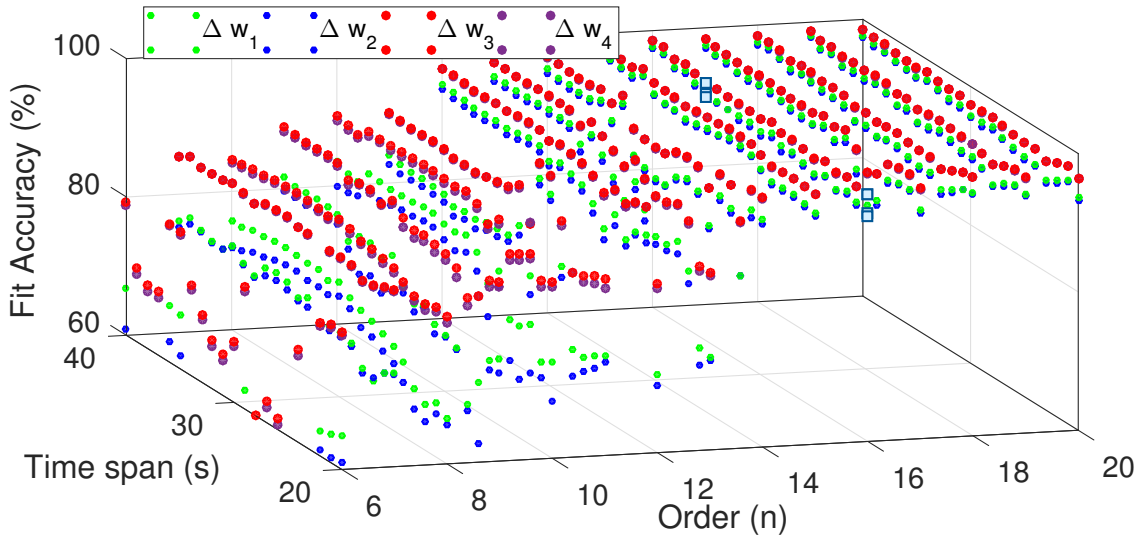

Figure 6.6: Fitting accuracy plotted as a function of order (n) of the estimated model and time span (in seconds) of data used for estimation

The fitting accuracy is the measure of how well the model estimate matches the actual measured output response. The fitting accuracy is expressed as:

$$Fit(\%) = (1 - \frac{|y - \hat{y}|}{|y - \overline{y}|}) \times 100 \tag{6.31}$$

Fitting accuracy of CVA identifier in estimating output response is plotted as discrete function of order(n) of estimated model and the window size (w_s) in seconds in Figure 6.6. 1 second correspond to 10 data samples. The plot shows fitting accuracy of four output signals i.e. slip of 4 synchronous generators, in z-axis, Order (n) of estimated model in x-axis and Window size along y-axis. The accuracy improves with increase in n and w_s. The achieved accuracy gain for increasing the order of estimation after n = 14 is very small.

6.3.1.2 Analysis of Computation Time

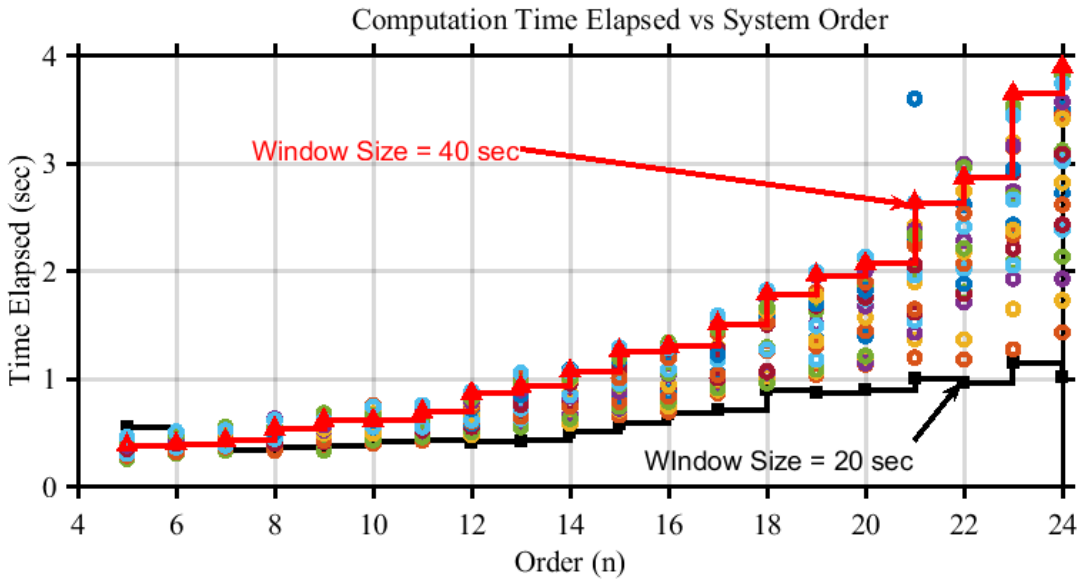

Figure 6.7: Computation time vs order of estimated size plotted for varying data window size (from 20 to 40 seconds)

The computation time required for state space model identification depends upon the value of n and w_s, and the computation power of the processor used. For the selected no. of inputs and outputs, Figure 6.7 shows the comparative analysis for computation time (t_{el}) against n for different w_s. t_{el} appears to be proportional to both n and w_s.

6.3.1.3 Selection of Order and Window Size

It should be noted that the increasing fitting accuracy always does not guarantee good model estimate because of overfitting. For example, the fitting accuracy for slip of generator G3 for model order 8, 13 and 16 using 30 seconds of measured input and output data are shown in Figure 6.8. The fitting accuracy for order 8

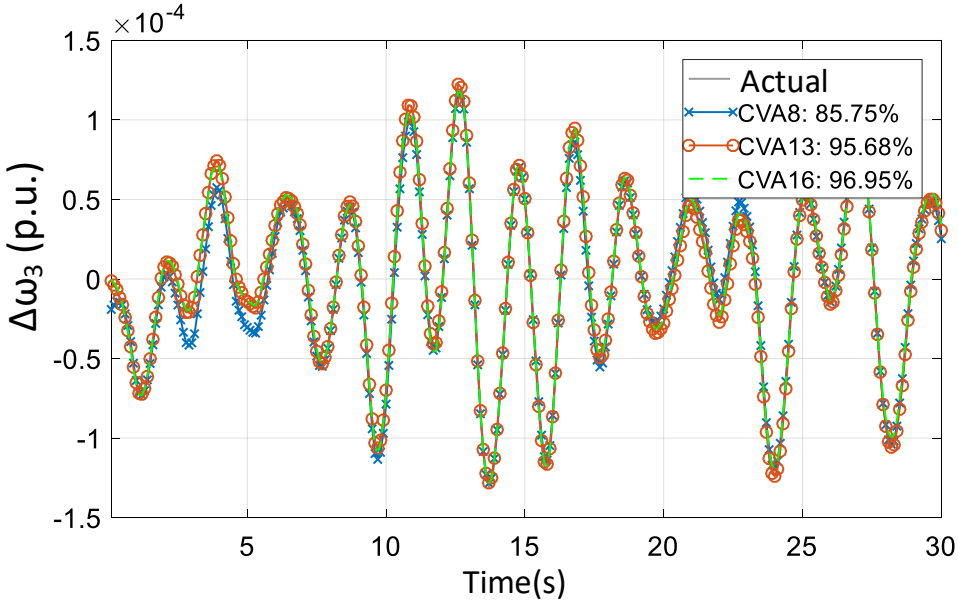

Figure 6.8: Comparison of Actual Output (slip of generator G3 Δw_3) and CVA Estimated Output using 8^{th}, 13^{th} and 16^{th} Order Identification.

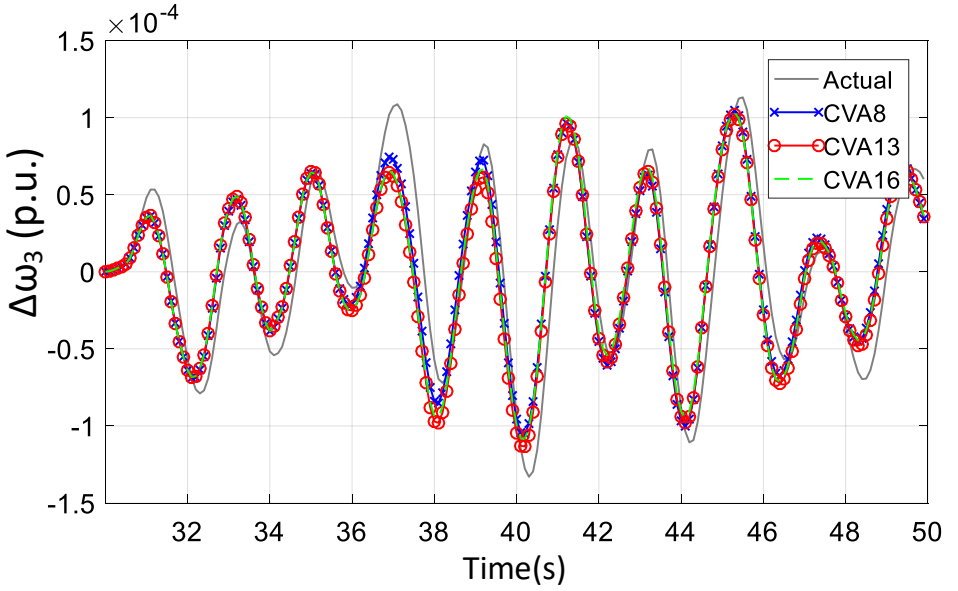

Figure 6.9: Validation of Estimated Model response against actual model response (Slip frequency of generator G3).

is 85.75% compared to order 16 fitting accuracy of 96.95%. The models are then validated against 20 seconds of measured input and output response which are not used in estimation as shown in Figure 6.9. The validation result shows the three different model fit the actual output data with very comparable accuracy. This infers that the lower 8^{th} order model successfully captured the dominant dynamics of the actual model as shown in Table 6.1. This statement can be further validated via bode response of the three estimated models against the actual model response as shown in Figure 6.10 where magnitude response of identified models of order 8, 13 and 16 are compared with actual system model.

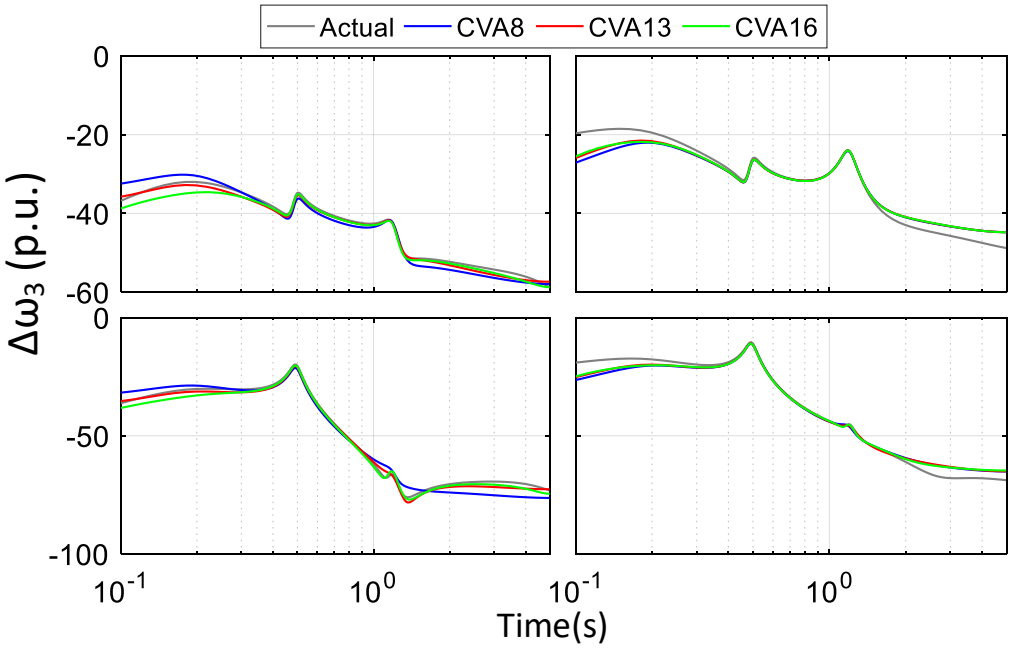

Figure 6.10: Bode Magnitude plot showing response of slip of generator G1 (upper) and G3 (lower) from supplementary active power P_{sc} and supplementary voltage V_{sc} of DFIG.

Table 6.1: Modes of Actual, Reduced and Identified Model

Mode	Actual		Reduced (n=12)		Estimated (CVA,n=8)	
No.	f (Hz)	$\zeta(\%)$	f (Hz)	$\zeta(\%)$	f (Hz)	$\zeta(\%)$
1	0.56	6.34	0.56	6.34	0.56	6.37
2	1.18	8.12	1.17	7.98	1.18	8.15
3	1.19	8.38	N/A	N/A	N/A	N/A

Table 6.1 shows the estimated modes and the modes of actual full order model and 8^{th} order reduced model. The inter-area mode and the area 1 local mode were retained by the reduced order model as well as CVA identified model with comparable accuracy. The reason behind the inability to retain area 2 local mode can be touted to the low residue in transfer function between the input perturbation at bus 6 DFIG to the measured output signals of area 2 i.e. slip of generators G3 and G4.

6.3.2 Model 2

The observability of the modes can be estimated by looking at the natural mode-shape of the inter-area modes. This system has four inter-area modes two of which are poorly damped. The slip frequency of generators G5, G13, G14, G15 and G16 are selected as the representative output signals because of the high observability of the inter-area modes which are of interest during power oscillation damping controller design [76]. The natural mode shape of slip frequency of 16 generators are shown in Figure 6.11. Similarly, the geometric controllability of the modes via available

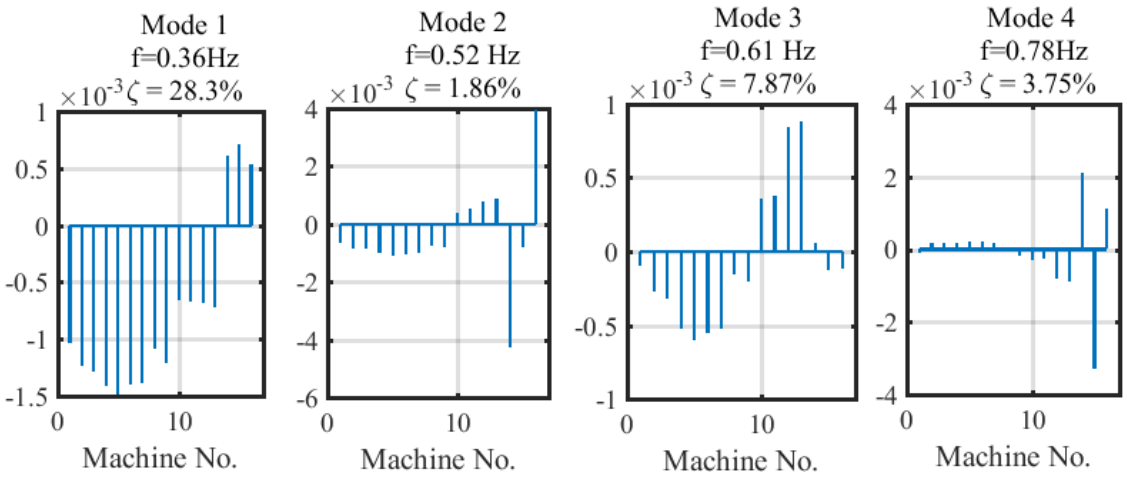

Figure 6.11: Natural Mode shape of inter-area modes corresponding to slip frequency of 16 generators

control inputs i.e. supplementary control loop for active and reactive power of DFIGs located at bus 30, 42 and 51, were computed to measure the controllability of the modes. The controllability of two least damped inter-area modes i.e. Mode 2 and

mode 4 are shown in Figure 6.12. The input signals that are perturbed with random

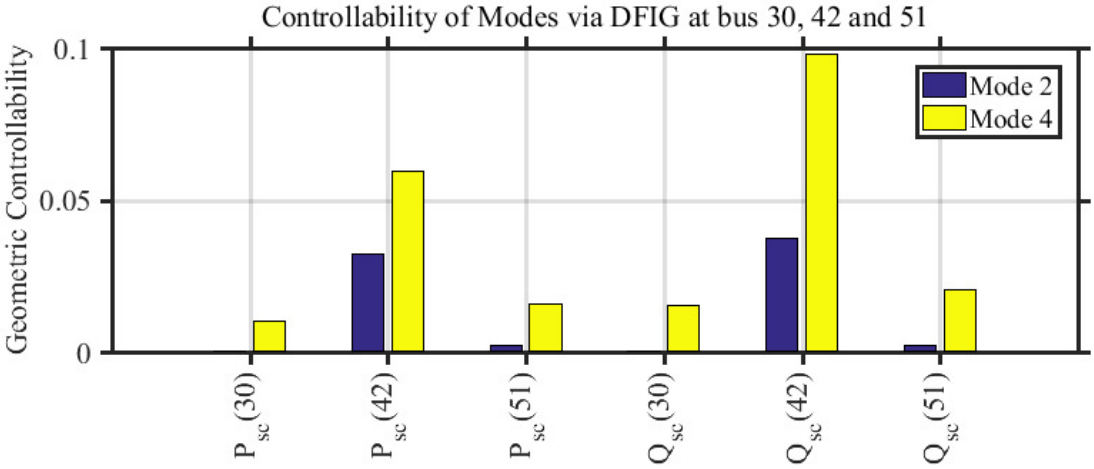

Figure 6.12: Controllability of Mode 2 and Mode 4 via active and reactive power modulation of DFIGs at bus 30, 42 and 51.

Gaussian white noise with zero mean are the active and reactive power reference of DFIGs in bus 30 , 42 and 51. In this test, the simulation was run for 70 seconds and the input and output data were collected every 0.1 seconds.

6.3.2.1 Analysis of Fitting Accuracy

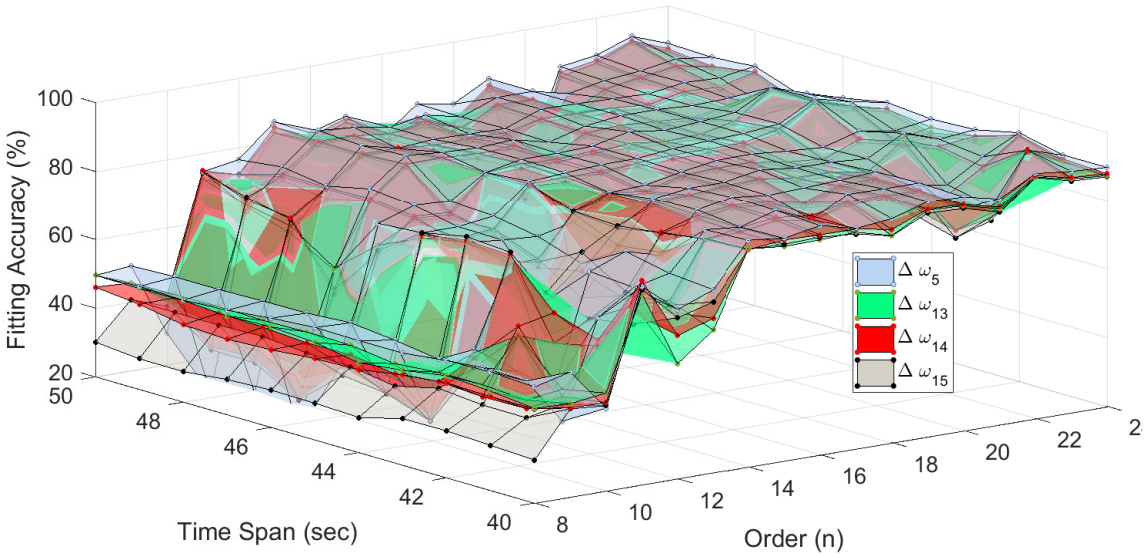

Figure 6.13: Fitting accuracy plotted as a function of order (n) of the estimated model and time span (in seconds) of data used for estimation

The fitting accuracy of slip speed of generator G3, G13, G14 and G15 is shown in Figure 6.13 for varying order of estimated model (n) from 8 to 25 and window size from 40 seconds to 50 seconds. The fitting accuracy increases with increase in n of estimated model, but the improvement is fairly minimal after $n = 14$. On the other hand, the fitting accuracy is fairly same for window size of 40 seconds to 50 seconds.

6.3.2.2 Analysis of Computation Time

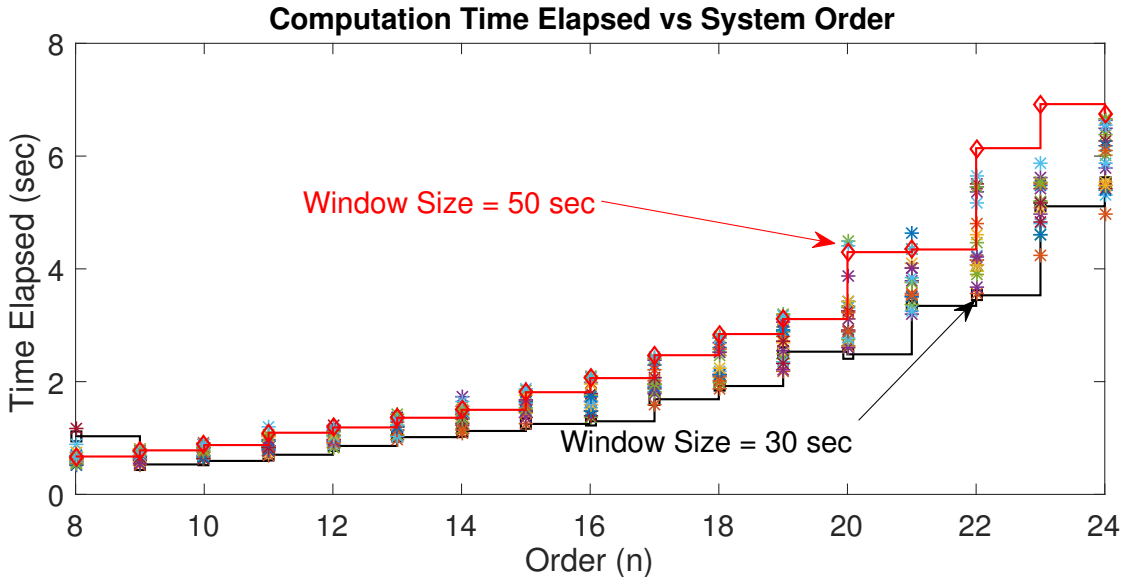

Figure 6.14: Computation time vs order of estimated size plotted for varying data window size (from 30 to 50 seconds)

The computation time required for state space model identification depends upon the value of n and w_s, and the computation power of the processor used. For the selected no. of inputs and outputs, Figure 6.14 shows the comparative analysis for computation time (t_{el}) against n for different w_s. t_{el} appears to be proportional to both n and w_s.

6.3.2.3 Selection of Order and Window Size

First 40 seconds of the data sample are used to estimate the plant model and the remaining 30 seconds data sample are used to validate the identified model. The

output response of the estimated model of order $n = 12$, 14 and 16 with fitting accuracy $\approx 62\%$, 8.% and 84% respectively are shown in Figure 6.15. The identified

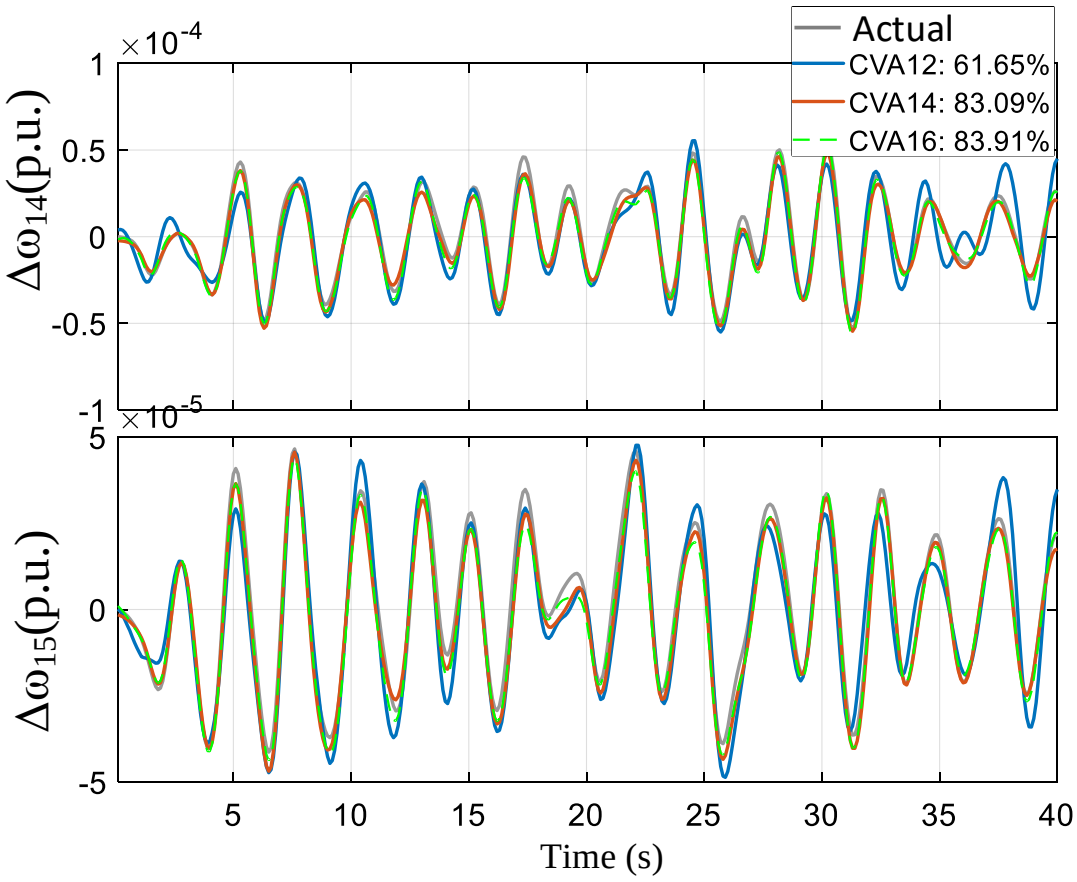

Figure 6.15: Actual and Estimated Output Response for $n = 12$, 14 and 16. (slip speed of generators G14 at the top and G15 at the bottom)

models are validated with validation data set in Figure 6.16. The 12^{th} order model captured the dominant inter-area modes, however, the fitting accuracy is $\approx 60\%$. The estimation accuracy of 14^{th} and 16^{th} order model are very similar at $\approx 85\%$. The improvement in estimation accuracy is minimal for $n \geq 16$. The bode magnitude plot in Figure 6.17 shows the close match between the frequency response of 16^{th} order CVA identified model with actual linearized full order model specifically at the frequency range of the system's inter-area modes. Increasing the order of the identified system to 20 did not yield any significant improvement. Thus, the order n

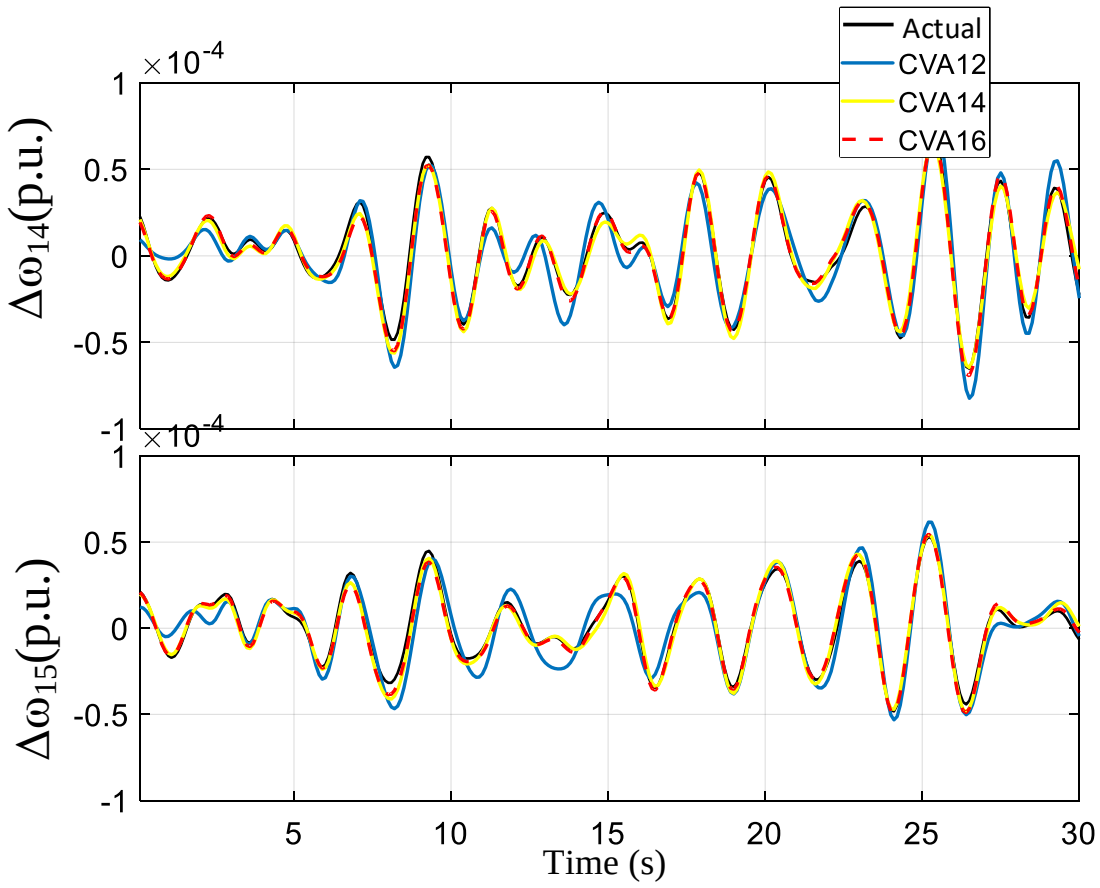

Figure 6.16: Validation of Identified Power System Model against Actual System Response. (slip speed of generators G14 at the top and G15 at the bottom)

= 16 is chosen for our study to test the performance of proposed controller.

Table 6.2: Inter-area Modes of Actual and Estimated Model

Mode	Actual		Estimated (CVA, n=16)	
No.	f(Hz)	$\zeta(\%)$	f(Hz)	$\zeta(\%)$
1	0.35	28.33	0.36	25.07
2	0.51	1.86	0.52	1.84
3	0.61	7.87	0.61	6.63
4	0.75	3.75	0.75	3.65

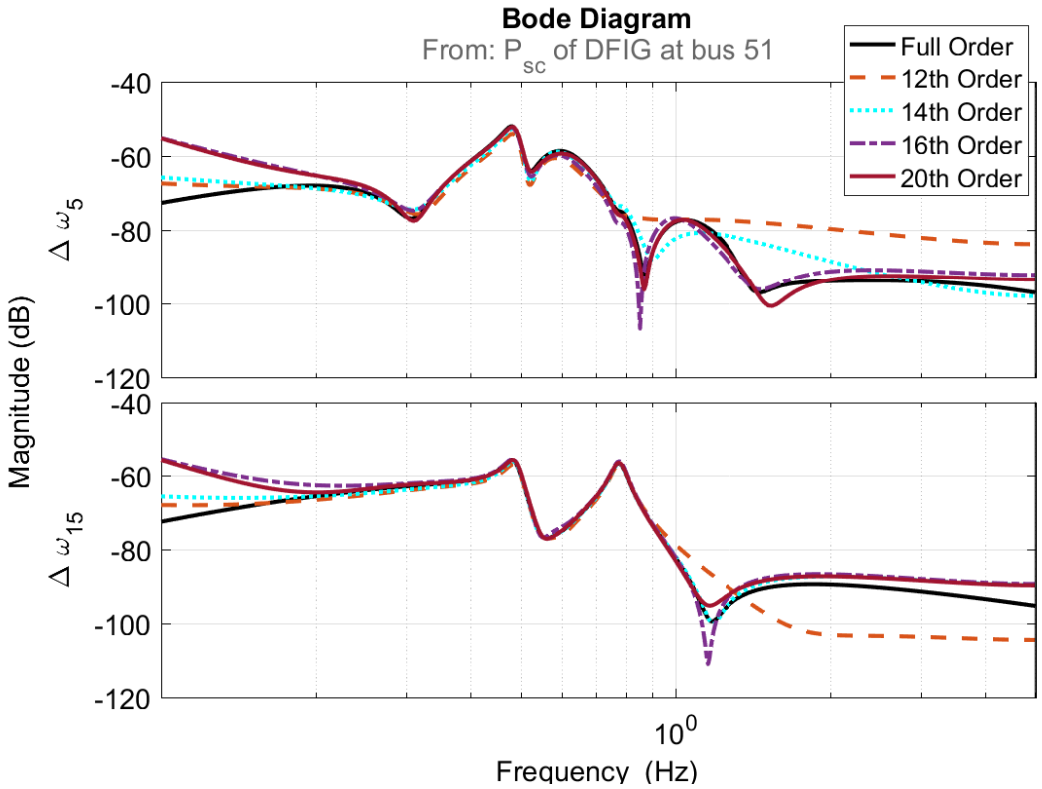

Figure 6.17: Frequency Response of Identified Model with n = 12, 14, 16, and 20 compared with Actual Model. The outputs are slip speed of generator G5 and G15 and input is supplementary power controller reference of DFIG at bus 51.

The 16^{th} order estimated model successfully identified the four dominant inter-area modes of the system including their frequency and damping ratio as shown in Table 6.2. The window size was chosen at w_s = 40 second because the improvement for increasing window size was found to be fairly minimal.

6.4 Simulation Results

Based on identified models of suitable order, output feedback gain matrix is optimized using SQP algorithm as discussed in section 6.2.2. The optimized feedback gain is implemented in actual system and the results are presented in this section.

6.4.1 Model 1

Two different approaches for optimal oscillation damping control (OODC) design are presented in this section for Model 1. First approach does not penalize the use of certain input over the others. The second approach creates a scenario for penalizing

the use of certain input over the another so that the input with lower cost is highly utilized during control.

6.4.1.1 First Approach

First, we present the effectiveness of the design methodology on two-area system by control design using cost function as given by 6.24. This does not penalize the inputs. This gives the best possible gain matrix to achieve the desired damping ratio of the inter-area modes. Note that only inter-area mode is targeted for this control design. Since our test system has one inter-area mode, we set the cost function as:

$$J_1^1 = |10 - \zeta_{iam}|$$

$$J_1^2 = |15 - \zeta_{iam}|$$

Here, J_1^1 tries to make the inter-area mode damping to 10% and J_1^2 tries to make the inter-area mode damping to 15%. The gain matrices are computed by solving the optimization problem using MATLAB Optimization Toolbox. The convergence of a solution of J_1^1 and J_1^2 are shown in left plot of Figure 6.18. The eigenvalues of the system without controller and with controller based on cost function J_1^1 and J_1^2 are shown in right plot of Figure 6.18. The computed gain matrices are:

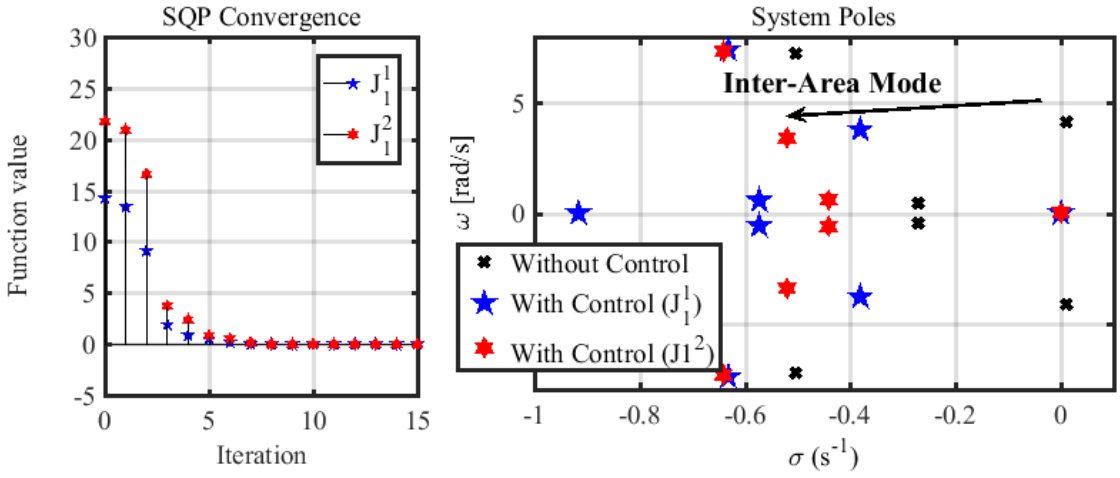

Figure 6.18: Convergence of SQP optimization and trajectory of modes of the system.

$$K_1^1 = \begin{bmatrix} 3.6409 & 5.5225 & -3.1522 & -2.2989 \\ -5.3634 & -9.2326 & 9.8545 & 7.8258 \end{bmatrix}$$

$$K_1^2 = \begin{bmatrix} 7.2576 & 7.9286 & -6.6406 & -5.0942 \\ -9.1434 & -11.4947 & 12.9123 & 10.7049 \end{bmatrix}$$

The eigenvalue plot in Figure 6.18 shows that both local area and inter-area mode damping were improved by implementing the proposed controller. The controller with J_1^2 provides better damping of inter-area mode compared to controller with J_1^1. Time domain simulation is performed to validate this.

The system was subjected to different faults to test the controller performance. Two of the selected fault scenarios and the results are presented.

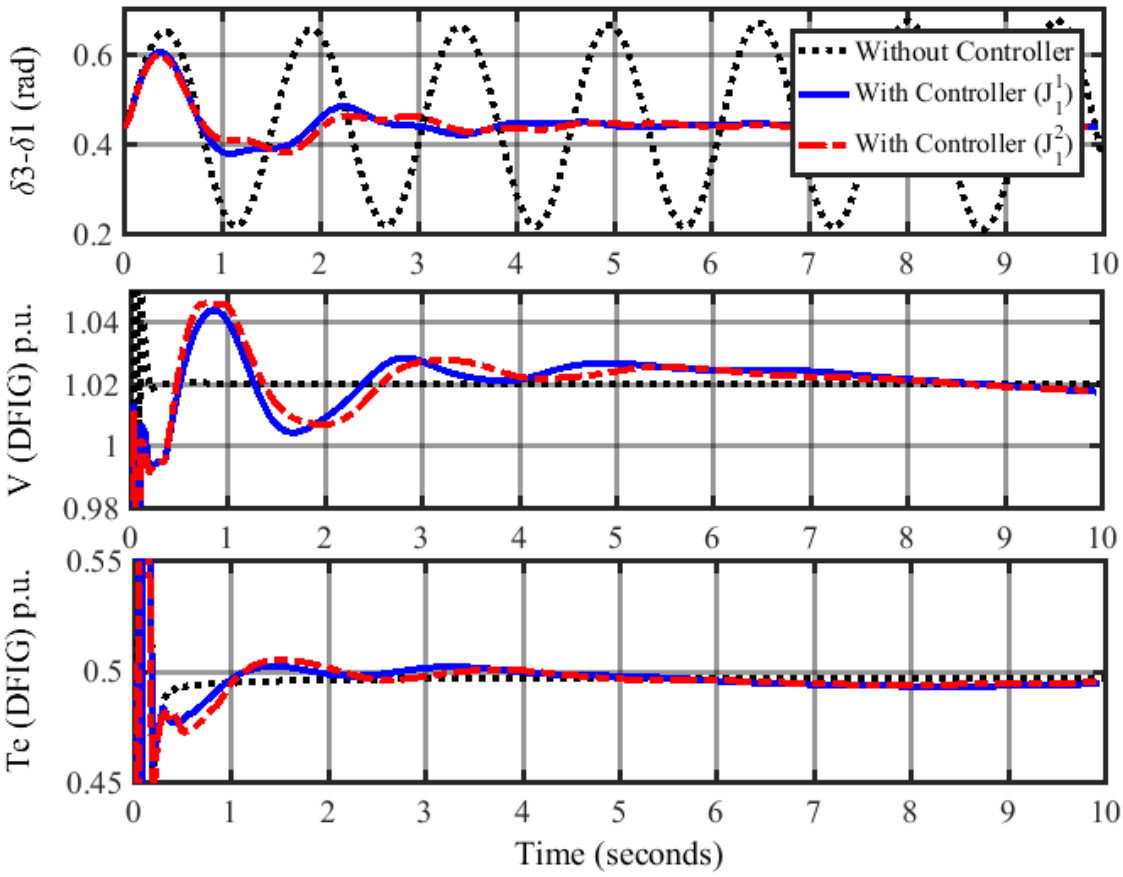

Figure 6.19: Comparison of open loop and closed loop response with J_1^1 and J_1^2 during 10 cycles fault naturally cleared 3L-G fault in bus 8 (Fault 1).

Fault 1: A 3phase line to ground fault is applied on bus 8 for 66 ms and cleared naturally to excite the inter-area mode of oscillation between area 1 and area 2. To illustrate the performance of OODC *first approach* which considers two different objective functions J_1^1 and J_1^2 yielded gain matrices K_1^1 and K_1^2, the results are shown in Figure 6.19.

The difference between angle of bus 3 and bus 1 was selected to observe the inter-area mode. Terminal voltage and electro-magnetic torque of DFIG in p.u. are also shown to illustrate the control action and its impact on DFIG. System is unstable when no OODC is implemented in DFIG. The proposed controller with J_1^1 and J_1^2 damped the post-fault oscillation. J_1^2 damps the oscillation faster than J_1^1.

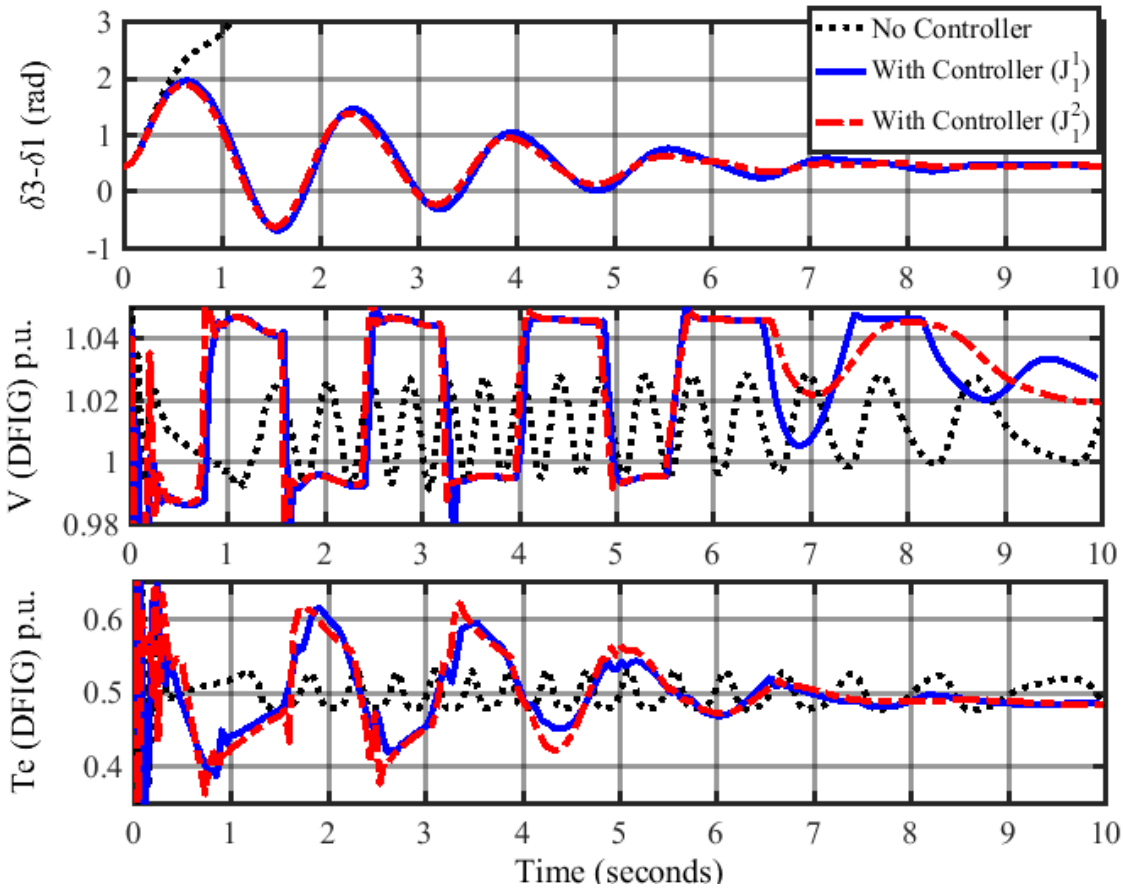

Figure 6.20: Comparison of open loop and closed loop response with J_1^1 and J_1^2 during 200 ms naturally cleared 3L-G fault in bus 8 (Fault 2).

Fault 2: A 3phase line to ground fault is applied on bus 9 for 200 ms and cleared

naturally to excite the inter-area mode of oscillation between area 1 and area 2. This example is useful to analyze the control performance and the system response during saturation. It should be noted that the OODC output is limited within ± 0.1 p.u. for P_{sc} and ± 0.03 p.u. for V_{sc}.

Figure 6.20 shows the performance of OODC *first approach*. Due to the nature of this transient resulting in high magnitude oscillation in measured outputs, the outputs of OODC are saturated. While the open-loop system is unstable as can be seen from increasing separation between the angles of bus 3 and bus 1, the system is transient stable when proposed OODC is implemented. Despite the saturation, the oscillation is damped and damping is better with J_1^2 than J_1^1.

6.4.1.2 Second Approach

In this design approach, the cost function defined in equation 6.25 is first used to compute the gain matrix. Since our test system has one inter-area mode, we set the cost function as:

$$J_2^1 = |10 - \zeta_{iam}| + \sum_{j=1}^{2} R1 \sum_{k=1}^{4} |K_y(j,k)|$$

$$J_2^2 = |10 - \zeta_{iam}| + \sum_{j=1}^{2} R2 \sum_{k=1}^{4} |K_y(j,k)|$$

where

$$R1 = \begin{bmatrix} 0.1 \\ 0 \end{bmatrix}, \qquad R2 = \begin{bmatrix} 0 \\ 0.1 \end{bmatrix}$$

Here, J_2^1 penalizes use of P_{sc} more via $R1$. This can be used in scenarios where the torsional dynamics of DFIG are poorly damped or vulnerable to oscillation, and modulation of active power can excite those oscillations. On the other hand, J_2^2 penalizes use of V_{sc} more. This is true in certain scenarios where tight control of

terminal voltage is required. The target damping ratio is 10% in both cases.

The computed gain matrix are shown below:

$$K_2^1 = \begin{bmatrix} 0.0000 & -0.0003 & -0.0002 & -0.0000 \\ -11.0547 & -8.9156 & 13.0435 & 9.1024 \end{bmatrix}$$

$$K_2^2 = \begin{bmatrix} 18.4797 & 18.5048 & -21.0276 & -17.0862 \\ 0.0027 & -0.0012 & 0.0020 & 0.0011 \end{bmatrix}$$

In order to validate the control performance and system response with the controller, different faults scenarios were considered. The results are presented for the two fault scenarios that were discussed in *First Approach*.

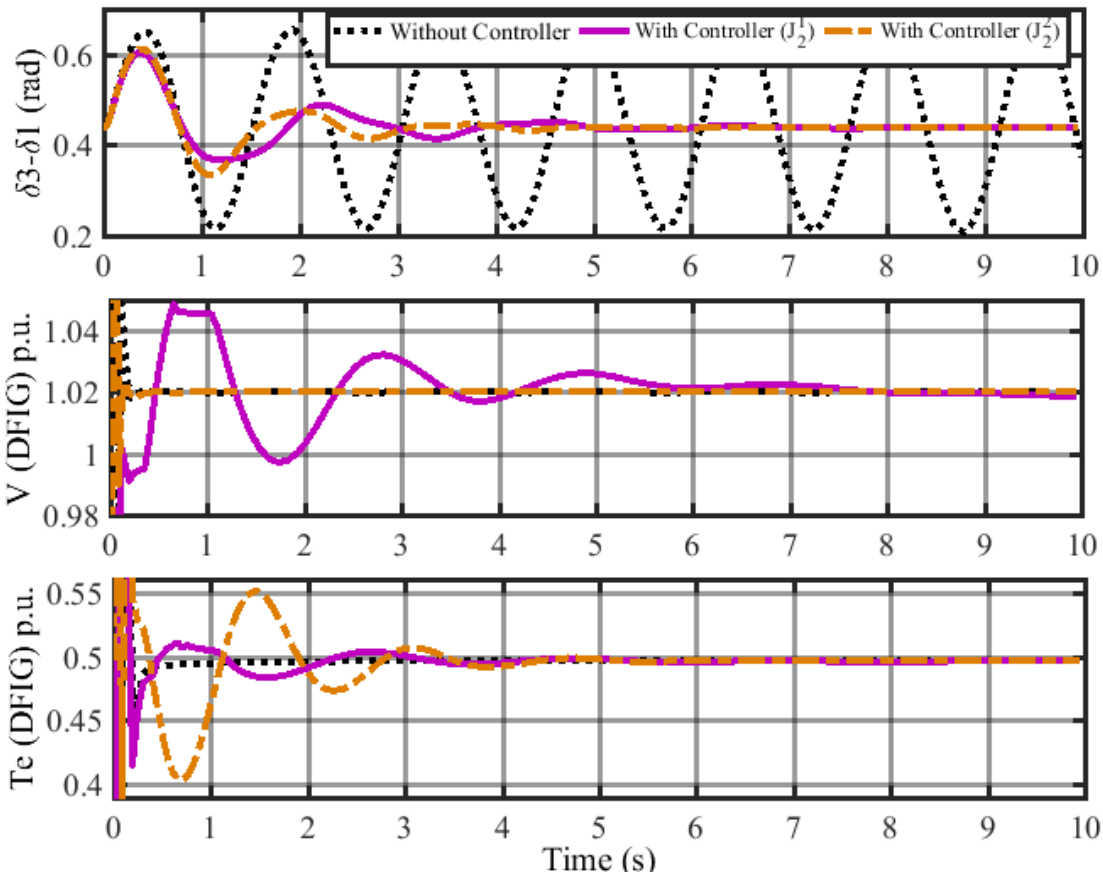

Figure 6.21: Comparison of open loop and closed loop response with J_2^1 and J_2^2 during 10 cycles fault naturally cleared 3L-G fault in bus 8 (Fault 1).

Figure 6.21 shows the performance of OODC *second approach* which considers two objective functions as J_2^1 and J_2^2 and yields gain matrices K_2^1 and K_2^2. Again, the post-fault system oscillation is damped with the OODC. Since J_2^1 penalized the use of P_{sc}, only V_{sc} is modulated for damping purpose. Oscillation in Te of DFIG is due to the voltage oscillation introduced by OODC, and not because of OODC modulating P_{sc}. On the other hand, J_2^2 penalizes the use of V_{sc}, and OODC only modulates P_{sc}. The objective of damping the inter-area oscillation has been fulfilled in both cases.

Figure 6.22 shows the response of OODC *second approach* during Fault 2. The system has been stabilized post-fault with both J_2^1 and J_2^2. The OODC saturation is observed in V_{sc} and T_e when gains K_2^1 and K_2^2 are used respectively. The pulse in T_e is observed in OODC J_2^1 due to changes in DFIG voltage.

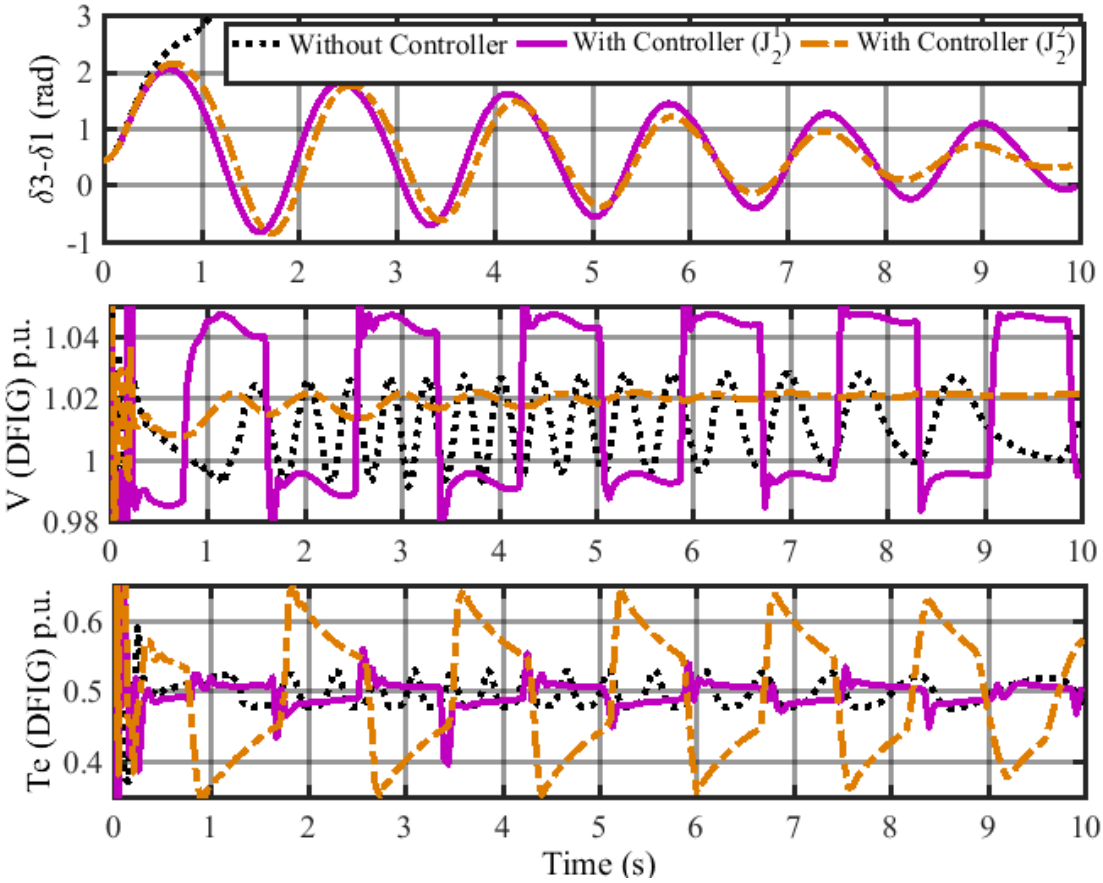

Figure 6.22: Comparison of open loop and closed loop response with J_2^1 and J_2^2 during 200 ms naturally cleared 3L-G fault in bus 8 (Fault 2).

This approach infers that the by manipulation of active power or reactive power or both, the damping criteria can be successfully achieved. This approach provides the flexibility to assign oscillation damping effort to active power and reactive power controller by merely changing the input vector R in the cost function given by 6.25.

6.4.2 Model 2

Similar to Model 1, two different approaches for control design will be discussed in this section. The first approach only includes the damping criteria, and penalizes all the control inputs equally. The second approach creates a penalty based approach which penalizes different generators (DFIGs) with different cost to demonstrate the flexibility of meeting the damping criteria by utilizing the generators with cheapest cost.

6.4.2.1 First Approach

This approach is similar to the first approach described for Model 1. The cost function given by 6.24 is used. Since there are three modes with damping less than 10%, the number of of critical modes $n_{cr} = 3$ and the cost function is represented as:

$$J_1 = \sum_{i=1}^{3} |10 - \zeta(i)|$$

The eigenvalues of the system with and without the OODC with cost function J_1 is shown in Figure 6.23. The plot shows that all the inter-area modes have damping of at least 10% as shown by the 10% damping line.

Non-linear time domain simulation of the system with 10 cycle 3ph-ground fault applied at bus 49 is performed to analyze the the controller performance in improving the damping of the dominant inter-area modes. The results are shown in Figure 6.24. The result shows that that the oscillation is damped faster with proposed controller implemented on DFIGs located at bus 30, 42 and 51. In order to validate that the expected damping of 10% is achieved, the time domain data was analyzed using

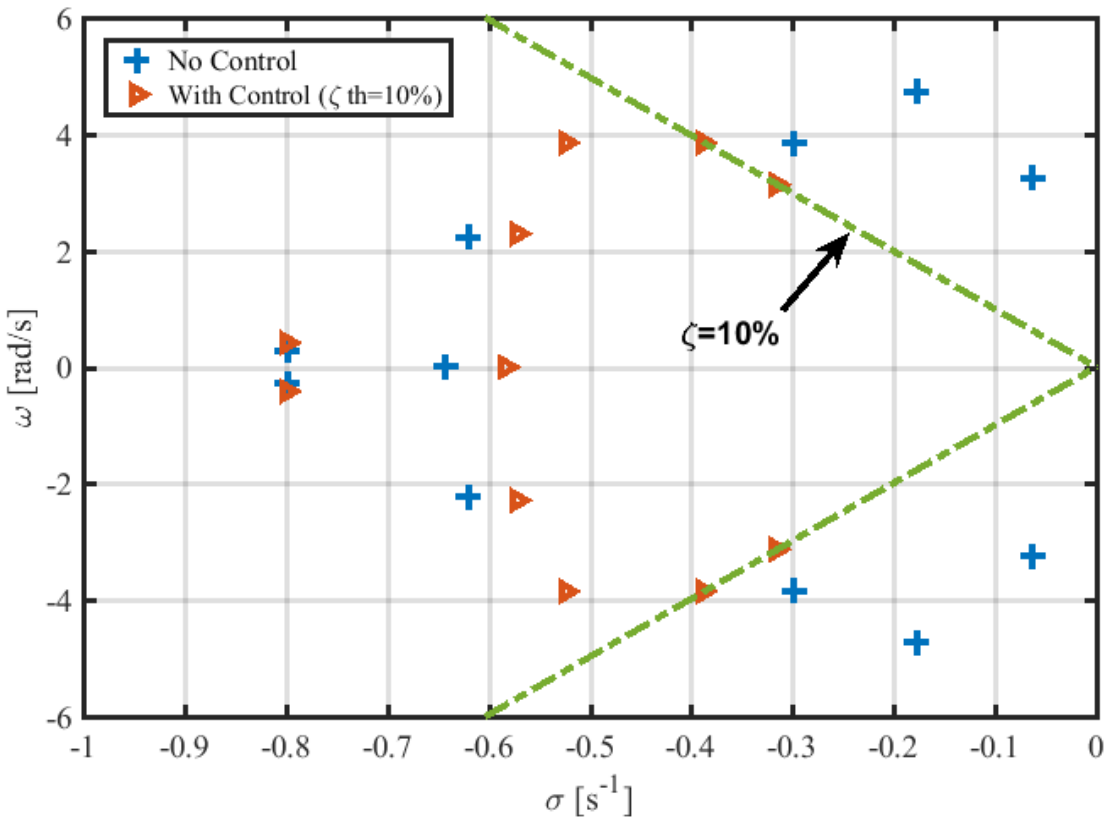

Figure 6.23: Eigenvalues of the system with and without OODC.

'*Prony*' method as shown in Table 6.3. The damping of the modes estimated by prony

Table 6.3: Prony Analysis of 68-bus system

Without Control		With Control	
Frequency (Hz)	Damping (%)	Frequency (Hz)	Damping (%)
0.51	2.41	0.51	9.68
0.75	4.19	0.61	9.85

are very close to 10% which verifies that the controller was successful in achieving the desired damping performance. The output active and reactive power of DFIG at bus 51 are shown in Figure 6.25. The oscillation in active power seen in the case of no controller is due to the inherent oscillation in the system which are poorly damped. The contribution of reactive power seems much higher compared to active power.

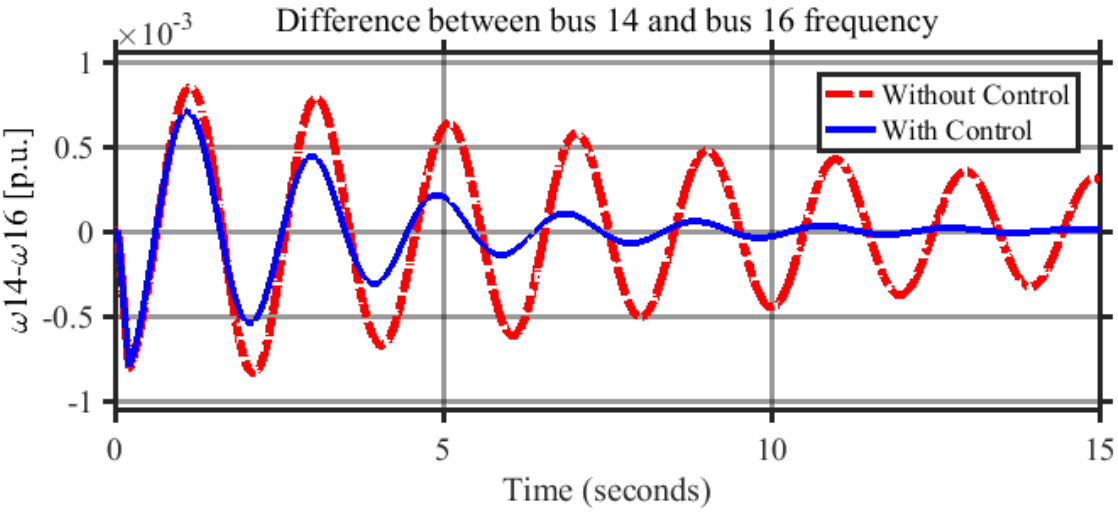

Figure 6.24: The difference between bus 14 and bus 16 frequency with and without the controller following 3phase-ground fault in bus49.

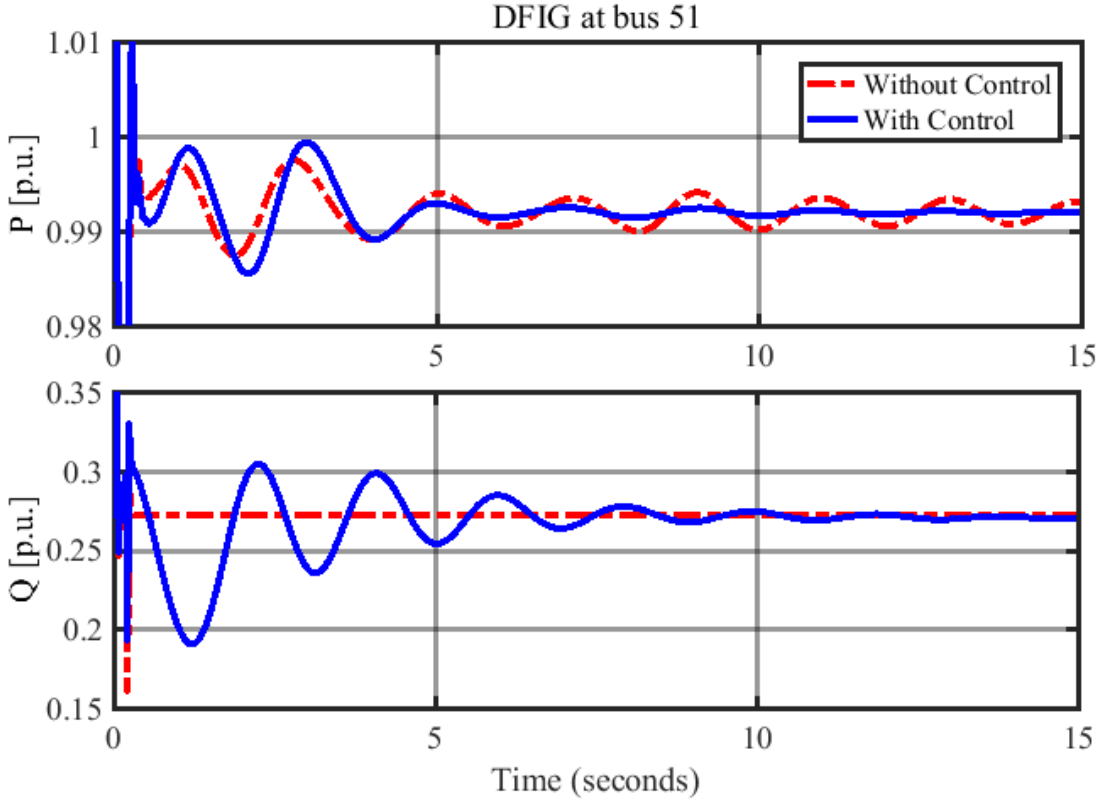

Figure 6.25: Output active and reactive power of DFIG at bus 51 with and without the controller.

6.4.2.2 Second Approach

In this approach, cost function given by 6.25 is used to show the controller flexibility in the sense that the similar damping performance can be achieved in different cost scenarios. The input weightage vector R is varied as given below:

$$R_1 = \begin{bmatrix} 0 & 0 & 0 & 0 & 0 & 0 \end{bmatrix}^T, R_2 = \begin{bmatrix} 1 & 0 & 1 & 1 & 0 & 1 \end{bmatrix}^T, R_3 = \begin{bmatrix} 1 & 1 & 0 & 1 & 1 & 0 \end{bmatrix}^T$$

where, first three elements correspond to the active power modulation of DFIGs at bus 30, 42 and 51 respectively and last three elements correspond to the reactive power modulation of DFIGs at bus 30, 42 and 51 respectively. Correspondingly,

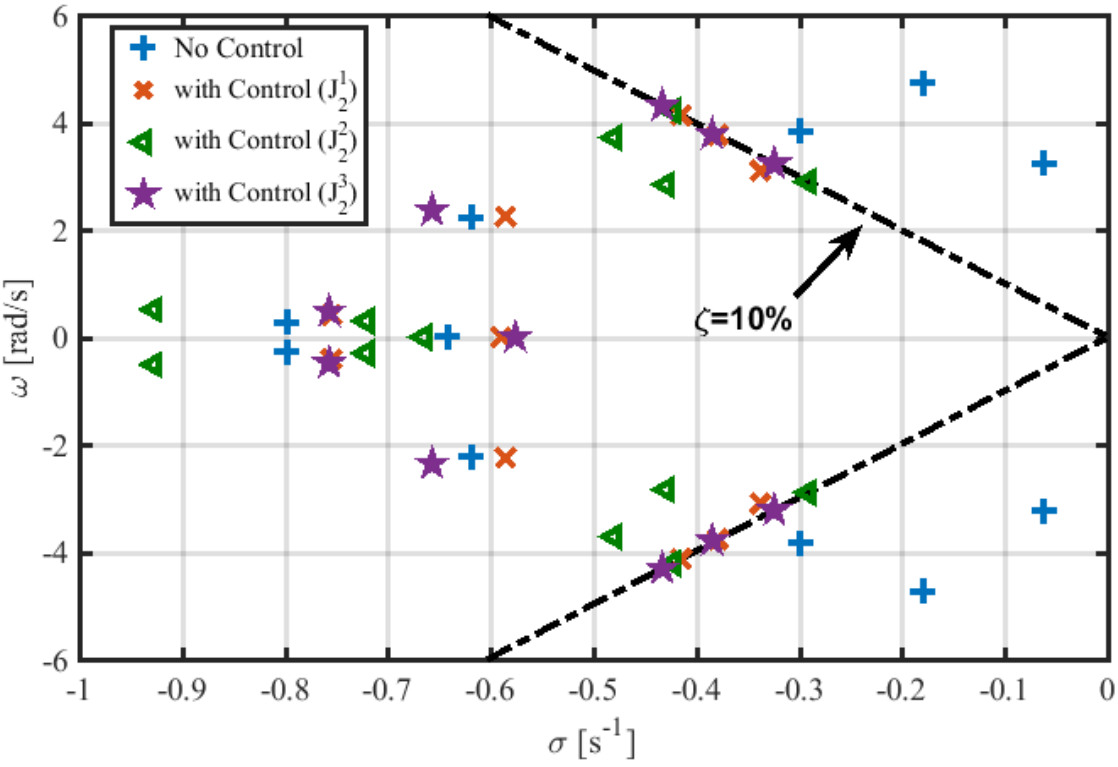

Figure 6.26: Eigenvalues of the open loop and closed loop systems

three cost functions are formulated and represented respectively as J_2^1, J_2^2 and J_2^3. The solution of the non-linear optimization using sequential quadratic programming

yield three different output feedback gain matrices K_2^1, K_2^2 and K_2^3 respectively.

The eigenvalues of the closed loop system with gain matrices K_2^1, K_2^2 and K_2^3 are plotted against the eigenvalues of the open loop system in Figure 6.26. The figure shows that the minimum damping criteria of 10% has been successfully achieved by each of the three gain matrices. The black dashed line represents the 10% damping.

Non-linear time domain simulation of the system with 10 cycle 3ph-ground fault applied at bus 49 is performed to analyze the the controller performance in improving the damping of the dominant inter-area modes. The difference between angular frequency of bus 14 and bus 16, and difference between angular frequency of bus 13 and bus 5 were monitored to observe the inter-area oscillation as shown in Figure 6.27.

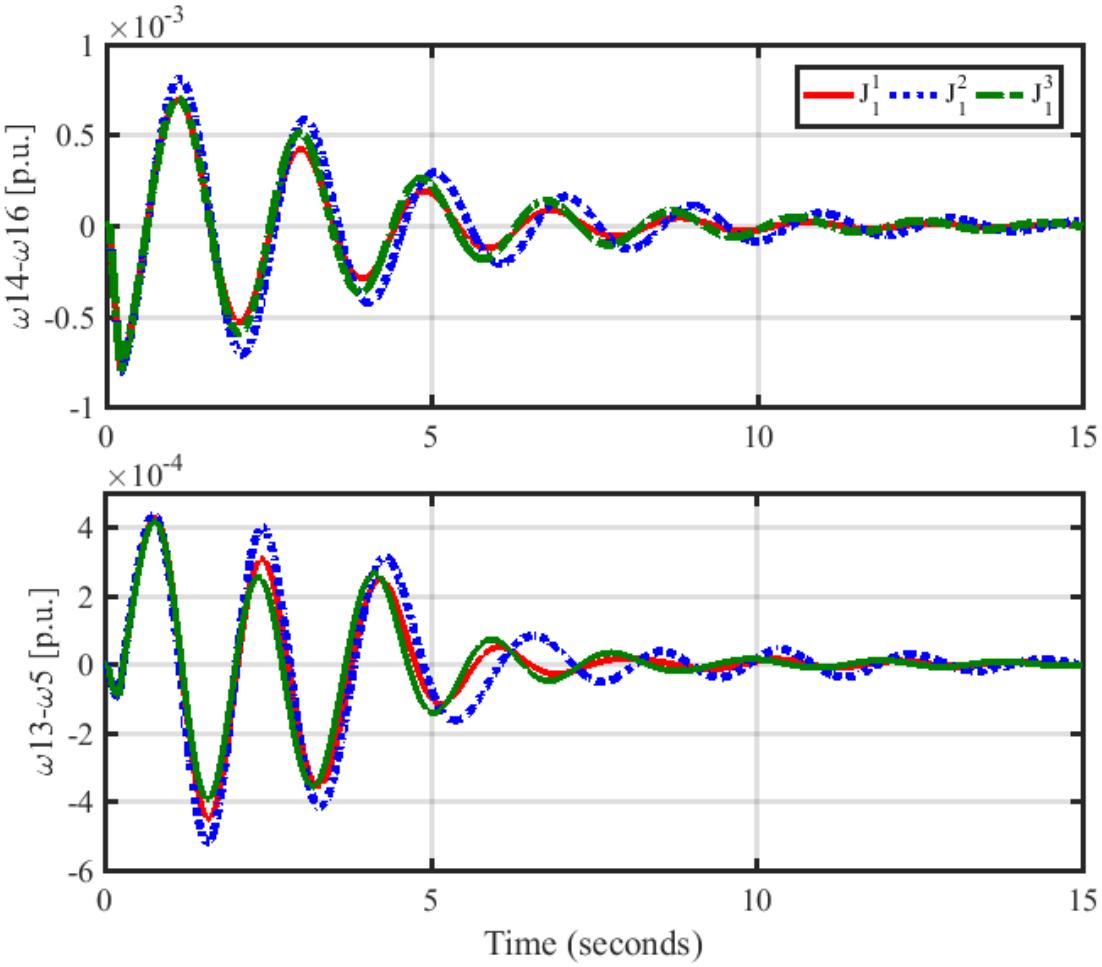

Figure 6.27: Comparison of system response to 3ph-ground fault applied at bus 49.

The system response infers that the oscillations are well damped in all three cases. However, the damping is comparatively better with J_2^1 and J_2^3 over J_2^2. More important would be analyze the contribution of three DFIGs connected at bus 30, 42 and 51 which are shown in Figure 6.28. When the objective function does not include

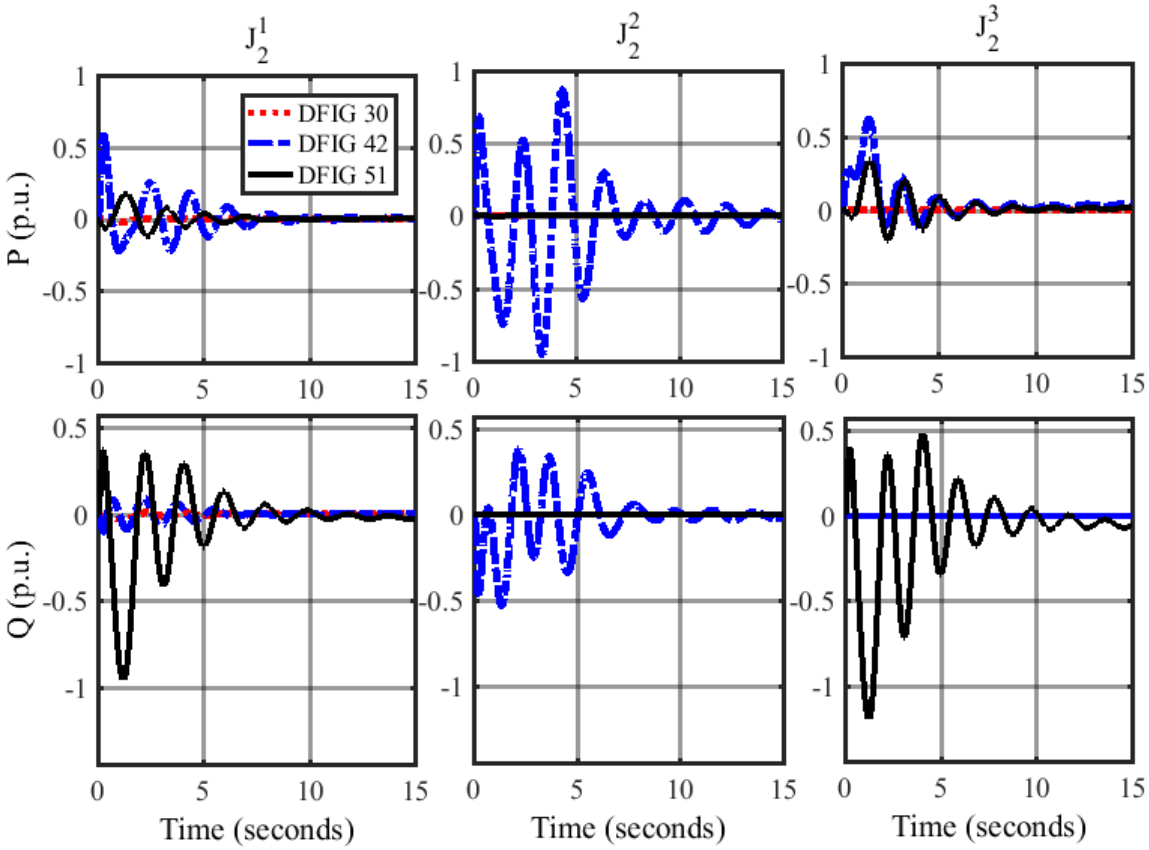

Figure 6.28: Active and Reactive power output of DFIGs at bus 30, 42 and 51 corresponding to feedback gains K_2^1, K_2^2 and K_2^3 following 3ph-ground fault at bus 49.

the cost of input i.e. J_2^1, the gains are assigned optimally to achieve the damping requirement. It is worth noting that the two generators located at bus 42 and 51 are contributing higher in damping the oscillation owing to their higher controllability of the modes 2 and 4. The DFIG at bus 30 has the least contribution. On the other hand, J_2^1 penalized the use of DFIGs at bus 30 and 51, forcing higher contribution of DFIG at bus 42, which can be inferred from the higher modulation of its active and reactive power. The contribution of other two generators are negligible in this

case. Similarly, J_2^3 penalized the use of DFIGs at bus 30 and 42 forcing maximum contribution from DFIG at bus 51.

The results show that this approach can be used to flexibly assign damping contribution among available generators based upon their capability, location, and controllability.

6.5 Summary

In this chapter, the design of optimal output feedback control design for modulation of active and reactive power/voltage of dfig has been presented. The optimization of the feedback gain is obtained by sequential quadratic programming (SQP). The feedback gain matrix optimization is based on state space identification of power system model using canonical variate analysis (CVA). CVA estimates the state space model of the system from uniformly sampled input and output measurement. The controllers are tested in DFIG integrated 11-bus, 2-area system and 68-bus, 5-area system. Following conclusion can be drawn based on the results and analysis presented in this chapter:

- The damping of the targeted inter-area modes can be enhanced via dfig active and reactive power modulation using proposed optimal output feedback control.

- The controller can be designed based on identification state space model. Since it is not easy to obtain accurate model of the system, the proposed CVA algorithm for state space model identification can be used to obtain a reduced order model of the power grid. The model can be used to design the controller as presented in this chapter. The identified model was successfully validated against the actual model via validation data set, frequency response and modal analysis. This technique can be used to track the accurate estimate of the system when the system operating point changes.

- The sequential quadratic programming can be used to obtain the optimal gain

matrix that maximizes the damping of targeted modes without violating the specified constraints.

- Flexible distribution of oscillation damping effort among available generators location and controllability can be achieved using the approaches discussed in this chapter.

CHAPTER 7: CONCLUSIONS AND FUTURE WORKS

7.1 Conclusions

In this work, the dynamic model of DFIG, which includes electrical transients of the generator and mechanical dynamics of the rotor/turbine, was first developed to study small signal stability of DFIG, and the DFIG behavior with the controller was distinguished from the open loop case. Modal analysis was used to formulate analytical interpretation of the results and were verified with non-linear time domain simulation. The sensitivity of the DFIG's oscillatory modes with respect to the turbine and machine parameters was studied to understand and identify the key modes of interest. The sensitivity analysis of the DFIG closed loop modes with respect to controller parameters provided an insight on choosing the appropriate controller gains to meet the performance requirements. Later, the DFIG model is incorporated into the power system models such as 11-bus system and 68-bus systems to simulate the penetration of DFIG based wind generation on the power grid. The participation factor analysis, observability analysis, and time domain analysis of DFIG integrated power system model showed that DFIGs do not introduce new electromechanical mode into the system. DFIG acts as dynamic power source, thanks to the converters with rapid active and reactive power control capability. The electromechanical modes of the system are, however, affected by increasing DFIG penetration in many ways such as replacing synchronous generators, reducing number of PSS, changing power flow in tie-lines, reducing system inertia and so on.

The growing level of renewable resources such as wind and solar that are usually interfaced with the grid using voltage source converters (VSC) ultimately leads to reduction of system inertia. Moreover, the power system dynamics are affected

by these resources, and sometimes drive the system towards instability. The Transmission System Operators (TSO)s/ and Independent System Operators (ISO)s will eventually require DFIG based wind farms and other renewable generators to support the damping of system oscillation. The advantage of these resources over the conventional generators is their ability to control active and reactive power rapidly. In this work, two types of approach have been used to design control for damping the oscillation in the grid. First approach is decentralized approach based on local measurement and are termed as PSS of DFIG analogous to PSS of generators. The advantage of this approach is that it is robust, reliable and do not require wide area communication between remote generators/equipment or control center. DFIG offers ability to control stator active and reactive power using RSC, and GSC control. This can be used to manipulate active and reactive power injection from GSC side. The concept of geometric modal observability and controllability was used to select the best available output and input pair. The signals such as bus frequency, angle or power injected in neighboring transmission lines show better visibility of those modes, and thus are the potential local signals that can be used for PSS design. While active power control can provide damping torque directly, the reactive power can also influence the production of damping torque and thus can be utilized to damp the electromechanical oscillation. The modulation of active power of DFIG affects the torsional dynamics of the wind turbine and generator rotor shaft, while reactive power modulation affects the voltage of the line. Modal controllability analysis and non-linear time domain analysis can aid in selection of the best control signal.

The major disadvantage of the decentralized approach is the limited observability of inter-area modes in the local measurement signals. This has been demonstrated in 68-bus system where DFIG PSS at bus 13 had limited impact on inter-area modes. The recent advancement in PMUs has resulted in realization of wide area control of power system. In this work, wide area signal are used to control active and reactive power

of available DFIGs. Control of DFIG based on Linear-Quadratic Gaussian technique was developed and its efficacy in enhancing oscillatory stability of the power system was shown using modal analysis and non-linear time domain simulation in small scale as well as larger scale power system model. LQG is a linear quadratic regulator (LQR) implemented with a state observer (Kalman Filter). The state observer is required because measuring all the states of a system as big and complex as modern power grid is not practically possible. Reduced order model of the power system is used to design a Kalman filter. The model reduction allows reduction in computation burden while maintaining the accurate representation of power system relevant dynamics. It is up to the control designer to select the most appropriate weights to the states and inputs to obtain optimal LQ-gain. Assigning larger weight to a particular state means penalizing more for oscillation of that state, while larger weight to a particular input means assigning higher cost of utilizing the particular input. In this work, the initial state and input weights were assigned based on participation factor analysis i.e. by giving higher penalty to the states with higher participation in the modes of interest. Then the weights are tuned to achieve the maximum damping to the selected modes without deteriorating the damping of other modes. The direction of weights i.e. either to decrease or increase the weight is based on sensitivity analysis of damping of modes with respect to weights of the state. Using this technique, a set of weights is obtained that meets the design requirements. The controller was tested for robustness by randomly varying the operating point of the system. The advantage of LQG based control using wide area signals over local PSS design for DFIG is evident when tested on 68-bus system. LQG control successfully damped the two critical inter-area modes of the system that was otherwise unaffected by PSS design approach. The stability of the closed loop system, however, is only guaranteed if the observer is stable and the plant can be stabilized with the LQR. Thus, the robustness has been an issue with LQG control. Another drawback of this method is

the lack of direct relationship between the weight matrices and the damping of the oscillatory modes.

One of the challenges in power system control design is the difficulty to obtain a detailed and accurate model of the power system. Usually the power system models used today are approximate models marred with modeling error and uncertainty. One approach that is gaining popularity lately is to estimate the reduced order model of the system based on measurement of input and output of a dynamically perturbed system. In this work, canonical variate analysis (CVA) algorithm is used, which provides the subspace state space model from block measurement of inputs and outputs of the system. The criteria and methodology for selection of inputs and outputs has been discussed. The accuracy of the estimated model frequency response has been shown using bode plot. The estimated model is validated using validation data set that was not used during the estimation of the model. Finally, the output feedback gain matrix is computed using non-linear optimization technique. The main objective of the power system damping controller is to shift the dominant eigenvalues towards the left half plane to ensure that the system is stable and the oscillations are damped faster. Thus, designing an output feedback based oscillation damping controller for power system was formulated as a nonlinear optimization problem with existing system constraints such as feedback gain limits. This approach was used to design an optimal output feedback gain matrix that would enhance the damping of the system. The controller performance and robustness against time delay and system operating point changes have been validated. The main advantage of this technique is that the system identification can track the changing operating point of the system, and the optimization algorithm can utilize the identified system model to compute new gain matrix that maximizes the damping of the least damped inter-area modes. Moreover, it does not require the construction of state observer to estimate the states as direct output feedback approach is used. Thus, it provides a direct methodology to achieve

the system damping requirement.

7.2 Future Works

The current work focused solely on the power oscillation damping capability of DFIG and design of oscillation damping control architecture that can be used with DFIGs. Similar control technique can be applied to other forms of distributed energy resources such as solar photovoltaics, battery energy storage system etc. which have fast response capability of controlling active and/or reactive power injection. These techniques are applicable to other power electronic devices such as FACTS and HVDCs. However, detailed study is necessary to study their individual potential and constraints considering their impact on system dynamics and machine itself. The present work can also be extended to design of coordinated wide area power system control considering existing synchronous generators, and all other forms of controllable devices available such as wind, solar, storage, FACTS, HVDC etc. The coordinated approach would provide better response to the system disturbance. Moreover, demonstration of the control in real-time simulation environment can be performed.

APPENDIX A: SMALL SIGNAL STABILITY

Small signal stability is defined as the ability of the power system to maintain synchronism when subjected to small disturbances [27]. The disturbance is regarded as small if the equations describing the system response can be linearized for the purpose of analysis. The small signal stability problem normally occurs due to insufficient damping torque which results in rotor oscillations of increasing amplitude [27]. The following general equations can be used to describe the dynamics of the power system,

$$\dot{x} = h(x, u, t) \tag{A.1}$$

$$y = g(x, u, t) \tag{A.2}$$

For small signal stability analysis, the nonlinear equations of the dynamic power system are first linearized around a specific operating point. The resulting set of linear differential equations describes the dynamic behavior of the power system subject to a small disturbance around this operating point. The linearized equation is of the form,

$$\Delta\dot{x}_i = \frac{\partial h_i}{\partial x_1}\Delta x_1 + ... + \frac{\partial h_i}{\partial x_n}\Delta x_n + \frac{\partial h_i}{\partial u_1}\Delta u_1 + ... + \frac{\partial h_i}{\partial u_r}\Delta u_r \tag{A.3}$$

$$\Delta\dot{y}_j = \frac{\partial g_j}{\partial x_1}\Delta x_1 + ... + \frac{\partial g_j}{\partial x_n}\Delta x_n + \frac{\partial g_j}{\partial u_1}\Delta u_1 + ... + \frac{\partial g_j}{\partial u_r}\Delta u_r \tag{A.4}$$

where, n is the order of the system and r is the number of inputs. The linearized equation can be written in the form,

$$\mathbf{\Delta \dot{x}} = \mathbf{A\Delta x} + \mathbf{B\Delta u} \tag{A.5}$$

$$\mathbf{\Delta y} = \mathbf{C\Delta x} + \mathbf{D\Delta u} \tag{A.6}$$

where, **A**, **B**, **C** and **D** are known as state or plant matrix, input matrix, output matrix and feed forward matrix respectively.

$$\mathbf{A} = \begin{bmatrix} \frac{\partial f_1}{\partial x_1} & \cdots & \frac{\partial f_1}{\partial x_n} \\ \cdots & \cdots & \cdots \\ \frac{\partial f_n}{\partial x_1} & \cdots & \frac{\partial f_n}{\partial x_n} \end{bmatrix}, \qquad \mathbf{B} = \begin{bmatrix} \frac{\partial f_1}{\partial u_1} & \cdots & \frac{\partial f_1}{\partial u_r} \\ \cdots & \cdots & \cdots \\ \frac{\partial f_n}{\partial u_1} & \cdots & \frac{\partial f_n}{\partial u_r} \end{bmatrix} \tag{A.7}$$

$$\mathbf{C} = \begin{bmatrix} \frac{\partial g_1}{\partial x_1} & \cdots & \frac{\partial g_1}{\partial x_n} \\ \cdots & \cdots & \cdots \\ \frac{\partial g_n}{\partial x_1} & \cdots & \frac{\partial g_n}{\partial x_n} \end{bmatrix}, \qquad \mathbf{D} = \begin{bmatrix} \frac{\partial g_1}{\partial u_1} & \cdots & \frac{\partial g_1}{\partial u_r} \\ \cdots & \cdots & \cdots \\ \frac{\partial g_n}{\partial u_1} & \cdots & \frac{\partial g_n}{\partial u_r} \end{bmatrix} \tag{A.8}$$

The state matrix A carries a lot of significant information about the dynamics of the system during small disturbance and thus characterize the stability of the system [27]. The change in design and operating condition of the power system is reflected in the eigenvalues of the system state matrix. The time dependent characteristic of a mode corresponding to an eigenvalue λ is given by $e^{-\lambda t}$. A real positive eigenvalue determines an exponentially increasing behavior while a negative real eigenvalue represents a decaying mode. A complex eigenvalue with positive real part results in an increasing oscillatory behavior and one with a negative real part results in damped oscillation. The real component of the eigenvalue gives the damping and the imaginary component gives the frequency of oscillation. The frequency of oscillation (f)

and damping ratio (ζ) of a complex eigenvalue ($\lambda = \sigma + j\omega$) can be represented as:

$$f = \frac{\omega}{2\pi} \tag{A.9}$$

$$\zeta = -\frac{\sigma}{\sqrt{\sigma^2 + \omega^2}} \tag{A.10}$$

The damping ratio gives the rate of decay of the amplitude of the oscillation. Eigenvalues of the state matrix A and the associated right eigenvector (ϕ) and left eigenvector (ψ) are defined as:

$$A\phi = \phi\lambda \tag{A.11}$$

$$\psi A = \lambda\psi \tag{A.12}$$

$$\phi\psi = I \qquad i.e. \qquad \psi = \phi^{-1} \tag{A.13}$$

The component of the right eigenvector gives the mode shape, that is, the relative activity of the state variables when a particular mode is excited. For example, the degree of activity of the state variable x_j in the i^{th} mode is given by ϕ_{ji} of right eigenvector ϕ_i. The j^{th} element of the left eigenvector psi_i weighs the contribution of this activity to the i^{th} mode. The participation factor of the jth state variable (x_j) in the i^{th} mode is defined as the product of the j^{th} component of the right and left eigenvectors corresponding to the i^{th} mode:

$$p_{ji} = \phi_{ji}\psi_{ij} \tag{A.14}$$

While designing output feedback supplementary controller such as power system stabilizer in synchronous generators or damping controllers in FACTS, it is very useful to analyze modal controllability, observability and residue of transfer function. If

$\Lambda = diag(\lambda_1, \lambda_2, ..., \lambda_n)$, we get

$$\psi A \phi = \Lambda \tag{A.15}$$

Using Laplace Transform, A.5 can be written as:

$$Y(s) = C\phi(sI - A)^{-1}\psi B U(s) + DU(s) \tag{A.16}$$

$$\frac{Y_j(s)}{U_i(s)} = G_{ij}(s) = D + \sum_{k=1}^{n} \frac{R_k}{s - \lambda_k} \tag{A.17}$$

R_k is the residue of the transfer function of the eigenvalue λ_k. The residue is determined as a product of modal controllability gramian m_c and modal observability gramian m_o such that:

$m_c = \psi B$

$m_o = C\phi$ and

$R_k = C_j \phi_k \psi_k B_i$

Participation factor analysis, controllability and observability gramian, and transfer function residue analysis are frequently used in designing control system of linear time invariant systems.

REFERENCES

[1] Lazrd, Lazard's Levelized Cost of Energy Analysis - Version 11.0, Nov. 2017.

https://www.lazard.com/media/450337/lazard-levelized-cost-of-energy-version-110.pdf

[2] "Wind Energy Facts at a Glance." AWEA - American Wind Energy Association. N.p., n.d. Web. 20 Apr. 2017.

[3] "U.S. number one in the world in wind energy production", www.awea.org. American Wind Energy Association. Retrieved 4 March 2016.

[4] "Wind Vision: A New Era for Wind Power in the United States", www.energy.gov U.S. Department of Energy. 2008.

[5] "Global Wind Statistics 2017", Global Wind Energy Council (GWEC)

$http : //gwec.net/wp - content/uploads/vip/GWEC_PRstats2017_EN - 003_FINAL.pdf$

[6] N. Miller, Z. Ye, "Report on distributed generation penetration study," National Renewable Energy Laboratory, CO, Tech Rep. August 2003. Available online: www.nrel.gov/docs/fy03osti/34715.pdf

[7] P. M. Anderson and A. A. Fouad, *Power System Control and Stability*, N.J.: John Wiley & Sons, Inc., 2002.

[8] M. Tsili and S. Papathanassiou, "A review of grid code technical requirements for wind farms," in *IET Renewable Power Generation*, vol. 3, no. 3, pp. 308-332, Sept. 2009. doi: 10.1049/iet-rpg.2008.0070

[9] Heier S (1998) *Grid integration of wind energy conversion systems*. Wiley, Chichester

[10] Slootweg JG, de Haan SWH, Polinder H, Kling WL (2003) "General model for representing variable speed wind turbines in power system dynamics simulations", *IEEE Trans Power Syst* 18(1):144-151

[11] Slootweg JG, "Wind Power: Modelling and Impact on Power System Dynamics". *PhD Thesis*, Power Systems Laboratory, Deft University of Technology, 2003.

[12] CIGRE (2000) "Modeling new forms of generation and storage", *CIGRE Technical Brochure*, TF 38.01.10

[13] Muyeen SM et al (2007) "Comparative study on transient stability analysis of wind turbine generator system using different drive train models", *IET Renew Power Gener* 1(2):131-141

[14] C. Eping, J. Stenzel, M. Poeller, H. Mueller, "Impact of large scale wind power on power system stability". *Fifth International Workshop on Large-scale Integration of Wind Power and Transmission Networks for Offshore Wind Farms*, Glasgow, 9 pp, 2005

[15] E. Muljadi, C. Butterfield, B. Parsons, A. Ellis, "Effect of variable speed wind turbine generator on stability of a weak grid." *IEEE Transactions on Energy Conversion* 2007;22:29-36.

[16] G. Tsourakis, B. M. Nomikos and C. D. Vournas, "Contribution of Doubly Fed Wind Generators to Oscillation Damping," in *IEEE Transactions on Energy Conversion*, vol. 24, no. 3, pp. 783-791, Sept. 2009.

[17] G. Tsourakis, B. Nomikos, C. Vournas, "Effect of wind parks with doubly fed asynchronous generators on small-signal stability." *Electric Power Systems Research* 2009;79:190-200.

[18] D. Vowles, C. Samarasinghe, M. Gibbard, and G. Ancell, "Effect of wind generation on small-signal stability a new zealand example," in *IEEE Power and Energy Society General Meeting - Conversion and Delivery of Electrical Energy in the 21st Century*, 2008, July 2008, pp. 1 -8.

[19] A. Mendonca and J. Lopes, "Impact of large scale wind power integration on small signal stability," in *International Conference on Future Power Systems*, 2005, nov. 2005, pp. 5 pp. -5.

[20] T. Knu andppel, J. Nielsen, K. Jensen, A. Dixon, and J. Ostergaard, "Small-signal stability of wind power system with full-load converter interfaced wind turbines," *IET Renewable Power Generation*, vol. 6, no. 2, pp. 79 -91, march 2012.

[21] L. Fan, H. Yin and Z. Miao, "On Active/Reactive Power Modulation of DFIG-Based Wind Generation for Interarea Oscillation Damping," in *IEEE Transactions on Energy Conversion*, vol. 26, no. 2, pp. 513-521, June 2011.

[22] J.B. Ekanayake, L. Holdsworth, XG. Wu, N. Jenkins, "Dynamic modelling of doubly fed induction generator wind turbines", *IEEE Trans. on Power Systems*, vol. 18, pp.803-809, May 2003.

[23] R. Pena, J.C. Clare, G.M. Asher, "Doubly fed induction generator using back-to-back PWM converters and its application to variable-speed windenergy generation", *IEE Proc. May 1996 - Electr. Power Appl.*, vol.143, No. 3, May 1996.

[24] R. Cardenas, R. Pena, S. Alepuz, G. Asher, "Overview of control systems for the operation of DFIGs in wind energy applications", *IEEE Trans. Ind. Electron*, vol. 60, no. 7, pp. 2776-2798, Jul. 2013.

[25] L. Xu, P. Cartwright, "Direct active and reactive power control of DFIG for wind energy generation", *IEEE Transactions on Energy Conversion*, vol. 21, no. 3, pp. 750-758, Sept 2006.

[26] F. Taveiros, L. Barros, F. Costa, "Back-to-back converter state-feedback control of DFIG (doubly-fed induction generator)-based wind turbines", *Energy*, vol. 89, pp. 896-906, 2015.

[27] P. Kundur, *Power System Stability and Control*, Mc Graw Hill 1994

[28] P. Kundur, J. Paserba, V. Ajjarapu, G. Andersson, A. Bose, C. Canizares, N. Hatziargyriou, D. Hill, A. Stankovic, C. Taylor, T. V. Custem and V. Vittal, "Definition and classification of power system stability," *IEEE Trans. Power Systems*, vol. 19, no. 2, pp. 1387-1401, May 2004.

[29] IEEE PES Task Force on Benchmark Systems for Stability Controls, "Benchmark Systems for Small-Signal Stability Analysis and Control", 1 Aug 2015. *http://resourcecenter.ieee-pes.org/pes/product/technical-reports/PESTR18*

[30] P. C. Krause, C. H. Thomas, "Simulation of symmetrical induction machinery", *IEEE Transactions on Power Apparatus and Systems*, vol. 84, no. 11, pp. 1038-1053, Nov 1965.

[31] Krause, C., *Analysis of electrical machinery*, McGraw-Hill Book Co., 1986.

[32] M. Singh, S. Santoso, "Dynamic models for wind turbines and wind power plants", *NREL Tech Report*, October 2011

[33] F. Mei, B.C. Pal, "Modelling and Small-Signal Analysis of a Grid Connected Doubly-Fed Induction Generator", *IEEE Power Engineering, Society General Meeting*, pp.2101-2108, Jun, 2005.

[34] F. Mei, B.C. Pal, "Modal Analysis of Grid-Connected Doubly Fed Induction Generators", *IEEE transactions on energy conversion*, vol. 22, no. 3, september 2007.

[35] R. Bhattarai, N. Gurung, and S. Kamalasadan, "Minimum variance adaptive speed estimation technique for vector control of doubly fed induction generator", in *North American Power Symposium (NAPS)*, 2015, pp. 16, Oct 2015.

[36] R. Bhattarai, N. Gurung, S. Kamalasadan, "Reduced order model based state feedback control of doubly fed induction generators", *Power and Energy Society General Meeting (PES GM)*, 2016, July 2016.

[37] N. Gurung, R. Bhattarai and S. Kamalasadan, "Optimal linear-quadratic-integral controller design for doubly-fed induction generator," *2017 IEEE Power and Energy Society General Meeting*, Chicago, IL, 2017, pp. 1-5.

[38] N. Gurung, S. Kamalasadan, "Linear-Quadratic Gaussian based Power Oscillation Damping Controller Design for Doubly Fed Induction Generator", *IEEE PES GM* 2018.

[39] N. Gurung, S. Kamalasadan, "Power System Oscillation Damping Capability of Doubly Fed Induction Generator (DFIG)", *IEEE T and D Conference*, 2018.

[40] R. Bhattarai, N. Gurung, A. Thakallapelli and S. Kamalasadan, "Reduced Order State Observer Based Feedback Control Methodologies for Doubly Fed Induction Machine," in *IEEE Transactions on Industry Applications*, vol. PP, no. 99, pp. 1-1.

[41] N. Gurung, S. Kamalasadan, "Model Identification based Wide Area Control of DFIG Integrated Power System", (in progress).

[42] WECC Modeling and V. W. Group, "WECC Wind Power Plant Dynamic Modeling Guide", *WECC Renewable Energy Modeling Task Force*, August 2010.

[43] WECC Modeling and V. W. Group, "WECC Wind Plant Dynamic Modeling Guidelines", *WECC Renewable Energy Modeling Task Force*, April 2014.

[44] M. Yamamoto, O. Motoyoshi, "Active and reactive power control for doubly-fed wound rotor induction generator", *IEEE Trans. Power Electron.*, 1991, 6, (4), pp. 624-629.

[45] N. Mohan, *Power Electronics*, 3^{rd} ed., John Wiley and Sons, 2003, p. 228.

[46] P. S. Sauer, M. A. Pai, *Power System Dynamics and Stability*, PrenticeHall 1998.

[47] F. M. Hughes, O. A. Lara, N. Jenkins, G. Strbac, "A power system stabilizer for DFIG-based wind generation", *IEEE Trans. Power Syst.*, vol. 21, no. 2, pp. 763-772, May 2006.

[48] F. M. Hughes, O. A. Lara, N. Jenkins and G. Strbac, "Control of DFIG-based wind generation for power network support", *IEEE Trans. Power Systems*, vol. 20, no. 4, pp. 1958-1966, November 2005.

[49] F. M. Hughes, O. A. Lara, N. Jenkins, G. Strbac, "A power system stabilizer for DFIG-based wind generation", *IEEE Trans. Power Syst.*, vol. 21, no. 2, pp. 763-772, May 2006.

[50] J. J. Sanchez Gasca, N. W. Miller, and W. W. Price, "A modal analysis of a two-area system with significant wind power penetration", in *Proc. 2004 IEEE PES Power Systems Conf. Expo.*

[51] D. Gautam,V. Vittal,and T. Harbour, "Impact of increased penetration of DFIG-based wind turbine generators on transient and small signal stability of power systems", *IEEE Trans. Power Syst.*, vol. 24,no. 3,pp. 1426-1434,Aug,2009.

[52] D. Gautam, "Impact of Increased Penetration of DFIG Based Wind Turbine Generators on Rotor Angle Stability of Power Systems", *PhD Thesis*, Arizona State University, December 2010

[53] D. Gautam, L. Goel, R. Ayyanar, V. Vittal and T. Harbour, "Control Strategy to Mitigate the Impact of Reduced Inertia Due to Doubly Fed Induction Generators on Large Power Systems," in *IEEE Transactions on Power Systems*, vol. 26, no. 1, pp. 214-224, Feb. 2011.

[54] L. P. Kunjumuhammed, B. C. Pal, K. K. Anaparthi, N. F. Thornhill, "Effect of wind penetration on power system stability", *Proc. IEEE Power and Energy Soc. General Meeting*, pp. 1-5, Jul. 2013.

[55] P. C. Young and J. C. Willems, "An approach to the linear multivariable servomechanism problem", *Int. J. Control*, vol. 15, pp. 961-979, 1972.

[56] M. Kayikci and J. V. Milanovic, "Assessing transient response of DFIG-based wind plants-the influence of model simplifications and parameters", *IEEE Trans. Power Systems*, vol. 23, no. 2, pp. 545-554, May 2008.

[57] L. Rouco, "Eigenvalue-based methods for analysis and control of power system oscillations," in Proc. *1998 IEE Colloquium on Power Dynamics Stabilization*, pp. 1-6.

[58] F. Blaabjerg, Z. Chen, "Power Electronics for Modern Wind Turbines," Morgan and Claypool, 2006.

[59] Y. Zhang and A. Bose, "Design of Wide-Area Damping Controllers for Interarea Oscillations," in *IEEE Transactions on Power Systems*, vol. 23, no. 3, pp. 1136-1143, Aug. 2008.

[60] Y. Li, C. Rehtanz, S. Ruberg, L. Luo and Y. Cao, "Wide-Area Robust Coordination Approach of HVDC and FACTS Controllers for Damping Multiple Interarea Oscillations," in *IEEE Transactions on Power Delivery*, vol. 27, no. 3, pp. 1096-1105, July 2012.

[61] Hui Ni, G. T. Heydt and L. Mili, "Power system stability agents using robust wide area control," in *IEEE Transactions on Power Systems*, vol. 17, no. 4, pp. 1123-1131, Nov 2002.

[62] I. Kamwa, R. Grondin and Y. Hebert, "Wide-area measurement based stabilizing control of large power systems-a decentralized/hierarchical approach," in *IEEE Transactions on Power Systems*, vol. 16, no. 1, pp. 136-153, Feb 2001.

[63] N. Martins and L. T. G. Lima, "Determination of suitable locations for power system stabilizers and static VAR compensators for damping electromechanical oscillations in large scale power systems," in *IEEE Transactions on Power Systems*, vol. 5, no. 4, pp. 1455-1469, Nov 1990.

[64] A. Zolotas, B. Chaudhuri, I. Jaimoukha, and P. Korba, "A study on LQG/LTR control for damping inter-area oscillations in power systems," *IEEE Trans. Control Syst. Technol.*, vol. 15, no. 1, pp. 151-160, Jan. 2007.

[65] A. K. Singh, B. C. Pal, "Report on the 68-bus 16-machine 5-area system", *IEEE PES Task Force on Benchmark Systems for Stability Controls Ver. 3.3*, 2013.

[66] U. P. Mhaskar and A. M. Kulkarni, "Power oscillation damping using FACTS devices: modal controllability, observability in local signals, and location of transfer function zeros," in *IEEE Transactions on Power Systems*, vol. 21, no. 1, pp. 285-294, Feb. 2006.

[67] A. Varga, "Balancing-Free Square-Root Algorithm for Computing Singular Perturbation Approximations," *Proc. of 30th IEEE CDC*, Brighton, UK (1991), pp. 1062-1065.

[68] J. J. Sanchez-Gasca and J. H. Chow, "Power system reduction to simplify the design of damping controllers for interarea oscillations," in *IEEE Transactions on Power Systems*, vol. 11, no. 3, pp. 1342-1349, Aug 1996.

[69] M. G. Safonov and R. Y. Chiang, "A Schur method for balanced-truncation model reduction," in *IEEE Transactions on Automatic Control*, vol. 34, no. 7, pp. 729-733, Jul 1989.

[70] S. Skogestad and I. Postlethwaite, Multivariable Feedback Control: Analysis and Design. New York: Wiley, 2000.

[71] P. Korba, K. Uhlen, "Wide -area monitoring of electromechanical oscillations in the Nordic power system: practical experience ." *IET Generation, Transmission & Distribution Journal*, Special Issue on Wide Area Monitoring, Protection and Control, Vol. 4, Iss. 10, 2010.

[72] N. Zhou, J. Pierre, and J. Hauer, "Initial results in power system identification from injected probing signals using a subspace method," *IEEE Trans. Power Syst.*, vol. 21, no. 3, pp. 1296-1302, Aug. 2006.

[73] R. Eriksson and L. Soder, "Wide-Area Measurement System-Based Subspace Identification for Obtaining Linear Models to Centrally Coordinate Controllable Devices," *IEEE Transactions on Power Delivery*, vol. 26, no. 2, pp. 988-997, April 2011.

[74] N. Zhou, J. W. Pierre, D. Trudnowski, and R. Guttromson "Robust RLS Methods for On-line Estimation of Power System Electromechanical Modes," *IEEE Transactions on Power Systems*, vol. 22, no.3, pp.1240-1249, August 2007.

[75] N. Zhou, D. J. Trudnowski, J. W. Pierre and W. A. Mittelstadt, "Electromechanical Mode Online Estimation Using Regularized Robust RLS Methods," *IEEE Transactions on Power Systems*, vol. 23, no. 4, pp. 1670-1680, Nov. 2008.

[76] H. Liu et al., "ARMAX-Based Transfer Function Model Identification Using Wide-Area Measurement for Adaptive and Coordinated Damping Control," in *IEEE Transactions on Smart Grid*, vol. 8, no. 3, pp. 1105-1115, May 2017. doi: 10.1109/TSG.2015.2470648

[77] H. Akaike, "Canonical Correlation Analysis of TIme Series and the Use of an Information Criterion," *System Identification: Advances and Case Studeis*, R.K. Mehra and D.G. Lainiotis, eds., New York: Academic Press, pp.27-96.

[78] H. Hotelling, "Relations Between Two Sets of Variates," *Biometrika*, Vol. 28,pp. 321-377

[79] W.E. Larimore, "A Unified View of Reduced Rank Multivariate Prediction Using a Generalized Singular Value Decomposition," Technical Report, Scientific Systems Inc., Cambridge, MA, 1987.

[80] W.E. Larimore, "System Identification, ReducedOrder Filtering and Modeling Via Canonical Variate Analysis", *Proc. 1983 American Control Conference*, H.S. Rao and T. DoratQ, Eds., pp. 445-51.New York: IEEE.

[81] R.P. Peloubet, R.L. Haller, R.M Bolding, "On-line Adaptive Control of Unstable Aircraft Wing Flutter," 29^{th} *IEEE Conference on Decision and Control*, 1990.

[82] M. Gevers, and V. Wertz, "On the Problem of Structure Selection for the Identification of Stationary Stochastic Processes", *Sixth IFAC Symposium on Identification and System Parameter Estimation*, Eds. G. Bekey and G. Saridis, Washington D.C.: McGregor & Werner, pp.387-92.

[83] A. Lindquist, and M. Pavon, "Markovian Representation of Discrete-Time Stationary Stochastic Vector Processes," 20^{th} *IEEE Conference on Decision and Control*, Vol. 3,pp. 1345-56.

[84] P.T. Boggs, J.W. Tolle, Sequential quadratic programming. *Acta Numerica* 1996, pp 1-000.